Politecnico di Torino

ScuDo
Scuola di Dottorato ~ Doctoral School
WHAT YOU ARE, TAKES YOU FAR

Doctoral Dissertation
Doctoral Program in Electrical, Electronics and Communications Engineering
(34^{th}cycle)

Boundary Conditions Estimation Techniques for Cardiovascular Modeling

By

Elisa Fevola

******

Supervisor(s):
Prof. Stefano Grivet-Talocia, Supervisor
Prof. Piero Triverio, Co-Supervisor

Doctoral Examination Committee:
Prof. David A. Steinman, Referee, University of Toronto
Prof. Owais Khan, Referee, Toronto Metropolitan University
Prof. Angelo Rivetti, Istituto Nazionale di Fisica Nucleare (INFN)
Prof. Zheng Zhang, University of California, Santa Barbara (UCSB)
Prof. Paolo S. Crovetti, Politecnico di Torino

Politecnico di Torino
2022

Declaration

I hereby declare that, the contents and organization of this dissertation constitute my own original work and does not compromise in any way the rights of third parties, including those relating to the security of personal data.

Elisa Fevola
2022

* This dissertation is presented in partial fulfillment of the requirements for **Ph.D. degree** in the Graduate School of Politecnico di Torino (ScuDo).

Acknowledgements

I would like to express my sincere gratitude to my advisor Stefano Grivet-Talocia, for his invaluable guidance throughout this journey. He encouraged me to follow my passion and explore my scientific curiosity, even when this required enormous trust in me. For this, I will be forever grateful.

I would like to extend my warmest gratitude to my co-advisor, Piero Triverio. His excitement for science, dedication, and scientific integrity have been a constant source of inspiration. I am also grateful for his warm hospitality during my visit to the University of Toronto, which, despite the difficult times, has been one of the most exciting parts of my Ph.D.

I would also like to thank Gianluigi Rozza for generously hosting me at the International School of Advanced Studies in Trieste and for providing me with his precious mentorship and guidance. I extend my warmest thanks to Francesco Ballarin for his patient and kind support throughout these years.

I also thank Laura Jiménez-Juan and Stephen Fremes for their precious insights during our collaboration.

I have been fortunate to share this journey with many wonderful colleagues and friends. I want to thank the members of the EMC group at Politecnico di Torino, especially my office mates, for the fruitful discussions and the fun moments we shared. I am also grateful to the members of the SISSA MathLab group, who warmly welcomed me in Trieste and made me feel part of their family. In particular, I want to thank Maria for her invaluable scientific support and for her help in finding my path. A special thank you goes to the members of the Modelics group at the University of Toronto, who accompanied me for a long part of this journey.

Finally, I thank my family and friends for their support during these years. I am grateful to my parents, Mariangela and Giorgio, and my sister, Ilaria, for their unconditional love, trust, and encouragement. The biggest thank you goes to Antonio, without whom none of this would have been possible.

Abstract

Cardiovascular diseases are the leading cause of mortality worldwide, responsible for more than 17 million deaths every year. For this reason, the study of the cardiovascular system and of the mechanisms governing blood flow has attracted significant and increasing interest from both the medical and engineering communities. In this context, computational models of the cardiovascular system have been increasingly adopted for studying the role of blood flow in the development of cardiovascular diseases, and have proved useful for a number of tasks, including surgical planning, non-invasive diagnostics, and medical device evaluation.

In order to be safely and effectively used in real-life clinical scenarios, cardiovascular models need to be accurate and reliable. One of the biggest challenges is represented by the estimation of appropriate boundary conditions (BCs), which need to be imposed at the boundaries of the domain of interest, to provide a description of blood flow dynamics outside the model. Boundary conditions are essential to guarantee a unique solution to the system, and they are a crucial step in the creation of any computational model. Specifically, the estimation of boundary conditions needs to be *automated*, to facilitate the adoption of cardiovascular models in the clinic, *robust*, to ensure reproducibility and prevent inter- and intra-operator variability, and *patient-specific*, to personalize the model to the specific patient. Toward these goals, this thesis proposes a set of novel, automated, and robust techniques for the estimation of boundary conditions.

The thesis is organized into three main parts. In the first part, a *data and model-driven* approach is presented, where resistive boundary conditions are estimated by solving an optimal control problem. The choice of boundary conditions, in fact, is guided by an effective combination of patient-specific data

and by a physical description of the underlying system, by means of the Stokes equations. The proposed method is tested on fully patient-specific cases, with anatomies reconstructed from CT images of the aortic arch, flow measurements coming from 4D-Flow MRI, and non-invasive pressure measurements.

The second part presents a novel framework for the automated estimation of higher order lumped parameter boundary conditions, by means of the time-domain vector fitting algorithm. The purely *data-driven* nature of this approach leads to a fast and inexpensive estimation process, while enabling the adoption of more accurate boundary conditions of arbitrary complexity, in the form of black-box models.

In the last part of the dissertation, a numerical investigation of the minimum energy principle in patient-specific anatomies is conducted. In view of the limited availability of patient-specific measurements, BC estimation techniques which do not require in-vivo measurements, and are instead *physics and anatomy-based*, are particularly attractive. Among these, the minimum energy principle is often adopted in the form of Murray's law, for the selection of resistive outlet boundary conditions. The proposed investigation verifies if a minimum energy point also exists in realistic anatomies, if it can be identified numerically, and if it can be used as a possible criterion for inlet flow estimation.

In summary, this dissertation provides a set of novel techniques for the estimation of boundary conditions. Their validity is documented with relevant numerical examples, which prove the effectiveness of an increasingly automated, robust, and patient-specific approach to boundary conditions estimation.

Contents

Chapter 1

Introduction

Cardiovascular diseases are currently the leading cause of mortality worldwide, causing around 17.9 million deaths every year [1]. In Europe, around 45% of all deaths can be imputed to cardiovascular diseases, and this number is expected to increase over the next decades, as a result of population growth and aging, combined with the rise of risk factors such as obesity, poor diet, high blood pressure, and diabetes [2]. For this reason, the study of the cardiovascular system and of the mechanisms governing blood flow, especially in presence of cardiovascular disease, has attracted significant and increasing interest from the medical, bioengineering, and mathematical communities.

In this context, computational fluid dynamics (CFD) has been increasingly adopted for studying the role of blood flow in the development of cardiovascular diseases [3, 4]. As in other engineering disciplines, where computational models are commonly used to avoid expensive experiments and virtually test different design choices, also in medicine and cardiology computational modeling represents a valuable tool in unfolding the mechanisms behind blood flow, and providing personalized therapies [5, 6].

Cardiovascular models can be employed for a number of tasks, from general research on cardiovascular disease, to surgical planning, non-invasive diagnosis, and possibly medical device evaluation [7, 8]. Computational models have been already extensively used to obtain a better understanding of haemodynamics in different parts of the cardiovascular system, such as the carotid arteries [9, 10], the coronary circulation [11], the heart [12, 13], and the cerebral circulation [14,

15]. In surgical interventions, surgeons could use computational models to support their decision making process, by simulating different surgical scenarios, and predict their outcomes [16]. Moreover, computational models can be used to obtain non-invasively clinical quantities of interest, which would not be measurable *in-vivo*, or which would require expensive and invasive procedures. An example is the measurement of pressure differences in coronary arteries, also known as fractional flow reserve (FFR), in place of catheterization [17]. In this case, an approach based on cardiovascular modeling is currently employed by clinicians for the computation of FFR, thanks to commercial products such as HeartFlow [18]. On a larger time-frame, computational investigations could enable personalized therapies and prospective studies on long-term effects of surgeries and treatments, and possibly the identification of new predictors for cardiovascular pathologies [19]. Finally, cardiovascular models can play an important role in the development of medical devices, by providing new information on the environment where devices are employed, and evaluating the effect of the devices on human physiology [20, 21].

In order to be safely and effectively used in real-life clinical scenarios, cardiovascular models need to be accurate and reliable. To this end, a first step has been made by combining CFD with advanced imaging techniques [22–24] to reproduce the functional and morphological conditions of a specific patient, by means of the so-called *patient-specific models*. Such models, in fact, are obtained by reconstructing a three-dimensional model of the anatomy of interest starting from imaging data, and then solving a set of partial differential equations (PDE), usually Navier-Stokes equations, describing the blood flow dynamics inside the model. Patient-specific models represent a promising instrument in view of an increasingly personalized approach to surgeries, treatments, and medicine at large. However, there are still a number of challenges to tackle in order to make cardiovascular models more accurate and reliable. Considering the extension and complexity of the cardiovascular system, usually only a limited portion of it is represented in 3D, while the rest is represented by means of boundary conditions (BCs), a set of conditions that need to be imposed at the boundaries of the domain of interest, to provide a description of blood flow dynamics outside the model. Boundary conditions are essential to guarantee a unique solution to the system, and they are a crucial step in the creation of any computational model. As a matter of fact, one of the biggest challenges in the

creation of an accurate cardiovascular model is represented by the estimation of appropriate boundary conditions. Specifically, the estimation of boundary conditions needs to be: i) automated, to facilitate the adoption of cardiovascular models in a clinical setting; ii) robust, to ensure reproducibility and prevent inter- and intra-operator variability; iii) patient-specific, to personalize the model to the specific patient. Toward these goals, we present in this thesis a set of novel, automated, and robust techniques for the estimation of boundary conditions.

This chapter first discusses the background related to boundary conditions needed to understand the rest of the dissertation, providing also an overview of other methods previously proposed in literature (Section 1.1). Then, the main contributions of this thesis are reviewed (Section 1.2), together with the overall organization of the dissertation (Section 1.3).

1.1 Background and motivation

The development of patient-specific cardiovascular models highly benefits from the advancements in both imaging and computational techniques, which have helped *in-silico* methods become a flexible and cost-effective alternative to both *in-vivo* and *in-vitro* approaches. A patient-specific cardiovascular model is generally created from a set of imaging data, which are converted to a three-dimensional model suitable for CFD simulations by a number of steps, as depicted in Fig. 1.1, where the standard pipeline for the creation of a cardiovascular model is displayed.

As indicated in Fig. 1.1, the starting point consists of a set of examinations performed on the patient through imaging techniques. These may be computed tomography (CT), magnetic resonance imaging (MRI), or ultrasound imaging [4]. CT is an X-ray angiography technique used for identifying the vessel lumen, where multiple X-ray sources and detectors are rotated rapidly around the patient, allowing to acquire images with good spatial resolution. MRI, instead, uses magnetic fields and radio waves to generate images of the vessels in the body. Lastly, ultrasound imaging is based on the transmission of beams of low power, high frequency sound waves. Whenever possible, additional patient-specific flow measurements can be gathered from imaging, either

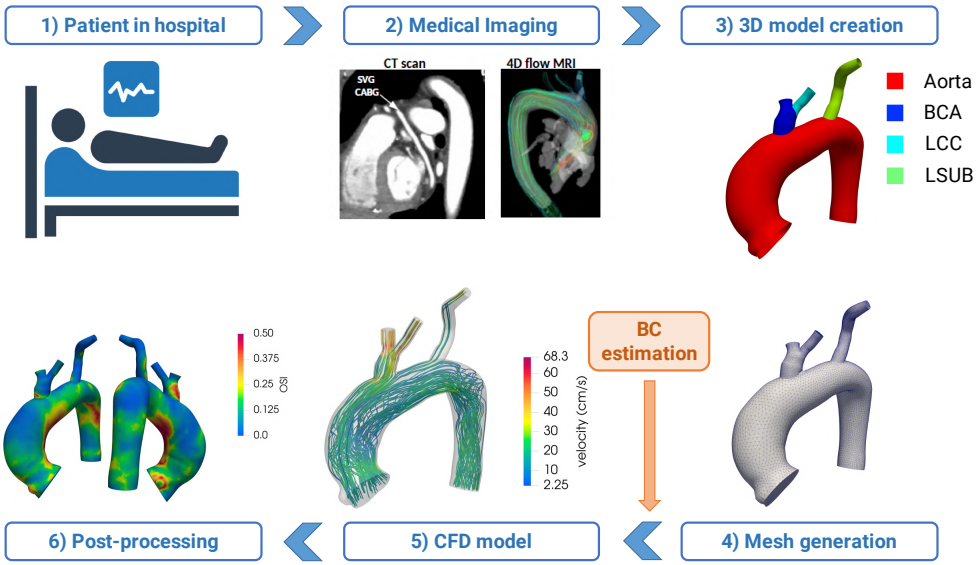

Fig. 1.1 Representation of the pipeline used for the creation of cardiovascular models.

from Doppler ultrasonography, or through phase-contrast magnetic resonance imaging (PC-MRI), a specific type of MRI employed to determine flow velocities. When three-dimensional PC-MRI is time-resolved, it is generally called 4D-Flow MRI, allowing to measure and visualize the temporal evolution of blood flow within a specific 3D volume [25]. Once the CT images have been acquired, they can be used to obtain a three-dimensional anatomical model of the vessels of interest (third step in Fig. 1.1). The segmentation of CT images detects the points of the image belonging to the vessel lumen, providing in this way a three-dimensional anatomical model of the vessels [4]. At this point, a volumetric mesh can be generated on the 3D model, as indicated in the fourth step of Fig. 1.1, which is instrumental to the following CFD analysis. The next step consists in solving a set of partial differential equations, usually Navier-Stokes equations, which describe the blood flow dynamics on the 3D anatomy of interest. The solution of these equations provides point-wise values for both pressure and velocity across the entire domain, enabling a post-processing phase (step 6), where clinically relevant quantities, such as wall shear stress and oscillatory shear index, are computed from CFD results [26].

When creating a cardiovascular model, the main goal is to produce results that are sufficiently accurate, reproducing in a virtual environment a good approximation of the blood flow dynamics occurring in the patient, while

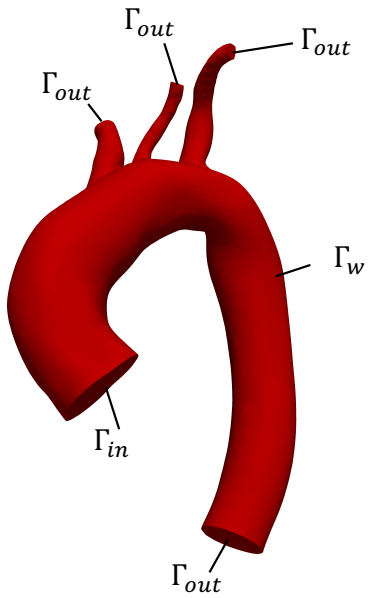

Fig. 1.2 3D rendering of the anatomy of an aortic arch, with the various parts of the boundary labeled. Γ_{in} denotes the surface of the inlet, Γ_w the walls of the vessels, and Γ_{out} combines the surfaces of all the outlets.

ensuring that the computational time of the simulations is under reasonable limits. In this sense, one of the major factors determining the accuracy of the computed flow fields is the appropriate specification of *boundary conditions*. The solution of a system of partial differential equations is uniquely determined only if proper conditions are imposed at the boundary of the domain, and for this reason a 3D simulation of blood flow can be performed only after boundary conditions have been specified, as indicated in Fig. 1.1. The role of boundary conditions is to provide a realistic representation of blood pressure and flow in the upstream and downstream regions of the cardiovascular system, outside the regions of interest. Referring for example to the model represented in Fig. 1.2, one has to define conditions at the inlet, at the outlets, and on the walls of the vessels. The latter is the only physical boundary, where generally a *no-slip* condition is imposed [4], meaning that the blood velocity is assumed to be zero in correspondence of the vessel walls. Both the inlets and the outlets, on the contrary, are *artificial* boundaries, which do not correspond to real boundaries in the original system. Nevertheless, they are essential to isolate a specific region of interest, as the simulation of the entire cardiovascular system would be computationally unfeasible.

Despite the advancements in haemodynamics modeling, the definition of proper boundary conditions is still a critical and challenging task. Specifically, there are two main challenges related to boundary conditions:

- choosing the *type* of boundary condition, which must give a good approximation of the blood flow dynamics in the upstream and downstream vasculature. Different types of boundary conditions, for example, may impose the pressure at the boundary, the flow rate, or a relationship between them;
- once the type of boundary condition has been chosen, its *parameters* must be estimated. Depending on the type of boundary condition selected, this process could translate into a large number of parameters to estimate.

The two challenges will be analysed separately in the following sections.

1.1.1 Types of boundary conditions

Generally, at the inlet a time and spatially varying velocity boundary condition is applied. The imposed velocity profile can be idealized (flat, fully developed or Womersley flow pattern), or based on clinical measurements, like PC-MRI, 4D-Flow MRI, or ultrasound [27, 28]. On the other hand, the use of time-dependent pressure waveforms as inlet boundary conditions is less common, mainly due to the difficulties in obtaining pressure measurements through catheterization, and their poor precision [29]. Alternatively, a lumped description of the heart can be coupled to the inlet boundary [30, 31].

The representation of outlet boundary conditions, instead, is typically more challenging, due to the limited availability of clinical measurements, but also to the intrinsic difficulty to model such a large portion of the vasculature. Different outlet conditions have been proposed, and the most common approaches consist in:

- applying a constant or time varying pressure value. In particular, the use of a "zero-pressure" outlet or traction-free boundary condition is popular due to its simplicity [32]. However, this is equivalent to assuming that the vessel has been cut and exposed to atmospheric pressure [33],

a rather unnatural and unrealistic assumption that neglects the rest of the downstream vessels. Additionally, the obtained blood pressure in the domain will not be in the physiologic range, hindering the validity of the obtained results [34]. For this reason, this type of condition should be avoided;

- prescribing a specific flow rate, which could have been measured in-vivo, or have been computed as constant fractions of the inflowing blood (flow-split condition). However, this type of condition is not realistic, and flow division is expected to change during the cardiac cycle [35];

- using a more advanced representation of the downstream vasculature by means of ordinary differential equations (ODE), which can be interpreted as the governing equations of lumped-parameter networks, also known as zero-dimensional (0D) models [36]. Lumped parameter models are described by resistance, capacitance and inductance parameters, which are set to describe the desired blood flow dynamics in the downstream domain;

- using one-dimensional (1D) models, also called distributed parameter models, where the length, diameter, and material properties of each vessel segment are assigned [36]. In this case, the three-dimensional space dependence is reduced to a single dimension, coinciding with the axial coordinate.

In many cases 0D boundary conditions are adopted, as they provide sufficient accuracy, while depending only on a few parameters, thus making their estimation feasible. By means of an analogy to an electrical circuit, in fact, the resistive, elastic, and inertial properties of blood flow through the vessels are lumped and represented as equivalent electrical elements. The relationship between pressure and flow at the outlet, then, is described by the associated set of ordinary differential equations (ODE) which govern the electrical circuit [4].

In the context of 0D outlet boundary conditions, various circuit models have been employed, from simple resistors, to more complex R-C-R circuits [37] and circuits describing circulation in the distal part of coronary arteries [38]. Here, again, the selected model represents a trade-off between accuracy and circuit complexity, reflected by the number of circuit elements. For this reason,

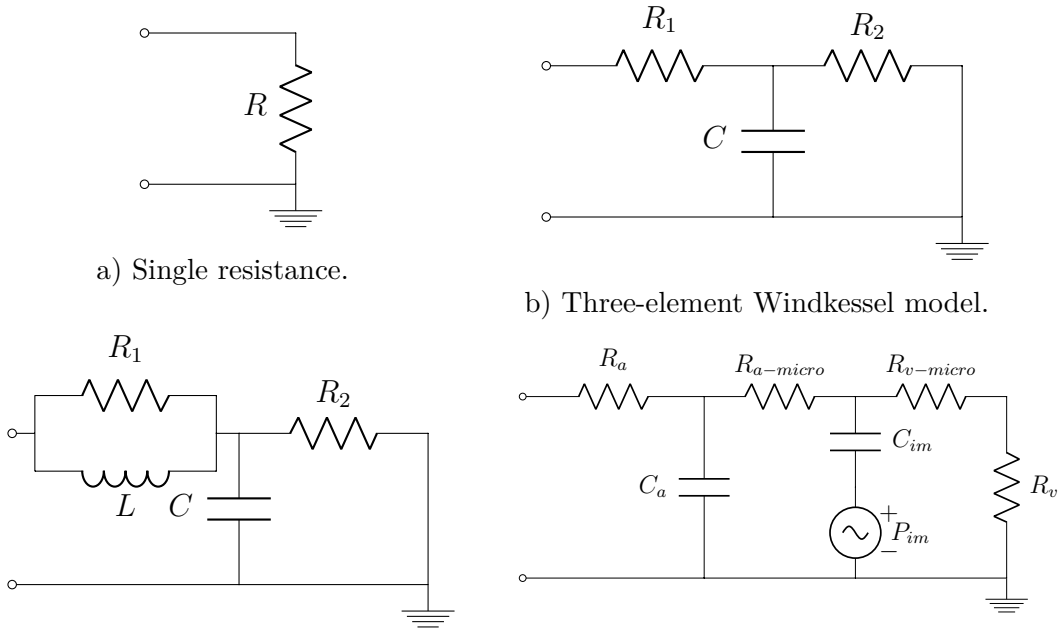

Fig. 1.3 A collection of lumped parameter models commonly used as 0D boundary conditions [4, 43].

a model commonly adopted is the three-element Windkessel model, a circuit composed by two resistances and a capacitance, as depicted in Fig. 1.3. It was originally proposed by Westerhof in 1971 [39], who expanded the original two-element Windkessel introduced by Hales in 1733 and mathematically described by Otto Frank in 1899 [40, 41]. Despite its reduced complexity, the Windkessel model is able to represent both the proximal and the distal resistance of the vessels (by means of the resistances R_1 and R_2 in Fig. 1.3-b, respectively), and their compliance (by means of the capacitor C in Fig. 1.3-b). To account for the inertial effects of blood flow, an inductance L can be added to the three-element Windkessel model, obtaining the four-element Windkessel represented in Fig. 1.3-c [42]. The model adopted for the distal coronary circulation reported in Fig. 1.3-d) is composed by multiple compartments, representing the different parts of the coronary circulation. In addition, the pressure source P_{im} takes into account the time-varying intramyocardial pressure.

In summary, different types of boundary conditions can be used in cardiovascular modeling, and the adoption of one type over the others will have a

significant impact on flow and pressure fields, resulting in differences also in the haemodynamic indicators used in clinical settings [44, 45].

1.1.2 Estimation techniques for boundary conditions

Once a BC model has been selected, it is necessary to estimate its parameters. These could be a single pressure value, in the case of a constant pressure condition, or a set of values for the electrical elements of a lumped parameter network. Ideally, boundary conditions should be set starting from pressure and flow rate measurements in the corresponding positions of the circulatory system. Having patient-specific boundary conditions directly estimated from in-vivo measurements, in fact, is essential to achieve accurate simulations [46, 47]. However, this process is far from trivial, and several difficulties make parameter estimation a challenging task.

An initial challenge is related to the limited availability of in-vivo measurements: the latter, in fact, are rarely available at the correct location, and when they are, they tend to be noisy, and with limited accuracy. Moreover, many of the measurements require invasive procedures on measurement sites with restricted access, due to the anatomical configuration of vessels. For this reason, a large class of solutions for the parameter estimation of boundary conditions still relies on literature data, animal models and generic population averages [48, 49]. Obviously, this type of approach limits the possibility of producing patient-specific models for a personalized approach to medicine.

If some pressure/flow rate measurements are available, a manual tuning approach is often adopted, where reasonable ranges for each parameter are identified (for example by estimating outlet resistances by means of Murray's law [50]), and the parameter values are iteratively adjusted to make the simulation results match available data [51, 52]. This technique, apart from being tedious and time-consuming, is prone to inconsistencies, and it is affected by inter- and intra-operator variability, with the final choice of parameters somewhat left to the user [53–55]. To overcome this issue, several algorithms and implementations have been presented in the literature, with the aim of automating the parameter tuning procedure [56, 57]. In the following, a general overview of the most common tuning algorithms is provided.

A first class of solutions is based on automated iterative approaches to reduce the difference between measurements and simulation results. Xiao et al. proposed a technique for iteratively calibrating three-element Windkessel boundary conditions to reach a desired systolic and diastolic pressure in a specific vessel [58]. Alimohammadi et al., instead, described an iterative minimization approach for parameter estimation in cardiovascular models for aortic dissection, where the Windkessel parameters were tuned based on invasive pressure measurements [59]. A different approach based on a quasi-Newton method was proposed by Spilker et al. [57], who devised an automated framework to estimate boundary conditions matching patient-specific flow rate and pressure waveforms. Troianowski et al. [60], instead, proposed a procedure to tune three-element Windkessel BCs for the pulmonary circulation, combining an iterative fixed-point approach to a morphometry-based one. More recently, Huang and Ying proposed a genetic algorithm combined with an on-line iterative optimization method to estimate the parameters of a five-element arterial model, starting from measurements of aortic flow rate, venous and arterial pressure [61].

Another class of solutions is based on the use of Kalman filters, which perform the assimilation of measurements *on the fly* by means of a sequential approach, and update the unknown parameters accordingly [62, 63]. For example, Huang et al. adopted an Iterated Unscented Kalman Filter to estimate the circuit parameters and layout of a four-element Windkessel model [64]. Arthurs et al. [53], instead, presented a reduced-order unscented Kalman filter for estimating the parameters of lumped boundary conditions. The estimation of n parameters, however, requires running $n+1$ forward simulations, which makes the data assimilation process computationally expensive.

The approaches presented until now provide a point estimate for the model parameters, without quantifying the uncertainty affecting those estimates. On the contrary, an approach based on Bayesian estimation can provide an estimate for the unknown parameters, while also accounting for the uncertainty arising from errors and assumptions in the collected patient-specific data [54, 55, 65, 66]. An example is the framework proposed by Tran et al. [54], where the Bayesian estimation approach was coupled to the Monte Carlo method to estimate the parameters of a multiscale coronary artery model, while quantifying the

uncertainty on the computed haemodynamic indicators, such as wall shear stress.

Finally, an advanced solution for boundary condition estimation resorts to a *variational* approach, and casts the estimation problem into the framework of PDE-constrained optimization and optimal control. In this approach, a model using either the Stokes or the Navier-Stokes equations is created, where unknown boundary conditions values are set as parameters. The latter are optimized by minimizing the error between pressure and flow rates estimated by the model, and those measured in-vivo [67, 68]. The advantage of optimal control is that the data assimilation process is done in a rigorous way, buy formulating an optimization problem which determines the optimal boundary condition parameters in a reproducible way, ensuring that the solution will be the closest to the provided set of in-vivo measurements. Moreover, differently from the standard optimization approaches presented at the beginning of this section, optimal control gives large flexibility in terms of the number and types of measurements to assimilate, without needing both pressure and flow waveforms at the exact location where the BC will be enforced. Thanks to variational approaches, in fact, it is possible to optimize the BC parameters defined on the boundary to make model results match pressure/flow rate values measured in other parts of the model, which could be more accessible during the measurement process. A similar approach, instead, would be more difficult to implement with manual tuning procedures. In addition, if in-vivo measurements are not sufficient, or not sufficiently accurate, variational methods allow to combine the assimilation of in vivo-measurements with other criteria from the literature. Finally, formulations based on a *least-squares* approach, such as the variational one, are particularly robust, and can handle both spatially and time resolved velocity, flow rate, and pressure measurements [69, 70].

In summary, the definition and estimation of appropriate boundary conditions is a pressing matter in cardiovascular modeling. Together with an accurate geometrical reconstruction of the patient's anatomy, boundary conditions are the key to the creation of models which are truly patient-specific, enabling a more personalized approach to medicine.

1.2 Contributions of this thesis

Despite the enormous improvements that the field of cardiovascular modeling has seen in the past decade, from automated solutions for image segmentation [71], to highly efficient numerical solvers for CFD problems [72], some major challenges still need to be overcome in order to make personalized models truly accessible to doctors and routinely employed in the clinic. One of the most pressing issues is the definition and estimation of accurate boundary conditions, which is the topic of this thesis. In particular, the proposed estimation techniques need to have the following features:

- **Automation** For cardiovascular models to be properly integrated in clinical procedures, it is essential to rely on a repeatable estimation process of BCs, eliminating any operator-dependent variability. Thus, the developed estimation methods need to be automated, robust, and reliable.
- **Ability to assimilate information including in-vivo measurements and statistics from the literature** Whenever possible, the choice of boundary conditions should be guided by the available clinical measurements to make models truly patient-specific. Thus, the proposed methods should be flexible enough to assimilate measurements coming from different sources, including estimates obtained from literature data or population-based values, and accounting for noisy data.
- **Advanced lumped parameter models** Lumped parameter networks are used to model realistic boundary conditions, exploiting the analogies between fluid dynamics and circuit theory. However, the complexity of estimating their parameters has prevented the use of circuits with more than three elements, limiting the capability of representing richer blood flow dynamics. Thus, the third objective is to investigate the use of more complex LPN models, and to provide a fast, scalable, and automated technique to estimate their parameters.

To this end, the main contributions of this thesis are a set of estimation techniques that, by exploiting different and somehow complementary approaches,

allow an *automated, robust and reliable* determination of boundary conditions. This dissertation will give the following three contributions:

- **An optimal control framework for the estimation of resistive boundary conditions**. We propose a computational framework for the automated estimation of resistance-type outlet boundary conditions. Optimal control determines unknown parameters by defining a constrained optimization problem based on the solution of a PDE system, which minimizes the distance between the model solution and a set of available pressure/flow rate measurements. This type of approach is what we call a *data and model-driven approach*: the choice of boundary conditions is guided by an effective combination of patient-specific data and the physical description of the underlying system, by means of PDE. Previous works have applied optimal control to boundary conditions estimation in idealized geometries [73], or with measurements coming from a glass replica of the anatomy of interest [74]. Moreover, the estimated BCs were either constant pressure or traction conditions [75], thus rather unrealistic with respect to lumped parameter models. The proposed method, instead, is tested on fully patient-specific cases, with anatomies reconstructed from CT images of the aortic arch, flow measurements coming from 4D-Flow MRI, and non-invasive pressure measurements obtained with the brachial-cuff method.

- **A time-domain vector fitting approach for the estimation of higher order LPN boundary conditions**. Despite the advantages of using lumped 0D models as BCs, very simple circuit structures are used, such that the number of parameters to estimate is kept to a minimum. Previous works, however, showed how more complex circuits are able to model blood flow dynamics more accurately [76]. For this reason, we propose a novel estimation method based on the time-domain vector fitting (TDVF) algorithm [77, 78] capable of estimating lumped BCs of arbitrary complexity in the form of black-box models. Differently from optimal control, this type of approach is purely *data-driven*, leading to a fast and inexpensive estimation. The proposed approach includes a number of novel contributions. We propose for the first time the use of black-box higher order boundary conditions, which can be used in place

of the less accurate Windkessel models, and estimated with TDVF with a negligible additional computational cost. The aforementioned approach can be directly used on patient-specific pressure and flow waveforms or, in absence of data, can be paired to a one-dimensional model of the entire circulatory system for a fast estimation of boundary conditions on a reduced order model. Moreover, since TDVF has been previously used mainly for electrical applications [77–79], this work also reinforces the analogies between fluid dynamics and electrical circuit theory [79].

- **A numerical investigation of the minimum energy principle in patient-specific anatomies**. In view of the limited availability of patient-specific measurements, BC estimation techniques which do not require them, and are instead *physics and anatomy-based*, are particularly attractive. Murray's law, for example, selects outlet resistances in bifurcating anatomies by exploiting the minimum energy principle. The proposed investigation verifies if a minimum energy point also exists in patient-specific anatomies, and if it is possible to identify it numerically, exploring the adoption of the minimum energy principle as a possible criterion for inlet flow estimation.

1.3 Outline

The thesis is organized as follows. In Chapter 2, a general background on cardiovascular modeling is provided. In particular, the most common mathematical models to describe blood flow are reviewed, together with a brief introduction to their numerical solution via the finite element method. Next, we present the most common reduced order models for the cardiovascular system, namely, one-dimensional and zero-dimensional models.

In Chapter 3, the optimal control framework for BC estimation is presented. After a brief overview of optimal control, and some theoretical background, the proposed method for the estimation of outlet resistances from 4D-Flow MRI data is presented. Numerical results are provided for four aortic arches, documenting the validity of the presented method.

The time-domain vector fitting framework is instead presented in Chapter 4, together with a brief overview of the existing techniques for the determination of Windkessel parameters. Experiments conducted on a 1D model comprising 55 arteries compare TDVF with other common techniques taken from the literature, and provide a systematic analysis of the benefits that higher order BCs bring in terms of accuracy.

Moving on to Chapter 5, an investigation on the validity of the minimum energy principle in patient-specific anatomies is presented. A literature review on the use of the minimum energy principle in cardiovascular modeling is followed by a description of the methodological aspects of the technique proposed to verify numerically the presence of a minimum energy point. Finally, the experimental assessment is conducted on a set of ideal and patient-specific anatomies.

The conclusions in Chapter 6 summarize the research contributions provided in this dissertation for boundary conditions estimation. Furthermore, objectives for future research are given.

Chapter 2

Background on cardiovascular modeling

In this chapter a general overview of the mathematical models of the cardiovascular system adopted throughout this thesis is provided. For a more detailed and extensive treatment of this topic, we refer the Reader to [4, 80, 81]. In Section 2.1, the most common mathematical models describing blood flow in the cardiovascular system are presented. Finally, Section 2.2 provides a short review of the finite element method for the numerical solution of the aforementioned models, together with some formal definitions of the spaces, operators, and functionals which will be used throughout this thesis.

2.1 Mathematical models for blood flow dynamics

Blood flow dynamics can be described by the mathematical equations used in fluid dynamics. Blood is a special type of fluid, composed by a water-based part, named plasma, and some particles (red cells, white cells, and platelets) that are suspended in it. The presence of these particles gives blood a *shear-thinning* property, meaning that its viscosity decreases with the increase of rate of deformation (or, in simpler terms, the more it stirs, the more it fluidifies). This effect is non-negligible in smaller vessels, where blood viscosity is dependent on

the vessel radius, and in the smallest capillaries, where the size of the vessel becomes comparable to that of a red blood cell [4]. In larger vessels, instead, shear thinning and viscoelastic effects can be neglected, and a *Newtonian model* is adopted. Moreover, blood is assumed to be incompressible, meaning that its volume or density does not change with pressure.

2.1.1 The Navier-Stokes equations

Blood flow in the cardiovascular system can be described by the Navier-Stokes equations, a system of partial differential equations. In a domain $\Omega \subset \mathbb{R}^3$, taking $t = 0$ as the initial time, for $t > 0$ the Navier-Stokes equations for an incompressible fluid read

$$\begin{cases} \dfrac{\partial \mathbf{v}}{\partial t} - \nu \Delta \mathbf{v} + \nabla p + (\mathbf{v} \cdot \nabla)\mathbf{v} = \mathbf{f} & \text{in } \Omega \\ \nabla \cdot \mathbf{v} = 0 & \text{in } \Omega, \end{cases} \tag{2.1}$$

where $\mathbf{v}$ is the velocity, p the pressure, and ν the kinematic viscosity, satisfying $\nu = \frac{\mu}{\rho}$, where μ is the dynamic viscosity, and ρ the blood density. The term $\mathbf{f}$, instead, accounts for the external forces that can act of the fluid, like gravity, and is usually assumed to be zero in haemodynamic models. In (2.1), the first equation represents the conservation of linear momentum, while the second is the continuity equation. The term $(\mathbf{v} \cdot \nabla)\mathbf{v}$ describes the process of convective transport, while $-\nu \Delta \mathbf{v}$ describes the effects of internal friction in the fluid.

For the solution of this system, we need to prescribe an initial condition for fluid velocity, such as

$$\mathbf{v}(t = 0, \mathbf{x}) = \mathbf{v}_0(\mathbf{x}), \quad \mathbf{x} \in \Omega. \tag{2.2}$$

Generally, an initial velocity equal to zero is assumed, since it is difficult to conceive an initial condition for the velocity field consistent with (2.1). In cardiovascular simulations, one is usually interested in the solution of the Navier-Stokes equations at steady state, since the excitation provided by the heart is periodic. If the initial condition (2.2) is used, then the solution will feature an initial transient, which will be discarded when looking at simulation results.

In addition, boundary conditions need to be imposed on the boundary $\partial\Omega$ of Ω. Referring to a typical computational domain, as the one represented in Fig. 1.2 of Chapter 1, we usually need to prescribe a condition at the inlet boundary Γ_{in}, a condition on the walls Γ_w, and one at the outlets Γ_{out}.

The most common types of boundary conditions which are mathematically compatible with the Navier-Stokes equations are:

- the *Dirichlet* boundary condition, consisting of a prescribed velocity

$$\mathbf{v} = \boldsymbol{\varphi}, \quad \text{on } \Gamma_D, \tag{2.3}$$

  where $\boldsymbol{\varphi} = \boldsymbol{\varphi}(\mathbf{x}, t) : \Gamma_D \times \mathbb{R}^+ \to \mathbb{R}^3$ is a given function, and where Γ_D denotes the boundary on which the Dirichlet condition is imposed. Usually, this condition is applied at the inlet(s), in the form of a specific velocity profile, and on the walls, where a velocity equal to zero (no-slip) condition is prescribed.

- the *Neumann* boundary condition, equivalent to the applied stress

$$\mathbf{T} \cdot \mathbf{n} = \boldsymbol{\psi}, \quad \text{on } \Gamma_N \tag{2.4}$$

  where $\mathbf{T}$ is the Cauchy stress tensor, defined as $\mathbf{T} = -p\mathbf{I} + \mu(\nabla\mathbf{v} + \nabla\mathbf{v}^T)$, where $\mathbf{I}$ is the identity tensor. The vector $\mathbf{n}$, instead, represents the outward normal to the surface. Moreover, $\boldsymbol{\psi} = \boldsymbol{\psi}(\mathbf{x}, t)$ is a given function and Γ_N represents the part of the boundary where a Neumann condition is imposed. This type of condition is sometimes imposed at the outlets, where it simulates the discharge of blood into a reservoir at constant pressure.

2.1.2 Stokes equations

Stokes equations are the linearized version of the steady Navier-Stokes equations, and are obtained by assuming that the inertial forces are negligible with respect to the viscous forces, and by removing the term representing the derivative of velocity in time. In this way, the nonlinear inertial term in the momentum

balance equation of system (2.1) can be eliminated, obtaining

$$\begin{cases} -\nu\Delta\mathbf{v} + \nabla p = \mathbf{f} & \text{in } \Omega \\ \nabla \cdot \mathbf{v} = 0 & \text{in } \Omega. \end{cases} \tag{2.5}$$

Stokes equations provide a simplified description of blood flow with respect to the Navier-Stokes equations. On one side, the Stokes problem is easier to solve than the Navier-Stokes one, but it provides a less accurate representation of the cardiovascular system, as flow results to be laminar.

2.2 Numerical solution via the Finite Element Method (FEM)

The mathematical models just introduced to describe blood flow in the cardiovascular system, which are characterized either by the Stokes or by the Navier-Stokes equations, cannot be solved analytically, except for some trivial cases. It is necessary, then, to resort to numerical techniques for their solution.

One of the most common techniques for the numerical solution of partial differential equations is the *Finite Element Method (FEM)*, which is based on the subdivision of the computational domain Ω into small elements, which constitute the so called computational mesh. Before presenting the finite element method, some preliminary definitions must be introduced in order to provide a precise theoretical framework in support of our developments. This material is standard, and can be found in textbooks such as [4, 80–82]. The experienced Reader can skip this section without loss of continuity.

2.2.1 Preliminary definitions

Banach spaces Let X be a linear space over the scalar field $\mathbb{R}$. A *norm* in X is a real function

$$||\cdot|| : X \to \mathbb{R} \tag{2.6}$$

such that, for each scalar λ and for every $x, y \in X$, the following properties hold:

- *positivity*: $||x|| \geq 0; ||x|| = 0$ if and only if $x = 0$;
- *homogeneity*: $||\lambda x|| = |\lambda| \cdot ||x||$;
- *triangular inequality*: $||x + y|| \leq ||x|| + ||y||$.

A normed space is a linear space X endowed with a norm $||\cdot||$. A norm induces a distance given by $d(x, y) = ||x - y||$, which makes X a metric space. A normed space which is complete with respect to this induced distance is called a *Banach space* [82].

Functionals, dual spaces and bilinear forms If X is a normed space, a linear operator $L : X \to \mathbb{R}$ is called a (linear) *functional* [4].

The space $\mathcal{L}(X, \mathbb{R})$ of linear and bounded (or continuous) functionals over X is a Banach space, called *dual space* of X, and is denoted by X^*. This space is endowed with the norm

$$||L||_{X^*} = \sup_{||x||_X = 1} |Lx| \quad \forall L \in X^* \tag{2.7}$$

To denote the action of an element $L \in X^*$ on $v \in X$ we adopt the notation $\langle L, v \rangle_{X^*,X}$. This is called duality pairing.

An application

$$a : X \times X \to \mathbb{R}, \tag{2.8}$$

that maps two elements of X to a real number is called a form. It is a *bilinear form* if it is linear with respect to each argument, taken singularly [4]. Equivalently

$$a(\lambda x + \mu y, z) = \lambda a(x, z) + \mu a(y, z), \quad \forall \lambda, \mu \in \mathbb{R}, \forall x, y, z \in X \tag{2.9}$$

$$a(x, \lambda y + \mu z) = \mu a(x, z) + \lambda a(x, y), \quad \forall \lambda, \mu \in \mathbb{R}, \forall x, y, z \in X. \tag{2.10}$$

Dual operators Let X, Y be Banach spaces. For an operator $T \in \mathcal{L}(X, Y)$ we can define the *dual* or *adjoint operator* $T^* \in \mathcal{L}(\mathcal{Y}^*, \mathcal{X}^*)$ by the relation

$$\langle T^* L, x \rangle_{X^*,X} = \langle L, Tx \rangle_{Y^*,Y} \tag{2.11}$$

for all $L \in Y^*, x \in X$. It holds that $||T^*||_{\mathcal{L}(Y^*,X^*)} = ||T||_{\mathcal{L}(X,Y)}$ [82].

Hilbert spaces Let X be a linear space over $\mathbb{R}$. An inner or scalar product in X is a function

$$\langle \cdot, \cdot \rangle : X \times X \to \mathbb{R} \tag{2.12}$$

with the following properties. For every $x, y, z \in X$ and every scalar $\lambda, \mu \in \mathbb{R}$:

- *positivity*: $\langle x, x \rangle \geq 0$ and $\langle x, x \rangle = 0$ if and only if $x = 0$;
- *symmetry*: $\langle x, y \rangle = \langle y, x \rangle$;
- *bilinearity*: $\langle \lambda x + \mu y, z \rangle = \lambda \langle x, z \rangle + \mu \langle y, z \rangle$.

A linear space endowed with an inner product is called an inner product space. An inner product induces a norm, given by

$$||x|| = \sqrt{\langle x, x \rangle}. \tag{2.13}$$

Let H be an inner product space. We say that H is a *Hilbert space* if it is complete with respect to the norm (2.13), induced by the inner product [82].

Support of a function The support of a function f is defined as the closure of the subset of Ω where $f \neq 0$. A function has *compact support* in Ω if its support is contained in a closed and bounded subset of Ω. So, if f has compact support in Ω, it means it is zero on the boundary of Ω [4].

Sobolev spaces The space $L^2(\Omega)$ is the space of square integrable functions, meaning

$$L^2(\Omega) = \{v : \Omega \to \mathbb{R}, \quad \int_\Omega v^2 d\Omega < +\infty\}. \tag{2.14}$$

This space is a Hilbert space with scalar product $\langle u, v \rangle_{L^2(\Omega)} = \int_\Omega uv d\Omega$ and norm $||v||_{L^2(\Omega)} = \sqrt{\int_\Omega uv d\Omega}$.

The space $H^s(\Omega)$ is defined as the space of functions of $L^2(\Omega)$ such that all derivatives of order up to s (partial derivatives if Ω is multidimensional) belong to $L^2(\Omega)$ as well [4]. For example, in the case $\Omega \subset \mathbb{R}$

$$H^1(\Omega) = \{v \in L^2(\Omega) : \quad \frac{dv}{dx} \in L^2(\Omega)\}. \tag{2.15}$$

The derivative in this definition is the so called *weak derivative* (or distributional derivative) [83]. In this case $dv/dx \in L^2(\Omega)$ means that there exists a $g \in L^2(\Omega)$ such that, for all functions $w \in C^\infty(\Omega)$ with compact support in Ω, the following equality holds

$$-\int_\Omega g w d\Omega = \int_\Omega v \frac{dw}{dx} d\Omega. \tag{2.16}$$

This definition of derivative extends the concept of derivative to non-differentiable functions in the classical sense.

The *Sobolev space* $H^s(\Omega)$, with s a positive integer and $\Omega \subset \mathbb{R}^d$, is a Hilbert space when endowed with the scalar product

$$\langle u, v \rangle_{H^s(\Omega)} = \sum_{|\boldsymbol{\alpha}| \leq s} \int_\Omega \frac{\partial^{|\boldsymbol{\alpha}|} u}{\partial x^{\alpha_1} ... \partial x^{\alpha_d}} \frac{\partial^{|\boldsymbol{\alpha}|} v}{\partial x^{\alpha_1} ... \partial x^{\alpha_d}} d\Omega \tag{2.17}$$

and the norm

$$||u||_{H^s(\Omega)} = \left[\sum_{|\boldsymbol{\alpha}| \leq s} \int_\Omega \left(\frac{\partial^{|\boldsymbol{\alpha}|} u}{\partial x^{\alpha_1} ... \partial x^{\alpha_d}} \right)^2 d\Omega \right]^{1/2}, \tag{2.18}$$

where $\boldsymbol{\alpha} = [\alpha_1, ..., \alpha_d]$ is a multi-index of non negative integers and $|\boldsymbol{\alpha}| = \alpha_1 + ... + \alpha_d$ [4].

Another important definition for the development of the finite element method is that of *trace*. If Ω is sufficiently regular (for example having a C^1 boundary) there exists a linear and continuous application

$$\gamma_0 : H^s(\Omega) \to L^2(\partial\Omega), \tag{2.19}$$

such that $\gamma_0 v = v|_{\partial\Omega}, \forall v \in H^s(\Omega) \cap C^0(\bar{\Omega})$. The application $\gamma_0 v$ is called *trace* of v on $\partial\Omega$.

The space $\boldsymbol{H_0^1(\Omega)}$ The space $H_0^1(\Omega)$ can be defined as the space of functions in $H^1(\Omega)$ with null trace on $\partial\Omega$ [4]

$$H_0^1(\Omega) = \{v \in H^1(\Omega) : \gamma_0 v = 0\}. \tag{2.20}$$

We can also define $H^1_\Gamma(\Omega)$ as the space of function with null trace on $\Gamma \subset \partial\Omega$,

$$H^1_\Gamma(\Omega) = \{v \in H^1(\Omega) : \gamma_\Gamma v = 0\}. \tag{2.21}$$

2.2.2 The weak formulation of Navier-Stokes equations

The first step for the solution of Navier-Stokes (or Stokes) equations via the finite element method is to derive their weak formulation. This operation consists in multiplying each term in (2.1) by a test function w belonging to a suitable space W, and then integrating over the domain Ω. Let us start from the first equation

$$\int_\Omega \frac{\partial \mathbf{v}}{\partial t} \cdot \mathbf{w} d\Omega - \int_\Omega \nu \Delta \mathbf{v} \cdot \mathbf{w} d\Omega + \int_\Omega [(\mathbf{v} \cdot \nabla)\mathbf{v}] \cdot \mathbf{w} d\Omega + \int_\Omega \nabla p \cdot \mathbf{w} d\Omega = \int_\Omega \mathbf{f} \cdot \mathbf{w} d\Omega, \tag{2.22}$$

which, by applying Green's formula becomes

$$\begin{aligned} \int_\Omega \frac{\partial \mathbf{v}}{\partial t} \cdot \mathbf{w} d\Omega - \int_\Omega \nu \nabla \mathbf{v} \cdot \nabla \mathbf{w} d\Omega + \int_\Omega [(\mathbf{v} \cdot \nabla)\mathbf{v}] \cdot \mathbf{w} d\Omega - \int_\Omega p \nabla \cdot \mathbf{w} d\Omega \\ = \int_\Omega \mathbf{f} \cdot \mathbf{w} d\Omega + \int_{\partial\Omega} \left(\nu \frac{\partial \mathbf{v}}{\partial \mathbf{n}} - p\mathbf{n} \right) \cdot \mathbf{w} d\gamma, \quad \forall \mathbf{w} \in W. \end{aligned} \tag{2.23}$$

The same operation can be done on the second equation of (2.1), which is multiplied by a test function q belonging to a suitable space Q, obtaining

$$\int_\Omega q \nabla \cdot \mathbf{v} d\Omega = 0 \quad \forall q \in Q. \tag{2.24}$$

The space W is chosen so that the test functions vanish on Γ_D, the part of the boundary where a Dirichlet condition has been prescribed on $\mathbf{v}$, obtaining

$$W = [H^1_{\Gamma_D}(\Omega)]^3 = \{\mathbf{w} \in [H^1(\Omega)]^3 : \ \mathbf{w}|_{\Gamma_D} = \mathbf{0}\} \tag{2.25}$$

If a Dirichlet condition is prescribed on the entire boundary (i.e $\Gamma_D = \partial\Omega$), then this space will coincide with $[H^1_0(\Omega)]^d$, where d is the dimension of the domain. Regarding the space Q, instead, we will choose $Q = L^2(\Omega)$ in presence of Neumann boundary conditions (if $\Gamma_N \neq \emptyset$). If only Dirichlet conditions have

been imposed ($\Gamma_N = \emptyset$), instead, we will choose

$$Q = L^2_0(\Omega) = \{p \in L^2(\Omega) : \int_\Omega p \, d\Omega = 0\}. \tag{2.26}$$

This condition, which corresponds to imposing that the pressure has null average, is necessary when only BCs of Dirichlet type have been imposed. In this case, in fact, the pressure in (2.1) appears only in terms of its gradient. This means that a solution for p is determined up to a constant c, so if p is a solution to (2.1), $p + c$ will be a solution too. By imposing that pressure has null average, such indeterminacy is avoided. The weak formulation of (2.1) then reads:
find $\mathbf{v} \in L^2(\mathbb{R}^+; [H^1(\Omega)]^d)$, $p \in L^2(\mathbb{R}^+, \Omega)$ such that

$$\begin{cases} \int_\Omega \dfrac{\partial \mathbf{v}}{\partial t} \cdot \mathbf{w} d\Omega + \nu \int_\Omega \nabla \mathbf{v} \cdot \nabla \mathbf{w} d\Omega + \int_\Omega [(\mathbf{v} \cdot \nabla)\mathbf{v}] \cdot \mathbf{w} d\Omega - \int_\Omega p \nabla \cdot \mathbf{w} d\Omega \\ \qquad = \int_\Omega \mathbf{f} \cdot \mathbf{w} d\Omega + \int_{\Gamma_N} \psi \cdot \mathbf{w} d\gamma & \forall \mathbf{w} \in W, \\ \int_\Omega q \nabla \cdot \mathbf{v} d\Omega = 0, & \forall q \in Q. \end{cases} \tag{2.27}$$

2.2.3 The Finite Element discretization

As already mentioned earlier, the numerical solution of Navier-Stokes equations is based on a subdivision of the domain into a grid, the computational mesh. The solution $(\mathbf{v}, p)$ is substituted by an approximation $(\mathbf{v}_h, p_h)$, where the subscript h represents the mesh resolution.

Let us consider a finite element partition $\mathcal{T}_h$ of the domain Ω, from which we construct the finite element spaces $W_h \subset W$ and $Q_h \subset Q$. Let us now briefly introduce the finite element spaces used for approximating pressure and velocity [84]. Considering the tetrahedral triangulation $\mathcal{T}_h$ of the domain $\Omega \in \mathbb{R}^3$, different kinds of basis functions can be adopted. A common choice consists in using the finite element space $P_{1,h}(\mathcal{T}_h)$, which consists of functions that are linear polynomials inside each tetrahedral element K. Thus, in a x, y, z space, they are functions of the form $a_0 + a_1 x + a_2 y + a_3 z$ for constants a_i, $i = 0, .., 3$. Such functions are uniquely determined by the value they assume at the four vertices of a tetrahedral element, corresponding to the orange triangles in the right

panel of Fig. 2.1. Another common finite element space is the $P_{2,h}(\mathcal{T}_h)$, which consists of quadratic polynomials inside each tetrahedron. This translates into functions of the form $b_0+b_1x+b_2y+b_3z+b_4x^2+b_5y^2+b_6z^2+b_7xy+b_8yz+b_9zx$, for constants b_i, $i=0,..,9$. In this case, the functions are determined by their values at the four vertices and the six midpoints of the edges, corresponding to the green dots in the right panel of Fig. 2.1. When it comes to the Stokes and the Navier-Stokes equations, a popular approach consists in choosing the linear space $P_{1,h}(\mathcal{T}_h)$ for approximating the pressure, and the quadratic space $P_{2,h}(\mathcal{T}_h)$ for approximating the velocity. This choice ensures "balanced" approximation properties, namely, $O(h^2)$ for V_h in the V-norm and for Q_h in the Q-norm [85]. This pair of elements (P2-P1) used for discretizing pressure and velocity in the Stokes and Navier-Stokes equations is better known as the Taylor-Hood element [86], and it is represented on the right panel of Fig. 2.1.

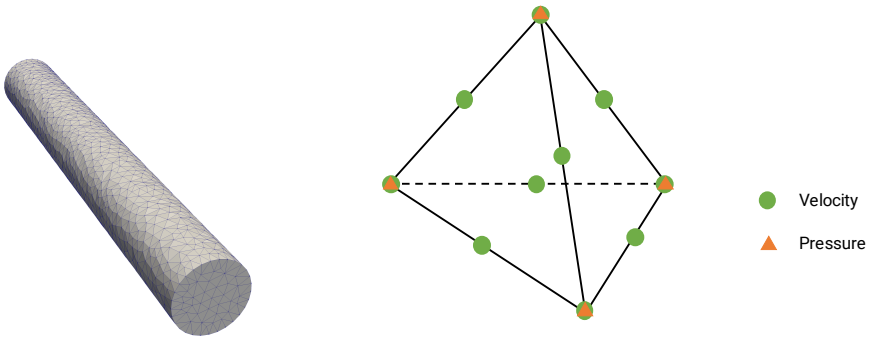

Fig. 2.1 Left: example of a tetrahedral mesh on a three-dimensional model. Right: Taylor-Hood (P2-P1) element pair used for the discretization of Navier-Stokes equations.

To guarantee the well-posedness of the discrete version of (2.27), both velocity and pressure spaces W_h and Q_h need to obey the inf-sup condition, given in Brezzi's theorem [87]:

$$\inf_{q_h\in Q_h}\sup_{\mathbf{w}_h\in W_h}\frac{\langle q_h,\nabla\cdot\mathbf{w}_h\rangle}{||\mathbf{w}_h||_W||q_h||_Q}\geq\beta>0. \tag{2.28}$$

The semi-discrete formulation of the Navier-Stokes equations then reads: find $\mathbf{v}_h \in W_h$, $p_h \in Q_h$ such that:

$$\begin{cases} \dfrac{d}{dt}\langle \mathbf{v}_h, \mathbf{w}_h \rangle + \nu \langle \nabla \mathbf{v}_h, \nabla \mathbf{w}_h \rangle + \langle (\mathbf{v}_h \cdot \nabla)\mathbf{v}_h, \mathbf{w}_h \rangle - \langle p_h, \nabla \cdot \mathbf{w}_h \rangle \\ \qquad = \langle \mathbf{f}, \mathbf{w}_h \rangle, & \forall \mathbf{w}_h \in W_h \\ \langle q_h, \nabla \cdot \mathbf{v}_h \rangle = 0, & \forall q_h \in Q_h. \end{cases} \tag{2.29}$$

Since both $\mathbf{v}_h, \mathbf{w}_h$ and p_h, q_h belong to the same spaces W_h and Q_h, respectively, this discretization technique is denoted as Galerkin method [88].

2.2.4 The algebraic system

The system of discrete equations (2.29) can be rewritten in a more compact form by introducing the notation

$$a_h(\phi, \psi) = \sum_{K \in \mathcal{T}_h} \nu \langle \nabla \phi, \nabla \psi \rangle_K \tag{2.30}$$

$$n_h(\phi, \psi, \xi) = \sum_{K \in \mathcal{T}_h} \langle \phi \cdot \nabla \psi, \xi \rangle_K \tag{2.31}$$

$$b_h(\chi, \phi) = -\sum_{K \in \mathcal{T}_h} \langle \chi, \nabla \cdot \phi \rangle_K, \tag{2.32}$$

where the discrete forms $a_h(\cdot,\cdot)$, $b_h(\cdot,\cdot)$, and $n_h(\cdot,\cdot,\cdot)$ have been defined in the piecewise sense, and where K indicates an element of the mesh $\mathcal{T}_h$. In this way system (2.29) can be rewritten as

$$\begin{cases} \frac{d}{dt}\langle \mathbf{v}_h, \mathbf{w}_h \rangle + a_h(\mathbf{v}_h, \mathbf{w}_h) + n_h(\mathbf{v}_h, \mathbf{v}_h, \mathbf{w}_h) + b_h(p_h, \mathbf{w}_h) = \langle \mathbf{f}, \mathbf{w}_h \rangle, \forall \mathbf{w}_h \in W_h \\ b_h(q_h, \mathbf{v}_h) = 0, & \forall q_h \in Q_h. \end{cases} \tag{2.33}$$

In order to be solved, this discrete problem needs to be converted into an algebraic system. For this reason, we need to introduce appropriate local nodal bases $\{\phi_h^i = i = 1, ..., N_v\}$ of space W_h, and $\{\chi_h^i, i = 1, ..., N_p\}$ of space Q_h. We can now expand the solution $(\mathbf{v}_h, p_h)$, still unknown, in the form

$$\mathbf{v}_h = \sum_{i=1}^{N_v} x_i \phi_h^i, \quad p_h = \sum_{j=1}^{N_p} x_i \chi_h^i, \tag{2.34}$$

where N_v and N_p are the numbers of velocity and pressure basis functions, respectively. The basis functions are defined on each element of the mesh. We can now introduce the following matrices:

$$\mathbf{M} = \left(\langle \phi_h^i, \phi_h^i \rangle \right)_{i,j=1}^{N_v} \tag{2.35}$$

$$\mathbf{A} = \left(a_h(\phi_h^i, \phi_h^j) \right)_{i,j=1}^{N_v}, \tag{2.36}$$

$$\mathbf{B} = \left(b_h(\chi_h^i, \phi_h^j) \right)_{i,j=1}^{N_p,N_v}, \tag{2.37}$$

$$\mathbf{N}(\mathbf{x}) = \left(n_h(\sum_{k=1}^{N_v} x_k \phi_h^k, \phi_h^i, \phi_h^i) \right)_{i,j=1}^{N_v} \tag{2.38}$$

$$\mathbf{b} = \left(\langle f, \phi_h^j \rangle \right)_{j=1}^{N_v}. \tag{2.39}$$

Matrix $\mathbf{M}$ is called the mass matrix, while matrix $\mathbf{A}$ is called the stiffness matrix, $\mathbf{B}$ the gradient matrix, while $\mathbf{N}$ is the nonlinear transport matrix and $\mathbf{b}$ the load vector. Thanks to this notation, the semi-discrete system (2.33) can be rewritten as an algebraic system for the vectors $\mathbf{k} \in \mathbb{R}^{N_v}$ and $\mathbf{y} \in \mathbb{R}^{N_p}$ of expansion coefficients:

$$\mathbf{M}\dot{\mathbf{k}} + \mathbf{A}\mathbf{k} + \mathbf{N}(\mathbf{k})\mathbf{k} + \mathbf{B}\mathbf{y} = \mathbf{b}, \tag{2.40}$$

$$-\mathbf{B}^T\mathbf{k} = 0. \tag{2.41}$$

2.3 Reduced models of the cardiovascular system

Although Navier-Stokes equations provide an accurate description of blood flow in vessels, it is computationally unfeasible to simulate the entire cardiovascular systems using such 3D model. For this reason, it is convenient to use simplified models of the cardiovascular system, which provide an estimate of $\mathbf{v}$ and p at a reduced computational cost. In particular, in this thesis we will adopt two types of reduced models:

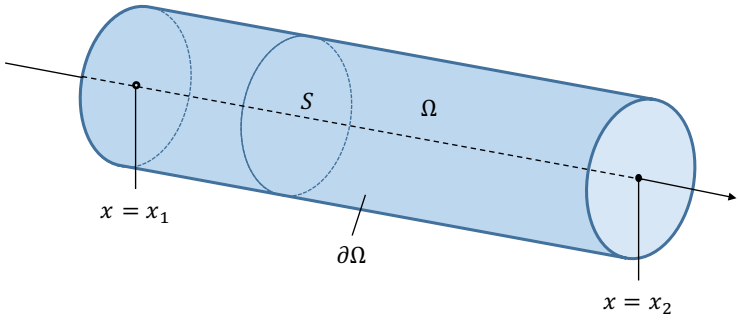

Fig. 2.2 Model of the compliant vessel used in Section 2.3.

- one-dimensional (1D) models, in which the space dependence is limited to the axial coordinate;
- lumped parameter (0D) models, where the space dependence is discretized, and the corresponding mathematical model is based on ordinary differential equations, which are often represented as lumped parameter electrical networks.

2.3.1 One-dimensional models

The governing equations describing blood flow in a one-dimensional model of a compliant vessel can be obtained in different ways. One approach consists in performing an asymptotic analysis starting from the incompressible Navier-Stokes equations, by assuming that the radius of the vessel is small compared to its length [89]. Another approach assumes that the vessel is cylindrical, and integrates the Navier-Stokes equations on a generic cross section [90]. In this section, instead, we derive the 1D Navier-Stokes equations starting from conservation principles, as described in [4, 91]. This approach is generally preferred because it does not make any assumptions on the geometry of the vessel section. We start by representing a generic artery by means of a simple compliant tube, as represented in Fig. 2.2. We denote as Ω the volume of the tube, and as $\partial\Omega$ its boundary, with outer normal $\mathbf{n}$. Moreover, S is a general cross section, with area $A = A(x,t) = \int_S d\sigma$. The 1D governing equations,

which will be derived later in this Section, take the form [92]

$$\frac{\partial A}{\partial t} + \frac{\partial Av}{\partial x} = 0, \tag{2.42}$$

$$\frac{\partial v}{\partial t} + (2\alpha - 1)v\frac{\partial v}{\partial x} + (\alpha - 1)v^2\frac{\partial A}{\partial x} + \frac{1}{\rho}\frac{\partial p}{\partial x} + K_R\frac{v}{A} = 0, \tag{2.43}$$

where α represents the Coriolis coefficient, and K_R the viscous resistance of the flow per unit length.

This system has three unknowns, namely, p, A, v, but only two equations. This means that an additional equation is needed to close the system. In particular, we use an explicit algebraic relationship between p and A, called tube law, to account for the fluid-structure interaction of the problem. In 1D modelling, the arterial wall is usually assumed to be thin, homogeneous, isotropic and incompressible, and to deform axisymmetrically with each circular cross section independent of the others [92]. This type of behavior can be represented by visco-elastic laws, like [92, 93]

$$p = p_e(A, x) + \frac{\Gamma(x)}{A_0(x)\sqrt{A}}\frac{\partial A}{\partial t}, \tag{2.44}$$

with

$$p_e(A, x) = p_{ext} + \frac{\beta(x)}{A_0(x)}\left(\sqrt{A} - \sqrt{A_0(x)}\right), \tag{2.45}$$

$$\beta(x) = \frac{4}{3}\sqrt{\pi}E(x)h(x), \tag{2.46}$$

$$\Gamma(x) = \frac{2}{3}\sqrt{\pi}\varphi(x)h(x) \tag{2.47}$$

where $p_e(A, x)$ is the elastic component of pressure, $h(x)$ is the wall thickness, $E(x)$ is the Young's modulus, $\varphi(x)$ is the wall viscosity, and $A_0(x)$ is the reference area, computed when $p = p_{ext}$ and $\frac{\partial A}{\partial t} = 0$.

In the following section, we will provide the formal derivation of (2.42) from conservation principles, as done in [4].

Derivation of the 1D governing equations

The first step consists in obtaining a one-dimensional form for the Reynolds' transport theorem [94], which for the volume Ω of Fig. 2.2 reads

$$\frac{d}{dt}\int_\Omega f d\Omega = \int_\Omega \frac{\partial f}{\partial t} d\Omega + \int_{\partial\Omega} f \mathbf{v}_b \cdot \mathbf{n} d\sigma, \tag{2.48}$$

where $f = f(\mathbf{x}, t)$ is a continuous function, with $\mathbf{x} = (x, y, z)$, and $\mathbf{v}_b$ is the velocity at the boundary $\partial\Omega$. A step-by-step derivation of the 1D version of (2.48) along the x direction can be found in [4]. We report here the final result, which reads

$$\frac{\partial}{\partial t}(A\bar{f}) + \frac{\partial}{\partial x}[A(\overline{fv_1})] = \int_S \left[\frac{\partial f}{\partial t} + \nabla \cdot (f\mathbf{v})\right] d\sigma + \int_{\partial S} f \mathbf{w} \cdot \mathbf{n} d\gamma, \tag{2.49}$$

where the term v_1 indicates the x-component of the velocity $\mathbf{v}$. where the overbar notation in this section indicates an area-averaged quantity. For example, $\bar{f}$ indicates the area-averaged value of f

$$\bar{f} = \frac{1}{A}\int_S f d\sigma. \tag{2.50}$$

Moreover, $\mathbf{w}$ indicates the relative velocity between the arterial wall $\mathbf{v}_w$ and the fluid inside the lumen $\mathbf{v}$

$$\mathbf{w} = \mathbf{v}_w - \mathbf{v}. \tag{2.51}$$

From this general formula, it is possible to obtain the 1D Navier-Stokes equations by deriving the principles of conservation of mass and balance of momentum from (2.49). The conservation of mass is obtained by imposing $f = 1$ in (2.49). Assuming that the fluid is incompressible, i.e. $\nabla \cdot \mathbf{v} = 0$, we obtain

$$\frac{\partial A}{\partial t} + \frac{\partial}{\partial x}(A\bar{v}_1) = \int_{\partial S} \mathbf{w} \cdot \mathbf{n}\, d\gamma. \tag{2.52}$$

The balance of momentum, instead, is obtained by taking $f = v_1$ in (2.49) and again assuming that the fluid is incompressible, which gives

$$\frac{\partial}{\partial t}(A\bar{v}_1) + \frac{\partial}{\partial x}[A(\overline{u_1^2})] = \int_S \left[\frac{\partial v_1}{\partial t} + \mathbf{v} \cdot \nabla v_1\right] d\sigma + \int_{\partial S} v_1\, \mathbf{w} \cdot \mathbf{n}\, d\gamma. \tag{2.53}$$

Equation (2.53) can be rewritten as

$$\frac{\partial}{\partial t}(A\bar{v}_1) + \frac{\partial}{\partial x}[A(\overline{u_1^2})] = \int_S \frac{Dv_1}{Dt}\sigma + \int_{\partial S} v_1 \, \mathbf{w}\cdot\mathbf{n} \, d\gamma, \tag{2.54}$$

by denoting with $\frac{D}{Dt} = \frac{\partial}{\partial t} + \mathbf{v}\cdot\nabla$ the material derivative, which is defined as the time rate of change of some physical quantity for a portion of a material with a velocity $\mathbf{v}$. The first term on the right-hand side of (2.54) can be rewritten by using the balance of momentum for a three dimensional volume Ω for a fluid with constant density ρ, which reads

$$\int_\Omega \frac{D\mathbf{v}}{Dt} \, d\Omega = \int_\Omega \mathbf{f}^b \, d\Omega + \frac{1}{\rho}\int_{\partial\Omega} \nabla\cdot\mathbf{T} \, d\Omega, \tag{2.55}$$

where $\mathbf{T}$ is the Cauchy stress tensor, and $\mathbf{f}^b$ is the body force per unit volume. Knowing that the tensor $\mathbf{T}$ can be written as $\mathbf{T} = -p\mathbf{I} + \mathbf{D}$ thanks to the constitutive equation of the fluid, we can write

$$\nabla\cdot\mathbf{T} = -\nabla p + \nabla\cdot\mathbf{D} = -\nabla p + \mathbf{d}, \tag{2.56}$$

where $\nabla\cdot\mathbf{D} = \mathbf{d}$. Equation (2.55) then becomes

$$\int_{x_1}^{x_2}\left(\int_S \frac{D\mathbf{v}}{Dt}d\sigma\right)dx = \int_{x_1}^{x_2}\left(\int_S \left[\mathbf{f}^b + \frac{1}{\rho}(-\nabla p + \mathbf{d})\right]d\sigma\right)dx. \tag{2.57}$$

By equating the arguments of the two integrals for the x-component we obtain

$$\int_S \frac{Dv_1}{Dt}d\sigma = \int_S \left[f_1^b + \frac{1}{\rho}(-\frac{\partial p}{\partial x} + d_1)\right]d\sigma, \tag{2.58}$$

which we can now substitute in (2.54), obtaining

$$\frac{\partial}{\partial t}(A\bar{v}_1) + \frac{\partial}{\partial x}(A\overline{u_1^2}) = \int_S \left[f_1^b + \frac{1}{\rho}(-\frac{\partial p}{\partial x} + d_1)\right]d\sigma + \int_{\partial S} v_1\mathbf{w}\cdot\mathbf{n}d\sigma. \tag{2.59}$$

The integral in the first term on the right-hand side is eliminated by using area-averaged values

$$\frac{\partial}{\partial t}(A\bar{v}_1) + \frac{\partial}{\partial x}(A\overline{u_1^2}) = \frac{A}{\rho}\left(\rho\bar{f}_1^b - \frac{\partial\bar{p}}{\partial x} + \bar{d}_1\right) + \int_{\partial S} v_1\mathbf{w}\cdot\mathbf{n}d\sigma. \tag{2.60}$$

The final form of the balance of momentum equation in 1D takes the form

$$\frac{\partial}{\partial t}(A\bar{u}_1) + \frac{\partial}{\partial x}(\alpha\bar{u}_1^2) = S\bar{f}_1^b - \frac{A}{\rho}\left(\frac{\partial\bar{p}}{\partial x}\right) - K_R\bar{u}_1 + \int_{\partial S} v_1\mathbf{w}\cdot\mathbf{n}d\sigma, \tag{2.61}$$

where the Coriolis coefficient α and the viscous resistance of the flow per unit length K_R have been introduced.

Equations (2.52) and (2.61) together form the system of equations describing blood flow dynamics in a one-dimensional domain. However, a number of assumptions allow to further simplify their form. In particular, we can assume that the vessel walls are impermeable ($\mathbf{w}\cdot\mathbf{n} = 0$), and that body forces are equal to zero ($\bar{f}_1^b = 0$). Moreover, we denote velocity with v instead of $\bar{v}_1$, and pressure with p instead of $\bar{p}$, obtaining

$$\begin{aligned} &\frac{\partial A}{\partial t} + \frac{\partial Av}{\partial x} = 0, \\ &\frac{\partial v}{\partial t} + (2\alpha - 1)v\frac{\partial v}{\partial x} + (\alpha - 1)v^2\frac{\partial A}{\partial x} + \frac{1}{\rho}\frac{\partial p}{\partial x} + K_R\frac{v}{A} = 0. \end{aligned} \tag{2.62}$$

This concludes the derivations for the 1D Navier-Stokes equations in compliant vessels. The system is usually reformulated in terms of the characteristic variables, which allow to define proper conditions at the proximal and distal boundaries of the segments, as well as at the junctions and bifurcations [4, 92]. The 1D governing equations thus obtained can be solved numerically with different methods, the most popular being the *Taylor-Galerkin* scheme [95] and the *discontinuous Galerkin* scheme [96]. For more details on the use of these methods for 1D Navier-Stokes equations, we refer to [4, 92].

2.3.2 Zero-dimensional models

Zero-dimensional models can be derived from one-dimensional models obtained in the previous section by means of an averaging procedure. We will consider again the single artery of Fig. 2.2, with volume Ω and length $l = |x_2 - x_1|$. We can define the mean flow rate over the entire artery as

$$\hat{Q} = \frac{\rho}{l}\int_{x_1}^{x_2}\left(\int_{S(x)} v_x d\sigma\right)dx = \frac{\rho}{l}\int_{x_1}^{x_2} Q(x)dx. \tag{2.63}$$

In the same way, we can define the mean pressure over the artery as

$$\hat{p} = \frac{1}{l}\int_{x_1}^{x_2} p dx, \tag{2.64}$$

and the mean area as

$$\hat{A} = \frac{1}{l}\int_{x_1}^{x_2} A dx. \tag{2.65}$$

We first rewrite equations in (2.62) in terms of A, Q, p, which will be more convenient for the following derivations:

$$\begin{aligned} &\frac{\partial A}{\partial t} + \frac{\partial Q}{\partial x} = 0, \\ &\frac{\partial Q}{\partial t} + \frac{\partial}{\partial x}\left(\alpha \frac{Q^2}{A}\right) + \frac{A}{\rho}\frac{\partial p}{\partial x} + K_R \frac{Q}{A} = 0. \end{aligned} \tag{2.66}$$

We can now integrate the first equation in (2.66), the continuity equation, along x, obtaining

$$l\frac{d\hat{A}}{dt} + Q_2(t) - Q_1(t) = 0, \quad \text{with} \quad Q_1(t) = Q(x_1, t), \quad Q_2(t) = Q(x_2, t). \tag{2.67}$$

We then do the same for the second equation (2.66), the momentum equation, by assuming that the convective term $\partial_x(\alpha Q^2/A)$ can be neglected, and that the area A can be assumed constant and equal to A_0

$$\frac{\rho l}{A_0}\frac{d\hat{Q}}{dt} + \frac{\rho K_R l}{A_0^2}\hat{Q} + P_2(t) - P_1(t) = 0, \quad \text{with} \quad P_1(t) = P(x_1, t), \quad P_2(t) = P(x_2, t). \tag{2.68}$$

We close the system by integrating the tube law in (2.45) along the x-direction and neglecting the viscous components, which gives

$$\frac{d\hat{A}}{dt} = k_1 \frac{d\hat{p}}{dt}, \tag{2.69}$$

where $k_1 = \frac{\sqrt{A_0}}{\beta}$. By substituting (2.69) in (2.67) we obtain the system of equations representing blood flow in a lumped parameter model of a vessel

$$k_1 l \frac{d\hat{p}}{dt} + Q_2 - Q_1 = 0, \tag{2.70}$$

$$\frac{\rho l}{A_0}\frac{d\hat{Q}}{dt} + \frac{\rho K_R l}{A_0^2}\hat{Q} + P_2 - P_1 = 0. \tag{2.71}$$

These kinds of equations are well known in circuit theory, where they are used to describe the behavior of a segment of a transmission line in analog electrical circuits. Indeed, the analogy between electric and hydraulic networks has been known and exploited for a long time, as the first simulations of blood flow in the cardiovascular system were based on electrical circuits [37]. In this analogy, flow rate is assimilated to the current, while pressure to the voltage. Moreover, the electric resistance R corresponds to blood viscosity, the inductance L to blood inertia, and the capacitance C to wall compliance.

By defining the resistance $R = \frac{\rho K_R l}{A_0^2}$, the inductance $L = \frac{\rho l}{A_0}$, and the capacitance $C = k_1 l$, the system (2.70) can be rewritten as

$$C\frac{d\hat{p}}{dt} + Q_2 - Q_1 = 0, \tag{2.72}$$

$$L\frac{d\hat{Q}}{dt} + R\hat{Q} + P_2 - P_1 = 0 \tag{2.73}$$

If we suppose, for example, that Q_1 and P_2 are given, we can approximate the unknowns at the other "boundaries" with the state variables,

$$\hat{p} \approx P_1, \quad \hat{Q} \approx Q_2, \tag{2.74}$$

obtaining the following system for the blood flow in a short pipe

$$\begin{aligned} C\frac{dP_1}{dt} + Q_2 &= Q_1, \\ L\frac{dQ_2}{dt} + RQ_2 - P_1 &= P_2. \end{aligned} \tag{2.75}$$

This system corresponds to the electrical circuit represented in Fig. 2.3 [4].

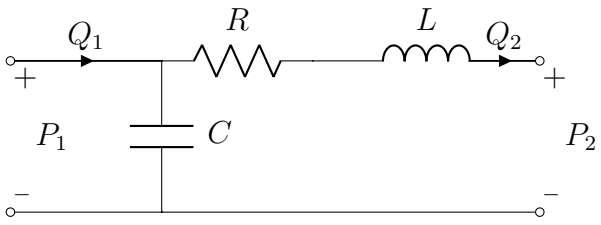

Fig. 2.3 Electrical network equivalent to a short arterial segment, represented by equations (2.75).

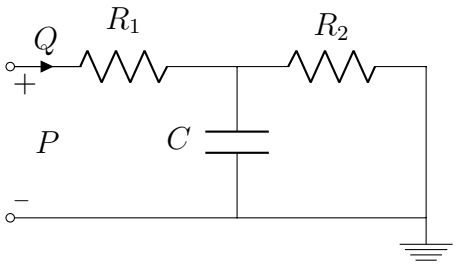

Fig. 2.4 Three-element Windkessel model commonly used as outlet boundary condition.

The three-element Windkessel model

Lumped parameter models are often adopted as terminal boundary conditions for both 3D and 1D vascular models. In particular, we introduce the most used lumped boundary condition, namely, the three element Windkessel model, represented in Fig. 2.4. The three-element Windkessel model was first introduced by Westerhof et al. [37]. It includes a capacitor C, to model the storage properties of arteries, the resistor R_1, representing the proximal resistance of the arterial network, and the resistor R_2, to model the resistance of the distal circulation. In particular, considering the lumped model of an arterial segment represented in Fig. 2.3, the three-element Windkessel model does not take into account the arterial inertance, modeled with the inductance L. The latter, in fact, can be neglected on a first approximation.

In the Windkessel model, the pressure P is related to the flow rate Q by means of the differential equation

$$Q\left(1+\frac{R_1}{R_2}\right)+CR_1\frac{dQ}{dt}=\frac{P}{R_2}+C\frac{dP}{dt}, \tag{2.76}$$

which can be easily derived from the equivalent circuit of Fig. 2.4. This type of boundary condition will be adopted both in Chapter 3 and in Chapter 4.

Chapter 3

An optimal control approach for resistive boundary conditions estimation

In this chapter, we will present a boundary condition estimation framework based on optimal control. This technique is what we call a *data and model-driven* approach, because the estimation is based on patient-specific measurements, as well as on a mathematical representation of the system underneath, obtained by means of PDE. The estimation framework proposed in this chapter allows to determine the values of resistive-type boundary conditions starting from pressure and flow rate measurements, and using a steady Stokes model to represent the blood flow dynamics. This is achieved by solving a so-called *Optimal Control Problem* (OCP). The optimal control framework is a powerful and elegant mathematical tool which has been employed in a wide variety of fields, from environmental sciences [97], to haemodynamics [98–101] and industrial applications [102–104]. Due to its generality and mathematical soundness, optimal control has been successfully used to tackle a number of different engineering problems, such as shape optimization [105, 101], data assimilation [106, 107] and parameter estimation [108, 109], where the OCP is used to identify some unknown parameters by relying on a set of measurements.

3.1 Introduction and related work

As explained in the introduction of this thesis, when dealing with computational models of the cardiovascular system, boundary conditions play an important role in the accuracy of the model, and several studies have shown how boundary conditions affect clinically relevant parameters, such as wall shear stress (WSS)[110–112]. The selection of proper boundary conditions benefits from the availability of patient-specific measurements, as BCs can be properly tuned to match available clinical data. For what concerns outlet boundary conditions, we have seen how the most realistic choice consists in using zero-dimensional models, also known as lumped parameter models. These conditions prescribe at the outlet specific pressure-flow relationships which, by exploiting the analogy between the electrical and hydraulic domains, can be represented as electrical networks [113–117]. Lumped models may consist of single resistances or more sophisticated models, such as the three-element Windkessel model [118] introduced in Chapter 2. Using this type of conditions, however, requires to choose appropriate values for the lumped elements.

In this chapter, we propose a novel framework to automatically estimate resistive-type outlet boundary conditions by solving an optimal control problem, which assimilates a set of patient-specific measurements, e.g., 4D-Flow MRI data. This is obtained by minimizing a cost functional which computes the distance between the OCP solution and measurements, subject to the constraints induced by the steady Stokes equations. The control variables are the unknown resistance values imposed at the outlets through the coupled multidomain method introduced by Vignon-Clementel et al.[44]. To ensure a better match between simulation results and *in-vivo* data, the inlet flow waveform measured with 4D-Flow MRI is imposed as a patient-specific inlet boundary condition. The proposed framework is general and can be applied to any part of the cardiovascular system, provided that some measurements are available. In this chapter, however, we demonstrate its use on patient-specific models of the aortic arch like the one represented in Fig. 3.1, where the boundary conditions have to be imposed at the inlet Γ_{in} and at the four outlets comprising the descending aorta (DAo) and the supra-aortic branches: brachiocephalic artery (BCA), left common carotid artery (LCC), and left subclavian artery (LSUB).

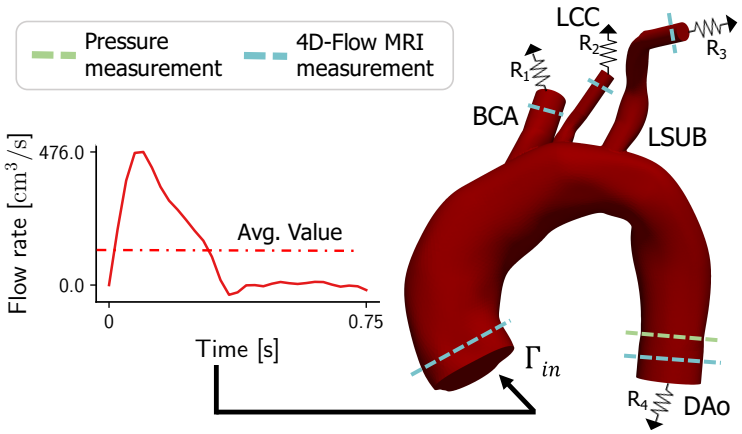

Fig. 3.1 General configuration for the proposed optimal control approach on a patient's aortic arch. Haemodynamics is simulated by prescribing the measured inlet flow rate and the optimized resistive-like boundary conditions at the outlets, being the outlets the brachiocephalic artery, the left common carotid artery, the left subclavian artery, and the descending aorta. These BCs are calculated using pressure and flow rate measurements at several locations.

Optimal control has been already successfully applied to several haemodynamics problems, from the shape optimization of aorto-coronaric bypass anastomoses [101], to vorticity minimization problems [119]. For boundary conditions estimation, an optimal control-based solution was proposed in [73], based on the assimilation of velocity measurements. The framework was validated on an idealized 2D geometry and tested on a 3D model of a brain aneurysm, but with the assimilated velocity data still synthetically generated. In [74], Koltukluouglu et al. proposed a data assimilation method based on optimal boundary control for 3D steady-state blood flow simulations. The authors validated the proposed framework with real 4D-flow MRI data measured on a glass replica of a human aorta. However, optimal control requires the solution of a constrained optimization problem, which is usually a computationally demanding task. To reduce the computational cost of optimal control, Romarowski et al. [69] proposed to estimate the parameters of three-element Windkessel models by means of a *least-squares* approach, by identifying a surrogate optimization problem for prescribing PC-MRI data as outlet boundary conditions. Optimal control has been also used in [120] to estimate the uncertainty coming from the segmentation process, which affects the definition of the geometry and, in turn, wall shear stress and its derived measures. Finally, Zainib et al. [100] brought optimal control closer to a real clinical setting, by presenting a reduced order

framework for the application of optimal control to coronary artery bypass grafts. In this case, the assimilated velocity data were synthetically generated, and the estimated boundary conditions were Neumann-type boundary conditions, so less realistic than lumped parameter models.

One of the novel aspects of the approach proposed in this chapter is the use of more realistic boundary conditions with respect to Neumann and Dirichlet BCs, up to now the standard in an optimal control setting. Its suitability for real clinical scenarios is demonstrated by validating the framework on four aortic arches, reconstructed from medical images of real clinical cases. The presented method is used in these cases to set the outlet BCs on the descending aorta and the supra-aortic branches, assimilating real 4D-Flow MRI data. To validate the obtained results, the estimated boundary conditions are compared to those provided by two alternative techniques, namely, Murray's law and Ohm's law, demonstrating the ability of optimal control to assimilate known physiological data consistently better. Moreover, an analysis of time-averaged wall shear stress and oscillatory shear index values obtained using the three different calibration methods is used to assess their effect on clinical haemodynamic indicators.

The rest of the chapter is organized as follows. First, a more general and theoretical introduction to the topic of optimal control is provided in Section 3.2, including a brief review of the most common approaches for the treatment, numerical approximation, and solution of optimal control problems. Then, in Section 3.3 a description of the adopted methodology for the proposed optimal control framework is provided, followed by some relevant numerical results in Section 3.4. Finally, Section 3.5 presents a discussion of the results, and Section 3.6 provides some conclusions and future perspectives.

3.2 Theoretical background on optimal control

It is common in engineering and applied sciences to model problems by means of a set of equations, usually PDE, dependent on some parameters, which could be material coefficients, geometrical or physical quantities, or boundary conditions.

Often, the problem described by PDE needs to be optimized or controlled in some way by changing these parameters. This typical scenario turns out to be a challenging mathematical task, which can be solved by means of an optimal control problem. Solving an OCP means finding a *control function* and a *state function* optimizing a quantity, called *cost* or *objective* function, which is dependent both on the control and on the state function. For this reason, an OCP is defined by the presence of three main ingredients:

- a **state problem**, in our case consisting of a system of PDE;
- a **cost functional**, which has to be minimized through the optimization process, and which sets the goal of the optimization problem;
- some **control variables**, which must be chosen in order to minimize the cost functional.

In synthesis, solving an OCP means finding the optimal pair of state and control variables minimizing the cost functional.

Let us define a generic optimal control problem, where y denotes the state variables, u the control variable, $J(y,u)$ the cost functional and $F(y,u)$ the state problem. The optimization problem then reads

Problem 3.2.1 *Find states y and controls u such that $J(y,u)$ is minimized subject to $F(y,u)=0$.*

Such a problem can be approached in two ways. The first approach is called "à la J.L. Lions", as it is based on the theoretical development of PDE-constrained optimal control proposed by J.L. Lions, which proved the existence and uniqueness of the solution of optimal control problems governed by elliptic, parabolic and hyperbolic PDEs [121, 122]. A second, more intuitive approach is instead the Lagrangian approach which, as the name suggests, is based on the use of a Lagrangian functional to make the definition of the optimality system straightforward. The general optimal control problem introduced in Problem 3.2.1, in fact, can be seen as a constrained optimization problem. Thanks to the definition of a Lagrangian functional, this can be recast as an unconstrained one, easier to treat. In this chapter we will present and adopt the Lagrangian approach; more information on the first approach can be found in [80].

3.2.1 The adjoint-based Lagrangian approach

Before introducing the Lagrangian approach for the treatment of OCPs, it is necessary to discuss the existence of the solution for a general nonlinear optimal control problem.

Existence results Let us consider three Banach spaces Y, U, Z and let us define the general optimal control problem as

$$\min_{(y,u)\in Y\times U} J(y,u) \quad \text{subject to } F(y,u)=0, \quad y\in Y_{ad}, u\in U_{ad}. \tag{3.1}$$

where the functional $J : Y \times U \to \mathbb{R}$ and the state equation $F : Y \times U \to Z$ are continuous. The subsets $U_{ad} \subseteq U$ and $Y_{ad} \subseteq Y$ are the control space and state space, respectively, and if $Y_{ad} = Y$ and $U_{ad} = U$ the problem is said to be unconstrained. To prove the existence of a solution for the optimal control problem (3.1), we need to make the following assumptions, which will be valid also in our specific case, presented later in Section 3.3:

1. Y_{ad} is convex and closed, such that (3.1) has a feasible point;
2. U_{ad} is convex, bounded and closed;
3. $F : Y \times U \to Z$ is continuous under weak convergence;
4. J is weakly lower semicontinuous[1];
5. the state equation $F(y, u) = 0$ has a bounded solution operator $u \in U_{ad} \to y(u) \in Y$.

Under these hypotheses, the following theorem holds [123] (see Section 1.5.2 of [123] for proof):

Theorem 3.2.1 *Under assumptions (1)-(5), the optimal control problem* (3.1) *has an optimal solution* $(\bar{y}, \bar{u})$.

[1] A functional $J : X \to \mathbb{R}$ is weakly lower semicontinuous in X if for all $x \in X$ and every sequence $x_n \to x$ which converges weakly to $x \in X$, we have

$$\lim_{x\to 0} \inf J(x_n) \geq J(x). \tag{3.2}$$

Now that the existence of a solution is guaranteed, we can proceed with the solution of the OCP. The first step consists in deriving a formulation of the OCP equivalent to (3.1), but using a *reduced space approach*.

The reduced problem We consider three Banach spaces Y, U, Z and a generic constrained OCP

$$\min_{(y,u)\in Y\times U} J(y,u) \quad \text{subject to } F(y,u)=0, \quad u\in U_{ad}. \tag{3.3}$$

We need to make the following assumptions, which again will be satisfied also in the case presented later in Section 3.3:

- U_{ad} is nonempty, closed, bounded and convex.
- J and F are continuously Frechét differentiable (meaning that they are differentiable in a Banach space);
- For all $u\in U_{ad}$, there exists a unique $y=y(u)\in Y$;
- the inverse $F_y(y(u),u)^{-1}$ is bounded $\forall u\in U_{ad}$.

Thanks to these assumptions, we can rewrite problem (3.3) in an equivalent form, known as the *reduced problem*:

$$\min_{u\in U} \hat{J}(u) = J(y(u),u) \quad \text{subject to } u\in U_{ad}, \tag{3.4}$$

where we introduced the reduced cost functional $\hat{J}(u) := J(y(u),u)$ and we substituted y with $y(u)$. Solving the optimization problem means minimizing $\hat{J}(u)$, and this requires finding an expression for its derivative, which will be denoted from now on as $\hat{J}'(u)$. This can be obtained by means of a sensitivity analysis approach [124, 123], or with the adjoint approach, which is the one we will adopt.

The adjoint-based Lagrangian approach We show how an explicit expression for the derivative of the reduced cost functional $\hat{J}(u)$ can be obtained thanks to the adjoint approach based on the Lagrangian functional. In order to

do this, let us start by defining the *Lagrangian functional* $\mathcal{L} : Y \times U \times Z^* \to \mathbb{R}$ as

$$\mathcal{L}(y, u, p) = J(y, u) + \langle p, F(y, u) \rangle_{Z^*,Z}, \tag{3.5}$$

where $p \in Z^*$ is called the adjoint variable, or Lagrange multiplier. Assuming that the initial assumptions needed for the derivation of the reduced problem (3.4) are still valid, we can rewrite the reduced cost functional $\hat{J}(u)$ in terms of the Lagrangian functional as

$$\hat{J}(u) = J(y(u), u) = J(y(u), u) + \langle p, F(y(u), u) \rangle_{Z^*,Z} = \mathcal{L}(y, u, p). \tag{3.6}$$

This expression can be differentiated, obtaining

$$\langle \hat{J}'(u), s \rangle_{U^*U} = \langle \mathcal{L}_y(y(u), u, p), y'(u)s \rangle_{Y^*,Y} + \langle \mathcal{L}_u(y(u), u, p), s \rangle_{U^*,U}. \tag{3.7}$$

Our goal is to find an expression for the cost functional derivative $\hat{J}'(u)$, so we seek a value for $p = p(u)$ such that $\mathcal{L}_y(y(u), u, p) = 0$. This implies

$$\hat{J}'(u) = \mathcal{L}_u(y(u), u, p(u)) = J_u(y(u), u) + F_u(y(u), u)^* p(u) \tag{3.8}$$

where the superscript * indicates the dual operator, as introduced in Section 2.2.1. In this way we have obtained an explicit expression for $\hat{J}'(u)$. Since $p(u)$ is still unknown, we use the condition $\mathcal{L}_y(y(u), u, p) = 0$ imposed earlier to obtain

$$\begin{aligned} \langle \mathcal{L}_y(y, u, p), z \rangle_{Y^*,Y} &= \langle J_y(y, u), z \rangle_{Y^*,Y} + \langle p, F_y(y, u)z \rangle_{Z^*,Z} \\ &= \langle J_y(y, u) + F_y(y, u)^* p, z \rangle_{Y^*,Y} = 0, \qquad \forall z \in Y \end{aligned} \tag{3.9}$$

Therefore, $p \in Z^*$ is the solution of the adjoint equation

$$F_y(y(u), u)^* p = -J_y(y(u), u). \tag{3.10}$$

We have then shown a method based on the Lagrangian representation to derive the adjoint equation. This approach will be instrumental to the definition of an optimality system for the optimal control problem, as it will be detailed in the following section.

3.2.2 The optimality system

At this point, finding a solution to the optimal control problem is equivalent to finding a stationary point for the Lagrangian $\mathcal{L}$, which means satisfying its first order optimality conditions. Thanks to the derivations carried out earlier, we can now exploit an important result, stated in the following theorem (see [123], Theorem 1.48):

Theorem 3.2.2 (Minimum principle) *Let us suppose that the assumptions required for the derivation of* (3.4) *hold. If $u^\star$ is a local solution of the reduced problem* (3.4)*, then the following inequality holds:*

$$\langle \hat{J}'(u^\star), v - u^\star \rangle_{U^*,U} \geq 0, \quad \forall v \in U_{ad}. \tag{3.11}$$

Exploiting the expression for $\hat{J}'(u^\star)$ derived earlier, we can state the following corollary to Theorem 3.2.2 [123], which provides first order optimality conditions.

Corollary 3.2.1 *Let $(y^\star, u^\star) \in Y \times U_{ad}$ be the solution to optimal control problem* (3.4)*. Then there exists a Lagrange multiplier (or adjoint state) $p \in Z^*$ such that the following optimality conditions hold*

$$\begin{cases} F(y^\star, u^\star) = 0, \\ F_y(y^\star, u^\star)^* p^\star = -J_y(y^\star, u^\star), \\ \langle J_u(y^\star, u^\star) + F_u(y^\star, u^\star)^* p^\star, v - u^\star \rangle_{U^*,U} \geq 0 \forall v \in U_{ad}. \end{cases} \tag{3.12}$$

Using the Lagrangian functional, this system is equivalent to

$$\begin{cases} \langle \mathcal{L}_p(y^\star, u^\star, p^\star), q \rangle_{Z,Z^*} = 0 & \forall q \in Z^* \\ \langle \mathcal{L}_y(y^\star, u^\star, p^\star), z \rangle_{Y^*,Y} = 0 & \forall z \in Y \\ \langle \mathcal{L}_u(y^\star, u^\star, p^\star), v - u^\star \rangle_{U^*,U} \geq 0 & \forall v \in U_{ad}. \end{cases} \tag{3.13}$$

The variational formulation (3.13) *expressed in terms of the functional* J *and the state equation* F *becomes*

$$\begin{cases} \langle F(\bar{y}, \bar{u}^\star), q\rangle = 0 & \forall q \in Z^* \\ \langle J_y(\bar{y}, \bar{u}^\star) + F_y(\bar{y}^\star, \bar{u}^\star)^* \bar{p}^\star, z\rangle_{Y^*,Y} = 0 & \forall z \in Y \\ \langle \hat{J}_u(y^\star, u^\star) + F_u(y^\star, u^\star)^* p^\star, v - u^\star\rangle_{U^*,U} \geq 0 & \forall v \in U_{ad}. \end{cases} \tag{3.14}$$

It can be noticed that the solutions of the system (3.13) are the stationary points of the Lagrangian functional $\mathcal{L}(\cdot,\cdot,\cdot)$, that is,

$$\nabla\mathcal{L}(y^\star, u^\star, p^\star)[z, v, q] = 0, \forall (z, v, q) \in Y \times U \times Z^*. \tag{3.15}$$

System (3.14) is also known as the coupled Karush-Kuhn-Tucker optimality system [80], which can be obtained from first order optimality conditions and is equivalent to system (3.13), derived from the Lagrangian functional.

3.2.3 The saddle-point formulation for Linear Quadratic OCPs

Before seeing how the optimality system obtained in the previous section can be properly discretized and solved, it is necessary to introduce a property of some optimal control problems. In particular, when we consider linear quadratic control problems, it can be demonstrated that their optimality system has a saddle-point structure. This fact is useful for a number of reasons. First, the existence and uniqueness of a problem with saddle-point structure has been proved by a number of theorems, which we will introduce in the following. Second, the saddle-point structure of the optimality system clarifies the choice we will make in terms of solution method, as the so-called *one-shot* approach becomes intuitively the best choice for this type of problem.

Let us first introduce a generic saddle-point problem, by considering two Hilbert spaces X and Q, and their dual spaces X^* and Q^*, respectively. We introduce two continuous bilinear forms $\mathcal{A}(\cdot,\cdot) : X \times X \to \mathbb{R}$ and $\mathcal{B}(\cdot,\cdot) : X \times Q \to \mathbb{R}$, and also the functionals $F : X^* \to \mathbb{R}$, $G : Q^* \to \mathbb{R}$. We can now define the following saddle-point problem:

Problem 3.2.2 *Find* $(x, p) \in X \times Q$ *such that*

$$\begin{cases} \mathcal{A}(x, v) + \mathcal{B}(v, p) = \langle F, v \rangle & \forall v \in X, \\ \mathcal{B}(x, q) = \langle G, q \rangle & \forall q \in Q. \end{cases} \tag{3.16}$$

The existence, uniqueness and stability of the solution to the saddle-point problem (3.16) is well-established by the Brezzi theorem (see [125] for details and proof). The theorem requires two main assumptions:

- the bilinear form $\mathcal{A}(\cdot, \cdot)$ must be weakly coercive[2] on the subspace $X_0 \subset X$, which is defined as

$$X_0 = \{w \in X : \mathcal{B}(w, q) = 0 \quad \forall q \in Q\}. \tag{3.18}$$

  In other words, there exists a constant $\alpha_0 > 0$ such that

$$\inf_{w \in X_0} \sup_{x \in X_0} \frac{\mathcal{A}(x, w)}{||x||_X ||w||_X} \geq \alpha_0 \quad \text{and} \quad \inf_{x \in X_0} \sup_{w \in X_0} \frac{\mathcal{A}(x, w)}{||x||_X ||w||_X} > 0. \tag{3.19}$$

- The bilinear form $\mathcal{B}(\cdot, \cdot)$ must satisfy the inf-sup condition, meaning that there exists a constant $\beta_0 > 0$ such that

$$\beta = \inf_{q \in Q} \sup_{w \in X} \frac{\mathcal{B}(w, q)}{||w||_X ||q||_Q} \geq \beta_0. \tag{3.20}$$

Under these assumptions the solution to problem (3.16) exists and is unique.

We now show how a linear quadratic OCP can be recast into a problem equivalent to (3.16), thanks to the following theorem (see [126], Proposition 1.7):

Theorem 3.2.3 *Assume that the hypotheses of the Brezzi theorem hold. Moreover, let* $\mathcal{A}(\cdot, \cdot)$ *be a symmetric, nonnegative and coercive bilinear form on* X_0

[2] A bilinear form $A : X \times X \to \mathbb{R}$, where X is a Hilbert space, is called coercive if there exists a constant $c > 0$ such that

$$A(x, x) \geq c||x||^2. \tag{3.17}$$

with coercivity constant α_0, meaning

$$\mathcal{A}(x,w) = \mathcal{A}(w,x), \mathcal{A}(x,x) \geq 0 \quad \forall x, w \in X \tag{3.21}$$

and

$$\mathcal{A}(x,x) \geq \alpha_0 ||x||_X \quad \forall x \in X_0. \tag{3.22}$$

Then, problem 3.2.2 is equivalent to the constrained optimization problem

$$\begin{cases} \min \mathcal{J}(\underline{x}) = \frac{1}{2}\mathcal{A}(\underline{x},\underline{x}) - \langle F, \underline{x} \rangle, & \textit{subject to} \\ \mathcal{B}(\underline{x}, q) = \langle G, q \rangle & \forall q \in Q. \end{cases} \tag{3.23}$$

3.2.4 Example of a linear quadratic optimal control problem

To better clarify the important connection between saddle-point problems and OCPs, let us show how a saddle-point problem can be derived from the optimality system of a linear quadratic optimal control problem through a running example. In particular, considering that the estimation framework presented in Section 3.3 will be based on Stokes equations, let us consider a distributed optimal control problem governed by Stokes equations. The problem has the following form:

$$\min_{\mathbf{v},p,\mathbf{u}} J(\mathbf{v},p,\mathbf{u}) = \frac{1}{2}\int_\Omega |\mathbf{v} - \mathbf{v}_d|^2 d\Omega + \frac{\alpha}{2}\int_\Omega |\mathbf{u}|^2 d\Omega, \tag{3.24}$$

such that

$$\begin{cases} -\nu\Delta\mathbf{v} + \nabla p = \mathbf{u} & \text{in } \Omega, \\ \nabla \cdot \mathbf{v} = 0 & \text{in } \Omega, \\ \mathbf{v} = 0 & \text{on } \partial\Omega. \end{cases} \tag{3.25}$$

In problem (3.25) ν represents the kinematic viscosity, $\mathbf{v} \in V := H_0^1(\Omega) \times H_0^1(\Omega)$ the velocity, $p \in P := L_0^2(\Omega)$ the pressure, and $\Omega \subset \mathbb{R}^2$ is an open, bounded and regular domain. This problem is a so-called *data assimilation* problem, since the cost functional represents the distance between velocity $\mathbf{v}$ and some

velocity measurements, indicated with $\mathbf{v}_d$. The solution to this optimal control problem, then, is the one which is closest to the available measurement data. The minimum will be reached by adjusting the control variable $\mathbf{u}$, which in this case is the forcing term in the first Stokes equation, the momentum balance equation. For this reason, this type of control is called *distributed control*, since it is defined and acts on the entire domain Ω. A slightly more advanced case is *boundary control*, when the control variable is only defined on the boundary. A boundary control problem will be presented in the second part of this chapter, when optimal control will be used to estimate boundary conditions (thus defining the control variable only at the boundary). For now, let us start from this simpler data assimilation problem.

The control variable $\mathbf{u}$ belongs to the space $U = L^2(\Omega) \times L^2(\Omega)$. We define also $Y = V \times P$ as the space of the state variable $y = (\mathbf{v}, p)$, such that the dual space is $Y^* = V^* \times P^*$. The next step consists in building the weak formulation of the state equations, which requires defining the bilinear forms $a(\cdot,\cdot) : V \times V \to \mathbb{R}$, $b(\cdot,\cdot) : V \times P \to \mathbb{R}$ and $c(\cdot,\cdot) : V \times V \to \mathbb{R}$ as

$$a(\mathbf{v}, \boldsymbol{\phi}) = \nu \int_\Omega \nabla \mathbf{v} \cdot \nabla \boldsymbol{\phi} \, d\Omega \tag{3.26}$$

$$b(\mathbf{v}, p) = -\int_\Omega \nabla \cdot \mathbf{v} p \, d\Omega \tag{3.27}$$

$$c(\mathbf{u}, \boldsymbol{\phi}) = \int_\Omega \mathbf{u} \cdot \boldsymbol{\phi} \, d\Omega \tag{3.28}$$

The weak formulation then reads: find $y = (\mathbf{v}, p)$ such that

$$\begin{cases} a(\mathbf{v}, \boldsymbol{\phi}) + b(\mathbf{v}, p) = c(\mathbf{u}, \boldsymbol{\phi}) & \forall \boldsymbol{\phi} \in V, \\ b(\mathbf{v}, \xi) = 0 & \forall \xi \in P. \end{cases} \tag{3.29}$$

The Stokes problem (3.29) is an example of saddle-point problem satisfying the assumptions of the Brezzi theorem [125] presented in Section 3.2.3. Then, we can use the Lagrangian functional to derive the optimality system. First we

define the Lagrangian functional

$$\begin{aligned}\mathcal{L}(\mathbf{v}, p, \mathbf{u}, \mathbf{w}, q) = \frac{1}{2}\langle \mathbf{v} - \mathbf{v}_d, \mathbf{v} - \mathbf{v}_d \rangle_{L^2} + \frac{\alpha}{2}\langle \mathbf{u}, \mathbf{u} \rangle_{L^2} + a(\mathbf{v}, \mathbf{w}) \\ + b(\mathbf{w}, p) - c(\mathbf{u}, \mathbf{w}) + b(\mathbf{v}, q).\end{aligned} \tag{3.30}$$

The optimality system is obtained by imposing that the derivatives of $\mathcal{L}(\cdot, \cdot, \cdot)$ with respect to $(\mathbf{v}, p, \mathbf{u}, \mathbf{w}, q) \in V \times P \times U \times V \times P$ must vanish, obtaining

$$\begin{cases} a(\mathbf{v}, \boldsymbol{\phi}) + b(\mathbf{v}, p) = c(\mathbf{u}, \boldsymbol{\phi}) & \forall \boldsymbol{\phi} \in V, \\ b(\mathbf{v}, \xi) = 0 & \forall \xi \in P, \\ a(\boldsymbol{\psi}, \mathbf{w}) + b(\boldsymbol{\psi}, q) = \langle \mathbf{v} - \mathbf{v_d}, \boldsymbol{\psi} \rangle_{L^2} & \forall \boldsymbol{\psi} \in V, \\ b(\mathbf{w}, \pi) = 0 & \forall \pi \in P, \\ \alpha \langle \mathbf{u}, \boldsymbol{\tau} \rangle_{L^2} = c(\boldsymbol{\tau}, \mathbf{w}) & \forall \boldsymbol{\tau} \in U. \end{cases} \tag{3.31}$$

The nested saddle-point structure for this problem reads:

$$\begin{cases} \langle \mathbf{v}, \boldsymbol{\psi} \rangle_{L^2} + a(\boldsymbol{\psi}, \mathbf{w}) + b(\boldsymbol{\psi}, q) = (\mathbf{v_d}, \boldsymbol{\psi})_{L^2} & \forall \boldsymbol{\psi} \in V, \\ \quad + b(\mathbf{w}, \pi) = 0 & \forall \pi \in P, \\ \quad + \alpha \langle \mathbf{u}, \boldsymbol{\tau} \rangle_{L^2} - c(\boldsymbol{\tau}, \mathbf{w}) = 0 & \forall \boldsymbol{\tau} \in U, \\ a(\mathbf{v}, \boldsymbol{\phi}) + b(\boldsymbol{\phi}, p) - c(\mathbf{u}, \boldsymbol{\phi}) = 0 & \forall \boldsymbol{\phi} \in V, \\ b(\mathbf{v}, \xi) = 0 & \forall \boldsymbol{\xi} \in P. \end{cases} \tag{3.32}$$

The visible compact block structure of system (3.32) simplifies its solution in a discretized setting, allowing to use a *one-shot* approach for its numerical solution. Some additional details on this solution approach are given in the next section.

3.2.5 Numerical approximations and solution methods

After covering the theoretical background on optimal control problems, it is necessary to transform the obtained problem into a discrete control problem,

so that it can be solved numerically. To do so, there are two alternative approaches:

- **discretize-then-optimize**: with this method, first the state equations are discretized, and the control problem is solved afterwards;
- **optimize-then-discretize**: in this case, first a system of optimality conditions is formalized at the continuous level, and subsequently the equations of the optimality system are discretized.

It must be noticed that the two methods do not always lead to the same result. Generally the first approach is adopted for *optimal design* problems, while it may cause numerical errors in other types of OCPs [127, 128]. For optimal control problems that do not involve the optimization of a design, instead, the second method is generally adopted. As a matter of fact, an optimize-then-discretize approach is used for the optimal control formulation proposed later in this chapter.

Regarding the solution method, there are two main approaches when solving a generic optimal control problem as defined in (3.1):

- **iterative method**. This approach consists in eliminating the PDE constraint by replacing y with $y(u)$, and keeping only the control u as optimization variable. The problem, then, consists in minimizing the reduced cost functional $\hat{J}(u) = J(y(u), u)$, which can be done by means of standard algorithms like gradient, conjugate gradient, Newton and quasi-Newton methods (see, e.g. [129, 130]).
- **one-shot method**. With this approach we solve the optimality system obtained with the Lagrangian approach, by means of direct or iterative system solvers.

Since the one-shot method is the approach adopted in the framework proposed in this chapter, we will briefly describe it in the following.

We first need to introduce a discretization of the problem (3.16). In particular, we will adopt a Galerkin finite element approximation, by considering the discretization $\mathcal{T}_h$ of the domain Ω with size $0 < h \in \mathbb{R}^+ < \infty$. Consequently,

we define the two finite dimensional spaces X_h and Q_h of the spaces X and Q, respectively. Also, we indicate their respective dimension as $\mathcal{N}_X$ and $\mathcal{N}_Q$. The Galerkin finite element approximation of problem (3.16) is:

Problem 3.2.3 *Find* $(x_h, p_h) \in X_h \times Q_h$ *such that*

$$\begin{cases} \mathcal{A}(x_h, v_h) + \mathcal{B}(v_h, p_h) = \langle F, v_h \rangle & \forall v_h \in X_h, \\ \mathcal{B}(x_h, q_h) = \langle G, q_h \rangle & \forall q_h \in Q_h. \end{cases} \tag{3.33}$$

We can now define the basis functions of the finite spaces X_h and Q_h with

$$\{\varphi_j \in X_h\}_{j=1}^{\mathcal{N}_X} \qquad \{\psi_k \in Q_h\}_{k=1}^{\mathcal{N}_Q}. \tag{3.34}$$

The solution $(x_h, p_h) \in X_h \times Q_h$ to the problem (3.33) can be rewritten as

$$\left(x_h = \sum_{j=1}^{\mathcal{N}_X} x_j \varphi_j(x),\ p_h = \sum_{k=1}^{\mathcal{N}_Q} p_k \psi_k(x) \right). \tag{3.35}$$

If we choose the basis functions (3.34) as test functions for the problem (3.33), we can define $A \in \mathbb{R}^{\mathcal{N}_X \times \mathcal{N}_X}, B \in \mathbb{R}^{\mathcal{N}_Q \times \mathcal{N}_X}, \mathbf{F} \in \mathbb{R}^{\mathcal{N}_X}$ and $\mathbf{G} \in \mathbb{R}^{\mathcal{N}_Q}$ as follows:

$$A_{ij} = \mathcal{A}(\varphi_i, \varphi_j), \quad B_{ml} = \mathcal{B}(\varphi_l, \psi_m), \quad \mathbf{F}_k = \langle F, \varphi_k \rangle, \quad \mathbf{G}_s = \langle G, \psi_s \rangle. \tag{3.36}$$

Thanks to these definitions, we can rewrite the saddle-point problem (3.33) as the following linear system with a block structure

$$\begin{pmatrix} A & B^T \\ B & 0 \end{pmatrix} \begin{pmatrix} \mathbf{x} \\ \mathbf{p} \end{pmatrix} = \begin{pmatrix} \mathbf{F} \\ \mathbf{G} \end{pmatrix}, \tag{3.37}$$

where $(\mathbf{x})_i = x_i$ and $(\mathbf{p})_k = p_k$. System (3.37) is the optimality system associated to an OCP problem with the following algebraic formulation:

$$\text{minimize } \frac{1}{2}\mathbf{x}^T A \mathbf{x} - \mathbf{F}^T \mathbf{x} \quad \text{subject to } B\mathbf{x} = \mathbf{G}. \tag{3.38}$$

The **one-shot** method exploits exactly the block structure that the optimality system of a linear quadratic OCP assumes, when recast into a saddle-point

framework. The one-shot method, in fact, provides a solution to the optimal control problem by directly solving the linear system (3.37).

In this section, we have provided a general overview on the topic of optimal control. In particular, we have introduced the generic structure of an OCP, and reviewed a common approach, i.e. the adjoint-based Lagrangian one, to derive the corresponding optimality system. We have then briefly introduced the one-shot method as a possible approach to solve the discretized version of the optimality system. These concepts will be used in the next section, where we finally present the proposed estimation method for resistive boundary conditions based on the solution of an optimal control problem.

3.3 Proposed methodology

In this section the methodological details of the proposed boundary conditions estimation approach will be presented. When dealing with patient-specific anatomies, some preliminary steps are required before solving the actual optimal control problem. In particular, one needs to reconstruct the patient-specific geometries from clinically acquired images (CT scans), and to acquire patient-specific data, in this case from 4D-Flow MRI measurements, which will be assimilated through optimal control. A representation of the experimental pipeline adopted for the proposed approach is represented in Fig. 3.2. In the following, we will first provide some details on the data acquisition and segmentation process in Section 3.3.1, before introducing the optimal control framework in Section 3.3.2.

3.3.1 Anatomical reconstruction and 4D-Flow MRI data acquisition

The proposed method has been tested on four clinical cases from a single-center prospective study conducted at the Sunnybrook Health Sciences Centre in Toronto, Canada. The study was approved by the local ethics board and informed consent was obtained. Moreover, all the measurements were acquired non-invasively. Patients presented at the hospital for coronary bypass graft surgery. Between three and six weeks after surgery, a cardiac CT was performed

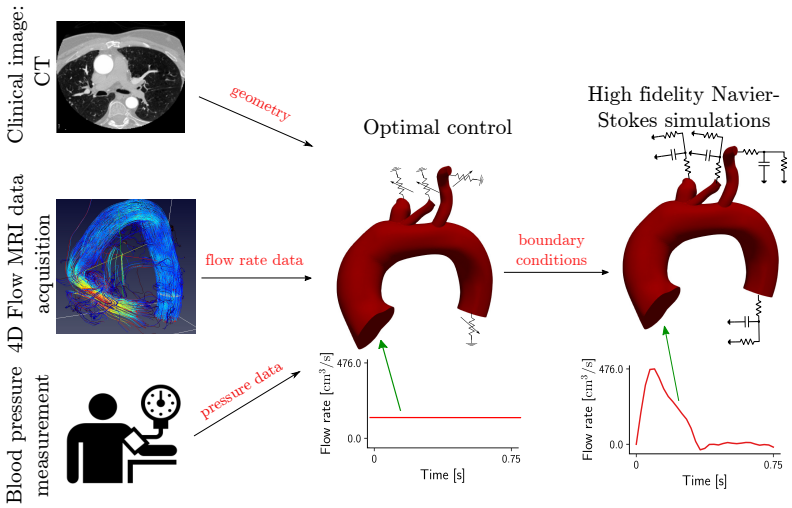

Fig. 3.2 Scheme of the proposed framework for boundary condition estimation through optimal control.

and anatomical information about their aorta and its supra-aortic branches was acquired using a 320-detector row CT scanner (Aquilion One, Canon Medical Systems). From CT images, the vessels surface was reconstructed using the open-source package SimVascular [26]. The reconstructed volume was discretised into tetrahedral elements using TetGen [131]. After the CT scan, the blood velocity in the aorta and its branches was acquired in-vivo using a 4D-flow MRI sequence, using a 3T MRI scanner (MAGNETOM Prisma, Siemens Healthineers). The acquisition was performed using a 4D flow imaging sequence with retro-gating and adaptive navigator respiratory gating. Imaging parameters were as follows: encoding velocity=150 cm/s, field of view=200-420 mm x 248-368 mm, spatial resolution=1.9-3.5 x 2.0-3.2 x 1.8-3.5 mm^3, temporal resolution=39.9-47.2 ms, flip angle=8°. After 4D-Flow MRI, diastolic blood pressure P_{diast} and systolic blood pressure P_{sys} were measured with the brachial cuff-based method. The mean arterial pressure P_{mean} was computed as [132]

$$P_{mean} = \frac{P_{sys} + 2P_{diast}}{3}. \tag{3.39}$$

The pressure and flow rate measurements collected on the patients were then assimilated into the mathematical model describing blood flow in the anatomy, thanks to the framework presented in the next section.

3.3.2 Determination of boundary conditions through optimal control

As explained in Section 3.2, an optimal control always includes a number of control variables (the resistive boundary conditions in our case), which are unknown quantities and must be determined, a cost functional to be minimized, and a set of equations describing the physics of blood flow. In this case, we used steady Stokes equations to model blood flow, ensuring a simpler optimal control problem with respect to nonlinear Navier-Stokes equations. However, this choice means that blood flow will be modeled in a less realistic way, which could potentially affect the quality of the estimated parameters. Thus, we will assess the effect that this choice has by validating the obtained results on a Navier-Stokes model, as reported in Section 3.4.

The state equations

Since the anatomies considered in this framework are composed of the aorta and supra-aortic branches, it is safe to assume that the dimension of blood particles is much smaller that vessel diameter, meaning that blood behaves as a Newtonian fluid with constant viscosity. An example of an aortic arch used in this framework is represented in Fig. 3.1, whose 3D volume constitutes the computational domain Ω, on which the incompressible Stokes equations will be solved. The boundary of Ω is referred to as $\partial\Omega = \Gamma_{in} \cup \Gamma_w \cup \Gamma_i$, where Γ_{in}, Γ_w, and Γ_i denote the inlet of the aorta, the vessel walls, and the outlets of the aortic arch, with $1 \leq i \leq i_{max}$ ($i_{max} = 4$ in the case of Fig. 3.1), respectively. The control variables, corresponding to the outlet resistances, are denoted as R_i. Thus, state equations can be written in strong form as

$$\begin{cases} -\nu\Delta\mathbf{v} + \nabla p = 0 & \text{in } \Omega, \\ \nabla \cdot \mathbf{v} = 0 & \text{in } \Omega, \\ \mathbf{v} = \mathbf{v}_{in} & \text{on } \Gamma_{in}, \\ \mathbf{v} = 0 & \text{on } \Gamma_w, \\ p = R_i \displaystyle\int_{\Gamma_i} \mathbf{v} \cdot \mathbf{n}\, d\Gamma_i & \text{on } \Gamma_i,\ 1 \leq i \leq i_{max}, \end{cases} \tag{3.40}$$

where $\nu = 0.04$ dynes/cm^{2}s the dynamic viscosity, and $\mathbf{n}$ the outward normal to the outlets. By means of the condition $\mathbf{v} = \mathbf{v}_{in}$, a plug profile is imposed at the inlet Γ_{in}, whose average value is extracted from the 4D-Flow MRI data. This profile choice is motivated by the fact that a plug profile is more realistic than a parabolic profile for the ascending aorta. These two types of inlet profiles are represented in Fig. 3.3. Despite the availability of 4D-Flow MRI

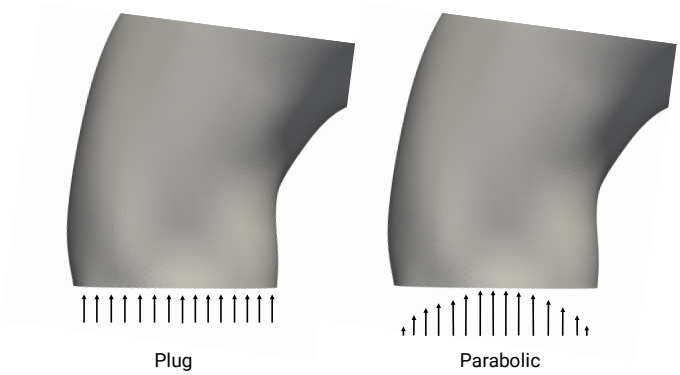

Fig. 3.3 Comparison of a plug profile (left) and a parabolic profile (right) which can be imposed at the inlet of the model.

data, a standard inlet profile was used instead of the measured one. This choice is motivated by the fact that imposing an inlet profile extracted from 4D-Flow MRI which is consistent with either the Stokes or the Navier-Stokes equations is far from trivial. Since the goal of this work is to demonstrate a new methodology based on optimal control, a plug profile was used for simplicity. The use of a more realistic profile, however, would not change the way in which the optimal control problem is solved. The vessel walls Γ_w are assumed to be rigid and non-permeable, and a no-slip condition is imposed on them ($\mathbf{v} = 0$). Finally, a resistive-type boundary condition is imposed at the outlets Γ_i, by prescribing that the pressure at the outlets must be equal to $R \int_{\Gamma_i} \mathbf{v} \cdot \mathbf{n} \, d\Gamma_i$, where R represents the resistance, while the integral of the velocity normal to the surface gives the outlet flow rate. For the 3D-0D coupling at the interface, the coupled multidomain method proposed by Vignon-Clementel et al. [44] was adopted.

The next step was to derive the weak formulation of the state equations. In order to do so, we need to introduce Hilbert spaces $V(\Omega)$ and $P(\Omega)$ for the

velocity $\mathbf{v}$ and the pressure p, respectively. In particular, we choose the function spaces $V(\Omega) = H^1(\Omega;\mathbb{R}^3)$ and $P(\Omega) = L^2(\Omega)$ (as velocity $\mathbf{v}(\mathbf{x})$ and pressure $p(\mathbf{x})$ are functions depending on the spatial coordinate $\mathbf{x} \in \Omega$. Moreover, we denote by $U = \mathbb{R}^{i_{max}}$ the space associated to the controls $\mathbf{R} = [R_1, \ldots, R_{i_{max}}]^T \in U$. Since the control variables R_i are scalar numbers, and not functions, the space U is simply an Euclidean space.

Starting from the strong form in (3.40), the weak formulation is derived as: given $\mathbf{R} \in U$, find

$$\mathbf{v} \in V_{in}(\Omega) = \{\tilde{\mathbf{v}} \in V(\Omega) : \tilde{\mathbf{v}}|_{\Gamma_{in}} = \mathbf{v}_{in} \text{ and } \tilde{\mathbf{v}}|_{\Gamma_w} = 0\} \quad \text{and} \quad p \in P(\Omega)$$

such that

$$\begin{cases} \nu \displaystyle\int_\Omega \nabla\mathbf{v}\cdot\nabla\mathbf{w}\, d\Omega - \int_\Omega p\,(\nabla\cdot\mathbf{w})\, d\Omega + \sum_{i=1}^{i_{max}} R_i \int_{\Gamma_i} \mathbf{v}\cdot\mathbf{n} d\Gamma_i \int_{\Gamma_i} \mathbf{w}\cdot\mathbf{n} d\Gamma_i \\ \qquad + \sum_{i=1}^{i_{max}} \int_{\Gamma_i} \mathbf{w}\cdot\mathbf{n}(\mathbf{n}\cdot\nu\nabla\mathbf{v}\,\mathbf{n}) d\Gamma_i - \sum_{i=1}^{i_{max}} \int_{\Gamma_i} \mathbf{w}\cdot\nabla\mathbf{v}\,\mathbf{n} d\Gamma_i = 0 \qquad \text{in } \Omega, \\ \displaystyle\int_\Omega q\,(\nabla\cdot\mathbf{v})\, d\Omega = 0 \qquad \text{in } \Omega, \end{cases} \tag{3.41}$$

for every

$$\mathbf{w} \in V_0(\Omega) = \{\tilde{\mathbf{w}} \in V(\Omega) : \tilde{\mathbf{w}}|_{\Gamma_{in}} = 0 \text{ and } \tilde{\mathbf{v}}|_{\Gamma_w} = 0\} \quad \text{and} \quad q \in P(\Omega),$$

where $\mathbf{w}$ and q are the test functions associated to velocity and pressure, respectively. We now reformulate the term

$$R_i \int_{\Gamma_i} \mathbf{v}\cdot\mathbf{n} d\Gamma_i \int_{\Gamma_i} \mathbf{w}\cdot\mathbf{n} d\Gamma_i$$

in $(3.41)_1$ to obtain an equivalent weak formulation which is more suitable for the forthcoming finite element discretization. In particular, since the *FEniCS* library [133, 134] adopted for the solution of this problem does not handle the product of integrals, we need to introduce a set of Lagrange multipliers λ_i, $1 \le i \le i_{max}$, defined as

$$\lambda_i = R_i \int_{\Gamma_i} \mathbf{v}\cdot\mathbf{n} d\Gamma_i.$$

We further denote by $\boldsymbol{\lambda} = [\lambda_1, \ldots, \lambda_{i_{max}}]^T \in Z = \mathbb{R}^{i_{max}}$ the vector collecting the Lagrange multipliers, and Z its associated space. Therefore, the equivalent

weak formulation is:
given $\mathbf{R} \in U$, find $\mathbf{v} \in V_{in}(\Omega), p \in P(\Omega), \boldsymbol{\lambda} \in Z$ such that

$$\begin{cases} \nu \int_\Omega \nabla\mathbf{v}\cdot\nabla\mathbf{w} d\Omega - \int_\Omega p\,(\nabla\cdot\mathbf{w}) d\Omega + \sum_{i=1}^{i_{max}} \int_{\Gamma_i} \lambda_i\,\mathbf{w}\cdot\mathbf{n} d\Gamma_i \\ \qquad + \sum_{i=1}^{i_{max}} \int_{\Gamma_i} \mathbf{w}\cdot\mathbf{n}\,(\mathbf{n}\cdot\nu\nabla\mathbf{v}\,\mathbf{n}) d\Gamma_i - \sum_{i=1}^{i_{max}} \int_{\Gamma_i} \mathbf{w}\cdot\nabla\mathbf{v}\,\mathbf{n} d\Gamma_i = 0 \quad \text{in } \Omega, \\ \int_\Omega q\,(\nabla\cdot\mathbf{v}) d\Omega = 0 \qquad \text{in } \Omega, \\ \dfrac{1}{|\Gamma_i|}\int_{\Gamma_i} \lambda_i\,\eta_i\,d\Gamma_i - \int_{\Gamma_i} R_i\,\mathbf{v}\cdot\mathbf{n}\,\eta_i\,d\Gamma_i = 0 \quad \text{on } \Gamma_i,\ 1 \le i \le i_{max}, \end{cases} \tag{3.42}$$

for every $\mathbf{w} \in V_0(\Omega), q \in P(\Omega), \boldsymbol{\eta} = [\eta_1, \ldots, \eta_{i_{max}}]^T \in Z$, where $\boldsymbol{\eta}$ collects the test "functions" associated to the Lagrange multipliers $\boldsymbol{\lambda}$. System (3.42) is the final system representing how the control $\mathbf{R}$ affects the underlying physics of the model.

The cost functional

The next step in the construction of the optimal control problem is the definition of a proper cost functional, which will allow to assimilate patient-specific pressure and flow rate data. The proposed cost functional J has the following form

$$J(\mathbf{v}, p) = \frac{\alpha_p}{2} \cdot \frac{\int_{\Gamma_p} ||p - p_d||^2 d\Gamma_p}{\int_{\Gamma_p} ||p_d||^2 d\Gamma_p} + \sum_{i=1}^{i_{max}} \frac{\alpha_i}{2} \cdot \frac{\left[\int_{\Gamma_i} \mathbf{v}\cdot\mathbf{n} d\Gamma_i - Q_i\right]^2}{Q_i^2}. \tag{3.43}$$

The first term in (3.43) represents the normalized difference between the state pressure p and the patient's average pressure p_d measured at the cross section Γ_p. Since the pressure drop across the aortic arch is small, the position of Γ_p will not have a significant impact on the result. As explained in Section 3.3.1, in this case p_d was assumed equal to the mean arterial pressure, computed from the measured systolic and diastolic pressure. The second term, instead, represents the normalized difference between the calculated flow rate (obtained integrating velocity on the outlet section) and the flow rate Q_i extracted

from 4D-Flow MRI data at each outlet Γ_i. By minimizing the normalized difference between simulated and measured quantities, each term gives the same contribution to the optimization process, even when assimilating measurements with different orders of magnitude. However, the contribution of each term to the optimization can be tailored individually by changing the weights α_p and α_i. For the aortic arches under analysis, α_p and all α_i were set to 1, meaning that all measurements contributed equally to the minimization process.

The optimal control problem

Having an expression for both the cost functional and the state equations, we are now ready to build the OCP. The optimal control problem then reads:

Problem 3.3.1 *Find* $\mathbf{R}$ *such that functional* (3.43) *is minimized, under the constraint that* $\mathbf{v}, p, \lambda$ *satisfy* (3.42)*.*

To solve the optimal control problem, we adopt the adjoint-based Lagrangian approach introduced in Section 3.2.1 [81, 123, 124, 135]. As explained previously, this method allows to convert the optimal control problem into an unconstrained minimization problem, whose solution corresponds to the minimum of a properly defined *Lagrangian functional*. In practice, the optimal solution is the one where all the derivatives of the Lagrangian functional vanish. In order to adopt the Lagrangian formulation, a set of adjoint variables must be introduced. In particular, we define $\mathbf{z} \in V_0(\Omega)$ as the adjoint of $\mathbf{v}$, $b \in P(\Omega)$ as the adjoint of p, and $\mathbf{t} = [t_1, \dots, t_{i_{max}}]^T \in Z$ as the adjoint variables of $\mathbf{R}$. The Lagrangian functional for this problem then reads

$$\begin{aligned}\mathcal{L}(\mathbf{v}, p, \boldsymbol{\lambda}, \mathbf{R}, \mathbf{z}, b, \mathbf{t}) = J(\mathbf{v}, p) &+ \nu \int_\Omega \nabla\mathbf{v}\cdot\nabla\mathbf{z} d\Omega - \int_\Omega p\,(\nabla\cdot\mathbf{z}) d\Omega \\ &+ \sum_{i=1}^{i_{max}} \int_{\Gamma_i} \lambda_i\, \mathbf{z}\cdot\mathbf{n}\, d\Gamma_i + \sum_{i=1}^{i_{max}} \int_{\Gamma_i} \mathbf{z}\cdot\mathbf{n}\,(\mathbf{n}\cdot\nu\nabla\mathbf{v}\,\mathbf{n}) d\Gamma_i \\ &- \sum_{i=1}^{i_{max}} \int_{\Gamma_i} \mathbf{z}\cdot\nabla\mathbf{v}\,\mathbf{n} d\Gamma_i + \int_\Omega b\,(\nabla\cdot\mathbf{v}) d\Omega \\ &+ \sum_{i=1}^{i_{max}} \frac{1}{|\Gamma_i|} \int_{\Gamma_i} \lambda_i t_i d\Gamma_i - \sum_{i=1}^{i_{max}} \int_{\Gamma_i} R_i \mathbf{v}\cdot\mathbf{n}\, t_i d\Gamma_i.\end{aligned} \tag{3.44}$$

As explained in Section 3.2.2 by means of the corollary 3.2.1, given (3.44), the optimality system can be obtained by imposing $\nabla\mathcal{L} = 0$. In other words, this condition is equivalent to requiring that the derivatives of $\mathcal{L}$ with respect to $(\mathbf{v}, p, \boldsymbol{\lambda}, \mathbf{R}, \mathbf{z}, b, \mathbf{t})$ must vanish. Taking the derivative of (3.44) with respect to $\mathbf{v}$ (denoted by $\mathcal{L}_\mathbf{v}$) in the direction $\mathbf{w}$ we obtain

$$\begin{aligned}\langle \mathcal{L}_\mathbf{v}, \mathbf{w}\rangle = \nu \int_\Omega \nabla\mathbf{w}\cdot\nabla\mathbf{z} d\Omega + \sum_{i=1}^{i_{max}} \mathbf{z}\cdot\mathbf{n}\,(\mathbf{n}\cdot\nu\nabla\mathbf{w}\,\mathbf{n}) d\Gamma_i \\ - \sum_{i=1}^{i_{max}} \int_{\Gamma_i} \mathbf{z}\cdot\nabla\mathbf{w}\,\mathbf{n} d\Gamma_i + \int_\Omega b\,(\nabla\cdot\mathbf{w}) d\Omega - \sum_{i=1}^{i_{max}} \int_{\Gamma_i} R_i \mathbf{w}\cdot\mathbf{n}\, t_i d\Gamma_i \\ + \sum_{i=1}^{i_{max}} \frac{\alpha_i}{Q_i^2}\left[\int_{\Gamma_i} \mathbf{v}\cdot\mathbf{n} d\Gamma_i \int_{\Gamma_i} \mathbf{w}\cdot\mathbf{n} d\Gamma_i - Q_i \int_{\Gamma_i} \mathbf{w}\cdot\mathbf{n} d\Gamma_i\right] = 0,\end{aligned} \tag{3.45a}$$

while taking the derivative of (3.44) with respect to p in the direction q we get

$$\langle \mathcal{L}_p, q\rangle = \alpha_p \int_{\Gamma_p} (p - p_d)\, q\, d\Omega - \int_\Omega q\,(\nabla\cdot\mathbf{z}) d\Omega = 0. \tag{3.45b}$$

Similarly, the derivatives of (3.44) with respect to $\lambda_i, R_i, \mathbf{z}, b, t_i$ are, respectively,

$$\langle \mathcal{L}_{\lambda_i}, m_i\rangle = \int_{\Gamma_i} m_i \mathbf{z}\cdot\mathbf{n} d\Gamma_i + \frac{1}{|\Gamma_i|}\int_{\Gamma_i} m_i t_i d\Gamma_i = 0, \quad 1 \le i \le i_{max}, \tag{3.45c}$$

$$\langle \mathcal{L}_{R_i}, r_i\rangle = -\int_{\Gamma_i} r_i \mathbf{v}\cdot\mathbf{n}\, t_i d\Gamma_i = 0, \tag{3.45d}$$

$$\begin{aligned}\langle \mathcal{L}_\mathbf{z}, \mathbf{s}\rangle = \nu \int_\Omega \nabla\mathbf{v}\cdot\nabla\mathbf{s} d\Omega - \int_\Omega p\,(\nabla\cdot\mathbf{s}) d\Omega + \sum_{i=1}^{i_{max}} \int_{\Gamma_i} \lambda_i \mathbf{s}\cdot\mathbf{n} d\Gamma_i \\ + \sum_{i=1}^{i_{max}} \int_{\Gamma_i} \mathbf{s}\cdot\mathbf{n}(\mathbf{n}\nu\nabla\mathbf{v}\cdot\mathbf{n}) d\Gamma_i - \sum_{i=1}^{i_{max}} \int_{\Gamma_i} \mathbf{s}\cdot\nabla\mathbf{v}\,\mathbf{n} d\Gamma_i = 0,\end{aligned} \tag{3.45e}$$

$$\langle \mathcal{L}_b, d\rangle = \int_\Omega d\,(\nabla\cdot\mathbf{v}) d\Omega = 0, \tag{3.45f}$$

$$\langle \mathcal{L}_{t_i}, \eta_i\rangle = \frac{1}{|\Gamma_i|}\int_{\Gamma_i} \lambda_i \eta_i d\Gamma_i - \int_{\Gamma_i} R_i \mathbf{v}\cdot\mathbf{n}\,\eta_i d\Gamma_i = 0, \quad 1 \le i \le i_{max}. \tag{3.45g}$$

Again, the presence in (3.45a) of a term containing the product of two integrals requires the use of an additional Lagrange multiplier to properly treat it numerically. We thus introduce the new variables $k_i = \int_{\Gamma_i} \mathbf{v} \cdot \mathbf{n} d\Gamma_i$, which we substitute in (3.45a), and we add the following equations to the system

$$\frac{1}{|\Gamma_i|} \int_{\Gamma_i} k_i \, c_i \, d\Gamma_i - \int_{\Gamma_i} \mathbf{v} \cdot \mathbf{n} \, c_i \, d\Gamma_i = 0, \quad \forall c_i \in \mathbb{R}, \quad 1 \leq i \leq i_{max}. \tag{3.46}$$

Equations (3.45a) through (3.46) form the so-called coupled optimality system, which we introduced in Section 3.2.2. As mentioned in Section 3.2.5, this coupled system can be solved through a *one-shot* approach [124, 136], where the system is solved directly for all the unknown variables. The adopted approach is the *optimize-then-discretize* one, where we first derive the optimality system (3.45a)-(3.46), and then we discretize it numerically, seeking a solution through Galerkin finite element methods.

Since the domain Ω was discretised into a finite mesh of size $h \in \mathbb{R}$, we introduce finite-dimensional solution spaces $V_h(\Omega), P_h(\Omega), U_h, Z_h$. In particular, we use Taylor-Hood elements for the velocity-pressure pair, i.e. P_2 finite elements to define $V_h(\Omega)$ and P_1 finite elements for $P_h(\Omega)$. Moreover, we set $U_h = U$ and $Z_h = Z$, as the spaces associated to control and Lagrange multipliers are already finite-dimensional. The discretised system is solved using the open-source libraries *FEniCS* [133, 134] and *multiphenics* [137], the latter being an open-source library developed at SISSA mathLab for easy prototyping of problems characterized by a block structure and boundary restricted variables. The numerical solution of the problem is obtained by means of MUMPS [138], a parallel sparse direct solver.

3.3.3 Alternative methods for the estimation of resistive BCs

We now look at some alternative methods that can be used to set the outlet resistances, starting from in-vivo measurements of blood pressure and flow rate. These methods will be compared in Section 3.4 to the proposed optimal control method.

Murray's law Murray's law [50], formulated by Cecil D. Murray in 1926, governs the branching pattern of vessels, such that the flow in each outlet is proportional to its cross-sectional area. In particular, the general form of Murray's law reads

$$\frac{Q_i}{Q_{tot}} = \frac{r_i^n}{\sum_i r_i^n} \tag{3.47}$$

where Q_i is the flow rate at the i-th outlet, Q_{tot} is the total flow rate, while r_i is the radius at the i-th outlet. The exponent n changes depending on the territory considered, and for the aortic arch is conventionally set to 2 [139]. Multiplying r_i by π to express the relationship in terms of outlet areas, and using $R \propto \frac{1}{Q}$, one can estimate the outlet resistances for the aorta and its main branches as

$$R_i = \frac{\sum_j |\Gamma_j|}{|\Gamma_i|} R_{tot}, \tag{3.48}$$

where $\sum_j |\Gamma_j|$ is the sum of the area of all the aortic outlets, while $|\Gamma_i|$ is the area of the outlet to which resistance R_i is associated. The total resistance R_{tot} was computed as the mean pressure p_d measured non-invasively on the patient, as reported in Section 3.3.1, divided by the mean aortic flow rate Q_0 measured at the inlet with 4D-Flow MRI, and then split among the outlet branches according to (3.48). The application of Murray's law for estimating flow splitting at vessel bifurcations has been largely investigated both on human and animal subjects by a number of studies [140–143], which confirmed its validity on a large portion of the cardiovascular system, even if with some limitations on the first branches of the aortic arch [144]. It is worth noticing that the flow splitting predicted by Murray's law is based exclusively on the patient's anatomy, as it assumes that branches with larger cross-section have higher flow rates. This method only requires the average pressure and inlet flow rate, but no patient-specific measurements at the outlets. This property justifies its use in those studies where in-vivo measurements of flow rates are not available [145–147].

Ohm's law It is possible to estimate outlet resistances by exploiting the analogy between the cardiovascular system and electrical circuits, by means of Ohm's law. In particular, knowing the mean pressure p_d computed from diastolic and systolic pressure measured non-invasively and the outlet flow rates

Q_i measured with 4D-Flow MRI, outlet resistances can be computed as

$$R_i = \frac{p_d}{Q_i}. \tag{3.49}$$

This method is also common [111] and it is based on the idea of performing the parameter estimation on 0D models [148] but, differently from Murray's law, it requires the availability of outlet flow rates measured in-vivo. This could lead to inaccurate estimations when the outlet flow rates violate the mass conservation principle, especially when dealing with 4D-Flow MRI data, where a 15% deviation is expected due to measurement uncertainty [149]. We proposed an alternative solution, still based on Ohm's law, to deal with inconsistent measurements.

Optimization based on Ohm's law Using Ohm's law, we developed a minimization problem which estimates outlet resistances R_i, while trying to impose the mass conservation principle. In this way, we try to compensate for the intrinsic inconsistency in the data, which is not accounted for in the standard version of Ohm's law of (3.49). This is achieved by approximating the aorta with its equivalent 0D model, which is displayed on the left of Fig. 3.4, and minimizing the cost function

$$J_{ohm} = \alpha_p \frac{||R_{tot} \cdot Q_0 - p_d||^2}{||p_d||^2} + \sum_{i=1}^{i_{max}} \alpha_i \frac{||\frac{p_d}{R_i} - Q_i||^2}{||Q_i||^2}. \tag{3.50}$$

The cost function was minimized using the Matlab function *fminsearch*, which employs a derivative-free simplex search method [150]. The cost functional reported in (3.50) deliberately replicates the one used inside the optimal control framework, reported in (3.43), with the first term representing the normalized difference between the computed pressure and the measured one (p_d), and the second term representing the outlet flow rates Q_i. However, optimal control relies on Stokes equations as a 3D-model of the underlying system, whereas here a 0D approximation is used. The weights α_p and α_i can be adjusted to change the contribution of each measurement to the optimization process, but in the following experiments were all set to 1.

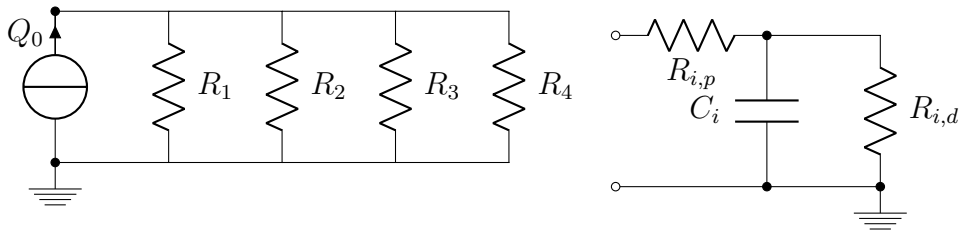

a) Equivalent circuit for optimization of Ohm's law.

b) Three-element Windkessel model.

Fig. 3.4 Adopted equivalent circuits. On the left, equivalent circuit used for Ohm's law method. On the right, 3-element Windkessel model used as outlet boundary condition for unsteady Navier-Stokes simulations.

3.4 Numerical results

3.4.1 Mesh convergence analysis

As a preliminary step, we conducted a mesh convergence analysis on the patient-specific meshes, which we later used for the experiments. The results of the convergence analysis for "case 1" are reported in Fig. 3.5, where the time-averaged wall shear stress (TAWSS, on the left) and oscillatory shear index (OSI, on the right) are plotted with respect to the number of mesh elements. Four different meshes were used, with edge length equal to 0.2, 0.15, 0.1 and 0.08 cm, respectively. It can be noticed how for the finest mesh considered, which contains around 2.5×10^6 elements, OSI has already reached convergence, but not TAWSS. Nevertheless, this was the mesh used in the following experiments, as it was determined to be the best compromise between computational time/cost of the simulations and accuracy of the results. Similar results were obtained for the other cases.

3.4.2 Validation with synthetic data

The proposed method was first validated on "case 1" with synthetically generated pressure and flow rate measurements.

As an initial step, the ground truth data were generated by simulating case 1 in Simvascular, using the unsteady Navier-Stokes equations. At the inlet, a velocity waveform with blunt profile and average flow rate $Q = 119.1$ cm^3/s

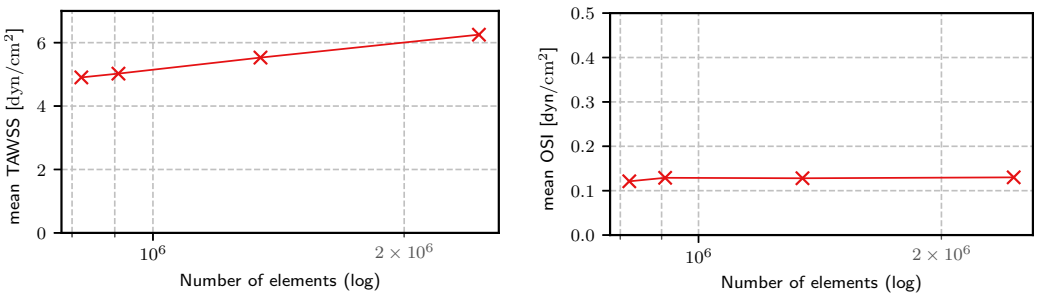

a) Convergence analysis of TAWSS.

b) Convergence analysis of OSI.

Fig. 3.5 Mesh convergence analysis for case 1.

was imposed, while at the outlets three-element Windkessel models were used as boundary conditions. A physiological value of the total resistance at each outlet was chosen, which was then split into a proximal one

$$R_{p,i} = 0.09 R_i, \tag{3.51}$$

and a distal one

$$R_{d,i} = 0.91 R_i, \tag{3.52}$$

as suggested by Kim et al [31]. The total resistance values selected for each outlet are reported in Table 3.1, in the "Reference" line. For the capacitance, a total value of 0.001 cm^5/dyn was assumed [151], which was then split among the four outlets proportionally to their area, according to the formula

$$C_i = \frac{|\Gamma_i|}{\sum_j |\Gamma_j|} C_{tot}. \tag{3.53}$$

The simulation was run for five cardiac cycles in order to reach periodic convergence. Then, the average pressure across the geometry and the average flow rates at the four outlets were measured from the last cardiac cycle. These extracted data were then assimilated with the optimal control method presented in Section 3.3 to estimate the total outlet resistances. At this point, the resistances estimated with optimal control were used to set the outlet boundary conditions of a second simulation, again in Simvascular. Both resistances and capacitances were split adopting the rules reported in (3.51)-(3.53).

A comparison between original and estimated resistance values is reported in Table 3.1, together with original and estimated average flow rates at the

outlets. Flow and pressure waveforms at the outlets are compared in Fig. 3.6, showing how the resistances chosen with optimal control allow to reconstruct the original flow waveform with a relative error of 0.09% for BCA, 0.09% for LCC, 0.1% for LSUB and 0.02% for DAo. The pressure waveform is recovered with a relative error of 0.005%.

	Resistance (dyn·s/cm^5)				**Flow rate (cm^3/s)**			
	BCA	LCC	LSUB	DAo	BCA	LCC	LSUB	DAo
Reference	7,000	21,000	16,000	1,700	19.02	6.30	8.13	80.02
Estimated	6,937	20,846	15,991	1,685	19.05	6.30	8.09	80.03

Table 3.1 Results of experiment with synthetic data conducted on case 1, described in Sec. 3.4.2. The first line ("Reference") reports the resistance values chosen for the four outlets, and the resulting flow rates obtained. The second line ("Estimates") reports the resistance values estimated with the proposed method, and the corresponding flow rates obtained.

3.4.3 Patient-specific measurements

After the verification and validation of the method, the proposed optimal control approach was tested on four patient-specific aortic arches, with flow data coming from 4D-Flow MRI. The obtained outlet resistances were compared to those obtained with the alternative estimation methods presented in Section 3.3.3.

The experiments described in this section were conducted on four patient anatomies, obtained as described in Section 3.3.1. Table 3.2 reports for each case the measured flow rates. Specifically, the column labeled *Net flow* quantifies the violation of mass conservation on the flow rate measurements obtained from 4D-Flow MRI, by indicating the difference between measured inlet flow and the sum of outlet flows. The inlet flow rate reported in Table 3.2 was obtained by subtracting 4% to the flow measured in the ascending aorta, which estimates the total coronary circulation [152], not considered in the models.

The presence of flow rate inconsistencies in 4D-Flow MRI data could be due to the finite resolution of 4D-flow MRI, motion artifacts, and the presence of noise, especially in presence of complex helical and vortical flows [153]. The amount of net flow is below 15% for all the cases under analysis, which is considered acceptable for 4D-Flow MRI measurements according to Dyverfeldt

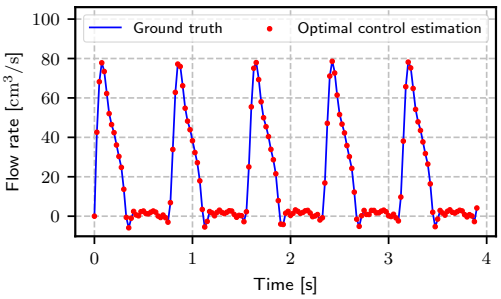

a) Flow rate waveform at Brachiocephalic artery (BCA)

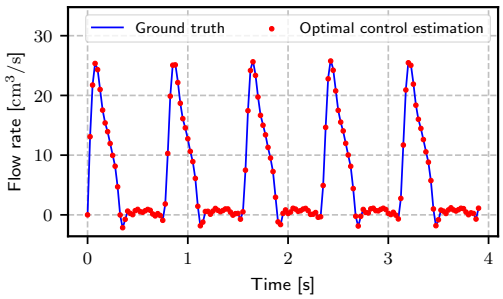

b) Flow rate waveform at Left Common Carotid artery (LCC)

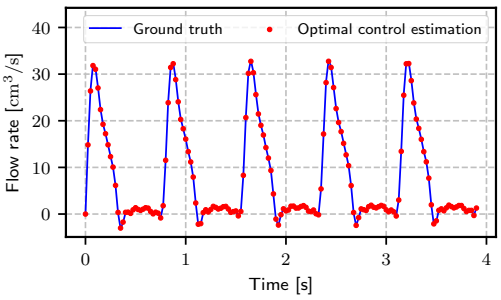

c) Flow rate waveform Left Subclavian artery (LSUB)

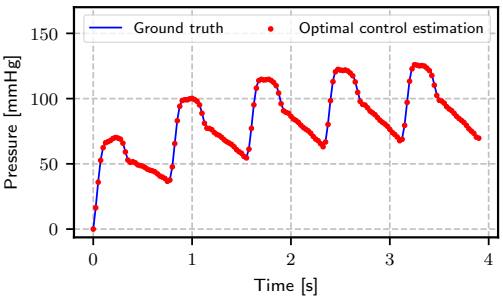

d) Pressure waveform at Descending Aorta (DAo)

Fig. 3.6 Comparison of flow rate waveforms at the three supra-aortic branches of case 1, and of pressure waveform at the descending aorta, for case 1 with synthetically generated data, described in Sec. 3.4.2.

et al. [149]. While in case 1 and case 4 the net flow is significant, for cases 2 and 3 it is practically negligible.

Case number	**Inlet flow (cm^3/s)**	**Total outlet flow (cm^3/s)**	**Net flow (cm^3/s)**	**Mass conservation violation (%)**
1	119.10	103.46	15.64	13%
2	107.00	107.18	-0.18	0.17%
3	125.63	125.60	0.03	0.02%
4	103.00	90.21	12.79	12.4 %

Table 3.2 Table summarizing, for each case, the measured inlet flow rate, the sum of the measured outlet flow rates, the difference between the two (net flow), and the percentage of mass conservation violation.

The resistance values obtained with the four different methods are reported in Table 3.3, where it can be noticed how Murray's law is the estimation technique providing the resistance values which most deviate from the other methods. The main results are reported in Table 3.4 where, for each case, the first row reports the patient's average pressure, measured non-invasively after MRI, and the flow rates measured in-vivo with 4D-Flow MRI at the four outlets: BCA, LCC, LSUB and DAo. The values obtained solving the Stokes equations on the 3D geometry, with the resistance values calculated by means of Ohm's law (3.49) are reported in the second row, while the third row contains the results obtained with the optimization based on Ohm's law as in (3.50). The fourth contains the results for Murray's Law. Finally, the fifth row shows the results obtained with the proposed method. For cases 2 and 3, where the net flow is negligible, both Ohm's law and the proposed method properly assimilate the available data, with a relative error of less than 1% on all the outlet flow rates. For cases 1 and 4, where the net flow is high, the proposed method outperforms the other techniques, achieving the smallest relative errors on pressure and BCA, LCC, LSUB flow rates. In presence of a large net flow, we cannot expect a perfect assimilation of measurements, as they are intrinsically non-physical. In that case, optimal control shows a smaller sensitivity to inconsistencies in the data, leading to a physical solution which is closer to measurements with respect to the other techniques. As expected, the optimization based on Ohm's law is more accurate than Ohm's law for cases 1 and 4, while the two methods are basically equivalent for cases 2 and 3. As already pointed out earlier, as Murray's law is the only technique which does not take into account the measured flow rates to set outlet boundary conditions and assumes mass conservation, the corresponding solution is the one that most deviates from patient measurements. The solution of the optimal control problem required an average of 6.75 minutes (wall clock CPU time), running on 18 Lenovo SD530 nodes, each with 40 Intel "Skylake" cores and 202 GB RAM. The large number of nodes used was due to the large working memory required to solve the optimality system.

Case number	Method	Resistance (dyn·s/cm^5)			
		BCA	**LCC**	**LSUB**	**DAo**
1	**Ohm's law**	8,288	21,979	15,518	1,800
	Opt. based on Ohm's law	8,190	21,981	15,511	1,679
	Murray's law	6,837	21,242	17,591	1,527
	Proposed	7,941	21,609	15,153	1,497
2	**Ohm's law**	10,690	21,003	18,847	1,764
	Opt. based on Ohm's law	10,737	20,987	18,867	1,767
	Murray's law	8,306	22,451	15,161	1,900
	Proposed	10,699	21,006	18,864	1,773
3	**Ohm's law**	7,248	12,142	13,094	1,624
	Opt. based on Ohm's law	7,255	12,145	13,090	1,629
	Murray's law	7,646	14,723	19,102	1,513
	Proposed	7,249	12,131	13,078	1,621
4	**Ohm's law**	13,600	31,060	19,391	1,943
	Opt. based on Ohm's law	13,500	31,069	19,399	1,815
	Murray's law	8,751	32,800	26,358	1,708
	Proposed	13,166	30,500	18,903	1,634

Table 3.3 Resistance values chosen by the different methods.

Case number	Method	Pressure (mmHg)	Flow rate (cm^3/s) (% error w.r.t. measurements)			
			BCA	LCC	LSUB	DAo
1	**Measurements**	98.7	15.9	5.98	8.48	73.1
	Ohm's law	113 (15%)	18.3 (15.3%)	6.89 (15%)	9.77 (15%)	84.2 (15%)
	Opt. based on Ohm's law	108 (9.5%)	17.6 (11%)	6.55 (9.5%)	9.28 (9.4%)	85.8 (17%)
	Murray's law	98.8 (0.1%)	19.2 (20%)	6.19 (3.5%)	7.48 (-11%)	86.2 (18%)
	Proposed	98.7 (0%)	16.6 (4.4%)	6.08 (1.7%)	8.67 (2.2%)	87.8 (20%)
2	**Measurements**	105	13.2	6.71	7.47	79.8
	Ohm's law	105 (0%)	13.1 (-0.7%)	6.68 (-0.4%)	7.44 (-0.4%)	79.5 (-0.4%)
	Opt. based on Ohm's law	105 (0%)	13.1 (-0.7%)	6.70 (-0.14%)	7.45 (-0.26%)	79.6 (-0.3%)
	Murray's law	106 (0.9%)	17.0 (29%)	6.28 (6%)	9.30 (24%)	74.2 (-7%)
	Proposed	106 (0.9%)	13.2 (0%)	6.71 (0%)	7.47 (0%)	79.5 (-0.4%)
3	**Measurements**	103	19.0	11.3	10.5	84.8
	Ohm's Law	103 (0%)	19.0 (0%)	11.3 (0%)	10.5 (0%)	84.9 (0.1%)
	Opt. based on Ohm's law	104 (0.65%)	19.1 (0.5%)	11.4 (0.62%)	10.5 (0%)	84.9 (0.1%)
	Murray's law	104 (0.65%)	18.1 (-5%)	9.37 (-17%)	7.22 (-31%)	91.2 (7%)
	Proposed	103 (0%)	19.0 (0%)	11.3 (0%)	10.5 (0%)	85.0 (0.2%)
4	**Measurements**	100	9.87	4.32	6.92	69.1
	Ohm's law	115 (15%)	11.3 (14%)	4.94 (14%)	7.91 (14%)	78.9 (14%)
	Opt. based on Ohm's law	109 (9%)	10.8 (9%)	4.68 (8.3%)	7.49 (8.2%)	80.1 (16%)
	Murray's law	101 (1%)	15.3 (55%)	4.09 (-5%)	5.09 (-26%)	78.6 (13.7%)
	Proposed	100 (0%)	10.1 (2.6%)	4.37 (1.1%)	7.04 (1.7%)	81.5 (18%)

Table 3.4 Comparison of pressure and flow rates for Stokes simulations with boundary conditions obtained with the different methods.

Case number	$\boldsymbol{\alpha_p}$, $\boldsymbol{\alpha_{BCA}}$, $\boldsymbol{\alpha_{OUT}}$	$\boldsymbol{\alpha_{LCC}}$, $\boldsymbol{\alpha_{LSUB}}$	**Pressure (mmHg)**	**Flow rate (cm^3/s)**			
				BCA	**LCC**	**LSUB**	**DAo**
3	1	1	103	19.0	11.3	10.5	85.0
	1	50	103	19.0	11.3	10.5	85.0
4	1	1	100	10.1	4.37	7.04	81.5
	1	50	100	10.1	4.29	6.87	81.8

Table 3.5 Comparison of pressure and flow rates for Stokes simulations obtained with the proposed method, using different values for the weights.

To verify that the choice of α's does not influence the result of the optimization process, we solved the optimal control problem with different values of the weights α_i associated to LCC and LSUB. Results are reported in Table 3.5. For case 3, different values of α result in the same resistance values estimated by optimal control, whereas, for case 4, higher weights associated to LCC and LSUB led to slightly more accurate flow rates in the corresponding branches at the expense of increasing the distance from flow rate measurements for the DAo branch. These results confirms that the optimization problem is stable and robust with respect to the choice of the weights, which, in the general case, do not need to be tuned and can be safely imposed equal to 1. However, in some specific cases, they can be used by the expert user to distribute the error in different ways over the various inlets and outlets of the geometry.

3.4.4 Considering inlet flow rate as a control parameter: extended optimal control formulation

In presence of a large violation of mass conservation, the presented approach compensates for the inaccuracy in the data by adjusting the outlet boundary conditions. This means that the inconsistencies in the measurements are resolved entirely at the outlets, while the measurement imposed at the inlet is considered deterministic. It would be desirable, instead, to gain some flexibility in the assimilation of the inlet flow, which is equally affected by uncertainty. In this case, we propose a modification of the approach presented in Section 3.3, which estimates both the inlet and outlet BCs by means of an additional control at the inlet Dirichlet boundary condition. In particular, the velocity at the

inlet in (3.40) is expressed as

$$\mathbf{v} = u_{in} \cdot \mathbf{v_{in}} \quad \text{on } \Gamma_{in}, \tag{3.54}$$

where u_{in} is an additional scalar control variable and $\mathbf{v_{in}}$ is the inlet velocity profile, with average value equal to the one measured with 4D-Flow MRI. By choosing the optimal value for u_{in}, the optimal control problem will be able to change the inlet flow rate to better assimilate the available data. This obviously requires a slight modification of the cost functional, with an additional term for assimilating the flow rate Q_{in} at the inlet Γ_{in}:

$$\begin{aligned} J(\mathbf{v}, p) = \frac{\alpha_p}{2} \cdot \frac{\int_{\Gamma_p} ||p - p_d||^2 d\Gamma_p}{\int_{\Gamma_p} ||p_d||^2 d\Gamma_p} + \sum_{i=1}^{i_{max}} \frac{\alpha_i}{2} \cdot \frac{\left[\int_{\Gamma_i} \mathbf{v} \cdot \mathbf{n} d\Gamma_i - Q_i\right]^2}{Q_i^2} \\ + \frac{\alpha_{in}}{2} \cdot \frac{\left[\int_{\Gamma_{in}} \mathbf{v} \cdot \mathbf{n} d\Gamma_{in} - Q_{in}\right]^2}{Q_{in}^2}. \end{aligned} \tag{3.55}$$

Moreover, the Dirichlet control requires weakly imposing the inlet condition by means of a Lagrange multiplier, thus increasing the final size of the system of equations (3.45a)-(3.46). In table 3.6 we report the results with this alternative formulation for cases 1 and 4, which had the largest net flow. As expected, acting on all boundary conditions allows to better manage the presence of a net flow, leading to lower differences between measured and simulated flow rates. As already mentioned, the additional control leads to an increase in the dimensions of the problem, and consequently larger computational cost (an average of 10 minutes of wall clock CPU time, running on 24 Lenovo SD530 nodes, each with 40 Intel "Skylake" cores and 202 GB RAM).

Case number	Method	Pressure (mmHg)	Flow rate (cm^3/s) (% error w.r.t. measurements)				
			Inlet	BCA	LCC	LSUB	DAo
1	**Measurements**	98.7	119.1	15.9	5.98	8.48	73.1
	Proposed	98.7 (0%)	107.9 (-9%)	16.1 (1.2%)	6.01 (0.5%)	8.53 (0.6%)	77.3 (5.7%)
4	**Measurements**	100	103.0	9.87	4.32	6.92	69.1
	Proposed	100 (0%)	94.3 (-8%)	9.95 (0.8%)	4.33 (0.23%)	6.96 (0.6%)	73.0 (6%)

Table 3.6 Comparison of measurements and pressure and flow rates for Stokes simulations obtained with the extended optimal control formulation, which controls both the inlet and the outlets boundary conditions.

3.4.5 Unsteady Navier-Stokes simulations

Despite the use of steady Stokes equations in the optimal control framework, an accurate representation of blood flow in the aorta is generally obtained through unsteady Navier-Stokes simulations, which provide a more realistic and accurate time evolution of blood flow. As a further analysis, we used the resistance values R_i reported in Table 3.3 as outlet boundary conditions of high-fidelity unsteady Navier-Stokes simulations, performed using SimVascular [26]. There are two main motivations behind this analysis. First, it verifies that the resistance values estimated with a steady linear Stokes model are still valid in a non-linear, unsteady scenario. Second, it allows to analyze the impact that boundary conditions obtained with different estimation techniques have on wall shear stress-related indicators, which are clinically relevant but can only be computed on time-dependent simulations. For unsteady Navier-Stokes simulations, the most common type of lumped outlet boundary condition is the three-element Windkessel model [111] represented in Fig. 3.4, right panel. Referring to Fig. 3.4, each resistance R_i previously estimated was split into a proximal one, $R_{p,i} = 0.09R_i$, and a distal one, $R_{d,i} = 0.91R_i$, as suggested by Kim et al [31]. For the capacitance, a total value of 0.001 cm^5/dyn was assumed [151], which was then split among the four outlets proportionally to their area. The dynamic viscosity was set to $\nu = 0.04$ $\text{dynes}/\text{cm}^2\text{s}$, a rigid wall model was assumed and a plug profile was imposed at the inlet. The inlet flow rate waveform was the one extracted from 4D-Flow MRI. The time-step value for the transient simulations was set to 0.5 ms, and 5 cardiac cycles were simulated to reach periodic convergence. The results reported here refer to the last cardiac cycle. Each simulation required an average of 8 hours (clock wall CPU time), running on 4 Lenovo SD530 nodes, each with 40 Intel "Skylake" cores and 202 GB RAM.

Figure 3.7 reports the velocity streamlines and pressure distribution for case 3 at three different time instants along the cardiac cycle. A comparison of pressure and outlet flow rates obtained with Navier-Stokes simulations using outlet boundary conditions estimated with the three different techniques introduced previously is reported in Fig. 3.8. The histograms represent, for each outlet, the relative difference of the average flow rate between the 4D-Flow measurements and the corresponding CFD result, with BCs estimated using

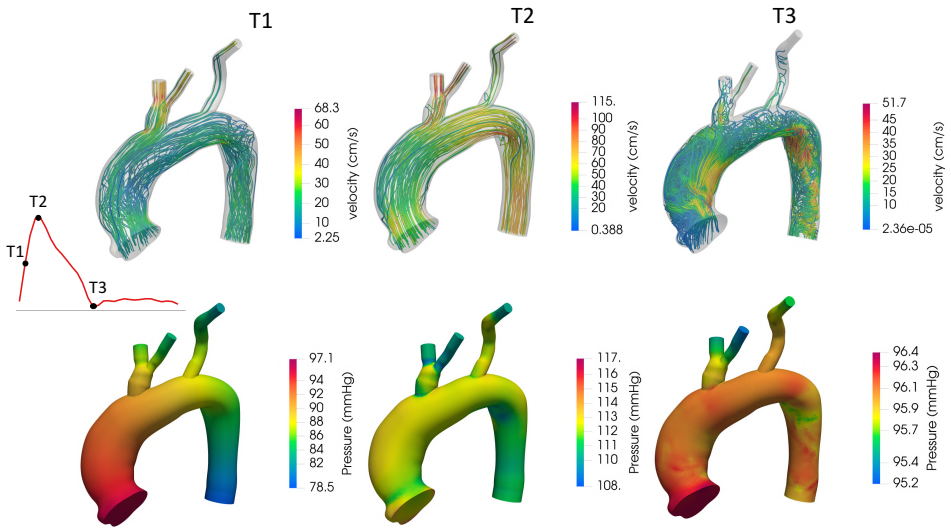

Fig. 3.7 Velocity streamlines (top row) and pressure distributions (bottom row) for case 3 at three different time instants. The time points T1 (mid-systolic acceleration, left column), T2 (peak systole, middle column) and T3 (diastole, right column) are defined along a flow waveform shown on the left.

Murray's law, the optimized version of Ohm's law, and the proposed method. Also, for these simulations, the inlet flow was imposed using a plug profile. As expected, the errors of the obtained flows with respect to the measured ones increased when moving from a Stokes model to a Navier-Stokes one, mostly due to the non-linearity and time-dependency introduced by the latter. Nevertheless, when moving to Navier-Stokes simulations we can observe similar trends to those observed for the Stokes experiments and reported in Table 3.4. In particular, both Ohm's law and the proposed method provide closer results to the measured pressure and flow rates, while Murray's law remains the method providing the largest deviations from measured data. With the exception of case 3, optimal control is still the method which best replicates measured flow rates. These results show that the BCs estimated with a linear, steady Stokes model prove to be a good choice when moving to high-fidelity Navier-Stokes simulations, thus supporting the approach of estimating BCs on a linearised Stokes model.

Figure 3.9 reports a comparison between time-dependent flow rates extracted from 4D-Flow MRI and those obtained from time-dependent simulations with boundary conditions estimated with optimal control. Even if with the proposed estimation method only the average flow rates are assimilated, the

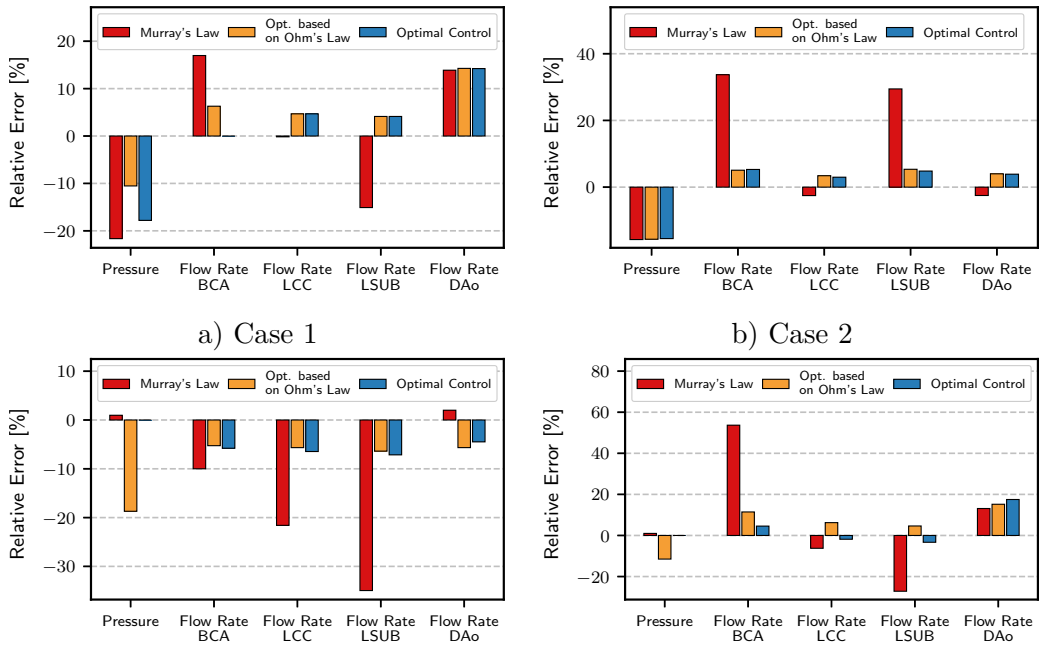

a) Case 1 b) Case 2

c) Case 3 d) Case 4

Fig. 3.8 Comparison of pressure and outlet flow rates for time-dependent Navier-Stokes simulations. The histograms report the relative difference with respect to the corresponding pressure and 4D-Flow MRI flow rate measurements.

time-dependent waveforms are still recovered with a good degree of accuracy. For the sake of space, only results for case 4 are reported, but the results obtained for the other cases are comparable.

As anticipated earlier, the second goal of this analysis was the assessment of the influence that the adopted BCs estimation technique may have on clinically relevant parameters. In order to do so, we carried out an additional analysis on two relevant haemodynamic indicators, namely, TAWSS and OSI, calculated from Navier-Stokes simulation results using the equations reported by Martin et al. [154]. For the sake of space, we report the analysis for case 3 and case 4, but similar results were obtained for the other cases. Figures 3.14 and 3.16 show, in the left column, the TAWSS obtained for the two cases with three different techniques (optimal control, Murray's law, and optimization based on Ohm's law), and in the right column the local relative difference with respect to optimal control results. The same analysis was repeated for the OSI in Figures 3.15 and 3.17. For each point of the surface anatomy, the local relative

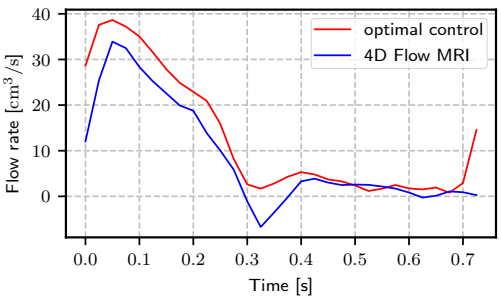

Flow rate waveform at Brachiocephalic artery (BCA)

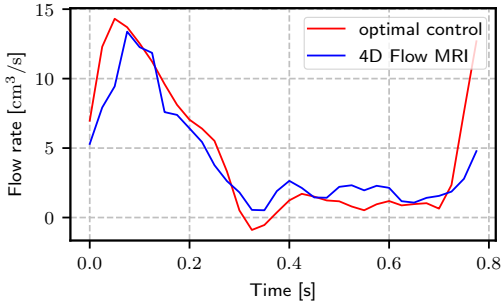

Flow rate waveform at Left Common Carotid artery (LCC)

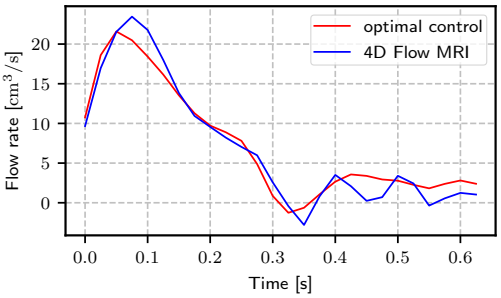

Flow rate waveform Left Subclavian artery (LSUB)

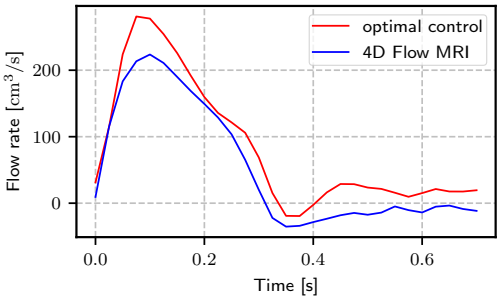

Flow rate waveform at Descending Aorta (DAo)

Fig. 3.9 Comparison of 4D-Flow MRI flow waveforms and simulated flow waveforms with boundary conditions estimated with the proposed optimal control approach for case 4.

difference was computed as:

$$\varepsilon_{r,TAWSS} = \frac{|\text{TAWSS} - \text{TAWSS}_{ocp}|}{max(\text{TAWSS}_{ocp})} \tag{3.56}$$

$$\varepsilon_{r,OSI} = \frac{|\text{OSI} - \text{OSI}_{ocp}|}{max(\text{OSI}_{ocp})} \tag{3.57}$$

For case 3, the difference in the TAWSS reaches a maximum relative difference of 24.8%, while the discrepancy in the OSI value reaches 55%. The largest differences for TAWSS occur in the Murray's law case, in the LSUB, which is also where the estimated resistance values differ the most (46%, as reported in Table 3.3). For OSI, instead, the region characterized by the largest difference is in the aorta, just after the LSUB. Similar results are obtained for case 4, where the difference in the TAWSS reaches a maximum of 47.2%, and 74% for OSI.

It is worth noticing that, outside some specific 'hot-spots', the relative error is generally lower, around 10%. This analysis reveals that the values of resistive boundary conditions have a non-negligible impact on haemodynamic indicators. In particular, given the relevance of TAWSS and OSI in a clinical context, the adoption of different techniques for BCs estimation could possibly affect the observations done by medical doctors, reaffirming the importance of estimating boundary conditions in an automated, reliable, and operator-independent way.

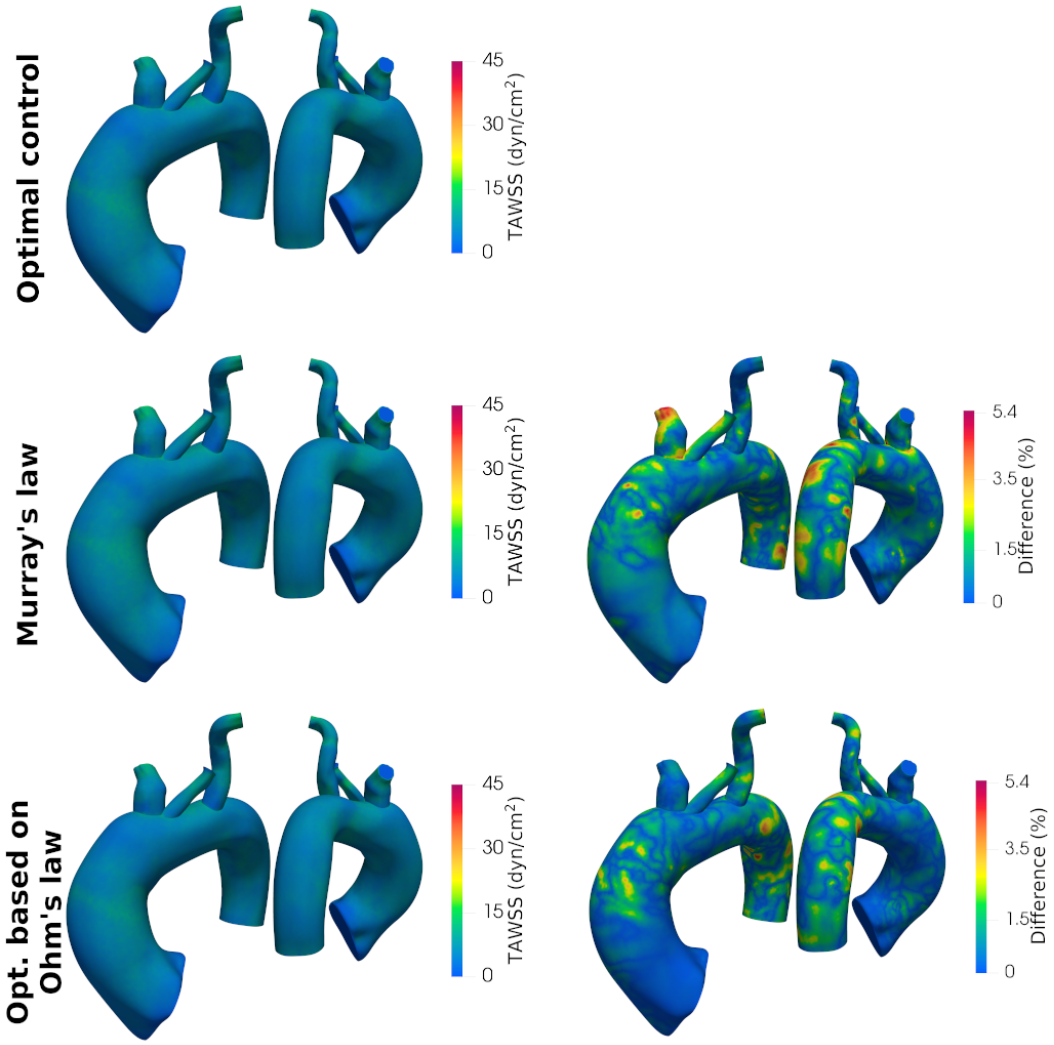

Fig. 3.10 Left: Time-averaged wall shear stress results obtained with the three different BC estimation techniques for case 1. Right: local absolute differences in TAWSS as compared to results obtained with optimal control. Anterior and posterior views of the anatomy are provided.

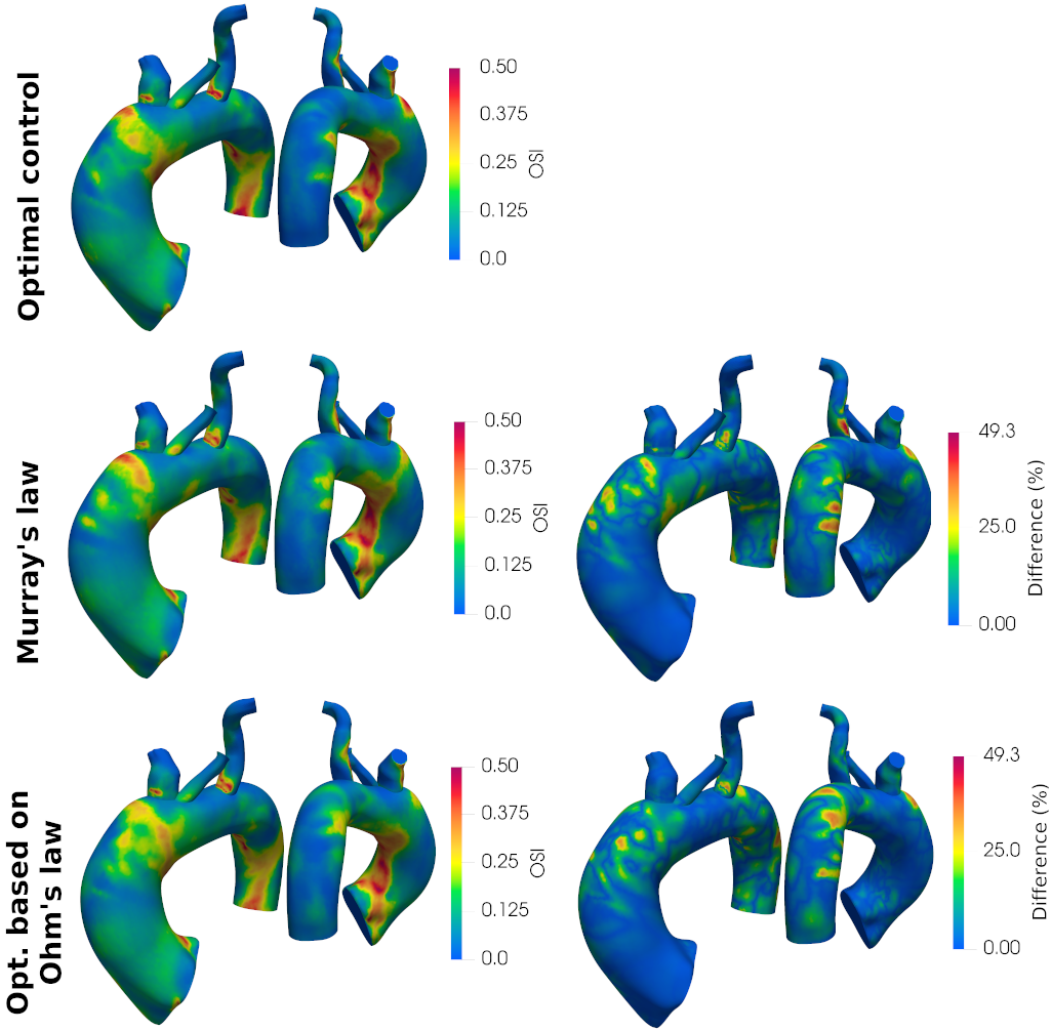

Fig. 3.11 Left: Oscillatory Shear Index results obtained with the three different BC estimation techniques for case 1. Right: local absolute differences in OSI as compared to results obtained with optimal control. Anterior and posterior views of the anatomy are provided.

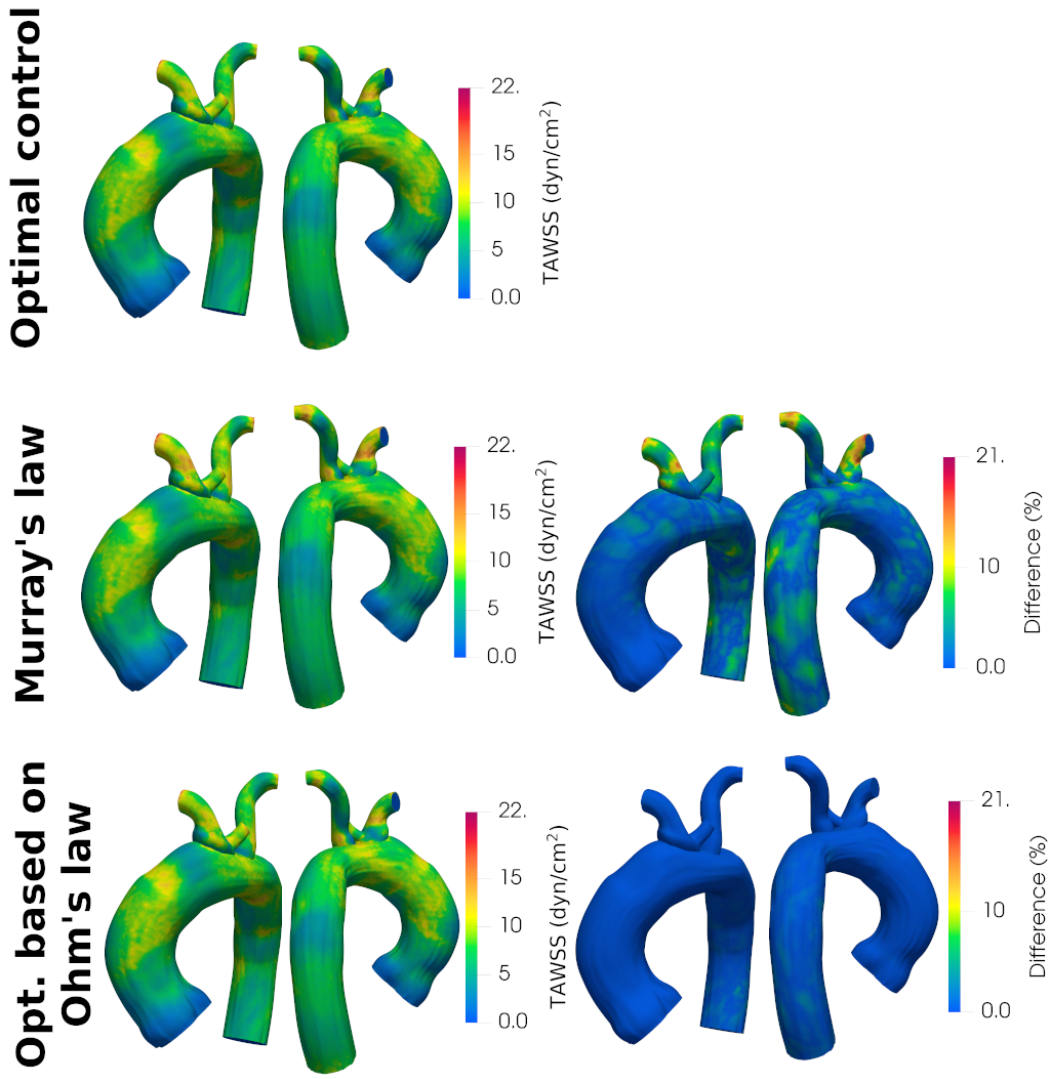

Fig. 3.12 Left: Time-averaged wall shear stress results obtained with the three different BC estimation techniques for case 2. Right: local absolute differences in TAWSS as compared to results obtained with optimal control. Anterior and posterior views of the anatomy are provided.

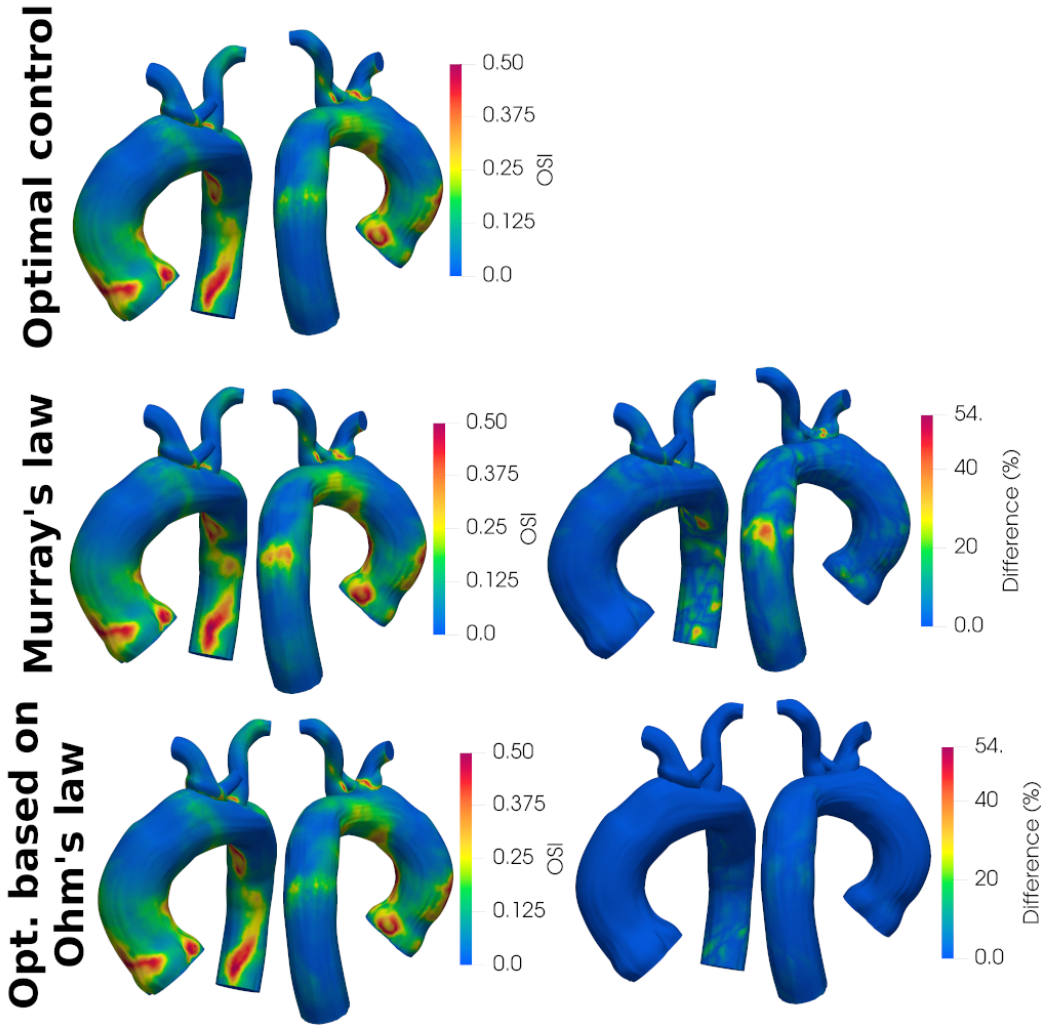

Fig. 3.13 Left: Oscillatory Shear Index results obtained with the three different BC estimation techniques for case 2. Right: local absolute differences in OSI as compared to results obtained with optimal control. Anterior and posterior views of the anatomy are provided.

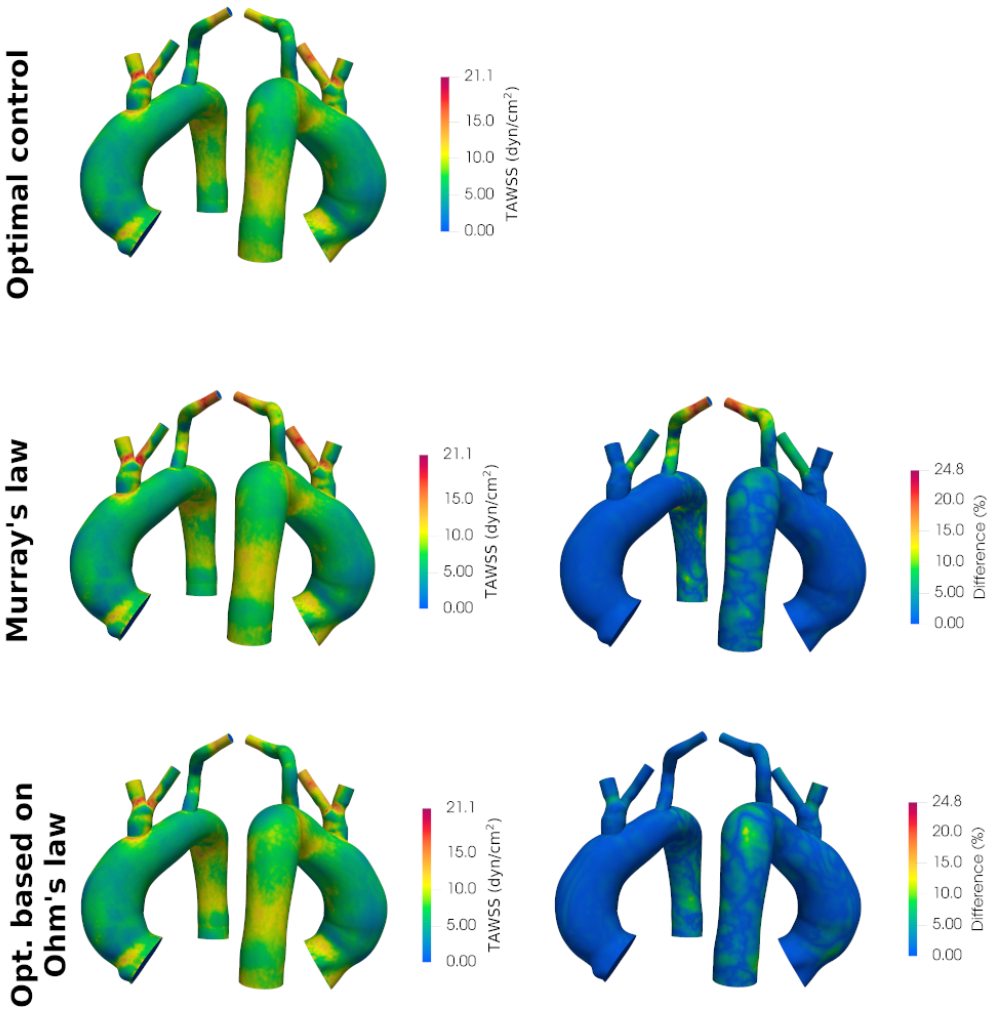

Fig. 3.14 Left: Time-averaged wall shear stress results obtained with the three different BC estimation techniques for case 3. Right: local absolute differences in TAWSS as compared to results obtained with optimal control. Anterior and posterior views of the anatomy are provided.

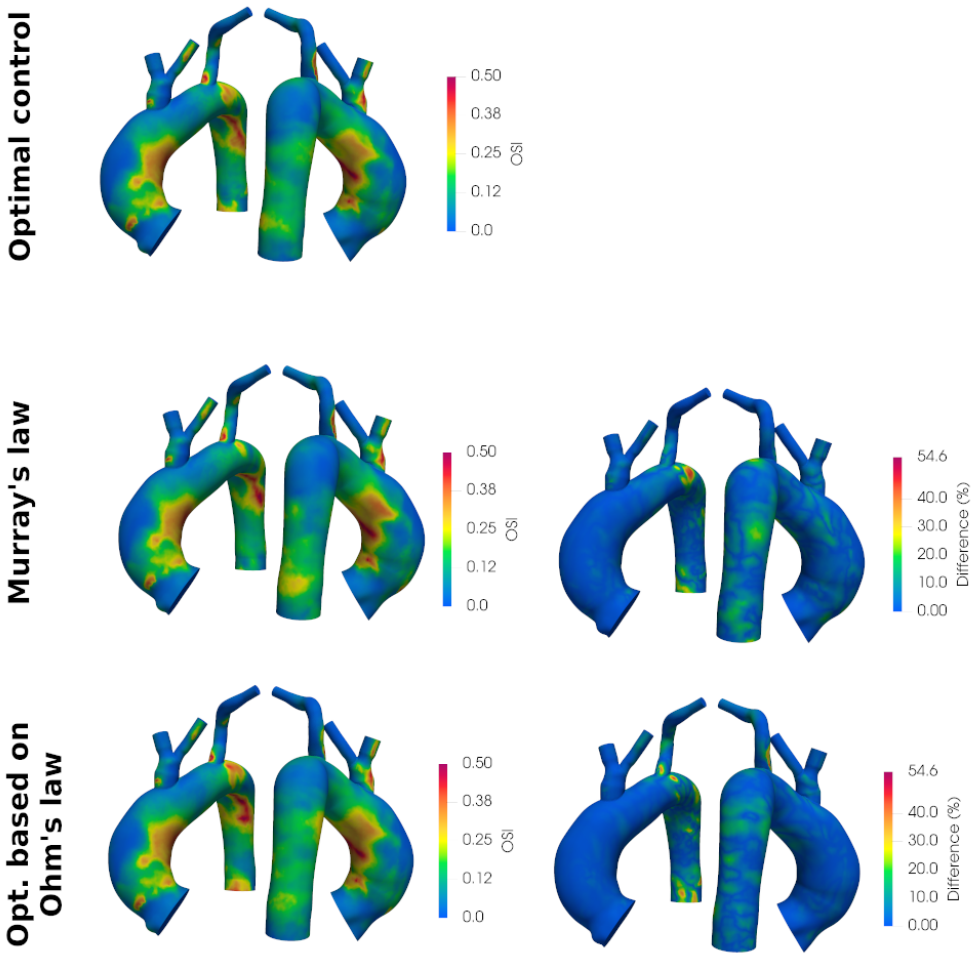

Fig. 3.15 Left: Oscillatory Shear Index results obtained with the three different BC estimation techniques for case 3. Right: local absolute differences in OSI as compared to results obtained with optimal control. Anterior and posterior views of the anatomy are provided.

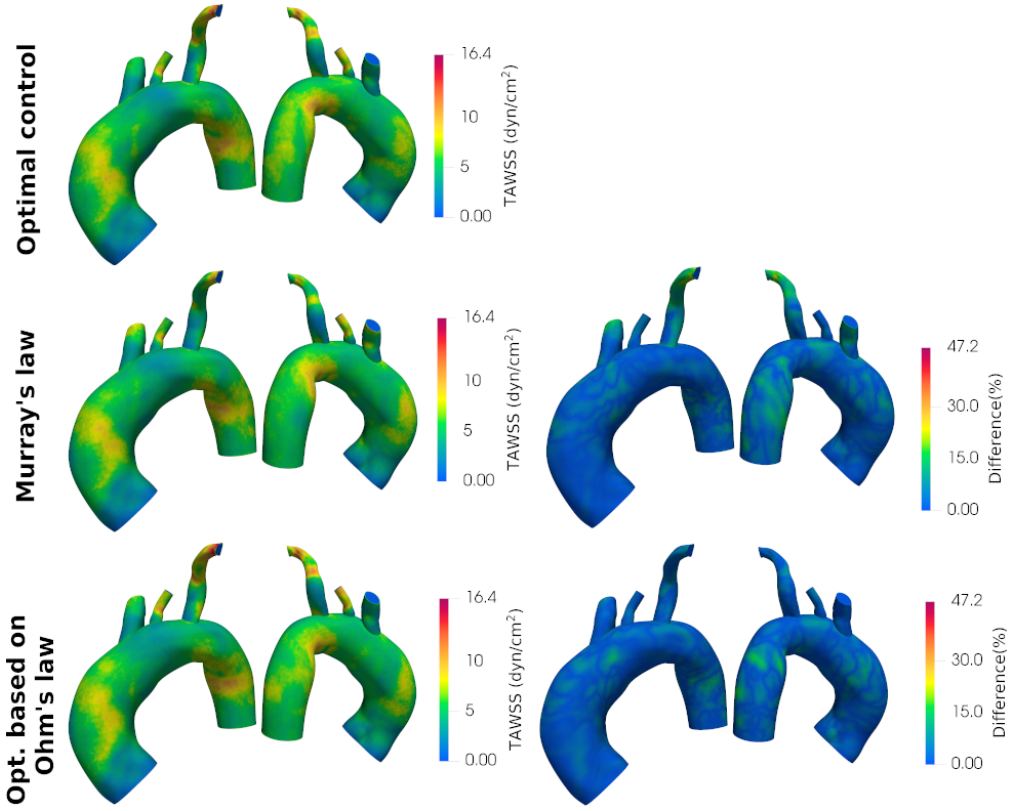

Fig. 3.16 Left: Time-averaged wall shear stress results obtained with the three different BC estimation techniques for case 4. Right: local absolute differences in TAWSS as compared to results obtained with optimal control. Anterior and posterior views of the anatomy are provided.

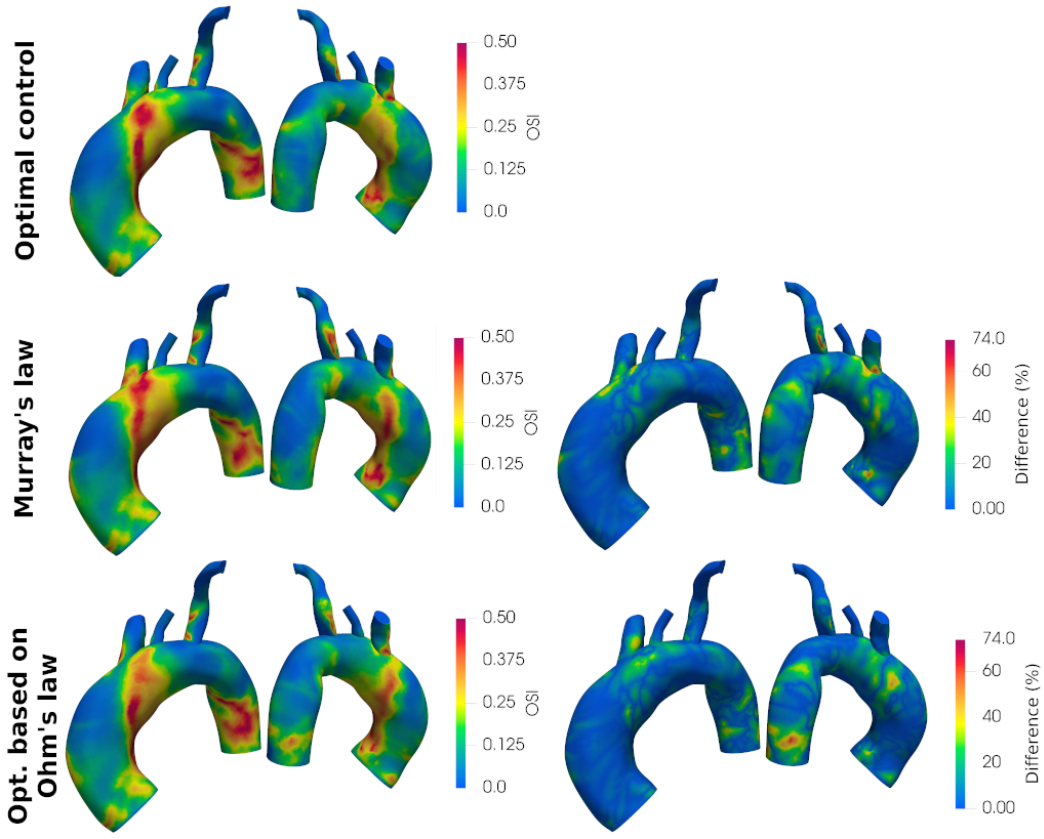

Fig. 3.17 Left: Oscillatory Shear Index results obtained with the three different BC estimation techniques for case 4. Right: local absolute differences in OSI as compared to results obtained with optimal control. Anterior and posterior views of the anatomy are provided.

3.5 Discussion and Limitations

The optimal control-based approach for boundary condition estimation that we proposed in this chapter has a number of advantages. The first one resides in the rigorous and general mathematical framework which characterizes optimal control problems. The proposed approach, in fact, can be applied to any region and vessel of the cardiovascular system, as long as patient-specific data are available. Again, thanks to the mathematical structure of optimal control, the user is left with a great flexibility in terms of the number and type of measurements to assimilate. This is particularly appealing in cardiovascular applications, where in-vivo measurements are often hard to obtain, and potentially noisy, scarce or defective. In this sense, the proposed method is compatible with any method providing flow rate information at the inlets and outlets of the region of interest, be it 4D-Flow MRI, or PC-MRI, or any other equivalent technique. Moreover, in absence of some measurements, a combination of patient-specific and literature data could also be used. Another advantage of the proposed formulation is that data are assimilated in a least-square sense [124], reducing the influence of stochastic measurement uncertainty on the solution. Generally, the proposed optimal control method presents all the advantages of a *model-based* approach, which we discussed at the beginning of this Chapter. The possibility to estimate boundary conditions not only from a set of data, but also from a mathematical description of the underlying physics, allows to obtain estimates that are patient-specific, yet physically consistent.

On the other side, the proposed method has some limitations. The first limitation comes from the use of steady, linear Stokes equations inside the optimal control problem. As already stated earlier in the chapter, this choice ensures a reduced computational cost, which for optimal control problems is generally really high. At the moment, the solution of a time-dependent optimal control problem on a 3D anatomy is computationally intractable, and Navier-Stokes equations may not converge to a steady-state solution for a complex flow like the one in the aortic arch. If on one side the use of steady Stokes equations reduces the computational cost and simulation time, on the other side steady Stokes equations are not the best choice to get a realistic representation of the flow in the aorta. For this reason, if the optimal control

framework is used to estimate the outlet resistances, for realistic pressure and velocity distributions a subsequent time-dependent simulation is still necessary.

The use of a steady-state formulation is responsible also of another limitation of the framework, which allows to estimate only resistive boundary conditions. More complex lumped models, in fact, usually include inductances and capacitances which, being dynamic elements with an inherently time-dependent behavior, would require a time-dependent Navier-Stokes problem for their estimation. For this reason, if one wanted to use more advanced BCs, such as a complete Windkessel model, it would be necessary to adopt capacitance values and rules for resistance splitting taken from literature.

Lastly, the proposed method can only assimilate average flow rates, and not time-dependent flow waveforms. However, the results presented in Section 3.4, in particular the simulated waveforms reported in Figure 3.9, prove that, when the resistance and capacitance values determined with the proposed method are used in an unsteady simulation, the obtained pressure and flow rates values seem to be in sufficient agreement with the in-vivo measurements used for BC estimation.

3.6 Conclusion and future perspectives

In this chapter, we proposed a framework based on optimal control for the automated estimation of resistance-type boundary conditions, while assimilating in-vivo pressure and flow rate measurements. We tested the proposed method on four patient anatomies, revealing the validity of the presented optimal control-based technique for assimilating 4D-MRI data. Specifically, when compared to two other common techniques, namely, Murray's law and Ohm's law, the proposed framework performed consistently better. Moreover, an additional analysis revealed the influence that the different estimation methods have on clinically relevant parameters, such as wall shear stress and oscillatory shear index, confirming the need for automated methods for BC estimation, such as those proposed in this thesis, which eliminate the expensive manual tuning phase, together with intra- and inter-operator variability. In this case, the proposed method represents a further step in the incorporation of optimal control into a framework that can be used by the medical community, providing

a reliable, automated and robust parameter estimation technique. The field is promising and opens important perspectives for mathematical modelling and numerical simulation in cardiovascular flows.

There are a number of extensions of the proposed framework which could be worth further investigation. First, it could be applied to other clinically relevant scenarios, such as coronary artery bypass grafts, where the scarcity and noise of available data limit the applicability of other estimation techniques. Furthermore, the current framework estimates only resistive-type quantities, while the capacitance values are still chosen based on generic information available in the literature, usually combined with a manual tuning process. Future works could be directed toward the automated tuning of capacitance values as well. Since the main obstacle in this case is the prohibitive computational cost of time-dependent optimal control, this could be significantly reduced by adopting a reduced one-dimensional model of the anatomy of interest.

In conclusion, the estimation solution proposed in this chapter clarifies the advantages and drawbacks of adopting a *data and model-driven* approach. If on one side the presence of a mathematical description of the system, in the form of PDE, facilitates the determination of physically meaningful boundary conditions, on the other side it makes the estimation process computationally expensive. In the next chapter, an alternative approach based on a purely *data-driven* method will be instead presented, underlining both benefits and disadvantages with respect to the approach presented in the current chapter.

Chapter 4

Time-Domain Vector Fitting for boundary conditions estimation

In this chapter, we will present a novel approach for boundary conditions estimation based on the Time-Domain Vector Fitting algorithm. Differently from the optimal control framework presented in Chapter 3, here the approach is completely *data-driven*, meaning that the choice for boundary conditions parameters is based solely on a set of measurements, without using any description of the physical system underneath. In other words, the cardiovascular system is treated like a *black-box*, characterized only through input-output responses, such as flow rate and pressure at a given location. The estimation approach, in this case, obviously differs from the one presented in the previous chapter. Before diving into the details of the proposed Vector Fitting framework, it may be useful to stress why a *data-driven* approach is interesting in the first place, and what are its advantages with respect to other possible approaches. First of all, a data-driven approach is generally faster than a model driven one, which instead requires the (expensive) solution of a mathematical model. At the same time, data driven methods tend to be easier to implement and integrate in pre-existing solvers. These advantages are particularly appealing when considering the end goal of developing computational tools for the clinical community.

In the work presented in this chapter, the technique adopted is Vector Fitting [155, 79], an algorithm originally developed and used by the electrical

engineering community, where it is commonly used to model the high-speed signal propagation in chips, packages and printed circuit boards [156]. In this field, Vector Fitting has quickly become one of the most popular techniques for reduced order modeling, mainly due to its efficiency (it converges in a small number of iterations), robustness, and ease of implementation.

In this chapter, we will show how the time-domain formulation of Vector Fitting can be successfully applied to cardiovascular modeling for estimating complex boundary conditions. In particular, the adoption of a *data-driven* approach allows to estimate lumped boundary conditions more complex than a single resistance, which was one of the main limitations of the optimal control approach presented in Chapter 3. At the same time, the estimation process itself is fast and inexpensive, requiring only a few seconds on a personal computer.

In the rest of the chapter, we will first provide some background in Sec. 4.1, then we will present the methodological aspects of the proposed approach in Sec. 4.2. In Sec. 4.3, the numerical results of experiments conducted on a one-dimensional model of the entire cardiovascular system will be provided, together with a discussion in Sec. 4.4. Finally, Sec. 4.5 will draw the conclusions on the proposed estimation framework.

4.1 Background and related work

As already mentioned throughout this thesis, different types of outlet boundary conditions have been proposed in the literature. The simplest choice consists in prescribing specific values for pressure or flow rates, by means of Dirichlet or Neumann boundary conditions. This choice, despite being the simplest to implement, is not realistic. It is better, instead, to define BCs that describe the relationship between pressure and flow rate, instead of defining one of the two quantities. This can be done either by prescribing a constant or varying resistance, which specifies a linear algebraic relation between pressure and flow rate, or by imposing a differential relation between pressure and flow rate by means of lumped parameter networks. The latter turns out to be the best approach, providing a relatively accurate and realistic representation of haemodynamics.

Lumped parameter networks are usually classified according to their *order*, which is the lowest possible order of the differential equation relating pressure and flow rate. Equivalently, this is the number of independent storage (L or C) elements of the equivalent circuit. In particular, the most common lumped boundary condition is the three-element Windkessel model (3WK) [157], a circuit represented in Fig. 4.1. Since the Windkessel model contains only one capacitor, it is a circuit of order one. Higher order Windkessel models have also been proposed [38], especially for those regions where the 3WK fails to accurately represent the flow dynamics, like in the coronary arteries. However, their application has been limited by the additional number of parameters to estimate, which increases with the number of elements in the circuit.

Even if the number of parameters in the Windkessel is limited, obtaining an accurate estimate is not straightforward. The simplest, yet most expensive approach, consists in choosing each parameter by means of an iterative tuning process, after having identified reasonable ranges for each parameter [118]. More advanced and automated approaches can be used if both pressure and flow data are available, and they generally consist in fitting the Windkessel models to available data. Some significative examples are the simplex search method [157], and the least-square minimization [69]. A similar approach is proposed in [158], where the Windkessel resistances are estimated from mean pressure and outflow measurements at each terminal vessel, while terminal compliances are obtained by distributing the total peripheral compliance according to the outflow cross-sectional areas. In [159], instead, the Windkessel parameters are estimated such that the net resistance and total compliance of the entire system are preserved. In synthesis, the solutions currently available for the estimation of Windkessel parameters tend to be empirical, time consuming, and only adequate to estimate a limited number of parameters. A major consequence is the limited use of higher order lumped boundary conditions, which, despite being more accurate and realistic than the three-element Windkessel model [157, 42], require to estimate a larger number of parameters. Moreover, probably due to their limited diffusion, the literature lacks a clear and systematic analysis of the effect that higher order boundary conditions have, the potential improvement in accuracy they provide, and indications on how to choose the best order.

In this chapter, a novel method for the automated estimation of boundary conditions of arbitrary order is presented. The proposed approach is based

on the Time-Domain Vector Fitting algorithm (TDVF), which, starting from pressure and flow rate samples at the truncation location, where we want to impose the boundary condition, provides a behavioral model of the downstream vasculature. The blood flow dynamics, in fact, is approximated by TDVF by means of differential equations relating pressure and flow rate [77, 78]. When estimating models of order one, TDVF automatically provides an estimate of the Windkessel parameters. For higher order models, instead, a *black-box* model representation is adopted, meaning that the BC is represented as a differential relation between pressure and flow rate, without synthesizing the model into an equivalent circuit. The provided model can be directly used as a boundary condition to Navier-Stokes equations, and can be easily implemented in CFD solvers.

The experiments to assess the capability of the proposed approach are conducted on a 1D model of the entire cardiovascular system, comprising the 55 largest systemic arteries [92]. More in detail, some portions of the system are truncated and replaced with boundary conditions of increasing order estimated with Vector Fitting. Experimental results show that the proposed method is able to estimate boundary conditions that provide accurate pressure and flow waveforms at the truncation locations. For the estimation of Windkessel parameters, Vector Fitting is compared to two other methods presented in the literature, one preserving the net resistance and total compliance of the original 55-artery system [159], and the other based on the Nelder-Mead simplex algorithm [150], against which Vector Fitting produces comparable, or better, results. Moreover, the proposed method is used to estimate boundary conditions of increasing order, revealing that models of increasing complexity provide results more accurate than the three-element Windkessel model. We also verify that TDVF can accurately fit pressure and flow waveforms affected by noise down to 20 dB of signal-to-noise ratio, and that the estimated terminations are valid in presence of physiological changes of the input waveforms (e.g., in case of mental stress [160, 161]).

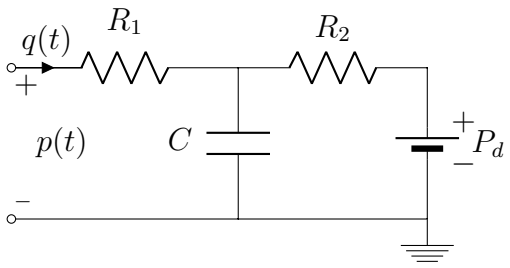

Fig. 4.1 Three-element Windkessel model used as outlet boundary condition. The circuit includes the proximal resistance R_1, the distal resistance R_2, the capacitance C and the distal pressure P_d.

4.2 Methodology

In this section, the proposed boundary conditions estimation framework based on Time-Domain Vector Fitting will be presented. A reference application for this type of framework is displayed in Fig. 4.2, where the BCs estimation process allows to move from the model on the left, representing the entire systemic arterial system, to its reduced version on the right, where parts of the vasculature have been substituted by lumped boundary conditions. In particular, the latter correspond to Windkessel models in Fig. 4.2, but we will see how the proposed method can estimate also higher order lumped boundary conditions.

This section is divided into four main parts. In Sec. 4.2.1, we will start by introducing the Windkessel model, and how it can be described by means of the well-known Laplace domain formulation. This is used in Sec. 4.2.2 to obtain a general representation for boundary conditions of arbitrary order. This generalization is necessary for the following step, presented in Sec. 4.2.3, which is the actual estimation of the BC parameters based on Time-Domain Vector Fitting. Lastly, in Sec. 4.2.4 we show how higher order boundary conditions can be implemented in CFD solvers.

4.2.1 The three-element Windkessel model

The standard three-element Windkessel model is displayed in Fig. 4.1. It includes a capacitor C, to model the storage properties of arteries, the resistor R_1, representing the proximal resistance of the arterial network, and the resistor

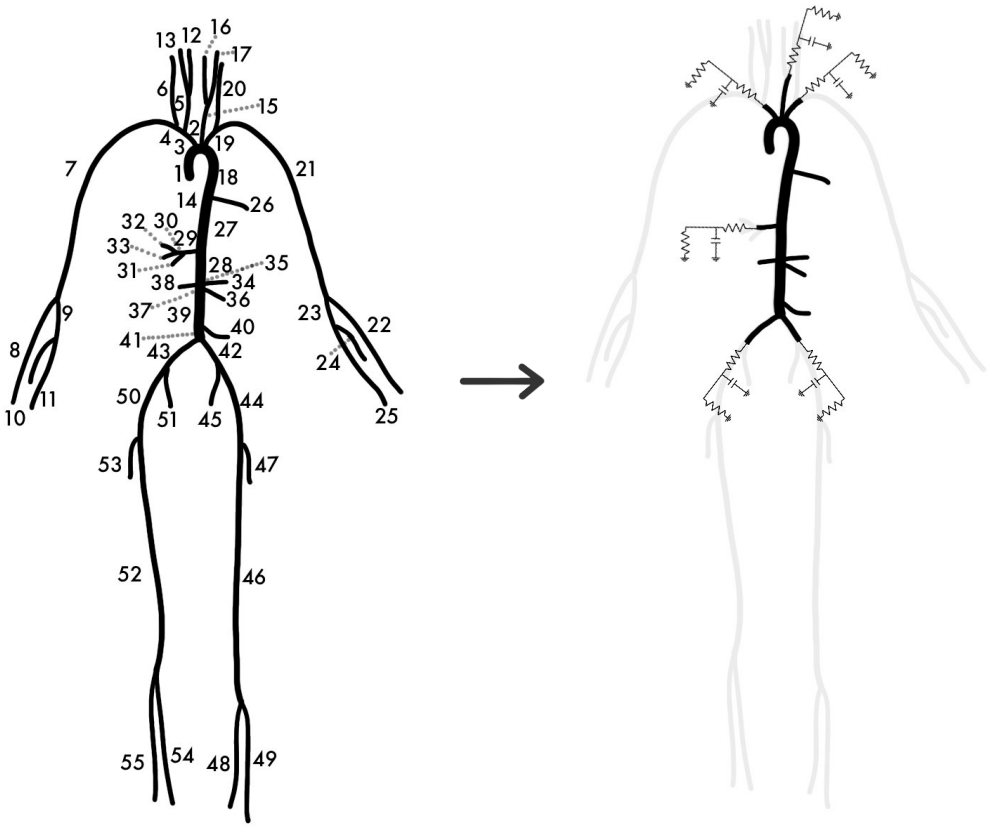

Fig. 4.2 Left: schematic representation of the complete 55-artery network. Right: representation of the reduced model after boundary conditions estimation with Vector Fitting. The arterial segments are reduced from 55 to 21, and the truncated parts of the system (in grey) are substituted with the estimated boundary conditions. These could be Windkessel models, as depicted here, or black-box models.

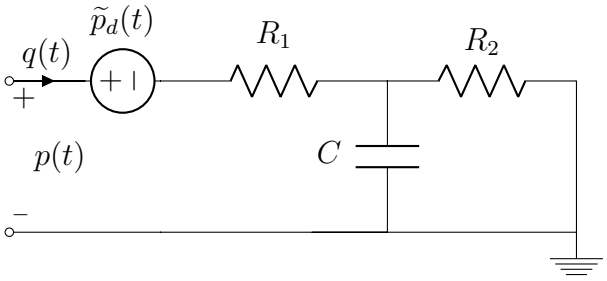

Fig. 4.3 Equivalent Windkessel model, obtained by relocating the distal pressure contribution.

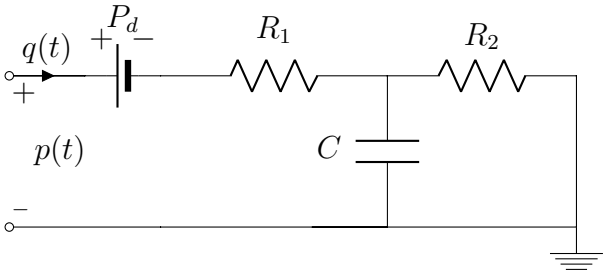

Fig. 4.4 Approximate Windkessel model.

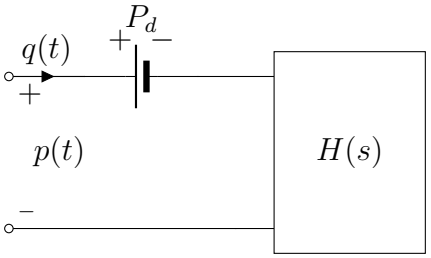

Fig. 4.5 Proposed high-order boundary condition model.

R_2, to model the resistance of the distal circulation. Moreover, a distal pressure contribution P_d is also generally defined, in order to represent the pressure at which flow to the microcirculation ceases [92].

In the Windkessel model, the pressure $p(t)$ is related to the flow rate $q(t)$ by means of the differential equation

$$q(t)\left(1+\frac{R_1}{R_2}\right)+CR_1\frac{dq(t)}{dt}=\frac{p(t)-P_d}{R_2}+C\frac{dp(t)}{dt}, \tag{4.1}$$

whose derivation from the equivalent circuit of Fig. 4.1 can be easily obtained by exploiting the equivalence between fluid dynamics (pressure, flow rate) and electrical quantities (voltage, current). Estimating the Windkessel boundary condition parameters consists in determining the optimal values for R_1, R_2,

C and P_d in (4.1) that best approximate the time domain evolution of the pressure and flow rate at the outlet.

Laplace-domain formulation

For the upcoming derivations, it is useful to move from the time domain to the Laplace domain, by means of the well-known Laplace transform [162]. The latter is a widely used mathematical tool that converts linear differential equations into symbolic algebraic equations, thus simplifying both the solution and the interpretation of differential models. Let us denote with s the Laplace variable (representing the time derivative operator d/dt), and define the (one-sided) Laplace transforms[1] of $p(t)$ and $q(t)$ as $P(s)$ and $Q(s)$, respectively. Assuming vanishing initial conditions at $t = 0$, the Laplace transform of (4.1) is

$$Q(s)\left(1 + \frac{R_1}{R_2}\right) + sCR_1Q(s) = \frac{P(s)}{R_2} - \frac{P_d}{sR_2} + sCP(s), \tag{4.3}$$

which is an algebraic relation between pressure and flow rate, parameterized by the constants R_1, R_2, C, and P_d. The distal pressure P_d can also be seen as an extra (constant) input, considering that it is interpreted as a voltage source in electrical terms (see Fig. 4.1). Equation (4.3) can be rewritten as

$$P(s) = H(s)Q(s) + H_d(s)\frac{P_d}{s}, \tag{4.4}$$

where $H(s)$ and $H_d(s)$ are the two transfer functions[2]

$$H(s) = R_1 + \frac{R_2}{sR_2C + 1} \tag{4.5}$$

$$H_d(s) = \frac{1}{sR_2C + 1}. \tag{4.6}$$

[1]The *one-sided* Laplace transform of $x(t)$ is defined as

$$\mathcal{L}(s) := \int_{0^-}^{+\infty} x(t)e^{-st}dt, \tag{4.2}$$

where s is a complex variable.

[2]In a linear system with input $q(t)$ and output $p(t)$, the transfer function is the function $H(s)$ which relates the Laplace transforms of the input $Q(s)$ and of the output $P(s)$ as $H(s) = \frac{P(s)}{Q(s)}$, assuming zero initial conditions.

Transfer functions are, in fact, mathematical functions modeling the system's output (in this case $P(s)$) for a specific input (here $Q(s)$ and $P_d(s)$). The two transfer functions $H(s)$ and $H_d(s)$ are first-order rational functions of the Laplace variable s, whose *order* is defined as the degree of the denominator polynomials. This is coherent with the differential equation (4.1) including only first-order derivatives.

These transfer functions can be rewritten in a more general form, called the pole-residue (partial fraction) form, which will be instrumental for the proposed generalization:

$$H(s) = c_0 + \frac{c_1}{s-a} \quad H_d(s) = \frac{b_1}{s-a}, \tag{4.7}$$

where the pole a, the residues c_1, b_1, and the direct coupling constant c_0 can be uniquely related to the Windkessel parameters through

$$R_1 = c_0, \quad R_2 = -\frac{c_1}{a}, \quad C = \frac{1}{c_1}, \quad \text{with} \quad b_1 = -a. \tag{4.8}$$

4.2.2 Generalization to high order boundary conditions

At this point the goal is to find a proper general form for boundary conditions of arbitrary order, starting from the 3WK model. In order to do so, some intermediate steps are necessary, which will be detailed in the following. In short, first the structure reported in (4.4) is simplified to include a single transfer function $H(s)$, and then it is extended to its higher order form exploiting again the pole-residue form.

Relocation of distal pressure contribution

As a first step, we apply Thevenin theorem [163] to the standard Windkessel circuit of Fig. 4.1, allowing us to move from a circuit with internal sources, to an equivalent one with a single equivalent source directly connect to the output. As a result, the circuit of Fig. 4.3 is obtained where, as expected, the original internal source P_d has been replaced with an equivalent source at the output, indicated as $\widetilde{p}_d(t)$.

The equivalence between circuits in Fig. 4.1 and Fig. 4.3 can be established in the Laplace domain by imposing

$$\widetilde{P}_d(s) = H_d(s)\frac{P_d}{s} \tag{4.9}$$

so that (4.10) can be rewritten as

$$P(s) = H(s)Q(s) + \widetilde{P}_d(s). \tag{4.10}$$

At this point, the two circuits in Fig. 4.1 and Fig. 4.3 are equivalent, meaning that they impose the same relationship between $P(s)$ and $Q(s)$.

Going back to time domain, we can apply the inverse Laplace transform to the source $\widetilde{P}_d(s)$, obtaining

$$\widetilde{p}_d(t) = P_d \left(1 - e^{at}\right) \theta(t), \tag{4.11}$$

where $\theta(t)$ is the unit step (Heaviside) function and where we made use of relationships in (4.7) and (4.8). Equation (4.11) shows that the new source converges exponentially to the asymptotic value P_d after an initial transient, whose duration is described by the equivalent time constant $\tau = -1/a = R_2C$.

Approximation of early-time transient behavior

To obtain a generalized form for lumped BCs, an approximation is required. Generally, time-domain simulations of cardiovascular models are initialized to a vanishing initial state for pressure and flow rate. However, the solution becomes of practical and clinical interest only when a periodic state has been reached, due to the pulsatile nature of blood flow in the arterial system. In numerical solvers such a periodic state is reached only after an initial transient, which is however discarded when interpreting the results of the simulation. Due to this reason, and reminding that the equivalent source $\widetilde{p}_d(t)$ converges to the value P_d after an initial time transient, we can safely replace $\widetilde{p}_d(t)$ with P_d in the circuit of Fig. 4.3, obtaining the new circuit of Fig. 4.4, which gives an approximation of the original Windkessel model. This is equivalent to imposing

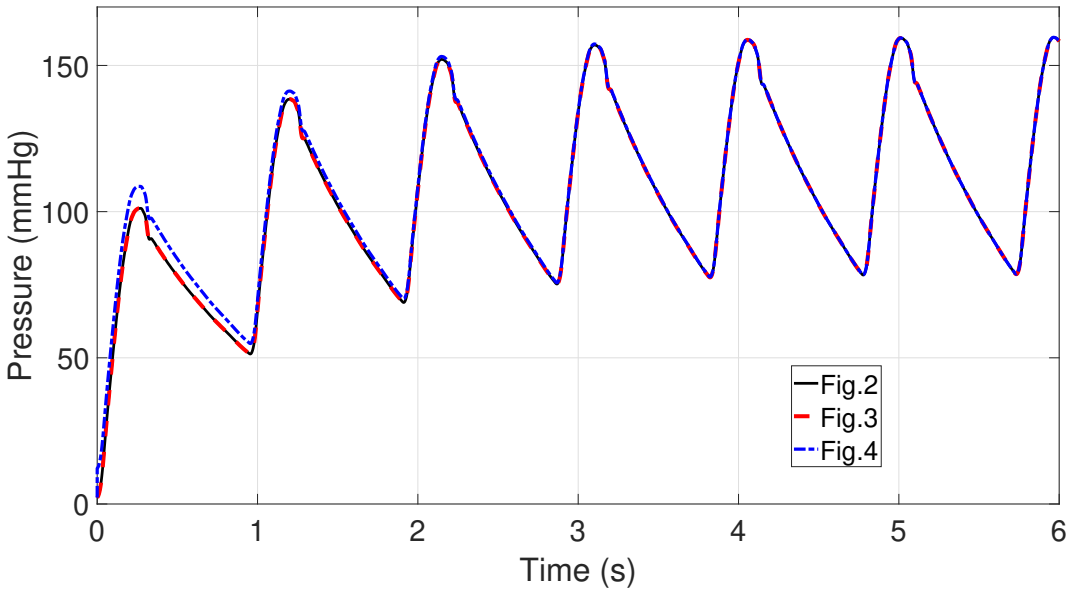

Fig. 4.6 Pressure signals obtained by exciting the three boundary condition models in Fig. 4.1 (black line), Fig. 4.3 (red dashed line) and Fig. 4.4 (blue line) with the same inlet flow excitation signal.

$H_d(s) = 1$ in (4.10), which takes then the form

$$P(s) \approx H(s)Q(s) + \frac{P_d}{s}. \tag{4.12}$$

Obviously, introducing an approximation means that the two circuits are no longer equivalent, but in this case the difference occurs only at early times, when the solution would be discarded anyway due to the presence of an early-time transient behavior. After that, the solutions are identical, as it is shown in Fig. 4.6, where the three models in Fig. 4.1, Fig. 4.3 and Fig. 4.4 have been excited with the same input flow waveform. As expected, the output pressure waveforms of models in Fig. 4.1 and Fig. 4.3 are identical, confirming the full equivalence of the two models, while the pressure waveform of model in Fig. 4.4 differs only during the initial transient, reaching full equivalence at the periodic state. In conclusion, as long as only the periodic state is required, the models considered up to now can be considered equivalent from a numerical standpoint.

Generalization to high order

With the approximation introduced just now, the generalization of the Windkessel model to higher order boundary conditions becomes straightforward. It is sufficient, in fact, to rewrite the transfer function $H(s)$ in its pole-residue form as a higher order rational function, obtaining

$$H(s) = c_0 + \sum_{i=1}^{n} \frac{c_i}{s - a_i}. \tag{4.13}$$

Thanks to this definition, the proposed higher order BC model can be seen as a black-box representation of the differential relation between outlet pressure and flow variables, characterized by richer dynamics and generally allowing for more accurate numerical results, as it will be demonstrated by the numerical results in Sec. 4.3. It is worth noticing that, adopting this generalized model, the interpretation of (4.12) in terms of an equivalent circuit is partially lost, but it is always possible to perform the synthesis of an equivalent circuit thanks to well known circuit synthesis techniques, which are detailed in [79]. On the other side, the use of a general formula such as (4.13) makes it straightforward to implement it in CFD solvers, as will be explained in Sec. 4.2.4.

Lastly, it is interesting to give an interpretation of the proposed approximation. Noticing the presence of s at the denominator associated to P_d in (4.12), and knowing that the inverse Laplace transform of $1/s$ is $\mathcal{L}^{-1}\{1/s\} = \theta(t)$, we can conclude that the distal pressure term in (4.12) can be interpreted as a time-domain source $\widetilde{p}_d(t) = P_d\,\theta(t)$. Therefore, the proposed higher order model assumes that the distal pressure P_d is applied instantaneously at $t = 0$, rather than through an exponential transient (4.11), hence the difference during the early time transient.

4.2.3 Time-Domain Vector Fitting for boundary conditions estimation

We now present how, starting from pressure $p(t)$ and flow rate $q(t)$ waveforms at some vessel cross section, the parameters of the corresponding boundary condition formulated as in (4.12)-(4.13) can be automatically estimated. As previously said, the estimation assumes that both pressure and flow rate

waveforms are available at a given vessel output

$$p(t_k),\ q(t_k), \quad k = 0, \ldots, K, \quad t_0 = 0, \tag{4.14}$$

where the sampling rate, defined as $\Delta t = t_{k+1} - t_k$, is assumed to be constant, and both waveforms are null at initial time $p(t_0) = q(t_0) = 0$. In Sec. 4.2.3 the method will be generalized to non-vanishing initial conditions, which is often the case when dealing with in-vivo measurements.

Model parameterization

The following model structure is assumed

$$H(s) = \frac{N(s)}{D(s)}, \tag{4.15}$$

meaning that the transfer function is expressed as the ratio of two rational functions, $N(s)$ and $D(s)$, having the form

$$N(s) = c_0 + \sum_{i=1}^{n} \frac{c_i}{s - a_i}, \tag{4.16}$$

$$D(s) = d_0 + \sum_{i=1}^{n} \frac{d_i}{s - a_i}. \tag{4.17}$$

Thus, the two functions (4.16) and (4.17) share the same set of common poles $\{a_i\}$, while the residues are denoted as $\{c_i\}$ and $\{d_i\}$, respectively. By substituting (4.16) and (4.17) in (4.15) and doing some basic algebraic manipulations, it is possible to show that the common denominators containing the poles $\{a_i\}$ eventually cancel out: thus, they are only instrumental variables which will be used in the identification algorithm. The general expression

$$H(s) = \frac{c_0 + \sum_{i=1}^{n} \frac{c_i}{s - a_i}}{d_0 + \sum_{i=1}^{n} \frac{d_i}{s - a_i}} \tag{4.18}$$

provides a parameterization of all proper rational functions with order n.

The VF iteration

For simplicity, let us start by assuming that the poles $\{a_i\}$ in (4.18) are known, such that the only unknowns in $H(s)$ are the numerator residues $\{c_i\}$ and the denominator ones $\{d_i\}$. These unknowns can be determined by enforcing (4.12) as a fitting condition, starting from the available pressure and flow rate waveforms. Thus, we can rewrite (4.12) using (4.15)

$$P(s) \approx \frac{N(s)}{D(s)} Q(s) + \frac{P_d}{s} D(s), \tag{4.19}$$

and then, multiplying both sides by $D(s)$ we obtain

$$D(s)P(s) \approx N(s)Q(s) + \frac{P_d}{s} D(s), \tag{4.20}$$

At this point we can substitute (4.16) and (4.17) into the fitting condition (4.20), obtaining

$$\left(d_0 + \sum_{i=1}^{n} \frac{d_i}{s - a_i}\right) P(s) \approx \left(c_0 + \sum_{i=1}^{n} \frac{c_i}{s - a_i}\right) Q(s) + \\ + P_d \left(\frac{d_0}{s} + \sum_{i=1}^{n} \frac{d_i}{s \cdot (s - a_i)}\right). \tag{4.21}$$

Since the estimation procedure is based on the use of time-domain measurements, the expression (4.21) is converted into time domain by applying the inverse Laplace transform, which leads to

$$d_0 \cdot p(t) + \sum_{i=1}^{n} d_i \cdot p_i(t) \approx c_0 \cdot q(t) + \sum_{i=1}^{n} c_i \cdot q_i(t) + \\ + P_d\, d_0 \cdot \theta(t) + \sum_{i=1}^{n} P_d\, d_i \cdot \theta_i(t). \tag{4.22}$$

The notation $q_i(t)$, $p_i(t)$ and $\theta_i(t)$ stands for, respectively, the time convolutions

$$q_i(t) = \int_0^t e^{a_i(t-\tau)} q(\tau) d\tau \tag{4.23}$$

$$p_i(t) = \int_0^t e^{a_i(t-\tau)} p(\tau) d\tau \tag{4.24}$$

$$\theta_i(t) = \int_0^t e^{a_i(t-\tau)}\theta(\tau)d\tau. \tag{4.25}$$

We recall, in fact, that the inverse Laplace transform of a product is the convolution of the individual inverse transforms, which for a generic signal $z(t)$ leads to

$$z_i(t) = \mathcal{L}^{-1}\{Z_i(s)\} = \mathcal{L}^{-1}\left\{\frac{1}{s-a_i}\right\} * z(t) = \int_0^t e^{a_i(t-\tau)}z(\tau)d\tau \tag{4.26}$$

We then introduce a new set of auxiliary variables $b_i = P_d\, d_i$, in order to make the approximation problem linear in the decision variable. Next, we write the fitting condition (4.22) for all discrete time samples $t = t_k$, leading to a homogeneous linear least squares problem in the unknowns $\{c_i\}$, $\{d_i\}$, $\{b_i\}$, which can be written as

$$A\,x \approx 0, \quad A = \begin{bmatrix} -\Phi & \Gamma & \Theta \end{bmatrix}, \quad x = \begin{bmatrix} d \\ c \\ b \end{bmatrix} \tag{4.27}$$

where the vectors and matrices take the form

$$\Phi = \begin{bmatrix} p(t_0) & p_1(t_0) & \dots & p_n(t_0) \\ \vdots & \vdots & \ddots & \vdots \\ p(t_K) & p_1(t_K) & \dots & p_n(t_K) \end{bmatrix}, \qquad d = \begin{bmatrix} d_0 \\ d_1 \\ \vdots \\ d_n \end{bmatrix} \tag{4.28}$$

$$\Gamma = \begin{bmatrix} q(t_0) & q_1(t_0) & \dots & q_n(t_0) \\ \vdots & \vdots & \ddots & \vdots \\ q(t_K) & q_1(t_K) & \dots & q_n(t_K) \end{bmatrix}, \qquad c = \begin{bmatrix} c_0 \\ c_1 \\ \vdots \\ c_n \end{bmatrix} \tag{4.29}$$

$$\Theta = \begin{bmatrix} \theta(t_0) & \theta_1(t_0) & \dots & \theta_n(t_0) \\ \vdots & \vdots & \ddots & \vdots \\ \theta(t_K) & \theta_1(t_K) & \dots & \theta_n(t_K) \end{bmatrix}, \qquad b = \begin{bmatrix} b_0 \\ b_1 \\ \vdots \\ b_n \end{bmatrix}. \tag{4.30}$$

The least squares problem in (4.27) is solved enforcing $x \neq 0$, so that the trivial null solution is discarded. In practice, this can be obtained by setting x

as the right singular vector of A, which corresponds to the least singular value, or by adding a linear equality constraint as in [155].

Pole relocation

In the process detailed above, the estimated unknowns were the residues $\{c_i\}$ and $\{d_i\}$, while the poles $\{a_i\}$ were considered as given, known quantities. In the following, we lift this assumption, and we add the poles to the set of unknowns to be determined. In particular, we introduce a so-called *pole relocation* process, through which the estimates for poles of $H(s)$, so the coefficients $\{a_i\}$, are iteratively refined [164, 79].

Since the pole relocation is an iterative process, we define ν as the iteration index. At the first iteration $\nu = 0$, the poles $\{a_i^0\}$ are randomly initialized to a set of values in the expected frequency band of the model [164]. Then, at each iteration ν, the set of current poles $\{a_i^\nu\}$ is used to build and solve the least squares problem defined in (4.27).

Let us write the model denominator as

$$D^\nu(s) = d_0^\nu + \sum_{i=1}^{n} \frac{d_i^\nu}{s - a_i^\nu}, \tag{4.31}$$

where the coefficients $\{d_i^\nu\}$ result from the solution of the least squares problem. Since, due to simple algebraic manipulations, in the final expression of the transfer function $H(s)$ the denominators of both $N(s)$ and $D(s)$ cancel out, the zeros of $D(s)$ become the poles of $H(s)$. Then, we can define the poles of the iteration ν as the zeros of $D^\nu(s)$

$$\{a^{\nu+1}\} = \{a_i : D^\nu(a_i) = 0\}. \tag{4.32}$$

This is equivalent to solving a small eigenvalue problem [79, 164]. As a first step, we derive the state-space form associated to the transfer function (4.31)

$$\begin{cases} \dot{x} = A + \mathbf{1}u \\ y = d^\intercal x + d_0 u \end{cases} \tag{4.33}$$

where, omitting iteration index ν

$$A = \text{diag}\{a_1, ..., a_n\}, \quad \mathbf{1} = (1, .., 1)^\intercal, \quad d^\intercal = (d_1, ..., d_n). \tag{4.34}$$

Since we are interested in finding the zeros of (4.31), this is equivalent to finding the poles of $1/D(s)$, whose state-space system reads [79]

$$\begin{cases} \dot{x} = (A - \mathbf{1}d_0^{-1}d^\intercal)x + \mathbf{1}d_0^{-1}y \\ u = -d_0^{-1}d^\intercal x + d_0^{-1}y \end{cases} \tag{4.35}$$

The poles correspond to the eigenvalues of the state-space matrix

$$\text{eig}\left(A - \mathbf{1}d_0^{-1}d^\intercal\right). \tag{4.36}$$

At the iteration ν, poles are computed as

$$\{a_i^{\nu+1}\} = \text{eig}\left(A^\nu - \mathbf{1}(d_0^\nu)^{-1}(d^\nu)^\intercal\right). \tag{4.37}$$

In summary, the proposed algorithm involves solving (4.27) and redefining poles through (4.37) for $\nu = 0, 1, \ldots$, until the set $\{a_i^\nu\}$ converges. Under this convergence condition, poles and zeros of $D^\nu(s)$ coincide so that $D^\nu(s) = d_0$, and the model (4.15) reduces to the numerator $N^\nu(s)$, characterized by poles $\{a_i^\nu\}$ and residues $\{d_i^\nu\}$. This algorithm constitutes an extension of the well-known TDVF scheme, suitably modified to account for the presence of the (unknown) distal pressure term, which produces the matrix block Ψ and the additional unknowns $\{b_i\}$ in (4.27).

Estimation of the distal pressure

Once the final transfer function $H(s)$ has been determined through the pole relocation process detailed above, the distal pressure P_d can be estimated. This estimation can be done in two alternative ways, which are presented in the following.

From least squares variables Considering the auxiliary variables defined as $b_i = P_d\, d_i$, and noting that both unknowns $\{b_i\}$ and $\{d_i\}$ are determined through the solution of the least squares problem (4.27) as vectors b and d, the value of P_d can be determined as a least squares solution itself, defining the problem

$$d\, P_d \approx b \quad \rightarrow \quad P_d = \frac{1}{\|d\|^2}\, d^T \cdot b. \tag{4.38}$$

As periodic state bias In this case, let us remind that, from (4.12), we can say that

$$\frac{P_d}{s} \approx P(s) - H(s)Q(s). \tag{4.39}$$

As already explained in Sec. 4.2.2, this approximation is exact at periodic state, after the transient of P_d has extinguished. Let as suppose that the periodic state holds for $t \geq t_c$; then, we can estimate P_d as the constant value that best fits the approximation

$$P_d \approx p(t) - p_m(t), \quad t \geq t_c \tag{4.40}$$

where

$$p_m(t) = \mathcal{L}^{-1}\{H(s)Q(s)\} \tag{4.41}$$

represents the output in absence of the distal pressure term. The optimal value for P_d is then simply computed as the average

$$P_d = \frac{1}{K - c + 1} \sum_{k=c}^{K} \left[p(t_k) - p_m(t_k)\right]. \tag{4.42}$$

For order equal to 1, the first approach provides the correct estimate of P_d. For orders higher than 1, instead, the second approach is preferred.

Estimation from *in vivo* measurements

The presented estimation process is based on the assumption that both pressure and flow waveforms have vanishing initial conditions. However, this assumption is not realistic when the estimation is based on *in vivo* or generally real-time measurements, where data recording starts at some time instant t_0, at which

$q(t_0) \neq 0$ and $p(t_0) \neq 0$. In this more realistic case, the dynamic evolution of the pressure waveform for $t \geq t_0$ includes not only the zero-state response analyzed in the previous sections, but also some contribution from the zero-input (natural) response. The latter arises from the nonvanishing initial conditions on the internal system states of the underlying dynamical system, which are unknown. An extension of the proposed algorithm is now presented to handle this more realistic case.

Let us first generalize the relation between pressure $P(s)$ and flow rate $Q(s)$ at the outlet as

$$P(s) \approx H(s)Q(s) + G(s) + \frac{P_d}{s}, \tag{4.43}$$

where $G(s)$ represents the zero-input natural response contribution. The latter can be parameterized as

$$G(s) = \frac{B(s)}{s \cdot D(s)}, \quad B(s) = r_0 + \sum_{i=1}^{n} \frac{r_i}{s - a_i} \tag{4.44}$$

based on the same starting poles $\{a_i\}$ and using the same denominator as in (4.15). This choice is motivated by the well-known fact that both input-output and natural response contributions of any linear time-invariant system share the same set of poles [79].

Substituting these definition in (4.43), we obtain

$$\begin{aligned}\left(d_0 + \sum_{i=1}^{n} \frac{d_i}{s - a_i}\right) P(s) \approx \left(c_0 + \sum_{i=1}^{n} \frac{c_i}{s - a_i}\right) Q(s) + \\ + P_d \left(\frac{d_0}{s} + \sum_{i=1}^{n} \frac{d_i}{s \cdot (s - a_i)}\right) + \frac{r_0}{s} + \sum_{i=1}^{n} \frac{r_i}{s \cdot (s - a_i)},\end{aligned} \tag{4.45}$$

which replaces the original fitting condition (4.21). The inverse Laplace transform is then applied to find the time domain equivalent

$$\begin{aligned}d_0 \cdot p(t) + \sum_{i=1}^{n} d_i \cdot p_i(t) \approx c_0 \cdot q(t) + \sum_{i=1}^{n} c_i \cdot q_i(t) + \\ + \underbrace{(P_d d_0 + r_0)}_{b_0} \cdot \theta(t) + \sum_{i=1}^{n} \underbrace{(P_d d_i + r_i)}_{b_i} \cdot \theta_i(t),\end{aligned} \tag{4.46}$$

where the common terms have also been collected. When compared to (4.22), this expression differs only in the way the auxiliary variables b_i are defined. However, these are nonetheless disregarded after solving the least squares problem (4.27). For what concerns the estimation of the coefficients $\{c_i\}$ and $\{d_i\}$, the two problems (4.22) and (4.46) are identical. Therefore, the proposed estimation algorithm can be applied without any modification to the case of non vanishing initial conditions.

4.2.4 Implementation of high-order boundary conditions

Once the estimation process is completed, the obtained model can be used as a boundary condition in cardiovascular simulations. We already showed in Sec. 4.2.1 how boundary conditions of order 1 can be represented as a three-element Windkessel model, and how it is possible to obtain Windkessel parameters from the general pole-residue form by means of (4.8).

For higher order BCs, different approaches can be adopted for their implementation into CFD solvers. One approach is to transform the final model expression (4.22) into its equivalent circuit by means of a synthesis process. The most common techniques for equivalent circuit synthesis can be found in [79, 165].

An alternative approach consists in using directly the discretized differential equations obtained with VF as boundary conditions, without resorting to their equivalent circuit realization. Since the poles identified by VF could be either real or complex, the general transfer function (4.13) can be rewritten as

$$H(s) = c_0 + \sum_{i=1}^{n_r} \frac{c_{r_i}}{s - a_{r_i}} + \sum_{i=1}^{n_c} \left(\frac{c_{c_i}}{s - a_{c_i}} + \frac{c_{c_i}^*}{s - a_{c_i}^*} \right), \tag{4.47}$$

where the first sum includes the n_r real poles, with $a_{r_i}, c_{r_i} \in \mathbb{R}$, while the second sum includes n_c couples of complex conjugate poles, with $a_{c_i}, c_{c_i} \in \mathbb{C}$, and where the superscript * denotes the complex conjugate. Transforming (4.47) into a set of differential equations in state space form, we obtain

$$\begin{cases} \dot{x}_i(t) &= a_{r_i} x_i(t) + q(t) \\ p_r(t) &= \sum_{i=1}^{n_r} c_{r_i} x_i(t) \end{cases} \tag{4.48}$$

for the real poles, and

$$\begin{cases} \dot{x}'_i(t) &= \sigma_{c_i} x'_i(t) + \omega_{c_i} x''_i(t) + 2q(t) \\ \dot{x}''_i(t) &= -\omega_{c_i} x'_i(t) + \sigma_{c_i} x''_i(t) \\ p_c(t) &= \sum_{i=1}^{n_c} (c'_{c_i} x'_i(t) + c''_{c_i} x''_i(t)) \end{cases} \tag{4.49}$$

for the complex poles, where $c_{c_i} = c'_{c_i} + jc''_{c_i}$ and $a_{c_i} = \sigma_{c_i} + j\omega_{c_i}$. The states $x_i(t)$ at the k-th time step t_k can be computed by means of standard time discretization techniques, which are usually employed to discretized Navier-Stokes equations in solvers. In Nektar1D [92], for example, the Forward Euler method was used, so the real pole states were computed as

$$x_i(t_k) = x_i(t_{k-1}) + \Delta t \cdot [a_{r_i} x_i(t_{k-1}) + q(t_{k-1})]. \tag{4.50}$$

An equivalent relationship can be derived also for the states associated with complex poles, obtaining

$$\begin{cases} x'_i(t_k) &= x'_i(t_{k-1}) + \Delta t \cdot [\sigma_{c_i} x'_i(t_{k-1}) + \omega_{c_i} x''_i(t_{k-1}) + 2q(t_{k-1})] \\ x''_i(t_k) &= x''_i(t_{k-1}) + \Delta t \cdot [-\omega_{c_i} x'_i(t_{k-1}) + \sigma_{c_i} x''_i(t_{k-1})]. \end{cases} \tag{4.51}$$

Finally, the total pressure $p(t)$ can be computed as

$$p(t_k) = p_r(t_k) + p_c(t_k) + c_0 q(t_k). \tag{4.52}$$

Alternatively, since the proposed estimation method represents the model by means of a transfer function, this can be used directly into some solvers for the simulation of dynamical systems, like Simulink [166], which are also adopted in cardiovascular settings.

4.3 Numerical results

In this section, numerical results on the estimation of higher order boundary conditions with TDVF will be presented. In particular, after a general description of the experimental setup and of the Navier-Stokes solver adopted in Sec. 4.3.1, in Sec. 4.3.2 we evaluate the ability of the proposed method

to estimate the parameters of 3WK models, compared to two other methods presented in the literature. We also quantify the level of accuracy obtained when these models are used as boundary conditions in place of a more detailed vascular model. Then, in Sec. 4.3.3, we quantify the sensitivity to noise of the obtained estimates, and their validity under changes of the physiological state of the patient (Sec. 4.3.4). Lastly, in Sec. 4.3.5 we evaluate the accuracy and robustness of the proposed algorithm for the estimation of higher order models.

4.3.1 Experimental setup

The experiments presented in this section were conducted on a 1D arterial network representing the 55 largest arteries, as depicted on the left of Fig. 4.2. It is well known that one-dimensional models are able to provide a reasonable approximation of real blood flow in larger compliant arteries, as documented in [167, 58], with a significant reduction in the computational cost with respect to 3D fluid-structure interaction (FSI) simulations. The parameters characterizing each segment are reported in [92], and refer to a normotensive case. The inlet boundary condition used in the experiments represents a realistic inlet flow at the aortic root [92], while the outlet boundary conditions at each terminal vessel consist of 3WK models, whose parameters are detailed in [92].

The 55-artery model was simulated using the Nektar1D solver [92], which solves the nonlinear, one-dimensional blood flow equations in a given network of compliant vessels. Specifically, Nektar1D uses the method of characteristics and the discontinuous Galerkin numerical scheme [92] to solve numerically the system of equations. The solution provided by Nektar1D on the 55-artery network represents the reference solution for the model.

The 55-artery model was then reduced to a 21-artery model, containing only segments from the aorta up to the first generation of bifurcations, by substituting the remaining segments with lumped parameter boundary conditions. A representation of the reduced model is shown on the right of Fig. 4.2, where the boundary conditions are represented as 3WK models. The original network on the left was truncated at the end of segment 3 (brachiocephalic artery), 15 (left common carotid artery), 19 (left subclavian artery), 29 (celiac artery), 42 (left common iliac artery), and 43 (right common iliac artery). The parameters of

these lumped parameter terminations were estimated with the TDVF algorithm presented in Sec. 4.2. In particular, the estimation procedure can be summerized with the following steps:

- The 55-artery model was simulated using Nektar1D, providing the reference solution of the model.
- Pressure and flow waveforms at the truncation sites were extracted from the reference solution of the 55-artery model.
- For each truncation location, pressure and flow rate data were fed into the TDVF algorithm, which estimated simultaneously the parameters of the lumped boundary conditions, as explained in Section 4.2.
- The segments below the truncation site were removed and substituted with the estimated boundary conditions.
- The reduced 21-artery model obtained in this way was simulated using Nektar1D.

4.3.2 Estimation of Windkessel Boundary Conditions

The results obtained with TDVF for the estimation of 3WK parameters have been compared to those obtained with two other different methods proposed in the literature. The first method is the one presented in [159], and estimates 3WK parameters such that the net resistance and total compliance of the entire system are preserved. The second method is based on the solution of a non-convex minimization problem through the *fminsearch* algorithm in MATLAB, which employs the Nelder-Mead simplex algorithm [150] to find the minimum of a given function. In particular, the minimization problem is defined as

$$\min_{R_1,R_2,C,P_d} \left\| p(t) - R_1 q(t) + \frac{1}{C}\int_0^t e^{-\frac{1}{R_2 C}(t-\tau)} q(\tau) d\tau + \right. \\ \left. + \frac{P_d}{R_2 C}\int_0^t e^{-\frac{1}{R_2 C}(t-\tau)} \theta(\tau) d\tau \right\|^2 \quad (4.53)$$

Equation (4.53) can be derived by transforming back into time domain Equation (4.3), and expressing the input $q(t)$ and the Heaviside function $\theta(t)$ by means of recursive convolutions. A normalization of the four unknown parameters R_1, R_2, C and P_d, which were determined by means of *fminsearch*, was used to obtain a faster convergence of the algorithm.

Fig. 4.7 displays the obtained pressure waveforms at the truncation locations of the model, comparing the reference solution from the 55-artery model (black curve) to those from the reduced 21-artery model with 3WK parameters obtained with the technique presented in [159] (dashed blue curve), with *fminsearch* (dashed green curve), and with TDVF (red dots). The curves obtained with *fminsearch* and TDVF represent the best approximation of the original responses. The average and maximum errors for the pressure curves displayed in Fig. 4.7 are reported in Table 4.1: the results obtained with *fminsearch* and TDVF are comparable in terms of accuracy, and with average errors always lower than 1.1%, up to one order of magnitude smaller than the alternative method. The latter, in fact, does not provide an estimation of P_d, so the original value of 10 mmHg used in the 55-artery model was maintained for all outlets. This choice causes a visible offset of the obtained pressure curves with respect to the original curves, noticeable in Fig. 4.7, confirming the necessity to estimate P_d from measurements at each truncation point, instead of treating it as global parameter.

A comparison of the 3WK parameters obtained with the different methods at each truncated segment is reported in Table 4.2. Even if the *fminsearch* method is a valid solution for estimating Windkessel parameters, its extension to higher order models is problematic, as it would require an increasing number of parameters to estimate. More importantly, the user would need to choose a representation of the model to define a suitable cost function that will be minimized, as in (4.53). The use of the pole-residue representation, for example, would require to know the exact number of real and complex poles beforehand. It would be even more difficult to set a specific topology for the lumped circuit beforehand, just inspecting the model response.

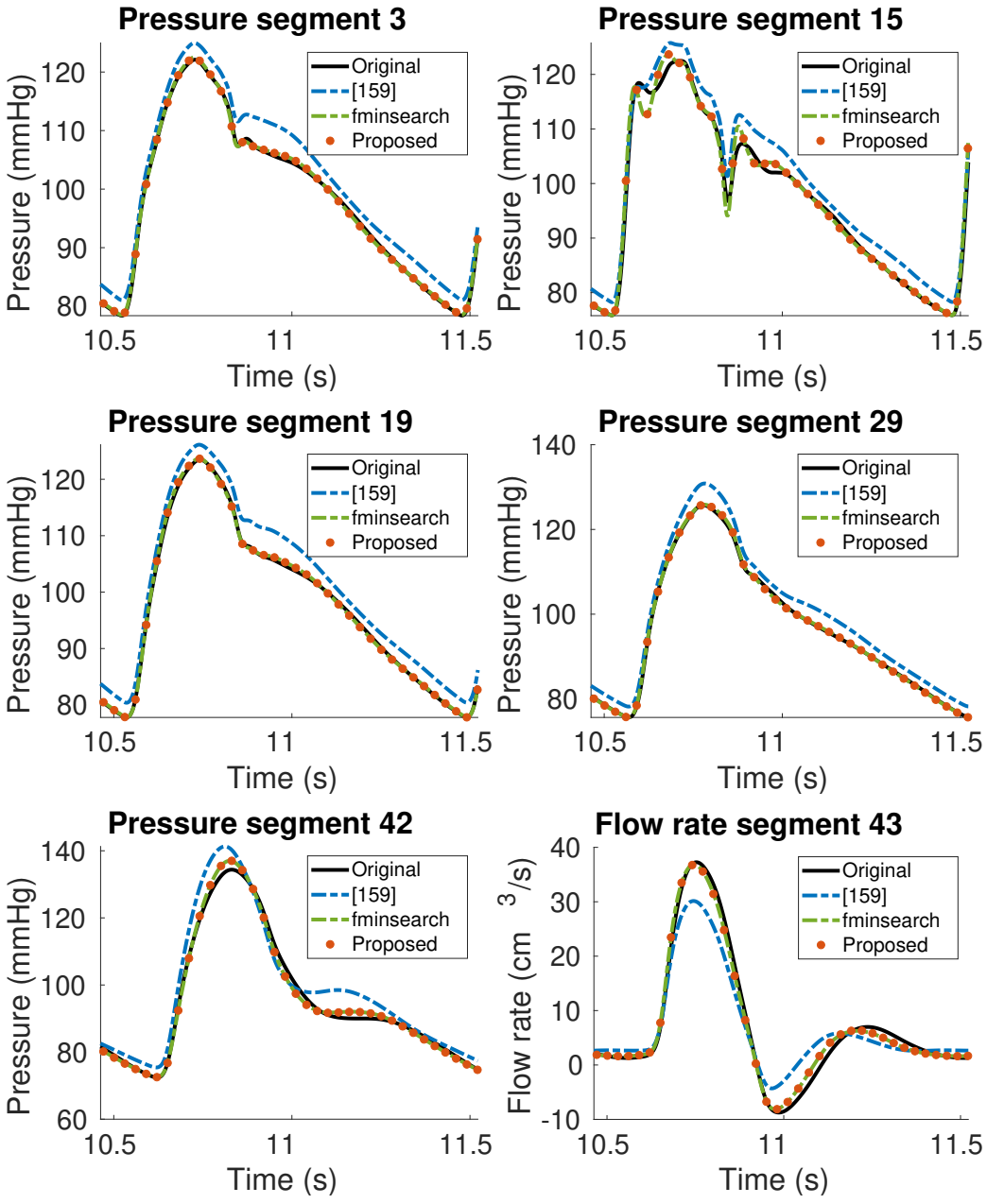

Fig. 4.7 Comparison of pressure and flow rate waveforms between original samples (solid black), reduction method from [159] (dashed blue), *fminsearch* method (dashed green), and proposed method (dashed red) for the three-element Windkessel boundary condition.

Table 4.1 Approximation errors for pressure curves at truncation locations, Windkessel case (Sec. 4.3.2).

Segment	Method	Max error (%)	Avg error (%)
3	[159]	5.1	3.08
	fminsearch	0.67	0.30
	Proposed	0.67	0.30
15	[159]	6.51	3.24
	fminsearch	4.40	0.89
	Proposed	4.30	0.88
19	[159]	4.85	3.15
	fminsearch	0.63	0.30
	Proposed	0.62	0.30
29	[159]	4.31	3.12
	fminsearch	0.77	0.25
	Proposed	0.76	0.26
42-43	[159]	9.16	4.2
	fminsearch	2.71	1.1
	Proposed	2.81	1.1

Table 4.2 Comparison of estimated Windkessel parameters at the outlets of the 21-artery model (Sec. 4.3.2).

Seg.	Method	R_1 (Pa s m^{-3})	R_2 (Pa s m^{-3})	C (m^3 Pa^{-1})	P_d (kPa)
3	[159]	$0.18{\cdot}10^8$	$9.26{\cdot}10^8$	$9.70{\cdot}10^{-10}$	1.33
	fminsearch	$0.27{\cdot}10^8$	$8.46{\cdot}10^8$	$10.5{\cdot}10^{-10}$	1.54
	Proposed	$0.26{\cdot}10^8$	$8.43{\cdot}10^8$	$10.5{\cdot}10^{-10}$	1.58
15	[159]	$3.60{\cdot}10^8$	$19.2{\cdot}10^8$	$1.14{\cdot}10^{-10}$	1.33
	fminsearch	$6.72{\cdot}10^8$	$14.2{\cdot}10^8$	$1.31{\cdot}10^{-10}$	1.58
	Proposed	$6.55{\cdot}10^8$	$14.2{\cdot}10^8$	$1.23{\cdot}10^{-10}$	1.64
19	[159]	$1.00{\cdot}10^8$	$17.0{\cdot}10^8$	$5.39{\cdot}10^{-10}$	1.33
	fminsearch	$0.67{\cdot}10^8$	$15.5{\cdot}10^8$	$6.17{\cdot}10^{-10}$	1.59
	Proposed	$0.67{\cdot}10^8$	$15.4{\cdot}10^8$	$6.13{\cdot}10^{-10}$	1.68
29	[159]	$1.62{\cdot}10^8$	$7.58{\cdot}10^8$	$3.06{\cdot}10^{-10}$	1.33
	fminsearch	$1.99{\cdot}10^8$	$6.90{\cdot}10^8$	$4.36{\cdot}10^{-10}$	1.41
	Proposed	$1.99{\cdot}10^8$	$6.91{\cdot}10^8$	$4.36{\cdot}10^{-10}$	1.41
42-43	[159]	$1.57{\cdot}10^8$	$14.8{\cdot}10^8$	$5.04{\cdot}10^{-10}$	1.33
	fminsearch	$0.98{\cdot}10^8$	$13.6{\cdot}10^8$	$6.11{\cdot}10^{-10}$	1.61
	Proposed	$0.97{\cdot}10^8$	$13.5{\cdot}10^8$	$6.06{\cdot}10^{-10}$	1.71

4.3.3 Sensitivity to noise

To investigate the robustness of the TDVF algorithm, both pressure and flow rate data were corrupted with zero-mean white Gaussian noise at different signal-to-noise ratio (SNR), defined as the ratio of signal power to the noise power. In particular, SNR ranged from 20 dB up to 100 dB, corresponding to a noise standard deviation ranging between 3.95 mmHg and $3.90 \cdot 10^{-4}$ mmHg for pressure and 1.18 cm^3/s and $1.15 \cdot 10^{-4}$ cm^3/s for flow rate, respectively. For each SNR level, we generated 50 different noise realizations to corrupt the data. Then, for each corrupted dataset the 3WK boundary conditions were estimated, both with TDVF and *fminsearch*. The results for this analysis are reported in Fig. 4.8, where the average of the absolute error between the pressure samples from the 55-artery network and the output of the Windkessel models are estimated at different SNR values. Moreover, at each SNR value, the bar indicates the standard deviation. Both techniques are able to estimate the correct boundary conditions starting from data samples with SNR ranging from 100 dB down to 40 dB, without any loss of accuracy. In both segment 3 and segment 19, at 30 dB and 20 dB, the estimated pressure is affected by an error less than 2.25% for TDVF, and less than 4% for *fminsearch*, with TDVF performing slightly better than *fminsearch*. These results verify the robustness of the TDVF estimation also in presence of noisy data, a condition more likely to occur when using patient-specific measurements instead of simulation results to drive the boundary conditions estimation.

4.3.4 Validity of Vector Fitting BCs in case of mental stress

In the previous section, boundary conditions were estimated from data coming from a simulation of the cardiovascular system in a normotensive case. However, under certain circumstances like physical exercise, or stressful situations, the cardiovascular system does not operate under normal conditions anymore, experiencing physiological changes in heart rate, maximum blood velocity and cardiac output. This can be modeled by properly changing the flow rate at the aortic root, which is the input imposed on the 55-artery model used in this chapter. It is interesting to verify if the boundary conditions estimated

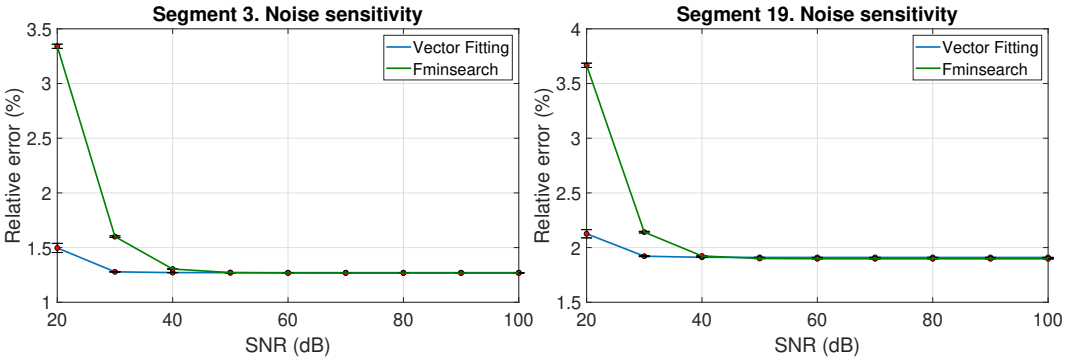

Fig. 4.8 Relative error between pressure samples obtained from the original 55-artery network and Windkessel models estimated from noisy data, with different SNR values. The Windkessel parameters were estimated with TDVF (blue curve) and *fminsearch* (green curve). Vertical bars in correspondence of the different SNR values indicate the standard deviation of the absolute error.

with a standard, normotensive input flow rate are still valid in presence of physiological changes of the system. In order to do so, we emulated a realistic variation of the input aortic flow rate under mental stress conditions by using the dataset presented in [160], which provides different aortic root flow rates corresponding to different levels of mental stress in a human subject. This translates into increased peak velocity and acceleration due to the increase in ejection fraction during stress [161]. An input flow with varying levels of mental stress was then generated and used as input for both the 55-artery model, chosen as a reference, and the 21-artery one. In the latter, the 3WK parameters previously estimated with TDVF in the normotensive case, and reported in Table 4.2, were used. Pressure waveforms at different points of the model are reported in Fig. 4.9, where the results in the reference 55-artery model (black line) are compared to those in the 21-artery model. The background colors in the left panel of Fig. 4.9 indicate the corresponding level of mental stress induced by the input aortic flow rate, varying from a relaxed state (light blue), to the baseline (purple), to medium (orange) and high (pink) levels of mental stress. The corresponding heart rate and cardiac output associated to each stress level can be found in [160]. From Fig. 4.9 it is possible to see that the reduced model is able to closely follow the changes caused by the varying input flow, with average relative errors smaller than 0.7% for both segments. The results confirm that the estimated boundary conditions are valid also in the case of a physiological change of the input flow rate.

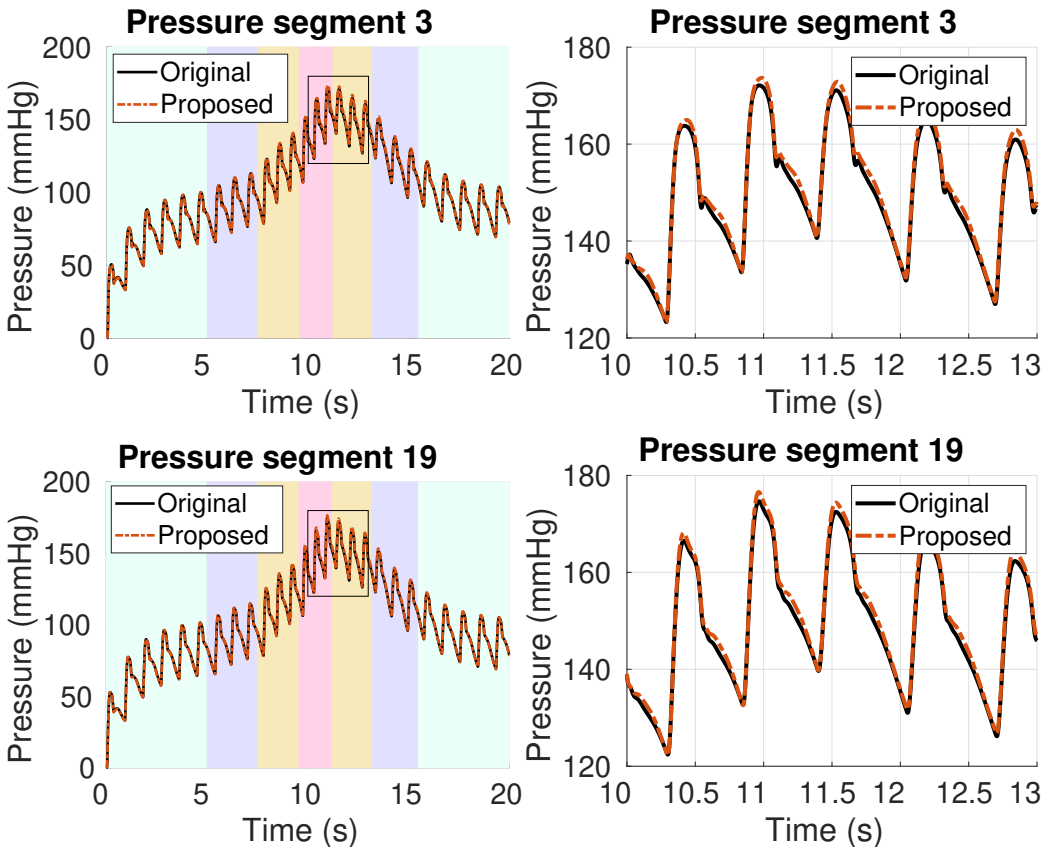

Fig. 4.9 Pressure waveforms at segment 3 (top) and 19 (bottom) for the case of mental stress. Background color indicates the level of stress: relaxation (light blue), baseline (purple), medium stress (orange), high stress (pink). The plots on the right zoom on the black rectangle displayed on the plots on the left.

4.3.5 Higher-order boundary conditions

In this section, we tested the use of TDVF for the estimation of higher order boundary conditions and we investigated their accuracy compared to standard 3WK models. The same experimental setup presented in Section 4.3.1, consisting of the reference 55-artery model and the reduced 21-artery model, was adopted. In Fig. 4.10, we first compared the reference pressure from the 55-artery model used for the estimation (blue line), to the pressure estimated by the TDVF model (dashed red line), for the same flow rate coming from the 55-artery model. The results reported in Fig. 4.10 refer to the pressure in segment 19 fitted with models of order up to 8 (comparable results were obtained for the other segments). It is clear from Fig. 4.10 that accuracy greatly improves by increasing the model order. The right panel on the third line of Fig. 4.10 shows the average relative error on pressure versus model order, suggesting a decrease of around one order of magnitude going from order 1 to order 8.

We then used the estimated models as boundary conditions for the reduced 21-artery model, simulated with Nektar1D. This step required a modification of the solver to accept boundary conditions defined as in Section 4.2.2. Pressure and flow rate curves up to order 4 at the truncated segments are displayed in Fig. 4.10, while the relative errors on pressure and flow rate waveforms up to order 8 are reported in Table 4.3 and Table 4.5 (average error), and in Table 4.4 and Table 4.6 (maximum error).

Both plots and numerical results reveal that higher order boundary conditions can model pressure and flow rate more accurately than a simple Windkessel (corresponding to order 1). In particular, a significant improvement can be seen between order 1 and order 2, where average errors can decrease up to one order of magnitude with respect to BCs of order 1. A slight improvement in accuracy can also be noticed between order 2 and order 4, while orders above 4 do not seem to provide an improvement in terms of accuracy. Segment 15 is the only case which does not seem to benefit from higher order boundary conditions, with the error remaining nearly constant for both pressure and flow rate, even for higher orders. Looking at the corresponding plots in Fig. 4.10, it can be noticed that the curves obtained after the truncation are qualitatively different from the original pressure and flow in 55-artery model (black curve). A possible

Table 4.3 Average relative errors (%) on pressure at truncation locations, higher order models case (Sec. 4.3.5)

Segment	Average relative error (%)				
	Order 1	Order 2	Order 4	Order 6	Order 8
3	0.30	0.12	0.078	0.084	0.079
15	0.88	0.75	0.65	0.67	0.67
19	0.30	0.1	0.069	0.079	0.068
29	0.26	0.15	0.11	0.093	0.079
42-43	1.1	0.36	0.31	0.23	0.21

Table 4.4 Maximum relative errors (%) on pressure at truncation locations, higher order models case (Sec. 4.3.5)

Segment	Maximum relative error (%)				
	Order 1	Order 2	Order 4	Order 6	Order 8
3	0.67	0.59	0.46	0.53	0.51
15	4.30	4.79	5.16	5.01	4.80
19	0.62	0.44	0.33	0.34	0.35
29	0.76	0.61	0.44	0.41	0.42
42-43	2.81	1.33	1.17	1.07	0.94

cause could be the higher wall viscosity of segment 15 with respect to the other terminal segments, which could increase the presence of nonlinear effects, hard to model with a linear boundary condition. However, no conclusive explanation was reached.

Table 4.5 Average relative errors (%) on flow rate at truncation locations, higher order models case (Sec. 4.3.5)

Segment	Average relative error (%)				
	Order 1	Order 2	Order 4	Order 6	Order 8
3	3.14	3.63	1.80	1.70	1.60
15	1.90	2.1	2.0	1.94	1.90
19	3.41	1.67	1.0	0.95	0.84
29	0.8	0.37	0.21	0.19	0.17
42-43	2.5	1.07	0.97	0.61	0.58

Table 4.6 Maximum relative errors (%) on flow rate at truncation locations, higher order models case (Sec. 4.3.5)

Segment	Maximum relative error (%)				
	Order 1	Order 2	Order 4	Order 6	Order 8
3	12.05	14.67	10.96	11.83	10.80
15	13.71	15.61	16.47	16.12	15.61
19	15.03	6.53	4.29	3.46	3.58
29	4.45	1.22	0.92	0.98	0.88
42-43	6.06	2.22	1.89	1.54	1.40

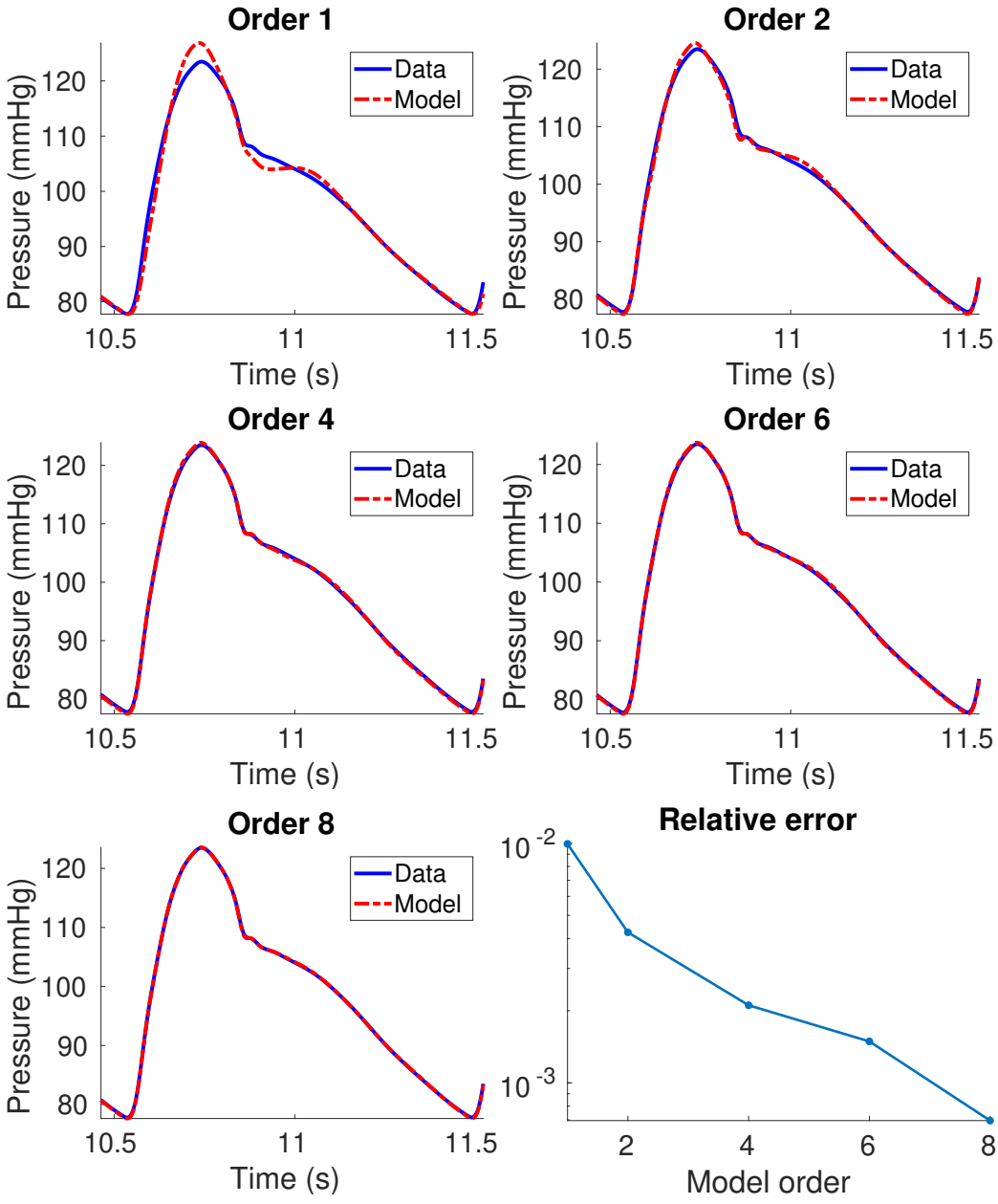

Fig. 4.10 Comparison of pressure waveform in segment 19 (blue curve) against models with different order obtained with Vector Fitting. In the last plot (third row, right panel) relative error on pressure vs model order.

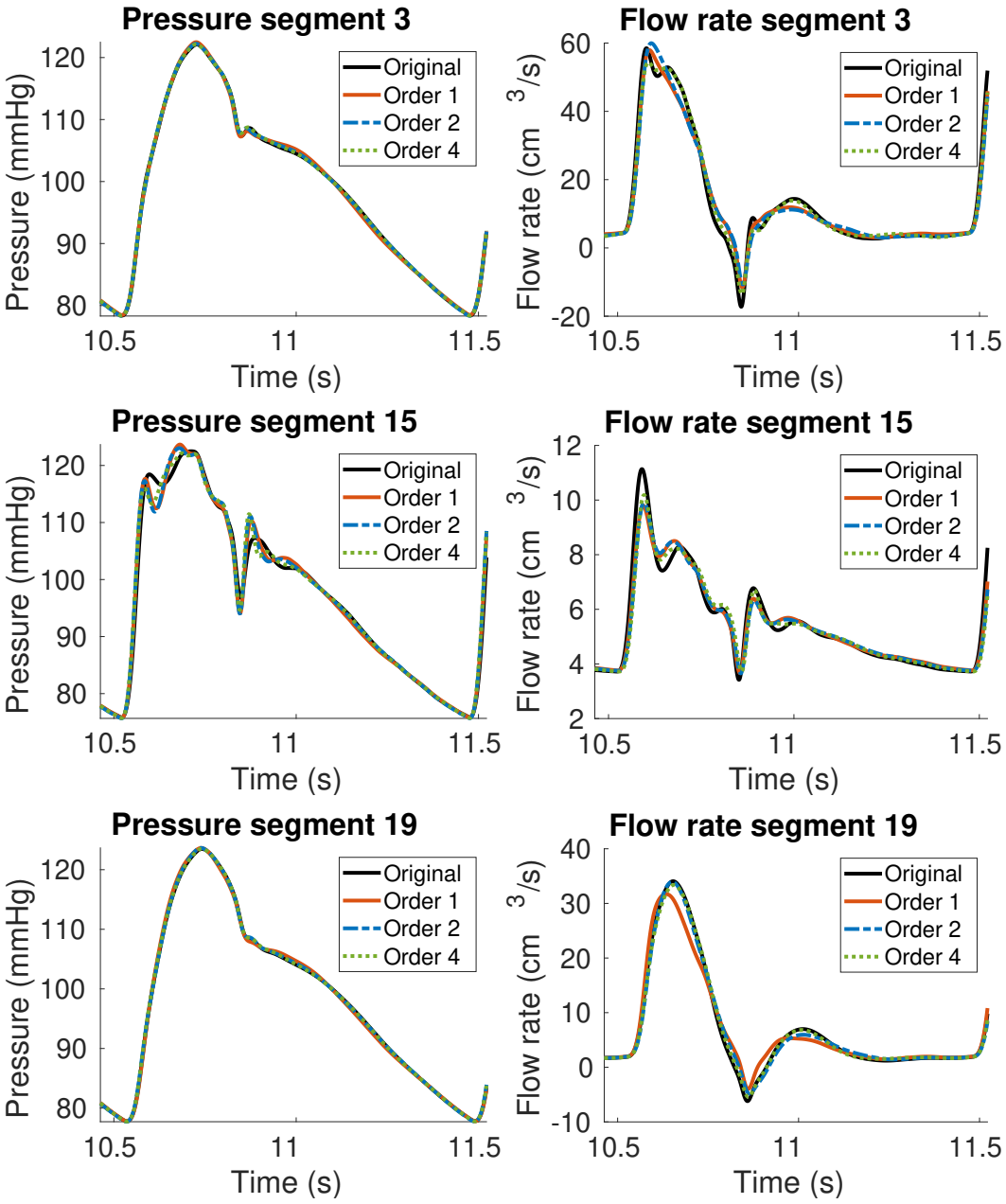
Pressure segment 3
Pressure (mmHg)
Time (s)
Flow rate segment 3
Flow rate (cm 3/s)
Time (s)
Pressure segment 15
Pressure (mmHg)
Time (s)
Flow rate segment 15
Flow rate (cm 3/s)
Time (s)
Pressure segment 19
Pressure (mmHg)
Time (s)
Flow rate segment 19
Flow rate (cm 3/s)
Time (s)
Original
Order 1
Order 2
Order 4

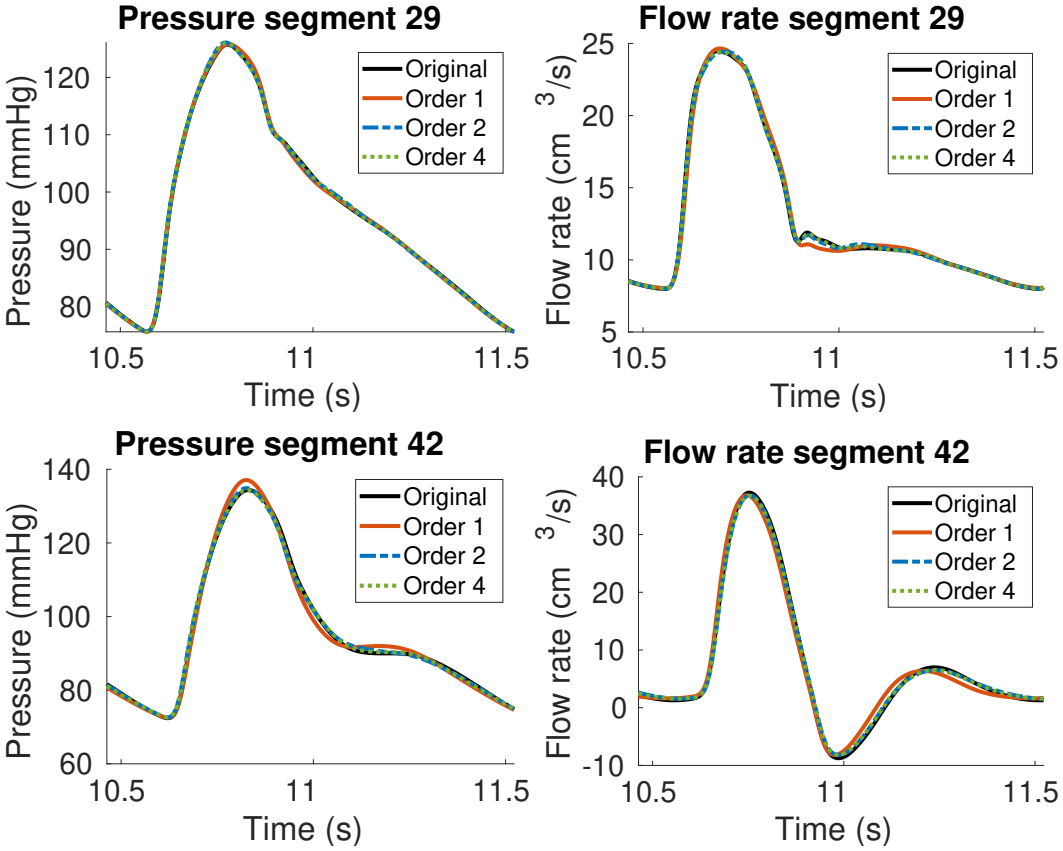

Fig. 4.10 Comparison of pressure and flow waveforms in the 55-artery model (solid black curve) and in the 21-artery one with boundary conditions of different orders, estimated with Vector Fitting.

4.4 Discussion

The results presented in Section 4.3 show the capabilities of Time-Domain Vector Fitting in estimating accurate lumped boundary conditions of arbitrary order. When used to estimate BCs of order one, which were synthesized as three-element Windkessel circuits, TDVF was able to accurately determine optimal values for the Windkessel parameters. Moreover, the results were further validated in presence of noise in the measurements, where TDVF provided accurate results with noise up to 20dB, and under physiological changes of pressure and flow rates induced by changing levels of mental stress. For BCs of order 1, the results obtained with Vector Fitting were comparable to, and sometimes better than those attained from two other estimation methods presented in the literature. The comparison was not possible for higher order BCs, since Vector Fitting was the only method capable of estimating them.

Apart from the accuracy, the main advantage of the proposed approach is the ability to estimate an increasing number of parameters simultaneously and automatically. The proposed model parametrization based on the use of transfer functions, in fact, can be used to describe any linear dynamical system, allowing a generalization of the BC model to differential relations of arbitrary order. The alternative solutions for higher order BCs proposed in the literature, instead, resort to specific circuit topologies, from which a generalization is difficult to obtain. Thanks to the aforementioned properties of the TDVF method, it was possible to formulate and estimate systematically boundary conditions of increasing order. For the case under analysis, consisting of a 55-artery model reduced to a 21-artery one, boundary conditions with order up to 8 were estimated and compared, in order to assess the effect that the BC model order has on its ability to accurately approximate the downstream vasculature. Results showed that an order of 2 provides a significant increase in accuracy with respect to BCs of order 1, the most common choice up to now in the form of Windkessel models. Orders above 4, instead, provided negligible improvements in terms of accuracy in the model of the systemic arterial system considered.

4.4.1 Limitations

The main limitation of the proposed approach is the fact that it requires time samples of both pressure and flow rate at the truncation location for the estimation of boundary conditions. This could be a limitation when pressure and flow rate measurements are not available simultaneously at the same location. However, pressure and flow rate data are available when moving from a large model to one including a smaller portion of the cardiovascular system, like in the application considered in this paper. When moving to patient-specific models, both pressure and flow rate measurements can be obtained by means of *in vivo* procedures and imaging techniques. In case pressure data are not available, pressure waveform generators can be used, which, given some patient-specific parameters (like brachial diastolic and systolic pressure) can generate realistic pressure waveforms [168, 169].

In this chapter, the Vector Fitting method has been tested only on 1D models of the cardiovascular system, but in the future it could be extended to three-dimensional models. In such a scenario, a 1D model of the cardiovascular system could still be employed to estimate the outlet boundary conditions, or, if available, patient-specific pressure and flow-rate measurements could be used.

4.5 Conclusion

In this chapter, we proposed a new automated method based on the Time-Domain Vector Fitting algorithm for the parameter estimation of lumped boundary conditions. Starting from pressure and flow rate samples, this method can estimate boundary conditions corresponding to differential equations of increasing order. First, the TDVF algorithm was used to automatically estimate 3WK boundary conditions, starting from a 1D model comprising the 55 main arteries of the human arterial system. The robustness of the estimation procedure was verified in presence of noisy data, with up to 20 dB of signal-to-noise ratio, and in presence of physiological changes of pressure and flow rate induced by high levels of mental stress. Second, we proposed a generalization of the 3WK model to obtain boundary conditions of arbitrary order. We estimated higher order boundary conditions with TDVF, and we

investigated the improvement in accuracy they provide with respect to the 3WK model. On the 55-artery model, experimental results showed that boundary conditions up to order 4 are able to model the downstream pressure and flow rate more accurately than the Windkessel model, while orders above 4 provided negligible improvements in term of accuracy.

Chapter 5

A numerical investigation of Murray's minimum energy principle

5.1 Introduction

In previous chapters we saw how the availability of in-vivo information about pressure and flow rate greatly facilitates the estimation of boundary conditions. However, in many cases this information is only partially available, or insufficient, or in some cases not available at all. In this chapter, we investigate a different criterion to estimate boundary conditions, which tries to rely only on *physics and anatomy*. Ideally, we would like to find a criterion that, in absence of in-vivo measurements, can derive boundary conditions based solely on physics and the anatomy, or, in case of incomplete measurements, that can be combined with in-vivo measurements to provide additional information, and improve the estimation of boundary conditions. The integration of this criterion and in-vivo information could be, for example, performed in an optimization framework like the one introduced in Chapter 3. In this chapter, in particular, we investigate the minimum energy principle as a possible criterion for inlet flow estimation. The minimum energy principle is at the basis of a number of laws and principles in hemodynamics, among which Murray's law is probably the most famous. From Murray's principle, one can derive flow splitting relations that are used

to estimate boundary conditions when in-vivo information is not available. However, Murray's law makes a number of assumptions, such as that vessels are straight, circular, and with Poiseuille's flow. For this reason, in this chapter we investigate if this minimum energy principle can be exploited numerically also for general, three-dimensional anatomies, paving the way for a possible future reuse of this generalized principle in boundary condition estimation. In particular, we propose a framework for the numerical investigation of the minimum energy principle behind Murray's law in patient-specific anatomies. An overview of Murray's law is given in Section 5.2, while a further discussion on the minimum energy principle is provided in Section 5.3. Section 5.4 presents the proposed numerical framework, together with an analysis of the challenges and open questions encountered during its development. Numerical results are presented in Section 5.5, while Section 5.6 contains the final remarks and conclusions for this chapter.

5.2 Murray's principle: linking form and function

As many other physiological and natural systems, the cardiovascular system is the result of a balance between form and function. When it comes to the cardiovascular system, its *form* refers to the anatomy of the vessels, while its *function* refers to the dynamics of blood flowing through such vessels. It is reasonable to say that the correct functioning of the cardiovascular system depends on both form and function, as well as on the effect that one has on the other. As a matter of fact, the anatomy of the heart, arteries and veins is clearly dictated by their primary function, which is the transport of nutrients and oxygen-rich blood to all parts of the body. On the other side, any anatomical modification to any part of the system will inevitably impact its functionality, as it happens in presence of many cardiovascular diseases, from the coarctation of the aorta [170] to the tetralogy of Fallot [171]. Since the cardiovascular system is governed by the interplay between its form and function, it has been theorized that evolution has brought to an optimization of the cardiovascular system in terms of these two factors. In particular, an interpretation of the cardiovascular system in these terms was provided in 1926 by the physiologist

Cecil Murray, who described the relationship between the flow rate in a vessel and its radius by means of the well known *Murray's law*. Murray hypothesized that, being subjected to natural selection through evolution, the cardiovascular system has achieved an optimal arrangement such that, in every vessel, blood flows with the least possible biological work [50]. He then supposed that the power required to sustain circulation is made up of two terms:

- the power P_f required to drive the flow, overcoming viscous drag,
- the power P_m required to metabolically maintain blood, called by Murray the *cost of blood*, which includes a number of different factors, such as the metabolism of blood itself, the cost of maintenance of all its constituents, like hemoglobin, and the cost placed on the body by the weight of blood itself [50].

The power required to drive the flow (P_f) decreases with the vessel radius, while the metabolic power (P_m) increases with the vessel radius. For this reason, if the total power

$$P_t = P_f + P_m \tag{5.1}$$

must be minimized, the radius can be neither too large nor too small.

Considering a straight cylindrical vessel, in which the flow is assumed to be laminar and described by Poiseuille's law, and assuming blood to be Newtonian, the power P_f for blood transport can be expressed as [50]

$$P_f = Q \cdot \Delta p = \frac{Q^2 l 8 \mu}{\pi r^4}, \tag{5.2}$$

where Q is the flow rate, Δp is the pressure drop across the vessel, l the vessel length, μ the dynamic viscosity of the fluid and r the vessel radius. On the other side, the metabolic power (called by Murray the *cost of blood* [50]), accounting for all those processes related to the maintenance of blood, is directly proportional to its volume as

$$P_m = bV = bl\pi r^2, \tag{5.3}$$

where V is the volume of a cylindrical vessel and b is the so called *metabolic constant*, defined by Murray as a dimensional parameter representing the cost

of blood per unit volume [50]. The total power P_t can then be expressed as

$$P_t = P_f + P_m = \frac{Q^2 l 8\mu}{\pi r^4} + bl\pi r^2 \tag{5.4}$$

From (5.4), we see that the total power consists of a first term inversely proportional to r^4, and a second term directly proportional to r^2. In order to find the minimum power required for blood flow, (5.4) can be differentiated with respect to r and equated to 0, obtaining

$$\frac{dP_t}{dr} = -\frac{4Q^2 l 8\mu}{\pi r^5} + 2bl\pi r = 0 \tag{5.5}$$

Rearranging (5.5), the following relationship is derived

$$Q = \sqrt{\frac{b\pi^2}{16\mu}} r^3. \tag{5.6}$$

Equation (5.6) describes the optimal relation between flow rate and radius in a vessel, such that power is minimal. This means that, assuming that the cardiovascular system is operating at maximum efficiency, an estimate of blood flow rate in a vessel can be obtained, provided that we know the vessel radius, the blood viscosity and the metabolic constant. Applying the conservation of mass at a branching point, the following law can be derived [172]

$$r_0^3 = \sum_{i=1}^{N} r_i^3, \tag{5.7}$$

where r_0 is the radius of the parent vessel, and r_i is the radius of the i-th daughter vessel (of N total daughter vessels). This principle is commonly referred to as *Murray's law*, and it is often used as a rule of thumb to predict the radii of branches in transport networks. From (5.7), it is possible to derive a general principle describing how flow rate splits among the branches of a vessel. At the outlet i, the flow rate Q_i can be computed as

$$Q_i = \frac{r_i^3}{\sum_{i=1}^{N} r_i^3} \cdot \sum_{i=1}^{N} Q_i. \tag{5.8}$$

In this form, often referred to as the outflow splitting method, Murray's law is used to set the outflow boundary conditions in a branching anatomy [173]. Murray's law has been observed and validated in many biological systems, such as the vascular and respiratory systems of animals [174–176], and the leaf veins of plants [177–179].

In summary, we refer to *Murray's principle* as the assumption that the cardiovascular system is overall optimized from an energetic point of view, meaning that the power required for blood flow, which Murray computed as in (5.4), is minimum. With *Murray's law*, instead, we refer to the relationship between blood flow and radius in a vessel, which is a consequence of Murray's principle, and takes the form of (5.6). Similarly, (5.7) and (5.8) are analytical laws derived from Murray's principle, which are used, respectively, to compute the radii of branching vessels, and to set their outflow boundary conditions.

Over the last few decades the validity, consequences, and limitations of Murray's law have been extensively studied. In 1977, Zamir verified experimentally Murray's cube law in the human body, suggesting that shear force could be the mechanism regulating vessels' radii [180]. In 1981, Sherman noticed that only the largest arteries and veins in the human body, where blood flow can be turbulent, do not follow Murray's law [172]. In 2004, Guo et al. suggested that radii in vessels could be regulated by growth and remodeling processes, which bring stress and strain to specific values, in order to restore an existing homeostatic state [181].

In its original formulation, Murray's law is based on some strong assumptions, such as that the flow is laminar, and that the vessels are straight and circular. Some works have tried to remove these limitations, by formulating more general analytical laws that would take additional features into account. In [182], for example, a contribution for the energy required to support smooth muscle tone was added to the viscous and metabolic contributions already considered by Murray. In [183], Murray's law was extended to pulsatile flow, while in [184] the effect of nonlinear elastic materials was included. A generalized law for asymmetric branching was proposed in [185], which was validated also in presence of turbulent flow. Another extension was presented in [186], with the goal of also obtaining an optimal wall shear stress distribution. Finally, Guer-

ciotti et al. proposed an extension of Murray's law to provide the flow split at bifurcations in case of stenotic vessels and non-Newtonian blood rheology [187].

In summary, Murray's law is still largely used and studied today, and several generalizations have been proposed. However, these extensions and generalizations refer to analytical cases, leaving two questions unanswered:

- in real, three-dimensional anatomies, and assuming blood flow is described by the Navier-Stokes equations, is there still a single minimum energy point?
- If the minimum energy point exists, can it be found numerically? Given the numerical challenges of solving the Navier-Stokes equations in a real anatomy, and assuming that the minimum point exists, the energy curves may be noisy and non-smooth, preventing a reliable identification. Furthermore, since the minimum point depends on the anatomy, it is necessary to smoothly deform the latter by changing the radius of the vessels. This is a non-trivial operation, so a related question is whether a reliable method exists to continuously deform complex, three-dimensional anatomies.
- If the minimum point can be identified numerically, can it be used to estimate the flow rate in a vessel which is not straight or circular, assuming that the given anatomy was energetically optimal, and using Murray's principle to determine the flow rate?

The next sections will analyze more in detail these open research questions, later describing the numerical framework proposed for their investigation.

5.3 A numerical investigation of Murray's minimum energy principle

As explained in the previous section, according to Murray's minimum energy principle the radius of a vessel is the result of an optimization process, whose aim is to balance two energetic contributions - the one coming from viscous forces, and the one due to metabolic processes. The goal, then, is to investigate

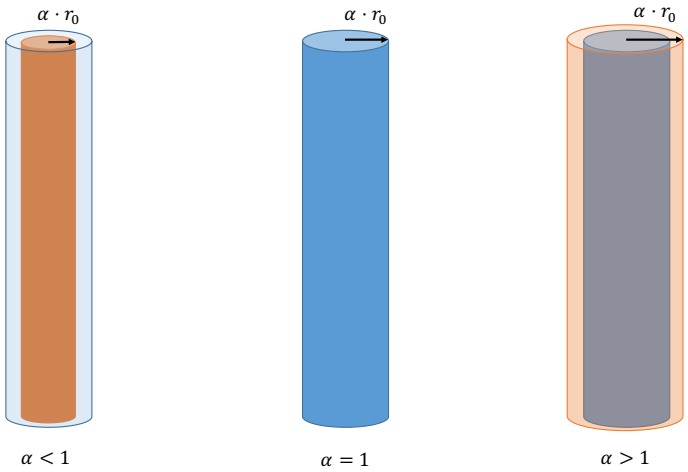

Fig. 5.1 Cylindrical vessel with radius defined as $\alpha \cdot r_0$. The cylinder in the middle has $\alpha = 1$, the one on the left has $\alpha < 1$ (deflation), while the one of the right has $\alpha > 1$ (inflation).

if such minimum energy point exists, even in patient specific anatomies and, if that is the case, if it is possible to identify it numerically.

To study how the total power required to sustain blood flow in a vessel changes with respect to its radius, we start by analyzing a straight vessel. For convenience, we indicate its radius as $r = \alpha \cdot r_0$, with $\alpha \in \mathbb{R}$. The coefficient α can be seen as an inflation/deflation factor: for $\alpha = 1$ we will get the original anatomy, while for $\alpha \neq 1$ we will get a re-scaled version in the radial direction. A graphical representation of the parameter α on a cylindrical vessel is displayed in Fig. 5.1.

Defining the total power as the sum of a viscous contribution and a metabolic one, it is intuitive to assume that, since $r = \alpha \cdot r_0$, the dependency of the total power P_t from α, $P_t(\alpha)$, will be the same as its dependency from the radius, $P_t(r)$. If α increases, in fact, the metabolic contribution will increase, while a decrease in α will cause an increase of the viscous effects. In analytical form this translates into

$$P_t = \frac{8Q^2 l\mu}{\pi\alpha^4 r^4} + bl\pi\alpha^2 r^2, \tag{5.9}$$

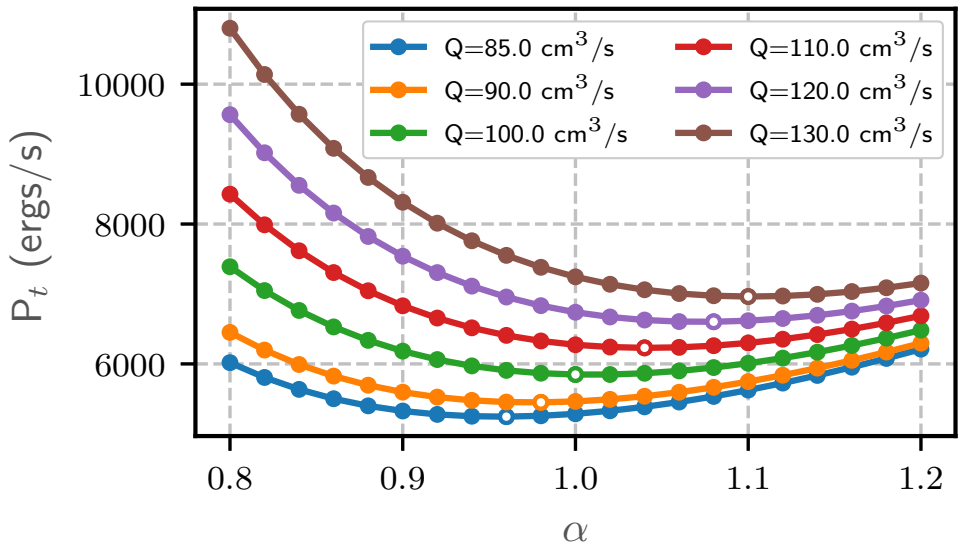

Fig. 5.2 Plot of total power P_t vs α for a straight vessel with a radius equal to 2 cm, and b= 10.14 ergs/cm^{3}s. The flow rate Q ranges from 85 to 130 cm^3/s. The white dots indicate the minimum point of each curve.

meaning that the total power P_t will depend both on Q and α. A plot of the variation of P_t with respect to α and Q according to (5.9) is reported in Fig. 5.2.

While on an ideal anatomy, such as the cylindrical vessel considered until now, it is possible to analytically validate Murray's principle and identify the minimum energy point from $P_t(\alpha, Q)$, this may not be necessarily the case for realistic anatomies, which may have a non-circular cross section, bendings, and non-laminar flows.

This investigation is motivated by the possible applications that, if properly validated, the minimum energy principle could lead to. In particular, looking at the curves plotted in Fig. 5.2, it is interesting to notice that for each flow rate Q there is only one minimum energy point, and that for each value of α there is only one curve at its minimum. This fact can in principle lead to an interesting approach for the estimation of boundary conditions. Imagine, in fact, that we are given a patient-specific anatomy and we want to find its inlet flow rate Q, which we don't know. We can assume that the given anatomy is optimal (which will correspond to $\alpha = 1$), according to Murray's principle, thus

$$\left.\frac{\partial P_t}{\partial \alpha}\right|_{\alpha=1} = 0. \tag{5.10}$$

Equation (5.10) could be in principle used to get an estimate of the unknown flow rate Q, which will be the only one for which the minimum of P_t occurs exactly at $\alpha = 1$. Looking at Fig. 5.2 it can be noticed how there is only one value of Q satisfying this condition, meaning that there is only one flow rate optimizing the anatomy from an energetic point of view. For this type of application, however, it is necessary to verify that the minimum exists, and that it is identifiable numerically. To the best of our knowledge, this type of numerical investigation has never been conducted, thus representing a further step in unveiling the energetic behavior of the human cardiovascular system. Such a framework would allow us to analyze the energetic behavior of some particular patient-specific anatomies where the many assumptions behind Murray's law do not hold. These include anatomies with curved vessels, non-circular cross sections, bifurcations and pulsatile, non-laminar blood flow.

5.3.1 Related works

Some previous works have tried to leverage the minimum energy principle for various applications, such as estimating boundary conditions, determining the degree of stenosis in occluded arteries, and optimizing geometrical parameters. In [188], for example, a method to estimate outflow pressure based on minimum energy loss at a bifurcation was proposed. By formulating an analytical expression for mechanical energy loss in a bifurcating artery, the optimal ratio between outlet flow rates in the daughter branches was obtained, and verified on a real carotid bifurcation. Similarly, in [189], minimum energy loss was used to set outlet boundary conditions on a carotid bifurcation with a stenosis. Even if for stenotic vessels Murray's law may not necessarily be valid anymore, the work in [189] started from the assumption that in a bifurcation there is only one flow split requiring minimum energy. The method was validated against patient specific flow and stenosis measurements in carotid arteries. A further development was presented in [190], where the principle of minimum energy loss was used to estimate stenosis severity in carotid arteries. Arguing that larger plaques cause higher energy loss, the authors used the deviation from minimum energy principle to estimate the grade of arterial stenosis. On a different note, in [191] Marsden et al. proposed a computational framework for derivative free optimization, which they tested on an ideal bifurcation, estimating the optimal

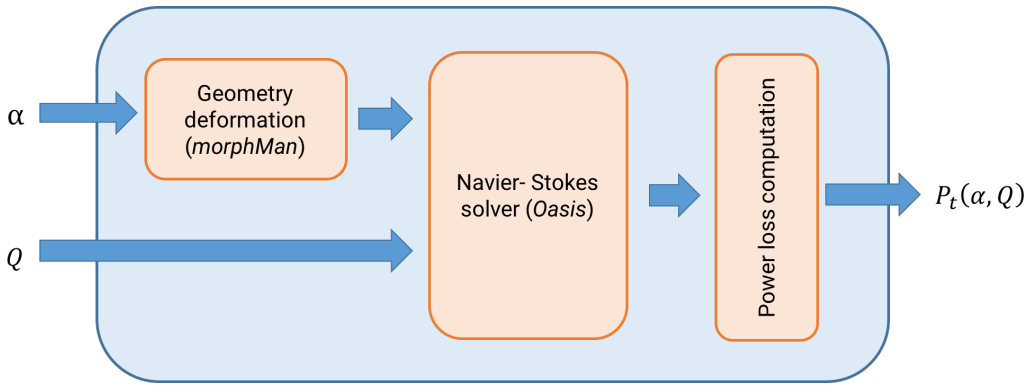

Fig. 5.3 Scheme of the proposed numerical framework.

radius and bifurcating angle while minimizing the total energy, as postulated by Murray in [50].

5.4 The proposed numerical framework

To investigate Murray's principle on real anatomies, a numerical framework must be devised to construct the curves reported in Fig. 5.2 starting from (5.1) for a general 3D anatomy, obtained from the reconstruction from medical images. Such curves are constructed in an iterative way: for a fixed flow rate Q, the value of α is changed and the total power P_t computed for each anatomy. This step is repeated for different values of Q. For a given anatomy, this process requires the following steps, which are represented schematically in Fig. 5.3:

- A certain flow rate Q is selected;
- The anatomy is morphologically manipulated to change the value of α;
- Using a CFD solver, Navier-Stokes equations are solved on the deformed geometry;
- From the solver solution, the total power P_t is computed.

These steps are repeated for different values of α and Q.

The approach proposed here to verify the existence of a minimum energy point relies on two main operations, which individually present their own set of challenges:

- modifying the real anatomy by changing the factor α, through a manipulation of the original geometry. The deformation of the anatomy must be smooth, robust, and produce accurate results on anatomies reconstructed by clinical images, which are generally less smooth than synthetic geometries;

- computing the total power P_t from the solution of the Navier-Stokes equations. The computation of P_t must be accurate enough to allow the reconstruction of the power curves for different inlet flow rates, and the curves must be smooth enough to allow the identification of their minimum point.

In the following, we will address these two main points and analyze the open questions and problems that each of them raised.

Morphological manipulation of the anatomy: morphMan

The morphological manipulation step is necessary to obtain anatomies with $\alpha \neq 1$. Starting from a patient-specific anatomy of the region of interest, the objective is to deform it according to the specific value of the parameter α. To this end, the open source framework *morphMan* [192], which allows to alter morphological features parametrically on patient-specific geometries, was employed and modified to meet our needs.

The *morphMan* framework performs the manipulation of anatomies by using the Voronoi diagram and its associated centerlines, as first suggested in [193] in relation to the Vascular Modeling Toolkit *vmtk*. A representation of the centerline and Voronoi diagram of an anatomy is reported in Fig. 5.4.

In short, the Voronoi diagram is a point cloud with associated radii corresponding to the radius of the minimal inscribed sphere of each point, and it can be used as an alternative representation of a surface by a union of spheres. By enveloping the union of spheres, the diagram can be converted back to the original surface. Exploiting this, the *morphMan* framework converts the surface into its Voronoi diagram, performs the alterations to the diagram, and then envelops it back to a surface [194]. In particular, *morphMan* can be used for altering the cross-sectional area of a vessel, by first measuring the area along

Fig. 5.4 On the left, a patient-specific aortic arch with the corresponding centerline. On the right, the same anatomy with the corresponding Voronoi diagram, where the colour represents the value of the inscribed sphere radius.

the region of interest and defining a variable F to control the cross-sectional area. By looping over each point in the Voronoi diagram, the distance to the centerline and the radius are changed by a factor F_j. The obtained Voronoi diagram is then transformed back to a regular surface [194].

A minor modification of the pre-existing framework allowed us to modify the entire vasculature by a constant factor α. In this case, then, the factor F_j is fixed and equal to α across the entire centerline. The Voronoi diagram was modified maintaining the approach presented in [194], where each point p_i in the Voronoi diagram is associated to its closest centerline point c_j. The vector $v_{ij} = p_i - c_j$ is defined, and the point p_i is moved by $v_{ij}(F_j - 1)$. The new radius of the associated minimal inscribed sphere radius will be $r_i^{new} = r_i^{old} F_j$. A visualization of this operation is represented in Fig. 5.5.

An example of the geometries obtained by modifying α is reported in Fig. 5.6, where a patient-specific aortic arch has been deformed with *morphMan*.

The power loss computation: control volume vs viscous dissipation

The idea of a numerical investigation of the minimum energy principle relies on the possibility of computing numerically the power loss of a fluid flowing into a vessel. The most common approach used in the literature to compute power loss is the so called control volume approach, which computes the net power absorbed by the structure from all the inlets/outlets. In this sense, power loss

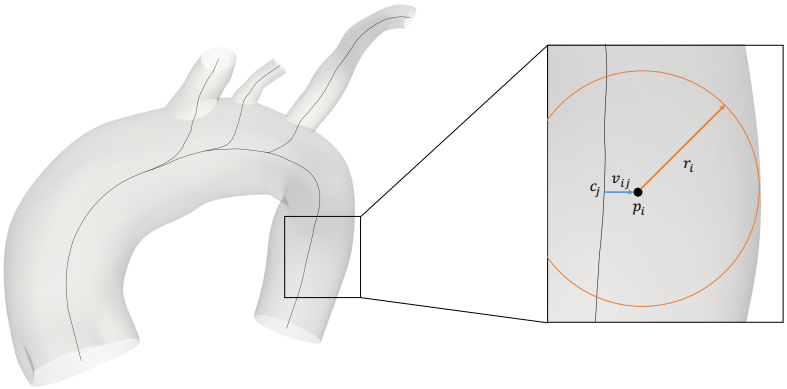

Fig. 5.5 Representation of the operation performed by *morphMan* for altering the cross-sectional area. The image refers to a point p_i, with the corresponding inscribed radius r_i. The vector v_{ij} represents the distance to the closest centerline point c_j.

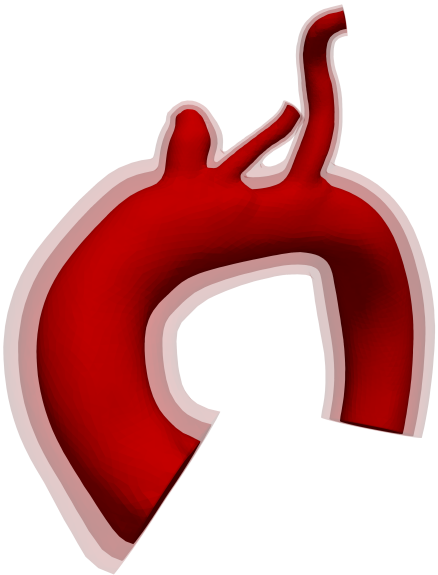

Fig. 5.6 Representation of a set of manipulated anatomies obtained with the *morphMan* package, where the inflation factor α was changed from 0.75 to 1.2.

can be expressed as

$$P_{diss} = -\sum_{i=1}^{N_{in}} \int_{\Gamma_i} (p + \frac{1}{2}\rho v^2)\mathbf{v} \cdot d\Gamma - \sum_{i=1}^{N_{out}} \int_{\Gamma_i} (p + \frac{1}{2}\rho v^2)\mathbf{v} \cdot d\Gamma, \tag{5.11}$$

where p is the pressure, $\mathbf{v}$ the velocity, ρ the density, N_{in} is the number of inlets, N_{out} the number of outlets, and Γ_i are the inlet and outlet surfaces. An alternative approach, instead, consists in evaluating the power loss due to viscous dissipation, using the expression

$$P_{vd} = \mu \int_{\Omega} |\nabla \mathbf{v}|^2 d\Omega, \tag{5.12}$$

where Ω is the domain of interest. Under the assumption that in a laminar blood flow all the dissipated energy is the result of frictional (viscous) forces, the two approaches can be considered equivalent [195]. We demonstrate this equivalence by deriving the kinetic energy equation from first principles, i.e. from Navier-Stokes equations.

Consider a domain Ω with boundary Γ, containing a fluid with velocity $\mathbf{v}$ and pressure p. Navier-Stokes equations take the form

$$\begin{cases} \rho \frac{\partial \mathbf{v}}{\partial t} + \rho \mathbf{v} \cdot \nabla \mathbf{v} = -\nabla p + \mu \nabla^2 \mathbf{v} & \text{in } \Omega, \\ \nabla \cdot \mathbf{v} = 0 & \text{in } \Omega. \end{cases} \tag{5.13}$$

The total kinetic energy in Ω can be expressed as

$$\mathcal{E} = \frac{1}{2} \int_{\Omega} \rho \mathbf{v} \cdot \mathbf{v} d\Omega, \tag{5.14}$$

and, assuming the fluid is incompressible, its derivative in time takes the form

$$\frac{\partial \mathcal{E}}{\partial t} = \frac{1}{2} \int_{\Omega} \rho \frac{\partial}{\partial t}[\mathbf{v}^2] d\Omega = \frac{1}{2} \rho \int_{\Omega} 2\mathbf{v} \cdot \frac{\partial}{\partial t}[\mathbf{v}] d\Omega = \rho \int_{\Omega} \mathbf{v} \cdot \frac{\partial \mathbf{v}}{\partial t} d\Omega \tag{5.15}$$

Since the goal is to make this term appear in Navier-Stokes equations, each term of the momentum balance equation in (5.13) is left multiplied by $\mathbf{v}\cdot$, and integrated over Ω, obtaining

$$\rho \int_{\Omega} \mathbf{v} \cdot \frac{\partial \mathbf{v}}{\partial t} d\Omega + \rho \int_{\Omega} \mathbf{v} \cdot [\mathbf{v} \cdot \nabla \mathbf{v}] d\Omega = -\int_{\Omega} \mathbf{v} \cdot \nabla p d\Omega + \mu \int_{\Omega} \mathbf{v} \cdot \nabla^2 \mathbf{v} d\Omega, \tag{5.16}$$

where the first term is the rate of change of kinetic energy in Ω, as reported in (5.15). The second term in (5.16) can be rewritten using Eq.(2.5) in [196] as

$$\rho \int_\Omega \mathbf{v}\cdot[\mathbf{v}\cdot\nabla\mathbf{v}]d\Omega = -\rho \int_\Omega \mathbf{v}\cdot[(\mathbf{v}\cdot\nabla)\mathbf{v}]d\Omega - \rho \int_\Omega (\nabla\cdot\mathbf{v})\mathbf{v}\cdot\mathbf{v}d\Omega + \rho \int_\Gamma |\mathbf{v}|^2(\mathbf{v}\cdot\mathbf{n})d\Omega, \tag{5.17}$$

where $\mathbf{n}$ is the outer normal to the boundary Γ. The second term on the right hand side of (5.17) is equal to zero, thanks to the continuity equation in the Navier-Stokes system (5.13). Rearranging, one obtains

$$\rho \int_\Omega \mathbf{v}\cdot(\mathbf{v}\cdot\nabla)\mathbf{v}d\Omega = \frac{1}{2}\rho \int_\Gamma |\mathbf{v}|^2(\mathbf{v}\cdot\mathbf{n})d\Gamma, \tag{5.18}$$

which represents an equivalent expression for the second term in (5.16). The third term in (5.16) can be transformed using the property [197]

$$\nabla\cdot\phi\mathbf{A} = \mathbf{A}\cdot\nabla\phi + \phi\nabla\cdot\mathbf{A}, \tag{5.19}$$

obtaining

$$-\int_\Omega \mathbf{v}\cdot\nabla p d\Omega = -\int_\Omega \nabla\cdot(p\mathbf{v})d\Omega + \int_\Omega p\nabla\cdot\mathbf{v}d\Omega = -\int_\Omega \nabla\cdot(p\mathbf{v})d\Omega = -\int_\Gamma p\mathbf{v}\cdot\mathbf{n}d\Gamma \tag{5.20}$$

Finally, the last term in (5.16) is rearranged using the Laplacian property for a product of fields [198]

$$\nabla^2(ab) = (\nabla^2 a)b + a\nabla^2 b + 2(\nabla a)\cdot(\nabla b), \tag{5.21}$$

which for the term in question gives

$$\mu \int_\Omega \mathbf{v}\cdot\nabla^2\mathbf{v}d\Omega = \mu \int_\Gamma (\mathbf{v}\cdot\nabla\mathbf{v})\cdot\mathbf{n}d\Gamma - \mu \int_\Omega |\nabla\mathbf{v}|^2 d\Omega \tag{5.22}$$

Summing up, (5.16) can be rewritten as

$$\frac{\partial\mathcal{E}}{\partial t} = -\int_\Gamma \left[\frac{1}{2}\rho|\mathbf{v}|^2 + p\right](\mathbf{v}\cdot\mathbf{n})d\Gamma + \mu \int_\Gamma (\mathbf{v}\cdot\nabla\mathbf{v})\cdot\mathbf{n}d\Gamma - \mu \int_\Omega |\nabla\mathbf{v}|^2 d\Omega, \tag{5.23}$$

which is known as the kinetic energy equation [199]. The term on the left hand side, in fact, corresponds to the rate of change of kinetic energy contained in Ω, while the first and the second terms on the right represent the power

absorbed through the boundary Γ. The last term, instead, accounts for the power dissipated by viscous forces in the volume Ω.

Considering the cases under analysis, where the inlet flow rate is steady, the rate of increase of kinetic energy is equal to 0. At the same time, the second term on the right-hand side accounts for the power flow across Γ due to viscous forces. For example, a fluid in motion outside Ω would put in motion also the fluid inside Ω, because of viscous forces, and this would generate a flow of energy through Γ from the outside to the inside of Ω. It is safe to assume that this term can be neglected, since its contribution will be minimal, as it will be verified later in Fig. 5.7. In light of this, we can rearrange (5.23) as

$$-\int_{\Gamma}\left[\frac{1}{2}\rho|\mathbf{v}|^2+p\right](\mathbf{v}\cdot\mathbf{n})d\Gamma=\mu\int_{\Omega}|\nabla\mathbf{v}|^2d\Omega, \tag{5.24}$$

proving the equivalence of the two approaches presented at the beginning, the control volume approach and the viscous dissipation one. The standard approach used in literature is the control volume one, adopted for example in [191], [190] and [189]. The viscous dissipation approach, however, has recently gained some attention [195, 200, 201], mainly due to the fact that it depends only on velocity, and not on pressure, which usually requires invasive measurements. In particular, this approach could potentially be used to measure dissipated energy directly from 4D-Flow MRI data, removing the need to run CFD simulations to retrieve pressure results, in order to estimate dissipated power. Several works have investigated the feasibility of this idea, together with the validity of the viscous dissipation formula for quantifying energy loss. Some relevant insights on this matter can be found in [195] and [202], where the viscous dissipation and the control volume approach were compared on ideal models of the total cavopulmonary connection, revealing a good agreement between the two. In [201], instead, the effect of the mesh size and generation method on power loss computation was estimated, concluding that the viscous dissipation approach required smaller mesh size than the control volume one, while tending to underestimate power loss with respect to in vitro values. Similar conclusions were drawn in [203] and in [204], where viscous dissipation results were compared to data from magnetic resonance velocity mapping images. Viscous dissipation required too high a spatial resolution to be able to estimate energy loss directly from MR data, without CFD simulations. The

need for a finer mesh is motivated by the presence of the gradient of velocity in (5.12), which is by nature more sensitive to mesh size. Lately, the advantage of using viscous dissipation was investigated in [200], where it was proposed as a Fontan haemodynamic metric.

Given the central role that energy loss has on the numerical investigation of the minimum energy principle, we verified numerically the equivalence of the control volume and viscous dissipation approaches, testing their suitability for our application. In particular, for the aortic arch presented in subsection 5.5.4, we computed the dissipated power with both approaches, imposing a steady inlet flow rate and resistance BCs at the outlets. We also verified that the second term on the right-hand side in (5.23) was in fact negligible.

The results of this analysis are reported in Fig. 5.7. After an initial transient, where the inlet flow goes from zero to its steady value, both the viscous dissipation and the control volume power converge to the same constant value. However, while viscous dissipation converges to a stable result, the control volume power is characterized by more oscillations, even after the transient of the inlet flow has extinguished. These oscillations can be explained by the presence of vortices and turbulent flows in the descending aorta, which may cause some backflow, and thus change the sign of this outlet contribution to (5.11). It was also noticed that the oscillations diminished as the mesh size was reduced. As predicted, the neglected term accounting for viscous forces is close to zero. In light of these results, we decided to use the viscous dissipation approach for our framework.

In particular, the power loss due to viscous dissipation was computed as

$$P_f = P_{vd} = \mu \int_\Omega |\nabla \mathbf{v}|^2 d\Omega. \tag{5.25}$$

The contribution due to the metabolic processes, instead, was computed as

$$P_m = b \cdot V, \tag{5.26}$$

where the volume can be easily computed as the sum of the volumes of the tetrahedral elements inside the mesh. The choice of an appropriate value for the metabolic constant b, instead, is a delicate question, and the approach adopted for its estimation will be detailed in Section 5.4.2. The total power

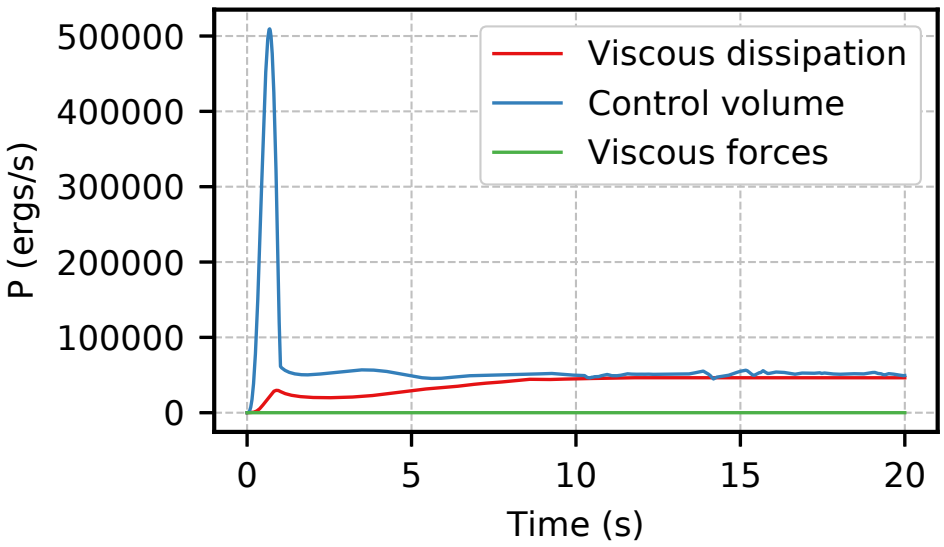

Fig. 5.7 Comparison of power loss due to viscous dissipation (5.12), power loss computed with control volume approach (5.11), and power loss due to viscous forces on the boundary, for the aortic arch in Fig. 3.1.

loss then takes the form

$$P_t = P_{vd} + P_m = \mu \int_\Omega |\nabla \mathbf{v}|^2 d\Omega + b \cdot V. \tag{5.27}$$

In all test cases, a steady flow was imposed at the inlet, with the inlet flow rate initially set to zero and reaching its steady constant value after a transient. This transient was introduced to avoid the convergence issues that may arise when an input flow rate rate with a large, abrupt change is imposed. The total power loss was then computed after the simulation had reached a steady state condition, with the inlet flow having extinguished its transient, and the final value for P_t was obtained by averaging its value over the final time steps. At the outlets, instead, resistive boundary conditions were imposed.

5.4.1 High-fidelity Navier-Stokes solver: Oasis

In order to compute the total dissipated power, it is necessary to have a solution for velocity and pressure at each point of the domain of interest, which can be obtained by solving the Navier-Stokes equations. In the proposed framework, the *Oasis* solver was employed for this step [72]. *Oasis* is a high-level/high-

performance open source Navier-Stokes solver written in Python. Standard CFD solvers usually employ finite-elements algorithms with stabilization schemes, like the streamline upwind Petrov-Galerkin (SUPG) algorithm [205]. Their popularity is motivated by their numerical robustness ensured by stabilization, which however introduces additional numerical dissipation. On the other side, the Galerkin finite element method used by *Oasis* contains very little numerical diffusion. The advantages of using this specific solver are multiple. First, *Oasis* is a high order and minimally dissipative finite-elements solver, which has been shown to achieve highly accurate results with coarser spatial and temporal meshes with respect to classic numerical schemes [72, 206]. This is particularly desirable in an application, such as the one proposed, where a large number of simulations must be performed. Second, the high-fidelity nature of *Oasis* allows to detect high-frequency flow instabilities, which are generally suppressed in regular CFD solvers, despite being potentially relevant from a clinical perspective, and may affect energy dissipation. Third, the user-friendly Python interface of *Oasis*, inherited by FEniCS [133, 134] and PETSc [207], makes it the best choice for our framework, where the CFD solver must be interfaced to the other building blocks for automation.

5.4.2 Identifying the minimum energy point: challenges and open problems

The framework presented in this section was devised to investigate the presence of a minimum energy point in realistic anatomies. This investigation, however, still presents a number of challenges and open problems which need to be properly addressed. We list here the main open questions, and we provide more details for each of them in the following.

- How can we choose an appropriate value for the metabolic constant b, appearing in the computation of the total power loss (5.27)?
- What happens in the portions of the cardiovascular system, such as the aortic arch, which deviate from the straight vessel considered by Murray in many ways, including curvature, pulsatile condition, bifurcations, and turbulence? How do these factors influence the presence of the minimum postulated by Murray?

- One of the assumptions behind Murray's law is the presence of laminar flow. What happens when this hypothesis is not valid anymore, and the flow becomes transitional, or turbulent?

The metabolic constant

The metabolic constant plays an important role in the power loss computation (5.27) at the centre of this investigation. The existence of a metabolic constant was first theorized by Murray in [50], but its real physiological meaning is to this day still unclear. In the analytical form of Murray's law (5.8), in fact, the metabolic constant drops out, so it does not play a role in the optimization process. Murray himself, in [50], tried to estimate it using four different methods, obtaining values ranging from 9,180 ergs/cm^{3}s to 22,950 ergs/cm^{3}s. The main method he proposed started by obtaining a formula for b from (5.5)

$$b = \frac{2Q^2 8\mu}{\pi^2 r^6}, \tag{5.28}$$

and, combining it with (5.2), gave the generic formula

$$b = \frac{2\Delta p \cdot Q}{V}. \tag{5.29}$$

By assuming a pressure drop across the entire system of $174 \cdot 10^3$ dyn/cm^2, an average flow rate of 83.3 cm^3/s, and a total volume of blood in the arterial system equal to 1,500 cm^3, he obtained a final value for b of $19,300$ ergs/cm^{3}s. This estimate, then, is supposed to represent the average metabolic cost of the whole cardiovascular system. In the same work [50], Murray came up with three other values for b. A value equal to 9,180 ergs/cm^{3}s was obtained by evaluating (5.28) on the capillaries, with the appropriate values for Q, μ, and r. An estimate of 22,950 ergs/cm^{3}s, instead, was obtained by considering the surface area of the capillaries, instead of the length, in (5.4). It is worth noticing how this last estimate is more than double the previous one, despite both being computed for the capillaries. The final estimate, instead, was obtained by averaging velocity and radius values obtained over five carotid arteries in dogs, and it amounted to 11,520 ergs/cm^{3}s. Even if Murray considered the agreement in terms of order of magnitude among the different estimates of b as a convincing evidence of the existence of a "cost of blood" [50], it is clear that there is a

Table 5.1 Estimates for the metabolic constant b found in the literature.

Original source	b (ergs/cm^{3}s)
Murray [50], generic	19,300
Murray [50], capillaries	9,180
Murray [50], capillaries	22,950
Murray [50], carotid artery	11,520
Zamir [180]	7,110
Taber [182]	778
Marsden [191]	3,166

large variability in its estimation, making the choice for a reasonable value for b particularly hard. In later works, others tried to estimate the metabolic constant more accurately. In [180], different values of average pressure and flow were used in (5.29), leading to a value of b of 7,110 ergs/cm^{3}s. In [182], instead, a value of 778 ergs/cm^{3}s was proposed for b, based on measured oxygen consumption rates for red and white blood cells in rats. Finally, in [191], a value of 3,166 ergs/cm^{3}s was used, which was obtained as the average between the values employed in [180] and [182]. For clarity, we report in Table 5.1 a summary of all the estimations of b found in the literature.

Even if the goal of our investigation was not to obtain an estimate of b, the role played by the metabolic constant in the proposed framework is significant, as it dictates the importance of the metabolic term relative to the energy dissipation term in (5.27). A slight variation of b, then, would have a large influence on the position of the minimum energy point estimated through our framework. For this reason, we decided to estimate a specific value for the metabolic constant for each anatomy considered. While for the straight vessel the value of b could be computed analytically, and for the ideal bifurcation we adopted the value estimated in [191], where the same geometry was employed, the real anatomies were treated differently. For both the aortic arch and the coronary bifurcation, we employed (5.29), with values of Q and V measured across different patient-specific anatomies, and successively averaged. In this way, a generic value of b was obtained, but still relative to the type of anatomy considered. That being said, the estimation of the metabolic constant is still largely an open problem.

The case of the aortic arch: does the minimum energy principle still hold?

When dealing with Murray's law, the aortic arch is often analyzed separately from the rest of the system, and treated as a special case. The aorta, in fact, is the largest blood vessel in the human body, and it begins at the left ventricle of the heart, from where it transports oxygenated blood to the rest of the body. Due to its peculiar position and function, it has often been questioned if the minimum energy principle, and consequently Murray's law, are still valid in the first part of the aorta. For this reason, our numerical investigation can be considered of particular interest when applied to a patient-specific aortic arch. Going back to the original paper from Murray [50], the author stated that its principle for computing radii at bifurcations could not be applied to the aorta. Murray's principle, in fact, takes into consideration only a portion of the work done by the aorta (to overcome friction), but it does not consider the work required to reduce the intermittent acceleration of the blood produced by the heart at each heart beat. This fact explains why the aorta, compared to the rest of the vascular system, seems to be larger than expected - it has to minimize the high acceleration associated to intermittent flow, and convert it to a continuous flow. The same conclusion was reached by Zamir in [180], where he said that a principle to predict vessels' radii is not expected to hold throughout the entire cardiovascular system. The aorta and its main branches, in particular, need to absorb and modulate the major impact of cardiac pulse, so we expect that their radii and volume are also suited for these functions. In [172], it was verified that Murray's law is not followed in the most immediate branching of the aorta, the pulmonary trunk, the venae cavae and the pulmonary veins. Moreover, Murray's law is not valid when flow is turbulent instead of laminar, and it is not expected to hold when blood flow is not a Poiseuille's flow. An alternative law was proposed in [144], where Murray's cube law (5.7) was shown to be inaccurate in the first branches of the aorta, where vessel capacitance and gross anatomy play a major role. Instead, it was suggested that a square law could be more appropriate. A further analysis can be found in [183], where the effect of pulsatile blood flow on Murray's law is investigated, concluding that arterial radii follow Murray's law for all but the largest arteries, as already suggested in [174].

In light of this, we hypothesized that, even if the cube law proposed by Murray is not valid in the aorta, still Murray's minimization principle could hold. In other words, the aorta could be still energetically optimal, even without following Murray's law. For this reason, one of the test cases presented in Section 5.5 was conducted on a patient-specific aortic arch.

The role of turbulence

As a last point, the role of turbulence and non-laminar flow in the energy principle was investigated. As pointed out earlier, one of the assumptions of Murray's law is the presence of laminar flow (Poiseuille). This is, however, not always the case when dealing with real-life scenarios. In particular, in the aortic arch the high Reynolds number puts the flow into transitional or turbulent regime, with the appearance of vortices and turbulences in the descending aorta. In order to see the effect that non-laminar flow has on the energy curves, we ran the simulations on the aortic arch using both the Stokes and the Navier-Stokes equations. Being the former the linearized version of the latter, they do not resolve turbulences and non-linearities. The results of this investigation are reported in Section 5.5.4.

5.5 Results

The proposed framework was first validated on two synthetic geometries, namely, an ideal straight vessel and a bifurcation, and then tested on two patient-specific anatomies, consisting of a portion of the coronary tree and an aortic arch. The numerical results for each case will be analyzed in the rest of the section.

5.5.1 Ideal straight vessel

The first example was an ideal straight vessel, for which the analytical version of Murray's principle can be used (5.4). The geometry was replicated from the cylinder test case provided as a SimVascular example project [208]. An ideal straight vessel (i.e., a cylinder) 30 cm long and with a radius of 2 cm was generated using the *mshr* package in FEniCS [133, 134]. An average inlet flow

rate of 100 cm^3/s was selected, to ensure that the flow would remain laminar. This was verified by computing the Reynolds number

$$Re = \frac{\rho D v}{\mu}, \tag{5.30}$$

where $\rho = 1.06$ g/cm^3 is the blood density, $\mu = 0.04$ poise is the dynamic viscosity, D is the diameter of the vessel, and v is a representative velocity of the flow, equal to the average inlet velocity, approximately 8 cm/s for a flow rate of 100 cm^3/s. In this case the Reynolds number was about 884, well below the critical value of 2300, above which flow becomes transitional. The parameter α was changed from 0.8 to 1.2, while the inlet flow rate, imposed with a constant parabolic profile at one end of the cylinder, was changed from 85 cm^3/s to 130 cm^3/s. At the outlet, a resistive-type boundary condition was imposed, with a resistance value computed for each flow rate as

$$R_{out} = \frac{p_{out}}{Q}, \tag{5.31}$$

where p_{out} indicates pressure at the outlet, and, as in [208], was imposed to be equal to 100 mmHg. For each combination of α and Q, the Navier-Stokes equations were solved with the finite element method in FEniCS - in fact, given the simplicity of this geometry, there was no need for an advanced solver like *Oasis*. The metabolic constant, considering an average flow rate of 100 cm^3/s, could be computed using the analytical formula (5.28), obtaining

$$b = \frac{16\mu Q^2}{\pi^2 r^6} = 10.14 \text{ ergs/cm}^3\text{s}. \tag{5.32}$$

The value obtained for b is at least two orders of magnitude smaller than the values proposed in the literature. This is motivated by the fact that we used values for Q and r specific to this geometry, while the values of b presented in Section 5.4.2 were estimated for the entire cardiovascular system. However, since the scope of this investigation was not to verify the validity of previous estimates for b, we adopted the value computed with (5.32).

The curves obtained for viscous dissipation, metabolic cost, and total power loss are reported in Fig. 5.8. The behavior of the viscous dissipation curves was the one predicted by Murray's minimum energy principle, with decreasing values

for increasing α. Moreover, as expected, viscous dissipation values increased for increasing values of inlet flow rate Q, with curves shifting vertically. The metabolic cost, instead, increased with α, but did not change with Q, as it depends only on volume, which is not influenced by flow rate. The plot of the total power was obtained by summing up viscous dissipation and metabolic cost. After that, the obtained curves were fitted with a least squares polynomial fit of degree 4, in order to better identify the minimum of the energy curves. As predicted, each curve has a minimum point, which shifts to the right for increasing values of Q.

Since the cylinder case is ideal, it was possible to compute analytically the optimal flow rate Q for each α, using (5.6). A comparison between analytical and numerical results, obtained with our framework, is reported on the fourth panel of Fig. 5.8, where the flow rates at which energy is minimum are plotted against α (blue crosses). The orange line, instead, represents the analytical solution of (5.6). The plot reveals a very good agreement between the results obtained with the two separate techniques, validating our numerical framework with an analytical solution.

5.5.2 Ideal bifurcation

The second geometry taken into consideration was an ideal carotid artery bifurcation, as depicted in Fig. 5.9. This anatomy reproduced the one used in [191], where a computational framework for derivative-free optimization was used to reproduce computationally Murray's law. In particular, the method proposed in [191] was used to predict the optimal radii and branch angle in an ideal bifurcation. For $\alpha = 1$, the parent radius was 0.3 cm, the daughter radius 0.238 cm, which are optimal radii according to Murray's law (5.7). In [191], an average flow rate of 6.46 cm^3/s was imposed at the inlet, obtained as the mean value of a typical carotid artery flow waveform. For this reason, we chose an interval for the inlet flow rate Q around this value. Specifically, a constant flow rate varying between 4 and 8 cm^3/s was imposed at the parent vessel, with a parabolic profile, while α was again changed between 0.8 and 1.2. The metabolic constant was set to 3,166 erg s/cm^3, as suggested in [191], where it was found that this value of b was the one providing the best agreement with the analytical Murray's law (5.7) for the anatomy under analysis. Resistive-type

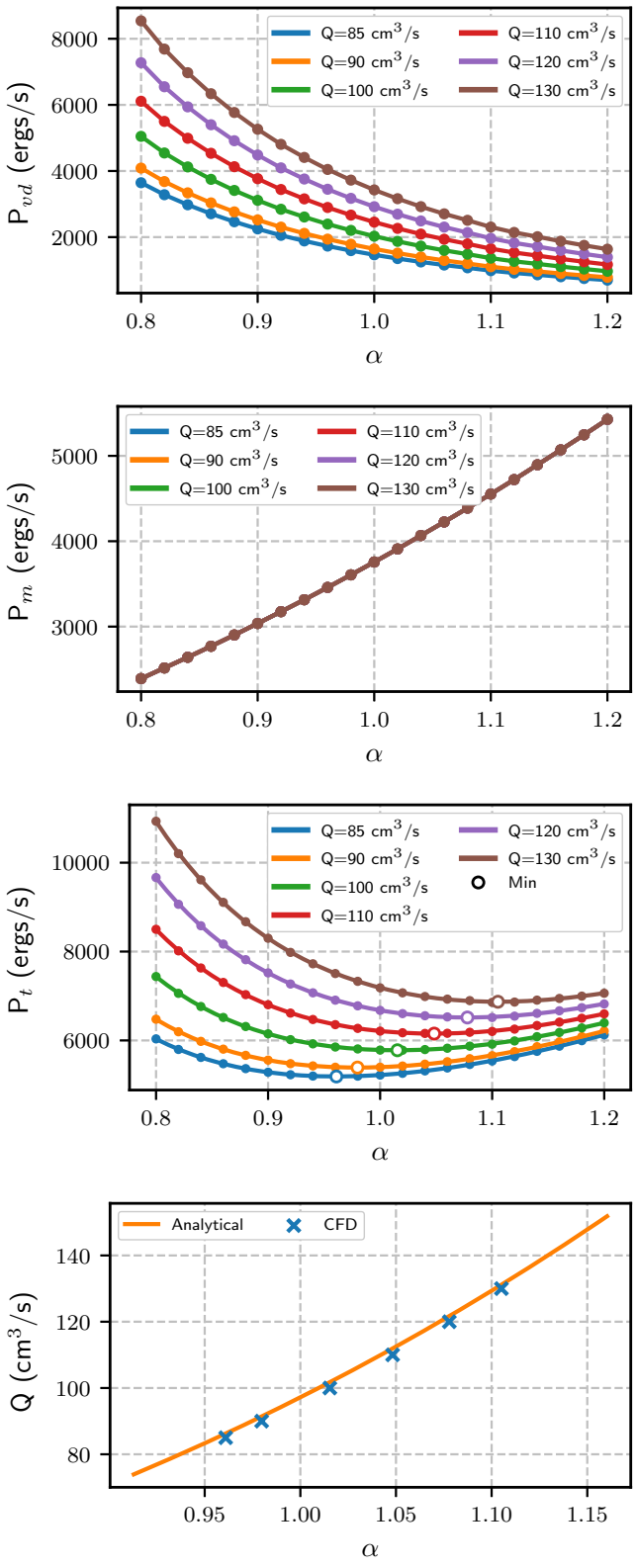

Fig. 5.8 Numerical results for the straight vessel (Section 5.5.1). The first plot represents the power loss P_{vd} due to viscous dissipation, the second one the power loss P_m due to metabolism, and the third one the total power loss P_t. The fourth plot compares the minimum energy points found analytically (5.6) (orange line) to those obtained numerically (blue crosses).

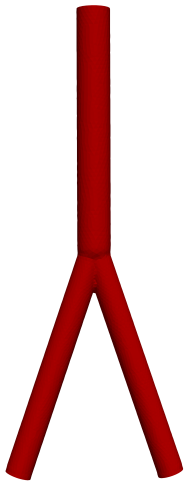

Fig. 5.9 Representation of ideal bifurcation used in Section 5.5.2 for the numerical investigation of minimum energy principle.

boundary conditions were imposed at the outlet. In order to get the same outlet pressure of 100 mmHg as in [191], total resistance was computed as in (5.31), setting p_{out} equal to 100 mmHg. The anatomy was modified using the morphMan package, and the simulations were run in FEniCS.

As for the ideal cylinder, the curves again followed the expected energetic behavior, with the viscous dissipation decreasing as α increased, and the metabolic cost increasing, as reported in Fig. 5.10. As shown in the total power plot, the minimum point moves to the right for increasing Q, as expected. The energy curves appear to be smooth, and there is a unique minimum energy point for each flow rate Q, occurring at different values of α. The energetic behavior, then, is in line with the one predicted earlier in Section 5.3. The minimum energy point for $\alpha = 1$ seems to occur for an inlet flow rate between 5 and 6 cm^3/s. Since in [191] a flow rate equal to 6.46 cm^3/s was considered a physiological value for this anatomy, we notice that this value is close to the optimal range of inlet flow rate identified by our framework, but it is not included in it. This may be due to the non ideal nature of blood flow in the bifurcation, or to the value used for the metabolic constant, which influences the position of the minimum energy point.

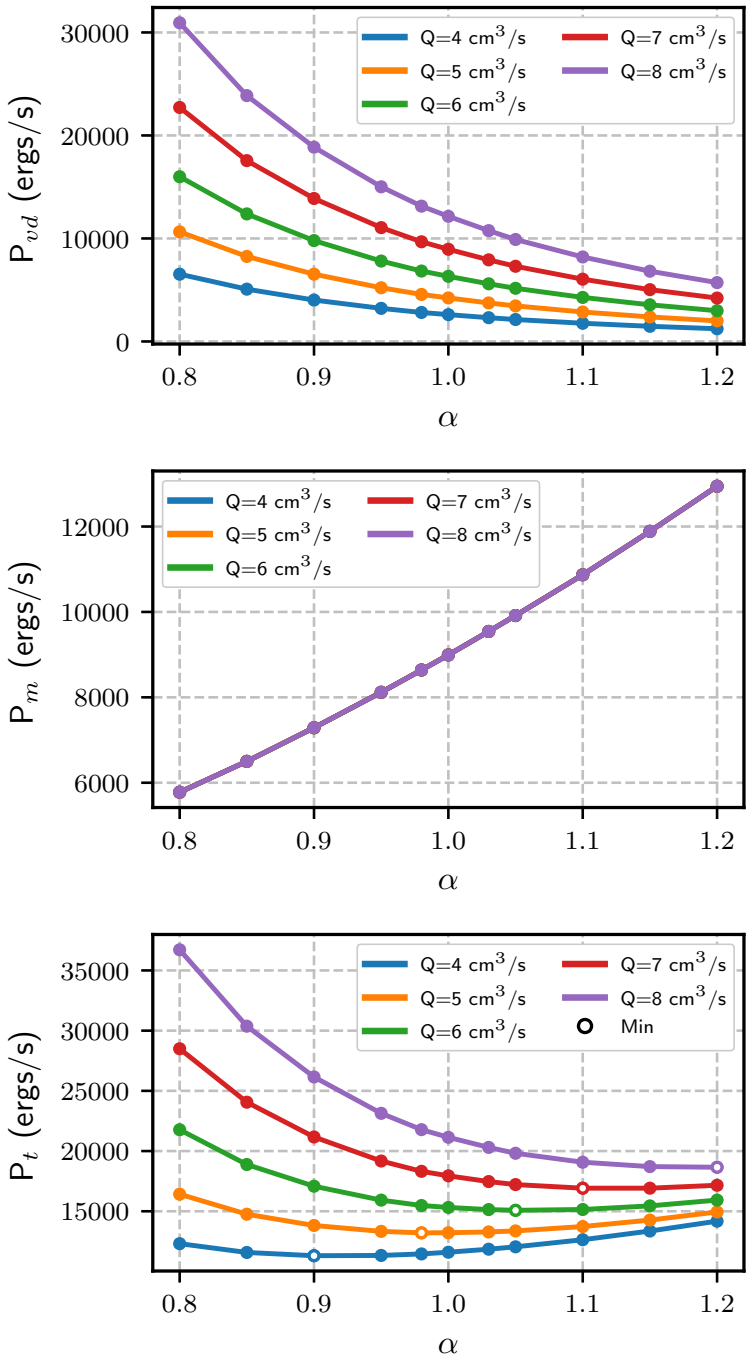

Fig. 5.10 Results for the ideal bifurcation (Section 5.5.2). The first plot represents the power loss curves due to viscous dissipation, the second one the metabolic cost, and the third one the total power loss, resulting from the sum of the two previous contributions.

5.5.3 Coronary bifurcation

The third case analyzed is a patient-specific coronary bifurcation, obtained from one of the patients enrolled in a single-center prospective study conducted at the Sunnybrook Health Sciences Centre in Toronto, Canada. Patients presented at the hospital for coronary bypass graft surgery. Between three and six weeks after surgery, a cardiac CT was performed and anatomical information about their aorta and coronary arteries was acquired using a 320-detector row CT scanner (Aquilion One, Canon Medical Systems). From CT images, the vessels surface was reconstructed using the open-source package SimVascular [26]. The reconstructed volume was discretised into tetrahedral elements using TetGen [131].

The anatomy considered is the one reported in Fig. 5.11, which is placed at the bifurcation of the left main coronary artery (LM) into the left circumflex artery (LCx) and the left anterior descending artery (LAD). The average flow rate in the coronary arteries is usually computed as 4% of the flow rate in the ascending aorta, further split between the left and the right coronary arteries with a 70%-30% ratio [209]. For this case, the aortic flow rate was measured non-invasively with 4D-Flow MRI, and it amounted to an average value of 107 cm^3/s. Considering the high-degree stenosis present in the vessels of interest, the average inlet flow rate was expected to be smaller than the one computed with the 4% rule [210], which in this case would have been equal to 2.9 cm^3/s. The range for the inlet flow rate was then selected between 0.5 and 1 cm^3/s, which was in line with the average flow rates measured in coronary arteries with severe stenoses [211]. The metabolic constant was set to 16,143 $ergs/cm^3s$, computed from (5.29) by assuming an average flow rate of 0.75 cm^3/s, a volume of 1 cm^3, and a pressure drop of about 8 mmHg, which was the pressure drop obtained on the anatomy by imposing a flow rate of 0.75 cm^3/s. At the outlet, resistive boundary conditions were imposed. The total resistance was computed for each flow rate as in (5.31), where an outlet pressure of 90 mmHg was imposed [43]. The total resistance was then split between the two branches according to Murray's law for flow split (5.8), with the exponent 2.6, as suggested in [212] for the coronary tree. The energetic behavior of this anatomy is coherent with the expected results, as depicted in Fig. 5.12, with the minimum progressively moving toward the right. The

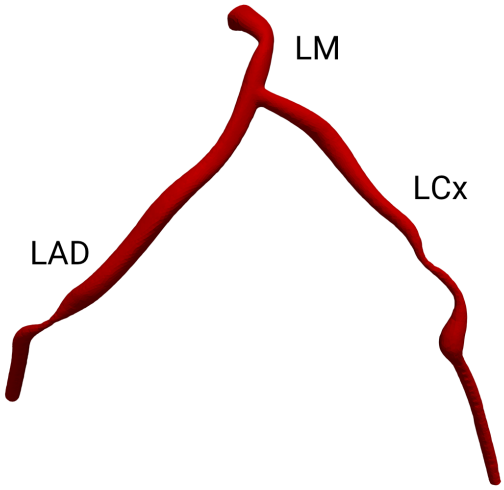

Fig. 5.11 Coronary bifurcation used for the experiments of Section 5.5.3. The anatomy was reconstructed from CT imaging by means of SimVascular, and represents the Left Main coronary artery (LM) splitting between the Left Anterior Descending artery (LAD) and the Left Circumflex artery (LCx).

curves of the power loss due to viscous dissipation, reported in the first panel of Fig. 5.12, are not perfectly smooth, especially for higher Q. This fact may be due to the difficulties in computing the power loss in a non-ideal anatomy, with high-degree stenoses. In the fourth panel of Fig. 5.12, the total power loss curves after applying a regression operation are displayed. Comparing to the same curves before regression, displayed in the third panel of Fig. 5.12, it is noticeable how the minimum points are more easily identifiable thanks to the regression. However, the regression step causes the position of the minimum points to move significantly, especially for Q=0.6 cm^3/s and 0.8 cm^3/s. In this case, the minimum at $\alpha = 1$ occurs for a flow rate between 0.5 and 0.6 cm^3/s. The total power curve associated to Q=1.0 cm^3/s seems to show a different trend with respect to the other curves. However, by visually inspecting the simulation results for Q=1.0 cm^3/s, no anomalies in the pressure and velocity fields were detected. In conclusion, a range of flow rates for which the total power is minimum appears to exist, confirming the presence of a minimum energy region for the anatomy under analysis. However, identifying precisely the position of the minimum does not seem to be a trivial task. For this reason, the proposed approach could be potentially used to obtain a rough estimate of the inlet flow rate.

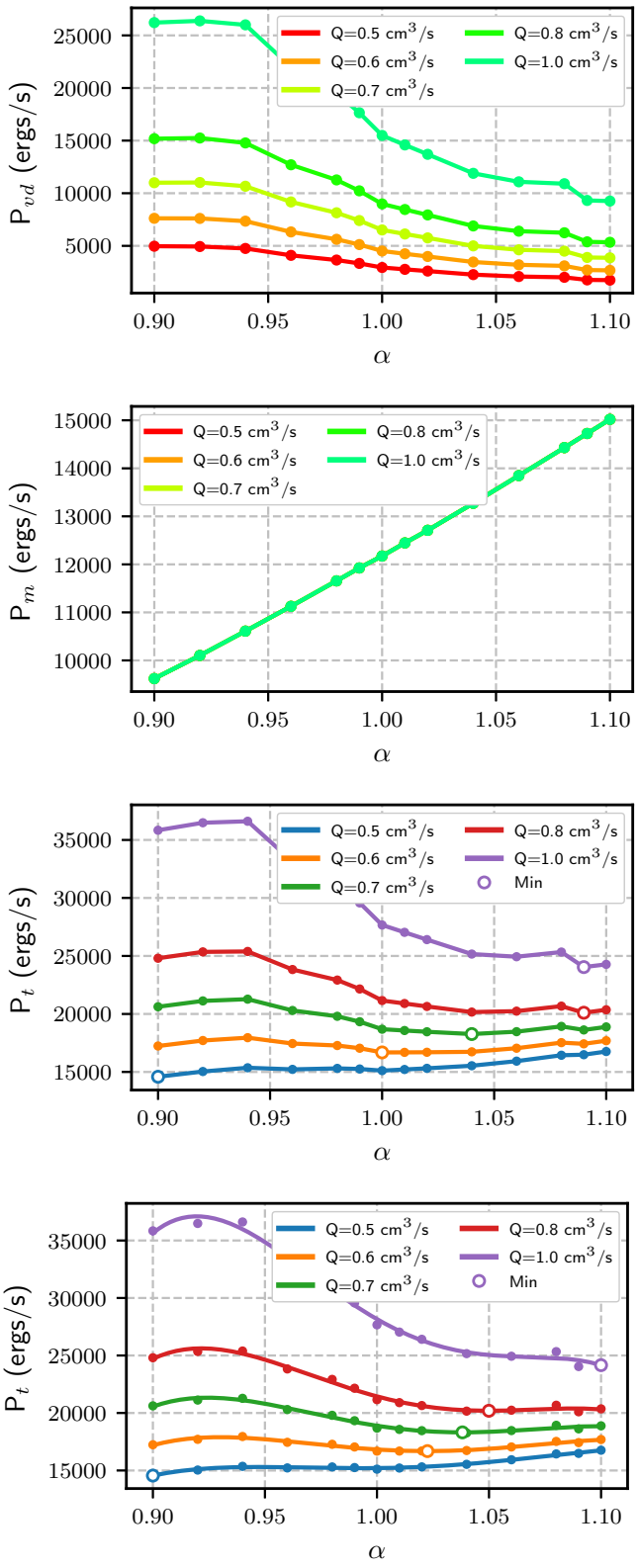

Fig. 5.12 Results for the coronary bifurcation (Section 5.5.3). The first plot represents the power loss curves due to viscous dissipation, the second one the metabolic cost, and the third one the total power loss. The fourth plot represents the total power loss curves after regression.

5.5.4 Aortic arch

The last case consists of an aortic arch, again obtained from one of the patient-specific anatomies provided by the Sunnybrook Health Sciences Centre in Toronto, Canada. As for the coronary bifurcation, the anatomy was reconstructed starting from CT images by means of SimVascular. A representation of the anatomy under analysis can be found in Fig. 5.13. The mean flow rate measured in the ascending aorta with 4D-Flow MRI was 107 cm^3/s. Then, the flow imposed for this analysis ranged from 100 cm^3/s to 120 cm^3/s, and it was imposed at the ascending aorta with a blunt profile, which is more realistic than the parabolic profile, given that the inlet is right after the aortic valve. In order to obtain a general value for the metabolic constant, the following procedure was adopted. The inlet flow rate was measured on four aortic arches for which 4D-Flow measurements were also available, together with their total volume. Then, for both quantities, an average across four patients was computed, and these average values were used to estimate a generic metabolic constant for the aortic arch. The obtained value for b was equal to 260 $ergs{\cdot}s/cm^3$. A resistive boundary condition was imposed at the outlets, with total resistance computed from (5.31), where Δp was chosen to be equal to 100 mmHg. The total resistance was then split among the four outlets according to Murray's law (5.8) with exponent 2, as suggested in [139] . The simulation results are reported in Fig. 5.14. Differently from previous cases, it is noticeable how the viscous dissipation curves are not perfectly smooth. This may be due to various factors, above all the complexity of the fluid flow in the aorta, where the high blood velocities can generate turbulence and a non-laminar flow, especially in the descending tract after the bend. It is possible that this is due also to the complexity of the anatomy. The weak "noise" in the viscous dissipation curves turns out to be relevant in the total energy plots, where, even if small, it causes the presence of some local minima, which make it difficult to identify the global minimum point. For this reason, we performed a polynomial regression operation of the total power curves. After regression, a global minimum of each curve was identifiable, and followed the predicted behavior. In this case, the optimal flow is between 100 and 105 cm^3/s. Considering that the inlet flow rate measured in the patient was equal to 107 cm^3/s, this value is not too far from the identified optimal range. Also in this case, as for the coronary bifurcation analysed previously, a precise identification of the minimum energy point, and

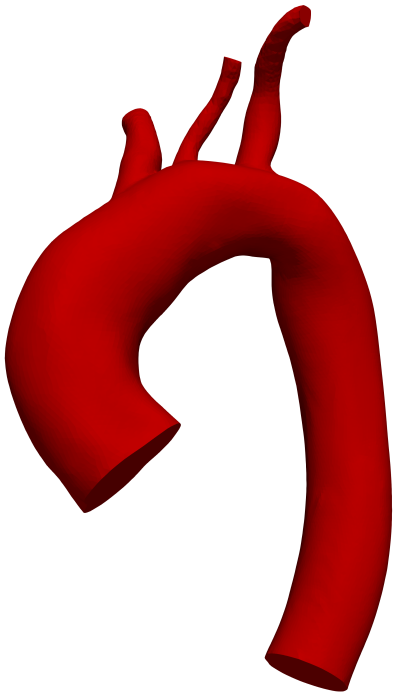

Fig. 5.13 Anatomy of the aortic arch used in the experiments of Section 5.5.4. The anatomy was reconstructed from CT images by means of SimVascular.

consequently of the optimal inlet flow rate, seems very difficult. However, the results confirm that there clearly exists a region in which the total power loss is minimum. This finding could be potentially leveraged to estimate the inlet flow rate just based on the anatomy, when in-vivo measurements are not available.

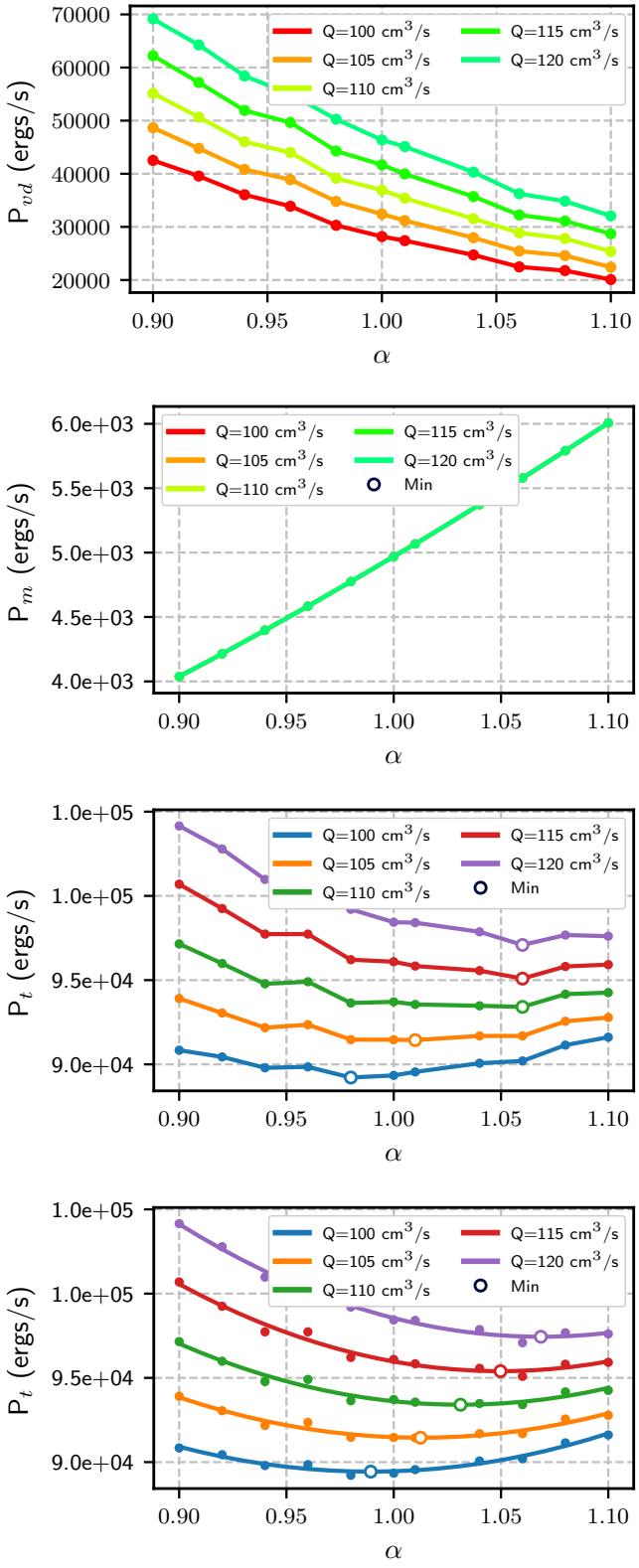

Fig. 5.14 Results for the aortic arch (Section 5.5.4). The first plot represents the power loss curves due to viscous dissipation, the second one the metabolic cost, and the third one the total power loss. The fourth plot represents the total power loss curves after regression.

To investigate the role that non-laminar flow may have on the presence of a minimum energy point, we repeated the experiments for the aortic arch using the Stokes equations in place of the Navier-Stokes ones. By neglecting the nonlinear inertial term in the momentum equation, in fact, which is responsible for the turbulent behavior of the flow, Stokes equations represent a linearized version of the Navier-Stokes equations. Results for the Stokes case are reported in Fig. 5.15. It can be noticed that, in this case, the viscous dissipation curves did not need to go through a regression step to smooth their curvature, suggesting that the noise in the Navier Stokes curves in Fig. 5.14 was due to the presence of non-laminar flow. This fact also confirms that the deformation produced by *morphMan* is sufficiently smooth, otherwise its effect would have caused some non-smoothness also in the Stokes curves. It was possible to identify the minimum energy points in the total power loss curves of Fig. 5.14, but none of the investigated flow rates had a minimum in $\alpha = 1$. This is probably due to the fact that, for laminar flow, the power loss due to viscous dissipation was about one order of magnitude smaller than the one computed in presence of non-laminar flow. The presence of transitional and turbulent flow, in fact, causes an increase in the power dissipation due to friction.

5.6 Final discussion and conclusions

In this chapter, we have proposed a framework for the numerical investigation of the Murray's minimum energy principle in patient-specific anatomies. With the goal of verifying if, for a given anatomy, a minimum energy point exists, a framework was developed to deform the anatomies, predict their haemodynamics by solving the Navier-Stokes equations, and then compute the total power loss. The proposed numerical framework was presented, validated on two synthetic geometries, and tested on two patient-specific anatomies. Numerical results confirmed the expected energetic behavior of the analyzed cardiovascular models, with a different minimum energy point for each inlet flow rate. The identifiability of such point, however, is hindered by a number of challenges, which have been reported and investigated in this chapter. In particular, the computation of the dissipated power, the role of the metabolic constant, and

the presence of transitional and turbulent flow have been found to play a major role in the possibility of identifying an optimal flow rate for a given anatomy.

The validity of Murray's minimum energy principle in patient-specific anatomies could have important applications, especially for the estimation of boundary conditions in absence of patient-specific data. The results obtained, in fact, suggest that, for each patient-specific anatomy, there is a single inlet flow rate placing the anatomy in a minimum energy condition. The investigation carried out in this chapter can be seen as a first step in the development of a method for inlet flow estimation based solely on physics and on the anatomy of the patient.

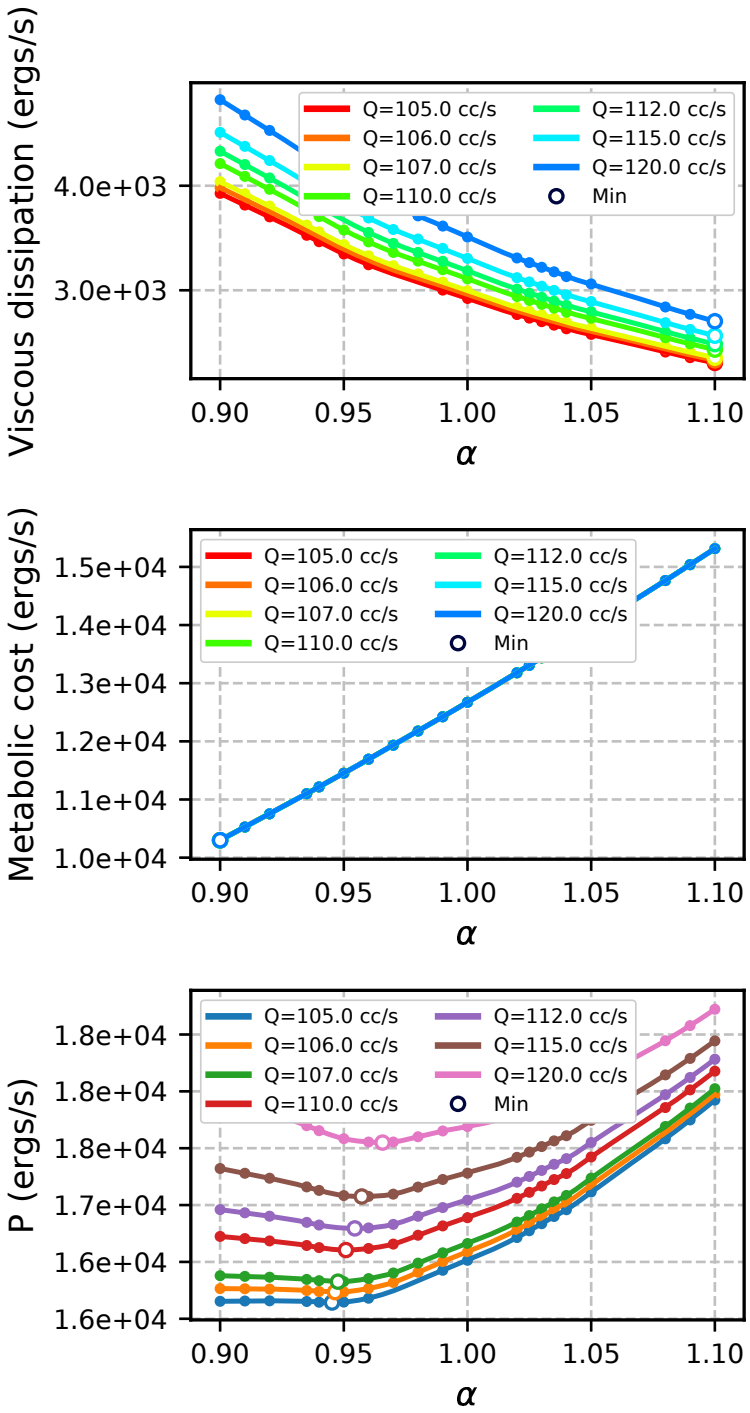

Fig. 5.15 Results for the aortic arch (Section 5.5.4) using Stokes equations. The first plot represents the power loss curves due to viscous dissipation, the second one the metabolic cost, and the third one the total power loss. The fourth plot represents the total power loss curves after regression.

Chapter 6

Conclusions and future perspectives

This dissertation investigated the use of novel techniques for boundary conditions estimation in cardiovascular modeling. Computational models are progressively emerging as powerful instruments for clinical treatment, but for their adoption in a real clinical setting a number of issues need to be overcome. Despite the evidence showing that patient-specific models provide information in a cheaper and more efficient way than standard approaches [213], to be effectively exploited in the clinic they need to be *fast, reliable,* and *easy to use*. Among the numerous challenges that arise from these requirements, the estimation of appropriate boundary conditions is one of the most crucial. The main contribution of this thesis is to provide a set of improvements for boundary conditions estimation, to make this process accurate, automated, and data driven.

In Chapter 3, we proposed a novel framework based on optimal control for the estimation of resistive boundary conditions. This chapter first reviewed the theoretical background behind optimal control for partial differential equations, presenting the main techniques for its treatment and solution. The second part of the chapter, instead, introduced the proposed framework for estimating outlet resistances from pressure and flow rate measurements, which are assimilated into the mathematical model describing blood flow by means of optimal control. The proposed method was tested on real clinical scenarios, through its application

on four patient-specific aortic arches and the assimilation of 4D-Flow MRI data, together with brachial pressure measurements. Moreover, the proposed framework was used to quantify the influence that different estimation methods have on wall shear stress and oscillatory shear index, confirming the need for automated methods for boundary conditions estimation.

Chapter 4 focused on a novel method for BC estimation based on the Time-Domain Vector Fitting algorithm. The method proposed in this chapter is purely data-driven, requiring time-dependent pressure and flow measurements for the estimation process, and it can determine boundary conditions of arbitrary complexity. The presented method was first used to estimate BCs of Windkessel type starting from a 1D model of the entire cardiovascular system, and then extended to more complex lumped boundary conditions, corresponding to differential equations of increasing order. Then, it was used to investigate the benefits in terms of accuracy that higher order boundary conditions can provide, revealing that, for larger arteries, models corresponding to differential equations up to order 4 are more accurate than the standard Windkessel model. In short, this chapter provided an advanced definition of lumped parameter-type boundary conditions, and an automated method to estimate its parameters from data.

In Chapter 5, we presented a numerical investigation of the minimum energy principle in patient-specific cardiovascular anatomies. The proposed numerical framework was used to verify the existence of a minimum energy point in patient-specific anatomies in order to potentially use the minimum energy principle as a criterion for inlet flow estimation. The presented results confirmed the predicted energetic behavior, but they also revealed the practical issues arising during the identification of the minimum energy point.

6.1 Future perspectives

This thesis provided a number of advancements in the field of parameter estimation for boundary conditions in cardiovascular models. The techniques proposed in this dissertation open up a number of possible investigations and future improvements, which will contribute to make patient-specific cardiovascular models fast, reliable, and easy to use.

In general, future works should aim at extending the proposed techniques to other regions of the cardiovascular system, especially coronary arteries. On one side, coronary arteries are characterized by a rich and complex blood flow dynamics, which requires boundary conditions more complex than a three-element Windkessel. On the other side, the physical dimensions of the vessels and their anatomical position make it really hard to obtain either pressure and flow data. This challenging scenario would benefit from the application of the techniques proposed in this thesis. In particular, the optimal control framework would estimate both inlet and outlet BCs in presence of a limited amount of data, while the vector fitting approach would allow to explore the advantages of higher order boundary conditions.

6.1.1 Optimal control for BC estimation

Despite the clear advantages in using automated estimation techniques for BC estimation, the proposed methods have some limitations, which lead to different future research directions. For what concerns the optimal control framework, its application is limited by the computational cost, and by the possibility to estimate only resistive conditions. Therefore, future research directions should aim at tackling these challenges. Boundary conditions more complex than a single resistance would include capacitors and inductors, which, due to their time-dependent behavior, require the use of unsteady Navier-Stokes equations instead of the steady Stokes ones. However, the solution of an optimal control problem using the unsteady Navier-Stokes equations has prohibitive computational costs, making this approach unfeasible.

A possible solution is represented by the use of reduced order modeling, which in this case can take different forms and meanings. A first approach consists in reducing the computational cost by adopting techniques such as reduced basis methods [214] and with Proper Orthogonal Decomposition [215], which have already been successfully applied to optimal control problems, delivering reduced computational times with minimal accuracy loss [97, 75, 216, 217]. The main drawback of this approach is the expensive *offline* phase, whose computational burden is proportional to the degrees of freedom of the Finite Element problem.

The second, probably more promising, approach consists instead in adopting simplified physics models. In this case, the 3D anatomical models used in Chapter 3 can be substituted with 1D models, or even with distributed lumped parameter models [218, 219]. As these models are described by ODEs instead of the more complex PDEs (Stokes and Navier-Stokes models), they are inherently simpler to treat and faster to solve. An exciting future direction would then be to extend the numerical framework presented in Chapter 3 to solve a state problem described by ODEs, and to reformulate the optimal control problem based on 1D or distributed lumped parameter models. We believe that the use of reduced order models is not expected to significantly affect the accuracy, especially considering that, with the optimal control framework proposed in this thesis, only time- and space-averaged measurements are assimilated.

Lastly, a possible research direction could explore the use of frequency-based numerical modeling tools, such as the harmonic balance method, in place of the classical mathematical formulation in time domain. This method takes advantage of the periodic, pulsatile nature of blood flow to transform the original problem into a family of equations in frequency domain. Some preliminary works have shown promising results, namely, reduced computational time and comparable accuracy with respect to traditional time-domain CFD solutions [220]. When adopted into a variational adjoint-based data assimilation framework, this method delivered accurate solutions in practicable wall clock times [221]. It would be interesting to adopt this approach for the estimation of lumped parameter boundary conditions, even if this would entail re-formulating the optimal control method from scratch, representing a new exciting research direction.

6.1.2 Time-Domain Vector Fitting for BC estimation

For what concerns the vector fitting method, instead, the main limitation is the requirement of both pressure and flow rate measurements, which are hardly available concurrently. This limitation clearly complicates the extension of the proposed method to realistic 3D anatomies, which represents the most natural next step for this work. For this reason, future research directions should explore the generation of data from defective measurements, which could then be used for parameter estimation inside the vector fitting framework.

To this end, a possible solution could be to adopt pressure waveform generators, to generate realistic pressure waveforms given brachial diastolic and systolic pressure values [168, 169]. If instead some pressure measurements are available but not at the correct location, some transfer function-based solutions have already been proposed to obtain pressure at the desired location [222, 223], or the Delayed Vector Fitting scheme could be explored to account for the expected delays in the pressure waveform measured at a different location [79].

An alternative solution consists in using a 1D model of the entire cardiovascular system, like the 55-segments one adopted in Chapter 4, to generate pressure and flow rate measurements at the required locations. This would allow a straightforward adoption of the proposed framework for the investigation of the Vector Fitting scheme on 3D models. The main drawback, however, is that a general 1D model of the entire circulatory system is not inherently patient-specific, a desirable feature for BC estimation methods. This limitation could be partially overcome by "personalizing" the 1D model. For example, using patient-specific information such as age, gender, height, some model parameters, such as stiffness, segment lengths, could be adjusted. Some efforts have already been done in this direction [224], which could be expanded to obtain automatically a personalized 1D model.

6.1.3 Numerical investigation of Murray's principle

The investigation of Murray's minimum energy principle has risen many questions, which can be the subjects of further investigation. In particular, the analysis conducted in Chapter 5 has highlighted the need for a robust estimation of the metabolic constant, a missing piece in unveiling the mechanisms governing the cardiovascular system. A future project could expand the preliminary work presented in this thesis by estimating the metabolic constant on a population of cases and on new different territories (e.g., the coronary arteries, the carotid bifurcation). The proposed investigation would benefit from a more efficient parameterization of the anatomies, modifying directly the mesh, instead of only the outer surface.

References

[1] Connie W. Tsao, Aaron W. Aday, Zaid I. Almarzooq, Alvaro Alonso, Andrea Z. Beaton, Marcio S. Bittencourt, Amelia K. Boehme, Alfred E. Buxton, April P. Carson, Yvonne Commodore-Mensah, Mitchell S.V. Elkind, Kelly R. Evenson, Chete Eze-Nliam, Jane F. Ferguson, Giuliano Generoso, Jennifer E. Ho, Rizwan Kalani, Sadiya S. Khan, Brett M. Kissela, Kristen L. Knutson, Deborah A. Levine, Tené T. Lewis, Junxiu Liu, Matthew Shane Loop, Jun Ma, Michael E. Mussolino, Sankar D. Navaneethan, Amanda Marma Perak, Remy Poudel, Mary Rezk-Hanna, Gregory A. Roth, Emily B. Schroeder, Svati H. Shah, Evan L. Thacker, Lisa B. VanWagner, Salim S. Virani, Jenifer H. Voecks, Nae-Yuh Wang, Kristine Yaffe, Seth S. Martin, and null null. Heart disease and stroke statistics - 2022 update: A report from the american heart association. *Circulation*, 145(8):e153–e639, 2022.

[2] Elizabeth Wilkins, L Wilson, Kremlin Wickramasinghe, Prachi Bhatnagar, Jose Leal, Ramon Luengo-Fernandez, R Burns, Mike Rayner, and Nick Townsend. European cardiovascular disease statistics 2017. 2017.

[3] Charles A Taylor and David A Steinman. Image-based modeling of blood flow and vessel wall dynamics: applications, methods and future directions. *Annals of biomedical engineering*, 38(3):1188–1203, 2010.

[4] Luca Formaggia, Alfio Quarteroni, and Allesandro Veneziani. *Cardiovascular Mathematics: Modeling and simulation of the circulatory system*, volume 1. Springer Science & Business Media, 2010.

[5] DA Steinman, DA Vorp, and CR Ethier. Computational modeling of arterial biomechanics: insights into pathogenesis and treatment of vascular disease. *Journal of vascular surgery*, 37(5):1118–1128, 2003.

[6] Irene E Vignon-Clementel, Alison L Marsden, and Jeffrey A Feinstein. A primer on computational simulation in congenital heart disease for the clinician. *Progress in Pediatric Cardiology*, 30(1-2):3–13, 2010.

[7] Silvia Schievano, Andrew M Taylor, Claudio Capelli, Louise Coats, Fiona Walker, Philipp Lurz, Johannes Nordmeyer, Sue Wright, Sachin Khambadkone, Victor Tsang, et al. First-in-man implantation of a novel

percutaneous valve: a new approach to medical device development. *EuroIntervention: journal of EuroPCR in collaboration with the Working Group on Interventional Cardiology of the European Society of Cardiology*, 5(6):745–750, 2010.

[8] D Rodney Hose, Patricia V Lawford, Wouter Huberts, Leif Rune Hellevik, Stig W Omholt, and Frans N van de Vosse. Cardiovascular models for personalised medicine: Where now and where next? *Medical engineering & physics*, 72:38–48, 2019.

[9] Ian Marshall, Shunzhi Zhao, Panorea Papathanasopoulou, Peter Hoskins, and X Yun Xu. Mri and cfd studies of pulsatile flow in healthy and stenosed carotid bifurcation models. *Journal of biomechanics*, 37(5):679–687, 2004.

[10] Quan Long, X Yun Xu, Ben Ariff, Simon A Thom, Alun D Hughes, and Alice V Stanton. Reconstruction of blood flow patterns in a human carotid bifurcation: a combined cfd and mri study. *Journal of Magnetic Resonance Imaging: An Official Journal of the International Society for Magnetic Resonance in Medicine*, 11(3):299–311, 2000.

[11] Jun-Mei Zhang, Liang Zhong, Boyang Su, Min Wan, Jinq Shya Yap, Jasmine PL Tham, Leok Poh Chua, Dhanjoo N Ghista, and Ru San Tan. Perspective on cfd studies of coronary artery disease lesions and hemodynamics: a review. *International journal for numerical methods in biomedical engineering*, 30(6):659–680, 2014.

[12] Nikoo R Saber, Nigel B Wood, AD Gosman, Robert D Merrifield, Guang-Zhong Yang, Clare L Charrier, Peter D Gatehouse, and David N Firmin. Progress towards patient-specific computational flow modeling of the left heart via combination of magnetic resonance imaging with computational fluid dynamics. *Annals of biomedical engineering*, 31(1):42–52, 2003.

[13] Siamak N Doost, Dhanjoo Ghista, Boyang Su, Liang Zhong, and Yosry S Morsi. Heart blood flow simulation: a perspective review. *Biomedical engineering online*, 15(1):1–28, 2016.

[14] MA Castro, Christopher M Putman, and JR Cebral. Computational fluid dynamics modeling of intracranial aneurysms: effects of parent artery segmentation on intra-aneurysmal hemodynamics. *American Journal of Neuroradiology*, 27(8):1703–1709, 2006.

[15] David A Steinman, Jaques S Milner, Chris J Norley, Stephen P Lownie, and David W Holdsworth. Image-based computational simulation of flow dynamics in a giant intracranial aneurysm. *American Journal of Neuroradiology*, 24(4):559–566, 2003.

[16] Theodorus MJ van Bakel, Kevin D Lau, Jennifer Hirsch-Romano, Santi Trimarchi, Adam L Dorfman, and C Alberto Figueroa. Patient-specific

modeling of hemodynamics: supporting surgical planning in a fontan circulation correction. *Journal of cardiovascular translational research*, 11(2):145–155, 2018.

[17] Charles A Taylor, Thomas JR Hughes, and Christopher K Zarins. Finite element modeling of blood flow in arteries. *Computer methods in applied mechanics and engineering*, 158(1-2):155–196, 1998.

[18] Heartflow. https://www.heartflow.com, 2022. Accessed: 09.06.2022.

[19] Zhongzhao Teng, Gador Canton, Chun Yuan, Marina Ferguson, Chun Yang, Xueying Huang, Jie Zheng, Pamela K Woodard, and Dalin Tang. 3d critical plaque wall stress is a better predictor of carotid plaque rupture sites than flow shear stress: an in vivo mri-based 3d fsi study. 2010.

[20] Timothy J Gundert, Alison L Marsden, Weiguang Yang, and John F LaDisa Jr. Optimization of cardiovascular stent design using computational fluid dynamics. 2012.

[21] Nic Smith, Adelaide de Vecchi, Matthew McCormick, David Nordsletten, Oscar Camara, Alejandro F Frangi, Hervé Delingette, Maxime Sermesant, Jatin Relan, Nicholas Ayache, et al. euheart: personalized and integrated cardiac care using patient-specific cardiovascular modelling. *Interface focus*, 1(3):349–364, 2011.

[22] F Auricchio, M Conti, A Lefieux, S Morganti, A Reali, F Sardanelli, F Secchi, S Trimarchi, and A Veneziani. Patient-specific analysis of post-operative aortic hemodynamics: a focus on thoracic endovascular repair (tevar). *Computational Mechanics*, 54(4):943–953, 2014.

[23] Boyi Yang, Bill Gogas, Gaetano Esposito, Olivia Hung, Emad Rasoul Arzrumly, Marina Piccinelli, Spencer King, Don Giddens, Alessandro Veneziani, and Habib Samady. Novel in-human four dimensional wall shear stress calculation of a coronary bioresorbable scaffold using optical coherence tomography images and blood flow simulations. *Journal of the American College of Cardiology*, 65(10S):A1832–A1832, 2015.

[24] Marina Piccinelli, Alessandro Veneziani, David A Steinman, Andrea Remuzzi, and Luca Antiga. A framework for geometric analysis of vascular structures: application to cerebral aneurysms. *IEEE transactions on medical imaging*, 28(8):1141–1155, 2009.

[25] Michael Markl, Alex Frydrychowicz, Sebastian Kozerke, Mike Hope, and Oliver Wieben. 4d flow mri. *Journal of Magnetic Resonance Imaging*, 36(5):1015–1036, 2012.

[26] Adam Updegrove, Nathan M Wilson, Jameson Merkow, Hongzhi Lan, Alison L Marsden, and Shawn C Shadden. Simvascular: an open source pipeline for cardiovascular simulation. *Annals of Biomedical Engineering*, 45(3):525–541, 2017.

[27] Diego Gallo, Gianluca De Santis, Federica Negri, Daniele Tresoldi, Raffaele Ponzini, Diana Massai, MA Deriu, Patrick Segers, Benedict Verhegghe, Giovanna Rizzo, et al. On the use of in vivo measured flow rates as boundary conditions for image-based hemodynamic models of the human aorta: implications for indicators of abnormal flow. *Annals of Biomedical Engineering*, 40(3):729–741, 2012.

[28] Alberto Marzo, Pankaj Singh, Philippe Reymond, Nikos Stergiopulos, Umang Patel, and Rodney Hose. Influence of inlet boundary conditions on the local haemodynamics of intracranial aneurysms. *Computer methods in biomechanics and biomedical engineering*, 12(4):431–444, 2009.

[29] Joong Yull Park, Chan Young Park, Chang Mo Hwang, Kyung Sun, and Byoung Goo Min. Pseudo-organ boundary conditions applied to a computational fluid dynamics model of the human aorta. *Computers in biology and medicine*, 37(8):1063–1072, 2007.

[30] Luca Formaggia, Daniele Lamponi, Massimiliano Tuveri, and Alessandro Veneziani. Numerical modeling of 1d arterial networks coupled with a lumped parameters description of the heart. *Computer methods in biomechanics and biomedical engineering*, 9(5):273–288, 2006.

[31] Hyun Jin Kim, Irene E Vignon-Clementel, C Alberto Figueroa, John F LaDisa, Kenneth E Jansen, Jeffrey A Feinstein, and Charles A Taylor. On coupling a lumped parameter heart model and a three-dimensional finite element aorta model. *Annals of Biomedical Engineering*, 37(11):2153–2169, 2009.

[32] Irene E Vignon-Clementel, CA Figueroa, KE Jansen, and CA Taylor. Outflow boundary conditions for 3d simulations of non-periodic blood flow and pressure fields in deformable arteries. *Computer methods in biomechanics and biomedical engineering*, 13(5):625–640, 2010.

[33] Ji Young Moon, Dae Chul Suh, Yong Sang Lee, Young Woo Kim, and Joon Sang Lee. Considerations of blood properties, outlet boundary conditions and energy loss approaches in computational fluid dynamics modeling. *Neurointervention*, 9(1):1, 2014.

[34] Jean-Frédéric Gerbeau, Marina Vidrascu, and Pascal Frey. Fluid–structure interaction in blood flows on geometries based on medical imaging. *Computers & Structures*, 83(2-3):155–165, 2005.

[35] Charles A Taylor, Christopher P Cheng, Leandro A Espinosa, Beverly T Tang, David Parker, and Robert J Herfkens. In vivo quantification of blood flow and wall shear stress in the human abdominal aorta during lower limb exercise. *Annals of biomedical engineering*, 30(3):402–408, 2002.

[36] Yubing Shi, Patricia Lawford, and Rodney Hose. Review of zero-d and 1-d models of blood flow in the cardiovascular system. *Biomedical engineering online*, 10(1):1–38, 2011.

[37] Nicolaas Westerhof, Frederik Bosman, Cornelis J De Vries, and Abraham Noordergraaf. Analog studies of the human systemic arterial tree. *Journal of biomechanics*, 2(2):121–143, 1969.

[38] Alena Jonášová and Jan Vimmr. On the relevance of boundary conditions and viscosity models in blood flow simulations in patient-specific aorto-coronary bypass models. *International Journal for Numerical Methods in Biomedical Engineering*, 37(4):e3439, 2021.

[39] Nicolaas Westerhof, GIJS Elzinga, and Pieter Sipkema. An artificial arterial system for pumping hearts. *Journal of applied physiology*, 31(5):776–781, 1971.

[40] Frank Otto. Die grundform des arteriellen pulses. *Zeitung fur Biologie*, 37:483–586, 1899.

[41] John KJ Li. *The arterial circulation: physical principles and clinical applications*. Springer Science & Business Media, 2000.

[42] Nikos Stergiopulos, Berend E Westerhof, and Nico Westerhof. Total arterial inertance as the fourth element of the windkessel model. *American Journal of Physiology-Heart and Circulatory Physiology*, 276(1):H81–H88, 1999.

[43] Hyun Jin Kim, IE Vignon-Clementel, JS Coogan, CA Figueroa, KE Jansen, and CA Taylor. Patient-specific modeling of blood flow and pressure in human coronary arteries. *Annals of biomedical engineering*, 38(10):3195–3209, 2010.

[44] Irene E Vignon-Clementel, C Alberto Figueroa, Kenneth E Jansen, and Charles A Taylor. Outflow boundary conditions for three-dimensional finite element modeling of blood flow and pressure in arteries. *Computer Methods in Applied Mechanics and Engineering*, 195(29-32):3776–3796, 2006.

[45] R Balossino, Giancarlo Pennati, Francesco Migliavacca, Luca Formaggia, A Veneziani, M Tuveri, and G Dubini. Computational models to predict stenosis growth in carotid arteries: which is the role of boundary conditions? *Computer methods in biomechanics and biomedical engineering*, 12(1):113–123, 2009.

[46] Amanda Randles, David H Frakes, and Jane A Leopold. Computational fluid dynamics and additive manufacturing to diagnose and treat cardiovascular disease. *Trends in biotechnology*, 35(11):1049–1061, 2017.

[47] Liang Zhong, Jun-Mei Zhang, Boyang Su, Ru San Tan, John C Allen, and Ghassan S Kassab. Application of patient-specific computational fluid dynamics in coronary and intra-cardiac flow simulations: Challenges and opportunities. *Frontiers in physiology*, 9:742, 2018.

[48] Eun-Ok Jung and Wan-Ho Lee. Lumped parameter models of cardiovascular circulation in normal and arrhythmia cases. *Journal of the Korean Mathematical Society*, 43(4):885–897, 2006.

[49] Jonathan P Mynard, Daniel J Penny, and Joseph J Smolich. Scalability and in vivo validation of a multiscale numerical model of the left coronary circulation. *American Journal of Physiology-Heart and Circulatory Physiology*, 306(4):H517–H528, 2014.

[50] Cecil D Murray. The physiological principle of minimum work: I. the vascular system and the cost of blood volume. *Proceedings of the national academy of sciences of the united states of america*, 12(3):207, 1926.

[51] Alessandro Boccadifuoco, Alessandro Mariotti, Katia Capellini, Simona Celi, and Maria Vittoria Salvetti. Validation of numerical simulations of thoracic aorta hemodynamics: comparison with in vivo measurements and stochastic sensitivity analysis. *Cardiovascular Engineering and Technology*, 9(4):688–706, 2018.

[52] Massimiliano Mercuri. Tuning of boundary conditions parameters for hemodynamics simulation using patient data. PhD thesis, University of Sheffield, 2019.

[53] Christopher J Arthurs, Nan Xiao, Philippe Moireau, Tobias Schaeffter, and C Alberto Figueroa. A flexible framework for sequential estimation of model parameters in computational hemodynamics. *Advanced Modeling and Simulation in Engineering Sciences*, 7(1):1–37, 2020.

[54] Justin S Tran, Daniele E Schiavazzi, Abhay B Ramachandra, Andrew M Kahn, and Alison L Marsden. Automated tuning for parameter identification and uncertainty quantification in multi-scale coronary simulations. *Computers & fluids*, 142:128–138, 2017.

[55] Daniele E Schiavazzi, Alessia Baretta, Giancarlo Pennati, Tain-Yen Hsia, and Alison L Marsden. Patient-specific parameter estimation in single-ventricle lumped circulation models under uncertainty. *International Journal for Numerical Methods in Biomedical Engineering*, 33(3):e02799, 2017.

[56] Mirko Bonfanti, Gaia Franzetti, Gabriele Maritati, Shervanthi Homer-Vanniasinkam, Stavroula Balabani, and Vanessa Díaz-Zuccarini. Patient-specific haemodynamic simulations of complex aortic dissections informed by commonly available clinical datasets. *Medical Engineering & Physics*, 71:45–55, 2019.

[57] Ryan L Spilker and Charles A Taylor. Tuning multidomain hemodynamic simulations to match physiological measurements. *Annals of Biomedical Engineering*, 38(8):2635–2648, 2010.

[58] Nan Xiao, Jordi Alastruey, and C Alberto Figueroa. A systematic comparison between 1-d and 3-d hemodynamics in compliant arterial models. *International journal for numerical methods in biomedical engineering*, 30(2):204–231, 2014.

[59] Mona Alimohammadi, Obiekezie Agu, Stavroula Balabani, and Vanessa Díaz-Zuccarini. Development of a patient-specific simulation tool to analyse aortic dissections: assessment of mixed patient-specific flow and pressure boundary conditions. *Medical engineering & physics*, 36(3):275–284, 2014.

[60] Guillaume Troianowski, Charles A Taylor, Jeffrey A Feinstein, and Irene E Vignon-Clementel. Three-dimensional simulations in glenn patients: clinically based boundary conditions, hemodynamic results and sensitivity to input data. *Journal of biomechanical engineering*, 133(11), 2011.

[61] Feng Huang and Shunv Ying. On-line parameter identification of the lumped arterial system model: A simulation study. *Plos one*, 15(7):e0236012, 2020.

[62] Rajnesh Lal, Bijan Mohammadi, and Franck Nicoud. Data assimilation for identification of cardiovascular network characteristics. *International Journal for Numerical Methods in Biomedical Engineering*, 33(5):e2824, 2017.

[63] Daniel Canuto, Joe L Pantoja, Joyce Han, Erik P Dutson, and Jeff D Eldredge. An ensemble kalman filter approach to parameter estimation for patient-specific cardiovascular flow modeling. *Theoretical and Computational Fluid Dynamics*, pages 1–24, 2020.

[64] Huan Huang, Ming Yang, Wangfu Zang, Shunjie Wu, and Yafei Pang. In vitro identification of four-element windkessel models based on iterated unscented kalman filter. *IEEE transactions on biomedical engineering*, 58(9):2672–2680, 2011.

[65] Marta D'Elia and Alessandro Veneziani. Uncertainty quantification for data assimilation in a steady incompressible navier-stokes problem. *ESAIM: Mathematical Modelling and Numerical Analysis*, 47(4):1037–1057, 2013.

[66] Paris Perdikaris and George Em Karniadakis. Model inversion via multi-fidelity bayesian optimization: a new paradigm for parameter estimation in haemodynamics, and beyond. *Journal of The Royal Society Interface*, 13(118):20151107, 2016.

[67] Guy Chavent. *Nonlinear least squares for inverse problems: theoretical foundations and step-by-step guide for applications*. Springer Science & Business Media, 2010.

[68] H Thomas Banks and Karl Kunisch. *Estimation techniques for distributed parameter systems*. Springer Science & Business Media, 2012.

[69] Rodrigo M Romarowski, Adrien Lefieux, Simone Morganti, Alessandro Veneziani, and Ferdinando Auricchio. Patient-specific cfd modelling in the thoracic aorta with pc-mri–based boundary conditions: A least-square three-element windkessel approach. *International Journal for Numerical Methods in Biomedical Engineering*, 34(11):e3134, 2018.

[70] David Nolte and Cristóbal Bertoglio. Inverse problems in blood flow modeling: A review. *International Journal for Numerical Methods in Biomedical Engineering*, pages e3613–e3613, 2022.

[71] Li Kuo Tan, Robert A McLaughlin, Einly Lim, Yang Faridah Abdul Aziz, and Yih Miin Liew. Fully automated segmentation of the left ventricle in cine cardiac mri using neural network regression. *Journal of Magnetic Resonance Imaging*, 48(1):140–152, 2018.

[72] Mikael Mortensen and Kristian Valen-Sendstad. Oasis: a high-level/high-performance open source navier–stokes solver. *Computer physics communications*, 188:177–188, 2015.

[73] Jorge Tiago, Telma Guerra, and Adélia Sequeira. A velocity tracking approach for the data assimilation problem in blood flow simulations. *International Journal for Numerical Methods in Biomedical Engineering*, 33(10):e2856, 2017.

[74] Taha S Koltukluoğlu and Pablo J Blanco. Boundary control in computational haemodynamics. *Journal of Fluid Mechanics*, 847:329–364, 2018.

[75] Zakia Zainib, Francesco Ballarin, Stephen Fremes, Piero Triverio, Laura Jiménez-Juan, and Gianluigi Rozza. Reduced order methods for parametric optimal flow control in coronary bypass grafts, toward patient-specific data assimilation. *International Journal for Numerical Methods in Biomedical Engineering*, 37(12):e3367, 2021.

[76] B Deswysen, AA Charlier, and Michel Gevers. Quantitative evaluation of the systemic arterial bed by parameter estimation of a simple model. *Medical and Biological Engineering and Computing*, 18(2):153–166, 1980.

[77] S Grivet-Talocia. Package macromodeling via time-domain vector fitting. *IEEE Microwave and wireless components letters*, 13(11):472–474, 2003.

[78] Tommaso Bradde, Samuel Chevalier, Marco De Stefano, Stefano Grivet-Talocia, and Luca Daniel. Handling initial conditions in vector fitting for real time modeling of power system dynamics. *Energies*, 14(9):2471, 2021.

[79] Stefano Grivet-Talocia and Bjorn Gustavsen. *Passive macromodeling: Theory and applications*. John Wiley & Sons, 2015.

[80] Andrea Manzoni, Alfio Quarteroni, and Sandro Salsa. Optimal control of partial differential equations.

[81] Alfio Quarteroni and Silvia Quarteroni. *Numerical models for differential problems*, volume 2. Springer, 2009.

[82] George Bachman and Lawrence Narici. *Functional analysis*. Courier Corporation, 2000.

[83] Lawrence C Evans. *Partial differential equations*, volume 19. American Mathematical Soc., 2010.

[84] Wei Leng, Lili Ju, Max Gunzburger, Stephen Price, and Todd Ringler. A parallel high-order accurate finite element nonlinear stokes ice sheet model and benchmark experiments. *Journal of Geophysical Research: Earth Surface*, 117(F1), 2012.

[85] Daniele Boffi, Franco Brezzi, and Michel Fortin. Finite elements for the stokes problem. In *Mixed finite elements, compatibility conditions, and applications*, pages 45–100. Springer, 2008.

[86] Cedric Taylor and Paul Hood. A numerical solution of the navier-stokes equations using the finite element technique. *Computers & Fluids*, 1(1):73–100, 1973.

[87] Franco Brezzi. On the existence, uniqueness and approximation of saddle-point problems arising from lagrangian multipliers. *Publications mathématiques et informatique de Rennes*, (S4):1–26, 1974.

[88] Singiresu S Rao. *The finite element method in engineering*. Butterworth-heinemann, 2017.

[89] ACL Barnard, WA Hunt, WP Timlake, and E Varley. A theory of fluid flow in compliant tubes. *Biophysical journal*, 6(6):717–724, 1966.

[90] Johnny T Ottesen, Mette S Olufsen, and Jesper K Larsen. *Applied mathematical models in human physiology*. SIAM, 2004.

[91] Thomas JR Hughes and J Lubliner. On the one-dimensional theory of blood flow in the larger vessels. *Mathematical Biosciences*, 18(1-2):161–170, 1973.

[92] Jordi Alastruey, Kim H. Parker, and Spencer J. Sherwin. *Arterial pulse wave haemodynamics*, pages 401–443. Virtual PiE Led t/a BHR Group, October 2012.

[93] Jordi Alastruey, Ashraf W Khir, Koen S Matthys, Patrick Segers, Spencer J Sherwin, Pascal R Verdonck, Kim H Parker, and Joaquim Peiró. Pulse wave propagation in a model human arterial network: assessment of 1-d visco-elastic simulations against in vitro measurements. *Journal of biomechanics*, 44(12):2250–2258, 2011.

[94] Alfio Quarteroni and Luca Formaggia. Mathematical modelling and numerical simulation of the cardiovascular system. *Handbook of numerical analysis*, 12:3–127, 2004.

[95] Randall J LeVeque and Randall J Leveque. *Numerical methods for conservation laws*, volume 214. Springer, 1992.

[96] Bernardo Cockburn and Chi-Wang Shu. The local discontinuous galerkin method for time-dependent convection-diffusion systems. *SIAM Journal on Numerical Analysis*, 35(6):2440–2463, 1998.

[97] Maria Strazzullo, Francesco Ballarin, Renzo Mosetti, and Gianluigi Rozza. Model reduction for parametrized optimal control problems in environmental marine sciences and engineering. *SIAM Journal on Scientific Computing*, 40(4):B1055–B1079, 2018.

[98] Francesco Ballarin, Elena Faggiano, Andrea Manzoni, Alfio Quarteroni, Gianluigi Rozza, Sonia Ippolito, Carlo Antona, and Roberto Scrofani. Numerical modeling of hemodynamics scenarios of patient-specific coronary artery bypass grafts. *Biomechanics and modeling in mechanobiology*, 16(4):1373–1399, 2017.

[99] Toni Lassila, Andrea Manzoni, Alfio Quarteroni, and Gianluigi Rozza. A reduced computational and geometrical framework for inverse problems in hemodynamics. *International journal for numerical methods in biomedical engineering*, 29(7):741–776, 2013.

[100] Zakia Zainib, Francesco Ballarin, Stephen Fremes, Piero Triverio, Laura Jiménez-Juan, and Gianluigi Rozza. Reduced order methods for parametric optimal flow control in coronary bypass grafts, towards patient-specific data assimilation. *International Journal for Numerical Methods in Biomedical Engineering*, page e3367, 2019.

[101] Alfio Quarteroni and Gianluigi Rozza. Optimal control and shape optimization of aorto-coronaric bypass anastomoses. *Mathematical Models and Methods in Applied Sciences*, 13(12):1801–1823, 2003.

[102] Luca Dede. Optimal flow control for navier–stokes equations: drag minimization. *International Journal for Numerical Methods in Fluids*, 55(4):347–366, 2007.

[103] Alfio Quarteroni, Gianluigi Rozza, and Annalisa Quaini. Reduced basis methods for optimal control of advection-diffusion problems. Technical report, RAS and University of Houston, 2007.

[104] Alfio Quarteroni, Gianluigi Rozza, Luca Dedè, and Annalisa Quaini. Numerical approximation of a control problem for advection-diffusion processes. In *IFIP Conference on System Modeling and Optimization*, pages 261–273. Springer, 2005.

[105] Yohei Ogawa and Mutsuto Kawahara. Shape optimization of body located in incompressible viscous flow based on optimal control theory. *International Journal of Computational Fluid Dynamics*, 17(4):243–251, 2003.

[106] J Monnier. Variational data assimilation, from optimal control to large scale data assimilation. In *Open Learning Resources INPT*. Citeseer, 2013.

[107] AW Heemink and IDM Metzelaar. Data assimilation into a numerical shallow water flow model: a stochastic optimal control approach. *Journal of Marine Systems*, 6(1-2):145–158, 1995.

[108] Thomas Richter and Thomas Wick. Optimal control and parameter estimation for stationary fluid-structure interaction problems. *SIAM Journal on Scientific Computing*, 35(5):B1085–B1104, 2013.

[109] Kathrin Hatz, Johannes P Schloder, and Hans Georg Bock. Estimating parameters in optimal control problems. *SIAM Journal on Scientific Computing*, 34(3):A1707–A1728, 2012.

[110] Umberto Morbiducci, Diego Gallo, Diana Massai, Filippo Consolo, Raffaele Ponzini, Luca Antiga, Cristina Bignardi, Marco A Deriu, and Alberto Redaelli. Outflow conditions for image-based hemodynamic models of the carotid bifurcation: implications for indicators of abnormal flow. *Journal of Biomechanical Engineering*, 132(9), 2010.

[111] S Pirola, Z Cheng, OA Jarral, DP O'Regan, JR Pepper, T Athanasiou, and XY Xu. On the choice of outlet boundary conditions for patient-specific analysis of aortic flow using computational fluid dynamics. *Journal of biomechanics*, 60:15–21, 2017.

[112] Alina G Van der Giessen, Harald C Groen, Pierre-Andre Doriot, Pim J De Feyter, Antonius FW Van der Steen, Frans N Van de Vosse, Jolanda J Wentzel, and Frank JH Gijsen. The influence of boundary conditions on wall shear stress distribution in patients specific coronary trees. *Journal of Biomechanics*, 44(6):1089–1095, 2011.

[113] Meena Sankaranarayanan, Leok Poh Chua, Dhanjoo N Ghista, and Yong Seng Tan. Computational model of blood flow in the aorto-coronary bypass graft. *Biomedical Engineering online*, 4(1):14, 2005.

[114] Sethuraman Sankaran, Mahdi Esmaily Moghadam, Andrew M Kahn, Elaine E Tseng, Julius M Guccione, and Alison L Marsden. Patient-specific multiscale modeling of blood flow for coronary artery bypass graft surgery. *Annals of Biomedical Engineering*, 40(10):2228–2242, 2012.

[115] Charles A Taylor, Timothy A Fonte, and James K Min. Computational fluid dynamics applied to cardiac computed tomography for noninvasive quantification of fractional flow reserve: scientific basis. *Journal of the American College of Cardiology*, 61(22):2233–2241, 2013.

[116] Xinyang Ge, Zhaofang Yin, Yuqi Fan, Yuri Vassilevski, and Fuyou Liang. A multi-scale model of the coronary circulation applied to investigate transmural myocardial flow. *International Journal for Numerical Methods in Biomedical Engineering*, 34(10):e3123, 2018.

[117] Leopold Grinberg and George Em Karniadakis. Outflow boundary conditions for arterial networks with multiple outlets. *Annals of biomedical engineering*, 36(9):1496–1514, 2008.

[118] Nico Westerhof, Jan-Willem Lankhaar, and Berend E Westerhof. The arterial windkessel. *Medical & biological engineering & computing*, 47(2):131–141, 2009.

[119] Federico Negri, Andrea Manzoni, and Gianluigi Rozza. Reduced basis approximation of parametrized optimal flow control problems for the stokes equations. *Computers & Mathematics with Applications*, 69(4):319–336, 2015.

[120] Jorge Tiago, Alberto Gambaruto, and Adelia Sequeira. Patient-specific blood flow simulations: setting dirichlet boundary conditions for minimal error with respect to measured data. *Mathematical modelling of natural phenomena*, 9(6):98–116, 2014.

[121] Jacques-Louis Lions. *Some aspects of the optimal control of distributed parameter systems*. SIAM, 1972.

[122] JL Lions. Optimal control of systems governed by partial differential equations, spring–verlag, 1971.

[123] Michael Hinze, René Pinnau, Michael Ulbrich, and Stefan Ulbrich. *Optimization with PDE constraints*, volume 23. Springer Science & Business Media, 2008.

[124] Max D Gunzburger. *Perspectives in flow control and optimization*. SIAM, 2002.

[125] Daniele Boffi, Franco Brezzi, Michel Fortin, et al. *Mixed finite element methods and applications*, volume 44. Springer, 2013.

[126] Pavel B Bochev and Max D Gunzburger. *Least-squares finite element methods*, volume 166. Springer Science & Business Media, 2009.

[127] Enrique Zuazua. Propagation, observation, control and numerical approximation of waves. *SIAM Review*, 47(2):197–243, 2005.

[128] Bijan Mohammadi and Olivier Pironneau. *Applied shape optimization for fluids*. OUP Oxford, 2009.

[129] Roger Fletcher. *Practical methods of optimization*. John Wiley & Sons, 2013.

[130] Stephen Wright, Jorge Nocedal, et al. Numerical optimization. *Springer Science*, 35(67-68):7, 1999.

[131] Hang Si. Tetgen, a delaunay-based quality tetrahedral mesh generator. *ACM Transactions on Mathematical Software (TOMS)*, 41(2):1–36, 2015.

[132] Mansour Razminia, Atul Trivedi, Janos Molnar, Monther Elbzour, Mayra Guerrero, Yasser Salem, Aziz Ahmed, Sandeep Khosla, and David L Lubell. Validation of a new formula for mean arterial pressure calculation: the new formula is superior to the standard formula. *Catheterization and cardiovascular interventions*, 63(4):419–425, 2004.

[133] Martin Alnæs, Jan Blechta, Johan Hake, August Johansson, Benjamin Kehlet, Anders Logg, Chris Richardson, Johannes Ring, Marie E Rognes, and Garth N Wells. The fenics project version 1.5. *Archive of Numerical Software*, 3(100), 2015.

[134] Anders Logg, Kent-Andre Mardal, and Garth Wells. *Automated solution of differential equations by the finite element method: The FEniCS book*, volume 84. Springer Science & Business Media, 2012.

[135] Kazufumi Ito and Karl Kunisch. *Lagrange multiplier approach to variational problems and applications*. SIAM, 2008.

[136] Martin Stoll and Andy Wathen. All-at-once solution of time-dependent stokes control. *Journal of Computational Physics*, 232(1):498–515, 2013.

[137] multiphenics – easy prototyping of multiphysics problems in fenics. https://mathlab.sissa.it/multiphenics, 2021. Accessed: 21.03.2021.

[138] Patrick R Amestoy, Iain S Duff, Jean-Yves L'Excellent, and Jacko Koster. A fully asynchronous multifrontal solver using distributed dynamic scheduling. *SIAM Journal on Matrix Analysis and Applications*, 23(1):15–41, 2001.

[139] Geoffrey B West, James H Brown, and Brian J Enquist. A general model for the origin of allometric scaling laws in biology. *Science*, 276(5309):122–126, 1997.

[140] Harald C Groen, Lenette Simons, Quirijn JA van den Bouwhuijsen, E Marielle H Bosboom, Frank JH Gijsen, Alina G van der Giessen, Frans N van de Vosse, Albert Hofman, Antonius FW van der Steen, Jacqueline CM Witteman, et al. Mri-based quantification of outflow boundary conditions for computational fluid dynamics of stenosed human carotid arteries. *Journal of Biomechanics*, 43(12):2332–2338, 2010.

[141] Bram Trachet, Joris Bols, Gianluca De Santis, Stefaan Vandenberghe, Bart Loeys, and Patrick Segers. The impact of simplified boundary conditions and aortic arch inclusion on cfd simulations in the mouse aorta: a comparison with mouse-specific reference data. *Journal of Biomechanical Engineering*, 133(12), 2011.

[142] Caroline Cheng, Frank Helderman, Dennie Tempel, Dolf Segers, Beerend Hierck, Rob Poelmann, Arie van Tol, Dirk J Duncker, Danielle Robbers-Visser, Nicolette TC Ursem, et al. Large variations in absolute wall shear stress levels within one species and between species. *Atherosclerosis*, 195(2):225–235, 2007.

[143] Robert S Reneman and Arnold PG Hoeks. Wall shear stress as measured in vivo: consequences for the design of the arterial system. *Medical & Biological Engineering & Computing*, 46(5):499–507, 2008.

[144] Mair Zamir, Paula Sinclair, and Thomas H Wonnacott. Relation between diameter and flow in major branches of the arch of the aorta. *Journal of Biomechanics*, 25(11):1303–1310, 1992.

[145] J Soulis, G Giannoglou, M Dimitrakopoulou, V Papaioannou, S Logothetides, and D Mikhailidis. Influence of oscillating flow on ldl transport and wall shear stress in the normal aortic arch. *The Open Cardiovascular Medicine Journal*, 3:128, 2009.

[146] Peter E Vincent, AM Plata, AAE Hunt, PD Weinberg, and SJ Sherwin. Blood flow in the rabbit aortic arch and descending thoracic aorta. *Journal of The Royal Society Interface*, 8(65):1708–1719, 2011.

[147] Mahdi Esmaily Moghadam, Yuri Bazilevs, Tain-Yen Hsia, Irene Vignon-Clementel, and Alison Marsden. A comparison of outlet boundary treatments for prevention of backflow divergence with relevance to blood flow simulations. *Computational Mechanics*, 48(3), 2011.

[148] Sanjay Pant, Benoit Fabrèges, J-F Gerbeau, and IE Vignon-Clementel. A methodological paradigm for patient-specific multi-scale cfd simulations: from clinical measurements to parameter estimates for individual analysis. *International journal for numerical methods in biomedical engineering*, 30(12):1614–1648, 2014.

[149] Petter Dyverfeldt, Malenka Bissell, Alex J Barker, Ann F Bolger, Carl-Johan Carlhäll, Tino Ebbers, Christopher J Francios, Alex Frydrychowicz, Julia Geiger, Daniel Giese, et al. 4d flow cardiovascular magnetic

resonance consensus statement. *Journal of Cardiovascular Magnetic Resonance*, 17(1):1–19, 2015.

[150] Jeffrey C Lagarias, James A Reeds, Margaret H Wright, and Paul E Wright. Convergence properties of the nelder–mead simplex method in low dimensions. *SIAM Journal on Optimization*, 9(1):112–147, 1998.

[151] WARREN K Laskey, H GRAHAM Parker, VICTOR A Ferrari, WILLIAM G Kussmaul, and ABRAHAM Noordergraaf. Estimation of total systemic arterial compliance in humans. *Journal of Applied Physiology*, 69(1):112–119, 1990.

[152] Parastou Eslami, Justin Tran, Zexi Jin, Julia Karady, Romina Sotoodeh, Michael T Lu, Udo Hoffmann, and Alison Marsden. Effect of wall elasticity on hemodynamics and wall shear stress in patient-specific simulations in the coronary arteries. *Journal of biomechanical engineering*, 142(2), 2020.

[153] Francisco J Contijoch, Michael Horowitz, Evan Masutani, Seth Kligerman, and Albert Hsiao. 4d flow vorticity visualization predicts regions of quantitative flow inconsistency for optimal blood flow measurement. *Radiology: Cardiothoracic Imaging*, 2(1):e190054, 2020.

[154] David M Martin, Eoin A Murphy, and Fergal J Boyle. Computational fluid dynamics analysis of balloon-expandable coronary stents: influence of stent and vessel deformation. *Medical engineering & physics*, 36(8):1047–1056, 2014.

[155] Bjørn Gustavsen. Improving the pole relocating properties of vector fitting. *IEEE Transactions on Power Delivery*, 21(3):1587–1592, 2006.

[156] Piero Triverio. 8 vector fitting. *System-and Data-Driven Methods and Algorithms*, page 275, 2021.

[157] Patrick Segers, ER Rietzschel, ML De Buyzere, N Stergiopulos, N Westerhof, LM Van Bortel, Thierry Gillebert, and PR Verdonck. Three-and four-element windkessel models: assessment of their fitting performance in a large cohort of healthy middle-aged individuals. *Proceedings of the Institution of Mechanical Engineers, Part H: Journal of Engineering in Medicine*, 222(4):417–428, 2008.

[158] Jordi Alastruey, K. H. Parker, J. Peiro, and S. J. Sherwin. Lumped parameter outflow models for 1-d blood flow simulations: Effect on pulse waves and parameter estimation. *Communications in Computational Physics*, 4(2):317–336, August 2008.

[159] Sally Epstein, Marie Willemet, Phil J. Chowienczyk, and Jordi Alastruey. Reducing the number of parameters in 1d arterial blood flow modeling: less is more for patient-specific simulations. *American Journal of*

Physiology-Heart and Circulatory Physiology, 309(1):H222–H234, 2015. PMID: 25888513.

[160] Peter H Charlton, Patrick Celka, Bushra Farukh, Phil Chowienczyk, and Jordi Alastruey. Assessing mental stress from the photoplethysmogram: a numerical study. *Physiological measurement*, 39(5):054001, 2018.

[161] Patrick Celka, Peter H Charlton, Bushra Farukh, Philip Chowienczyk, and Jordi Alastruey. Influence of mental stress on the pulse wave features of photoplethysmograms. *Healthcare technology letters*, 7(1):7, 2020.

[162] Murray R Spiegel. *Laplace transforms*. McGraw-Hill New York, 1965.

[163] Leon O Chua, Charles A Desoer, and Ernest S Kuh. *Linear and nonlinear circuits*. McGraw-Hill College, 1987.

[164] Bjorn Gustavsen and Adam Semlyen. Rational approximation of frequency domain responses by vector fitting. *IEEE Transactions on power delivery*, 14(3):1052–1061, 1999.

[165] Giulio Antonini. Spice equivalent circuits of frequency-domain responses. *IEEE transactions on electromagnetic compatibility*, 45(3):502–512, 2003.

[166] Simulink Documentation. Simulation and model-based design, 2020.

[167] Jordi Alastruey, Nan Xiao, Henry Fok, Tobias Schaeffter, and C Alberto Figueroa. On the impact of modelling assumptions in multi-scale, subject-specific models of aortic haemodynamics. *Journal of The Royal Society Interface*, 13(119):20160073, 2016.

[168] Jorge Mariscal-Harana, Peter H Charlton, Samuel Vennin, Jorge Aramburu, Mateusz Cezary Florkow, Arna van Engelen, Torben Schneider, Hubrecht de Bliek, Bram Ruijsink, Israel Valverde, et al. Estimating central blood pressure from aortic flow: development and assessment of algorithms. *American Journal of Physiology-Heart and Circulatory Physiology*, 320(2):H494–H510, 2021.

[169] Thomas Weber, Siegfried Wassertheurer, Martin Rammer, Edwin Maurer, Bernhard Hametner, Christopher C Mayer, Johannes Kropf, and Bernd Eber. Validation of a brachial cuff-based method for estimating central systolic blood pressure. *Hypertension*, 58(5):825–832, 2011.

[170] P Syamasundar Rao. Coarctation of the aorta. *Current cardiology reports*, 7(6):425–434, 2005.

[171] Christian Apitz, Gary D Webb, and Andrew N Redington. Tetralogy of fallot. *The Lancet*, 374(9699):1462–1471, 2009.

[172] Thomas F Sherman. On connecting large vessels to small. the meaning of murray's law. *The Journal of general physiology*, 78(4):431–453, 1981.

[173] C Chnafa, O Brina, VM Pereira, and DA Steinman. Better than nothing: a rational approach for minimizing the impact of outflow strategy on cerebrovascular simulations. *American Journal of Neuroradiology*, 39(2):337–343, 2018.

[174] Ghassan S Kassab and Yuan-Cheng B Fung. The pattern of coronary arteriolar bifurcations and the uniform shear hypothesis. *Annals of biomedical engineering*, 23(1):13–20, 1995.

[175] Theodore A Wilson. Design of the bronchial tree. *Nature*, 213(5077):668–669, 1967.

[176] M Zamir and N Brown. Arterial branching in various parts of the cardiovascular system. *American Journal of Anatomy*, 163(4):295–307, 1982.

[177] Katherine A McCulloh, John S Sperry, and Frederick R Adler. Water transport in plants obeys murray's law. *Nature*, 421(6926):939–942, 2003.

[178] KA McCulloh, JS Sperry, and FR Adler. Murray's law and the hydraulic vs mechanical functioning of wood. *Functional Ecology*, 18(6):931–938, 2004.

[179] Katherine A McCulloh and John S Sperry. The evaluation of murray's law in psilotum nudum (psilotaceae), an analogue of ancestral vascular plants. *American Journal of Botany*, 92(6):985–989, 2005.

[180] M Zamir. Shear forces and blood vessel radii in the cardiovascular system. *The Journal of general physiology*, 69(4):449–461, 1977.

[181] Xiaomei Guo and Ghassan S Kassab. Distribution of stress and strain along the porcine aorta and coronary arterial tree. *American Journal of Physiology-Heart and Circulatory Physiology*, 286(6):H2361–H2368, 2004.

[182] Larry A Taber. An optimization principle for vascular radius including the effects of smooth muscle tone. *Biophysical journal*, 74(1):109–114, 1998.

[183] Page R Painter, Patrik Edén, and Hans-Uno Bengtsson. Pulsatile blood flow, shear force, energy dissipation and murray's law. *Theoretical Biology and Medical Modelling*, 3(1):1–10, 2006.

[184] Stefan B Lindström, Ganarupan Satha, and Anders Klarbring. Extension of murray's law including nonlinear mechanics of a composite artery wall. *Biomechanics and Modeling in Mechanobiology*, 14(1):83–91, 2015.

[185] David Stephenson and Duncan A Lockerby. A generalized optimization principle for asymmetric branching in fluidic networks. *Proceedings of the Royal Society A: Mathematical, Physical and Engineering Sciences*, 472(2191):20160451, 2016.

[186] Matin Golozar, Mohammad Sayed Razavi, and Ebrahim Shirani. Theoretical and computational investigation of optimal wall shear stress in bifurcations: a generalization of murray's law. *Scientia Iranica*, 24(5):2387–2395, 2017.

[187] Bruno Guerciotti, Christian Vergara, Sonia Ippolito, Alfio Quarteroni, Carlo Antona, and Roberto Scrofani. Computational study of the risk of restenosis in coronary bypasses. *Biomechanics and modeling in mechanobiology*, 16(1):313–332, 2017.

[188] Chang-Joon Lee, Nahoko Uemiya, Shoichiro Ishihara, Yu Zhang, and Yi Qian. A comparison of estimation methods for computational fluid dynamics outflow boundary conditions using patient-specific carotid artery. *Proceedings of the Institution of Mechanical Engineers, Part H: Journal of Engineering in Medicine*, 227(6):663–671, 2013.

[189] Yu Zhang, Toyoki Furusawa, Sheau Fung Sia, Mitsuo Umezu, and Yi Qian. Proposition of an outflow boundary approach for carotid artery stenosis cfd simulation. *Computer methods in biomechanics and biomedical engineering*, 16(5):488–494, 2013.

[190] Sheau Fung Sia, Xihai Zhao, Rui Li, Yu Zhang, Winston Chong, Le He, and Yu Chen. Evaluation of the carotid artery stenosis based on minimization of mechanical energy loss of the blood flow. *Proceedings of the Institution of Mechanical Engineers, Part H: Journal of Engineering in Medicine*, 230(11):1051–1058, 2016.

[191] Alison L Marsden, Jeffrey A Feinstein, and Charles A Taylor. A computational framework for derivative-free optimization of cardiovascular geometries. *Computer methods in applied mechanics and engineering*, 197(21-24):1890–1905, 2008.

[192] Henrik A. Kjeldsberg, Aslak W. Bergersen, and Kristian Valen-Sendstad. morphman: Automated manipulation of vascular geometries. *Journal of Open Source Software*, 4(35):1065, 2019.

[193] Luca Antiga, Marina Piccinelli, Lorenzo Botti, Bogdan Ene-Iordache, Andrea Remuzzi, and David A Steinman. An image-based modeling framework for patient-specific computational hemodynamics. *Medical & biological engineering & computing*, 46(11):1097–1112, 2008.

[194] Aslak W Bergersen, Henrik A Kjeldsberg, and Kristian Valen-Sendstad. A framework for automated and objective modification of tubular structures: Application to the internal carotid artery. *International journal for numerical methods in biomedical engineering*, 36(5):e3330, 2020.

[195] Timothy M Healy, Carol Lucas, and Ajit P Yoganathan. Noninvasive fluid dynamic power loss assessments for total cavopulmonary connections using the viscous dissipation function: a feasibility study. *J. Biomech. Eng.*, 123(4):317–324, 2001.

[196] JC Simo and F Armero. Unconditional stability and long-term behavior of transient algorithms for the incompressible navier-stokes and euler equations. *Computer Methods in Applied Mechanics and Engineering*, 111(1-2):111–154, 1994.

[197] Chris Doran, Steven R Gullans, Anthony Lasenby, Joan Lasenby, and William Fitzgerald. *Geometric algebra for physicists*. Cambridge University Press, 2003.

[198] R Horan and M Lavelle. The laplacian. *The University of Plymouth*, 4, 2005.

[199] R Byron Bird. Transport phenomena. *Appl. Mech. Rev.*, 55(1):R1–R4, 2002.

[200] Zhenglun Alan Wei, Michael Tree, Phillip M Trusty, Wenjun Wu, Shelly Singh-Gryzbon, and Ajit Yoganathan. The advantages of viscous dissipation rate over simplified power loss as a fontan hemodynamic metric. *Annals of biomedical engineering*, 46(3):404–416, 2018.

[201] Yutong Liu, Kerem Pekkan, S Casey Jones, and Ajit P Yoganathan. The effects of different mesh generation methods on computational fluid dynamic analysis and power loss assessment in total cavopulmonary connection. *J. Biomech. Eng.*, 126(5):594–603, 2004.

[202] Keesuk Ryu, Timothy M Healy, Ann E Ensley, Shiva Sharma, Carol Lucas, and Ajit P Yoganathan. Importance of accurate geometry in the study of the total cavopulmonary connection: computational simulations and in vitro experiments. *Annals of biomedical engineering*, 29(10):844–853, 2001.

[203] Merih Cibis, Kelly Jarvis, Michael Markl, Michael Rose, Cynthia Rigsby, Alex J Barker, and Jolanda J Wentzel. The effect of resolution on viscous dissipation measured with 4d flow mri in patients with fontan circulation: Evaluation using computational fluid dynamics. *Journal of biomechanics*, 48(12):2984–2989, 2015.

[204] Anand K Venkatachari, Sandra S Halliburton, Randolph M Setser, Richard D White, and George P Chatzimavroudis. Noninvasive quantification of fluid mechanical energy losses in the total cavopulmonary connection with magnetic resonance phase velocity mapping. *Magnetic resonance imaging*, 25(1):101–109, 2007.

[205] Alexander N Brooks and Thomas JR Hughes. Streamline upwind/petrov-galerkin formulations for convection dominated flows with particular emphasis on the incompressible navier-stokes equations. *Computer methods in applied mechanics and engineering*, 32(1-3):199–259, 1982.

[206] MO Khan, K Valen-Sendstad, and DA Steinman. Narrowing the expertise gap for predicting intracranial aneurysm hemodynamics: impact of solver numerics versus mesh and time-step resolution. *American Journal of Neuroradiology*, 36(7):1310–1316, 2015.

[207] Satish Balay, Kris Buschelman, William D Gropp, Dinesh Kaushik, Matthew G Knepley, L Curfman McInnes, Barry F Smith, and Hong Zhang. Petsc. *See http://www. mcs. anl. gov/petsc*, 2001.

[208] Simvascular cylinder example. https://simvascular.github.io/docsFlowSolver.html, 2022. Accessed: 12.06.2022.

[209] Abhay B Ramachandra, Andrew M Kahn, and Alison L Marsden. Patient-specific simulations reveal significant differences in mechanical stimuli in venous and arterial coronary grafts. *Journal of cardiovascular translational research*, 9(4):279–290, 2016.

[210] Haroon Zafar, Faisal Sharif, and Martin J Leahy. Measurement of the blood flow rate and velocity in coronary artery stenosis using intracoronary frequency domain optical coherence tomography: Validation against fractional flow reserve. *IJC Heart & Vasculature*, 5:68–71, 2014.

[211] Dawod Sharif, Amal Sharif-Rasslan, Camilia Shahla, and Edward G Abinader. Detection of severe left anterior descending coronary artery stenosis by transthoracic evaluation of resting coronary flow velocity dynamics. *Heart International*, 5(2), 2010.

[212] Yifang Zhou, Ghassan S Kassab, and Sabee Molloi. On the design of the coronary arterial tree: a generalization of murray's law. *Physics in Medicine & Biology*, 44(12):2929, 1999.

[213] James K Min, Charles A Taylor, Stephan Achenbach, Bon Kwon Koo, Jonathon Leipsic, Bjarne L Nørgaard, Nico J Pijls, and Bernard De Bruyne. Noninvasive fractional flow reserve derived from coronary ct angiography: clinical data and scientific principles. *Cardiovascular Imaging*, 8(10):1209–1222, 2015.

[214] Janet S Peterson. The reduced basis method for incompressible viscous flow calculations. *SIAM Journal on Scientific and Statistical Computing*, 10(4):777–786, 1989.

[215] Anindya Chatterjee. An introduction to the proper orthogonal decomposition. *Current science*, pages 808–817, 2000.

[216] Maria Strazzullo, Zakia Zainib, Francesco Ballarin, and Gianluigi Rozza. Reduced order methods for parametrized non-linear and time dependent optimal flow control problems, towards applications in biomedical and environmental sciences. In *Numerical Mathematics and Advanced Applications ENUMATH 2019*, pages 841–850. Springer, 2021.

[217] Maria Strazzullo, Francesco Ballarin, and Gianluigi Rozza. Pod–galerkin model order reduction for parametrized time dependent linear quadratic optimal control problems in saddle point formulation. *Journal of Scientific Computing*, 83(3):1–35, 2020.

[218] Mehran Mirramezani and Shawn C Shadden. A distributed lumped parameter model of blood flow. *Annals of Biomedical Engineering*, 48(12):2870–2886, 2020.

[219] Ryan Pewowaruk and Alejandro Roldán-Alzate. A distributed lumped parameter model of blood flow with fluid-structure interaction. *Biomechanics and Modeling in Mechanobiology*, 20(5):1659–1674, 2021.

[220] Taha Sabri Koltukluoğlu, Gregor Cvijetić, and Ralf Hiptmair. Harmonic balance techniques in cardiovascular fluid mechanics. In *International Conference on Medical Image Computing and Computer-Assisted Intervention*, pages 486–494. Springer, 2019.

[221] Taha Sabri Koltukluoğlu. Fourier spectral dynamic data assimilation: interlacing cfd with 4d flow mri. In *International Conference on Medical Image Computing and Computer-Assisted Intervention*, pages 741–749. Springer, 2019.

[222] David Gallagher, Audrey Adji, and Michael F O'Rourke. Validation of the transfer function technique for generating central from peripheral upper limb pressure waveform. *American journal of hypertension*, 17(11):1059–1067, 2004.

[223] Mingwu Gao, William C Rose, Barry Fetics, David A Kass, Chen-Huan Chen, and Ramakrishna Mukkamala. A simple adaptive transfer function for deriving the central blood pressure waveform from a radial blood pressure waveform. *Scientific reports*, 6(1):1–9, 2016.

[224] Peter H Charlton, Jorge Mariscal Harana, Samuel Vennin, Ye Li, Phil Chowienczyk, and Jordi Alastruey. Modeling arterial pulse waves in healthy aging: a database for in silico evaluation of hemodynamics and pulse wave indexes. *American Journal of Physiology-Heart and Circulatory Physiology*, 317(5):H1062–H1085, 2019.